Title
Advanced Imaging Spectroscopy and Chemical Sensing in Archaeometry and Archaeological Forensics

Author
Radpour, Roxanne

Publication Date
2019

Peer reviewed|Thesis/dissertation

UNIVERSITY OF CALIFORNIA

Los Angeles

Advanced Imaging Spectroscopy and Chemical Sensing in Archaeometry and Archaeological Forensics

A dissertation submitted in partial satisfaction

of the requirements for the degree

Doctor of Philosophy in Materials Science and Engineering

by

Roxanne Radpour

2019

ABSTRACT OF THE DISSERTATION

Advanced Imaging Spectroscopy and Chemical Sensing in Archaeometry and Archaeological Forensics

by

Roxanne Radpour
Doctor of Philosophy in Materials Science and Engineering
University of California, Los Angeles, 2019
Professor Ioanna Kakoulli, Chair

Archaeological materials science or archaeometry is the scientific study of material culture, which plays an important role in the development and interpretation of archaeological theory by establishing links between an object's materiality and its societal context. Driven by the complex nature of archaeological materials and the necessity to improve analysis, interpretation, and access of material culture and scientific research in the field, in the last decade there has been a significant advancement in instrumentation development for rapid, non-invasive and high-specificity materials characterization. To this end, imaging spectroscopy and portable chemical sensing modalities have played a revolutionary role in the identification and chemical mapping of constituent materials in ancient and historical wall paintings and other immovable artifacts.

In this research, different imaging and spectroscopic modalities are explored: direct-detection terahertz (THz) imaging, hyperspectral imaging spectroscopy (HSI), and high-resolution scanning reflectance spectroscopy. First, a novel direct-detection THz imaging system, adopted from biomedical imaging applications, was used to probe hierarchically-complex painting targets for sub-surface imaging of hidden decorative features and structural defects that are difficult to discern by X-ray and infrared imaging techniques. The

imaging system's deep signal penetration depth and high contrast sensitivity can successfully penetrate overlaying layers of strong signal scatterers such as lead white and chalk and to identify internal voids, hidden text, and topographic details of concealed iconography, which has important implications for future applications of this system on the study of wall paintings covered by whitewash or plaster layer(s).

Investigations of two different collections of painted artifacts were performed using novel imaging spectroscopy applications, supplemented by forensic photography and portable chemical sensing modalities, fiber-optic reflectance spectroscopy (FORS) and X-ray fluorescence (XRF) spectroscopy: (1) Cypriot wall paintings, and (2) Greco-Roman funerary portraits from Egypt. A comprehensive in situ characterization of Hellenistic, Roman and Byzantine Cypriot wall paintings in the region of Paphos, Cyprus was achieved for the first time, applying a non-invasive multi-scale approach, employing a commercial hyperspectral imaging (HSI) camera operated in reflectance and luminescence modes and a custom-made high-resolution scanning reflectance spectroscopy system developed and adapted for field research. The HSI and the scanning reflectance spectroscopy system offered complementary, powerful high-spectral and spatial resolution 3D data cubes to reconstruct the palette of Cypriot painters. From an archaeological materials science perspective, the characterization and mapping of pigments through derivative spectral analysis provided important information on pigment layering and mixtures used to produce complex hues and special optical effects, such as shading and translucency. Combined with FORS and XRF, these techniques offered fast, in-depth studies of large painted surfaces, inferring material and artistic choices and the chaîne opératoire of production technology. Similarly, the analysis of funerary portraits of ancient Egypt (first to fourth century AD) identified technological choices, materials selection and application methodology, revealing the vogue of Greco-Roman society.

From a materials engineering perspective, the study of these paintings lead to adaptations and development of novel methods of analysis: luminescence imaging spectroscopy was for the first time employed to collect and map luminescence signatures of Egyptian blue and madder lake, two of the most important synthetic pigments of antiquity, over painting sur-

faces; and the success of forensic and spectral imaging in producing luminescence/chemical maps across 2D surfaces led to the development of a streamlined, accessible methodology to construct luminescence-textured 3D models for new visualizations and analyses of high-relief/3D polychrome artifacts that feature photoluminescent pigments and conservation materials.

The dissertation of Roxanne Radpour is approved.

Meredith Cohen

John Delaney

Bruce Dunn

Jaime Marian

Ioanna Kakoulli, Committee Chair

University of California, Los Angeles

2019

To my parents,

who persisted with me in this adventure,

and for their ever-continuous love and support.

Table of Contents

List of Figures

Acknowledgements

In truth, I am very lucky and overwhelmed to be producing these acknowledgements. I had no idea upon starting this Ph.D. that I would embark on a journey that would introduce me to so many new wonderful mentors, collaborators, and friends, and I am beyond grateful to witness how my family and friends rose to the task of providing me the necessary support to see this degree through.

Thank you, Professor Ioanna Kakoulli, my amazing advisor and mentor, for giving me the opportunity to pursue this Ph.D. with you, a dream deeply entrenched in my mind for so many years, which I was able to realize by joining the Archaeomaterials Research Group. I will be forever grateful for the instruction and opportunities you provided and the skills you helped to foster over the years with much patience. Your passion in this field and drive for excellence has left an indelible mark.

Thank you, Dr. Christian Fischer, for engaging me in the most wonderful discussions about science (especially dark matter), teaching me the intricacies of working with Junior, and truly pushing me and my peers to be curious, strong scientists. I am so thankful to have been able to work with you throughout my Ph.D.; you have taught me so much.

The Archaeomaterials Research Group has been very supportive, and I have made many wonderful friends. Through this group, I have been fortunate to have the mentorship of Dr. Sergey Prikhodko and Dr. Magdalena Balonis-Sant. I am also so grateful to my close friends and previously fellow graduate students, Dr. Xiao Ma and Dr. Yuan Lin who were there with me from the beginning and helped mentor me to the end. Both are fantastic, inspiring researchers. Thank you to Karime Castillo and Xuanyi Wu for being such wonderful friends and support systems, two of the sweetest, most diligent and committed Ph.D. students I have ever met. Many thanks to Gabriel Gorelick, Fidel Ruiz Robles, Moupi Mukhopadhyay, Haroula Kyriacou, Dr. Krystal Cunningham, and the dedicated undergraduates of our research group who have provided kind words and support. I also wish to acknowledge the valuable support and resources of the Molecular and Nano Archaeology

Laboratory and the UCLA/Getty Conservation program for my research.

I am very grateful to all of the members of my doctoral committee, who served an important role in the course of my Ph.D. and for the extremely helpful guidance and feedback on my dissertation: Professors Meredith Cohen, Bruce Dunn, Jaime Marian, Vidvuds Ozolins, and Dr. John Delaney. I particularly want to recognize my committee member, the late Professor Warren Grundfest, who opened the door for me to explore terahertz imaging for cultural heritage science and allowed me to immerse within his research group where I was able to receive the very helpful instruction of Drs. Zachary Taylor, Shijun Sung, Neha Bajwa and Jim Garritano while pursuing terahertz imaging studies.

I must also give a heartfelt thanks to Professor Enrique Castro-Camus of the Applied THz Science Group at the Center for Optics Investigations in Leon, Mexico, and Dr. Corinna Koch-Dandolo for the opportunity to engage in impactful research in terahertz time-domain imaging applications for Mexican cultural heritage.

As the title of this dissertation indicates, imaging spectroscopy has played an important role in my research. I owe my education in this field to Dr. John Delaney, the senior imaging scientist at the National Gallery of Art in Washington D.C. You have had a profound impact on my work and on my development as a scientist. Thank you so much for sharing your knowledge with me and your critical eye (and for introducing me to Tom Lehrer). I also am so grateful to Dr. Kathryn Dooley and Dr. Francesca Gabrieli for their endless patience, guidance, and laughs in my learning journey. My visits to the NGA would not have been possible or as fruitful without the welcome and kindness of Dr. Barbara Berrie and the Scientific Research Department. I will forever cherish my time at the Gallery.

I also wish to thank Dr. Marcello Picollo of IFAC-CNR for his support during my Ph.D., and to the research team at IFAC-CNR including Dr. Costanza Cucci and Andrea Casini for their insight on imaging spectroscopy.

Once again, I must thank Ioanna Kakoulli, for she gave me a research topic that allowed me to study the rich cultural heritage of Cyprus and encouraged me to apply for a Fulbright research grant. I am so grateful to the Fulbright Program, the US State Department, and

especially Sondra Sainsbury for making that experience possible. With the kind permission of the Department of Antiquities and the director, Dr. Marina Solomidou-Ieronymidou, and of Professor Demetrios Michaelides, Dr. Sophocles Hadjisavvas, Dr. Eustathios Raptou, Dr. Henryk Meyza, and Margarita Kouali, I was able to indulge in the study of ancient Cypriot paintings. Of course, this would not have been feasible without the support of the archaeological officers, conservators, and museum staff at both the Paphos Archaeological Museum and the Cyprus Museum. Special thanks must be given to Margarita, Neoptolemos, Marios, Kokos, Andreas, Kathy, Modestos, Maria, Yiannis, Panikos, Eve, Stella, Christos, and Leftheris. I must also thank Skyler Jenkins for assisting me with my experiments while sitting in the tombs and storerooms with me for hours in the warm Cyprus summer.

I also had the opportunity to study important Byzantine Cypriot paintings from the Enkleistra and the Church of St. Paraskevi, thanks to the permission of the Monastery of St. Neophytos, the Bishop of Paphos, Father Alexios, and Father Giorgos. My research on the island relied and benefited immensely on the strong institutional support of the University of Cyprus and the Geological Survey Department, and the amazing mentorship of Professor Ioannis Ioannou and Dr. Andreas Zissimos. You kept my spirits high and helped me feel so welcome. I am in debt to your kindness.

Needless to stay, Cyprus became a second home to me, as I returned two more times to continue my research on the ancient and Byzantine paintings. I made very wonderful friends on the island who also helped support my research - thank you Christos, Marika, Sveta, and Tasos for all of your help. My Fulbright cohort, Olivia, Kirsten, Eilis, Christiana, and Tasha made that first year extremely special, as well. Finally, I wish to give my love and gratitude to my “adoptive” parents, Nadina and Pedrakis Kakoulli.

I was also fortunate to study a very special group of paintings, the Greco-Roman Egyptian funerary portraits, from various institutions in the U.S., starting with the J. Paul Getty Museum collection at the Getty Villa, thanks to the invitation of Marie Svoboda, founder and organizer for the APPEAR project. These studies eventually expanded to include portraits from the National Gallery of Art in Washington D.C. and the Walters Art Museum. I wish

to thank all of these institutions for allowing me to analyze the paintings, and particularly Marie Svoboda, Dr. John Delaney, and Dr. Glenn Gates, for making these studies possible.

As part of my research, I also explored applications of 3D modeling for cultural heritage science and, in turn, met two very delightful individuals. Thank you Dr. Lisa Snyder and Deidre Whitmore for your support, insightful discussions, and cheery auras that made my work in digital humanities all the more meaningful. I am also thankful for the institutional support of the Technology Sandbox at IDRE and the Digital Archaeology Lab at the Cotsen that made the studies in 3D modeling feasible. Part of this work included the study of Hellenistic Canosa terracota vases at the Getty Villa, and I wish to express gratitude for the permission given by Marie Svoboda and the J. Paul Getty Museum to analyze the vases.

I am very lucky, as I initially said, to have had this extremely rich Ph.D. experience. This research was facilitated and benefited greatly from the financial and academic resources of many institutions. So I wish to thank here the following programs, foundations, research institutes and centers for their support: The U.S. Fulbright Program; The Cyprus American Archaeological Research Institute; The John Anson Kittredge Fund; The Steinmentz Family Foundation and Friends of Archaeology of the UCLA Cotsen Institute of Archaeology; The UCLA Center for Medieval and Renaissance Studies; Dumbarton Oaks; and The UC MEXUS program.

However, I am most fortunate to have had an amazing group of friends who have supported me during this very long journey. They have listened for so many years, sent cards, given hugs, and provided advice as good friends are wont to do. In particular, Jackie, Jessica, Ranmali, Erica, Sidd, Chilan, and Umut: thank you.

In the end, none of this would have been possible without my family. Thank you for your patience, your steadfastness, for helping to keep me on my path, and the love. It meant more than you will ever know.

Curriculum Vitae

2005 – 2009	B.S. in Physics, University of California, San Diego
2009 – 2011	M.S. in Physics, University of Minnesota, Twin Cities
2013 – 2015	M.S. in Materials Science and Engineering, University of California, Los Angeles
2015 – Present	Ph.D. student in Materials Science and Engineering, University of California, Los Angeles.

2018	Dissertation Year Fellowship, Graduate Division, University of California, Los Angeles
2018	John Anson Kittredge Fund Grant
2016	Fulbright U.S. Student Research Award
2016	Danielle Parks Memorial Fellowship, The Cyprus American Archaeological Research Institute
2016	UC MEXUS Small Grant Award
2016	Best Student Poster, Southern California Society for Microscopy and Microanalysis

Publications

Radpour, R., Christian Fischer, and Ioanna Kakoulli. "New Insight into Hellenistic and Roman Cypriot Wall Paintings: An Exploration of Artists' Materials, Production Technology, and Technical Style." Arts. Vol. 8. No. 2. Multidisciplinary Digital Publishing Institute, 2019.

Delaney, J. K., Dooley, K. A., Radpour, R., Kakoulli, I. (2017). "Macroscale multimodal imaging reveals ancient painting production technology and the vogue in Greco-Roman

Egypt". Scientific Reports, 7(1), 15509.

Kakoulli, I., Radpour, R., Lin, Y., Svoboda, M., Fischer, C., "Application of forensic photography for the detection and mapping of Egyptian blue and madder lake in Hellenistic polychrome terracottas based on their photophysical properties." Dyes and Pigments, 136 (2017), 104-115.

Gomez-Sepulveda, A. M., Hernandez-Serrano, A. I., Radpour, R., Koch-Dandolo, C. L., Rojas-Landeros, S. C., Ascencio-Rojas, L. F., ... and Castro-Camus, E., "History of Mexican Easel Paintings from an Altarpiece Revealed by Non-invasive Terahertz Time-Domain Imaging." Journal of Infrared, Millimeter, and Terahertz Waves (2016), 1-10.

Radpour, R., Bajwa, N., Garritano, J., Sung, S., Balonis-Sant, M., Tewari, P., Kakoulli, I., Grundfest, W., Taylor, Z., "THz imaging studies of painted samples to guide cultural heritage investigations at the Enkleistra of St. Neophytos in Paphos, Cyprus." SPIE Optical Engineering+ Applications. International Society for Optics and Photonics, 2014.

CHAPTER 1

Introduction

This research explores the materiality of ancient polychrome artifacts using materials science principles and methods combined with social and humanistic methodologies and has a two-fold goal: 1) the scientific analysis of materials and operational sequences of production technologies of Hellenistic, Roman and Byzantine paintings within their art historical and archaeological context, and 2) the application, adaptation and development of novel approaches and field-deployable analytical instruments to address the complex nature of archaeological materials. This research, both inspired by and directed towards driving advanced technologies in cultural heritage and archaeological sciences, specifically addresses the challenge of performing scientific analyses in the field, where wall paintings from the ancient world remain on site, as part of the original architectural. It further demonstrates, evaluates, and establishes imaging spectroscopy and novel material visualization techniques as fundamental applications to methodologies for scientific fieldwork to perform reliable materials characterization and interpretations of archaeological paintings. Imaging spectroscopy (IS), in reflectance and luminescence modes, and terahertz (THz) imaging were applied for the study of ancient and historical paintings and laboratory test targets imitating archaeologically and historically-significant paintings, both in terms of materials and application methodology, performing materials characterization, visualization of obscured features, and 2D chemical mappings. These techniques were able to reveal ancient imagery that has been concealed or deteriorated over time, filling in prevailing technological and knowledge gaps in the analysis of ancient painting in order to answer major archaeological questions.

1.1 The intention and motivation behind the scientific study of archaeological paintings

The study of ancient artifacts provides a glance into the past. The materials choices, production technology and imagery offer a reflection of ancient practices, human agency and the society. The use of madder lake (a red organic/inorganic hybrid pigment containing alizarin and purpurin dye compounds) as a pigment of choice to paint the reddish/purple garments of figures in ancient paintings [57] represents an excellent example of real life practices described by ancient writers [158] and alchemists [35] to produce red colorants for the dyeing of yarns and textiles. The decorative arts of antiquity are therefore important and provide crucial archaeological records complementing ancient treatises and alchemical manuscripts that describe 'recipes' for the production of materials; they praise artists who pioneered and mastered materials and their application to provide innovations in the art of painting such as three-dimensionality and shading and, offered art historical commentary on monumental works. Such texts included Vitruvius' *De Architectura* [142], Pliny the Elder's *Natural History* [158], Theophrastus' *On Stones* [194], and the Leyden and Stockholm Papyri (the latter also known as the Papyrus *Graecus Holmiensis*) [34][35].

Though written text provides invaluable information on ancient materials and artistic processes, they remain secondary sources of information. As such, they have not always been correct or thorough in documenting the technologies used. The archaeological record provides a direct source to understand ancient practices, the artists themselves and the society at large. The scientific study of material culture is therefore essential to answer questions about the ancient world including knowledge and technology transfer; the migration and development of decorative styles that demonstrate cultural exchange; and changes occurred owing to socio-political and religious systems.

In some cases, unsubstantiated identifications of material use in a painting, such as the types of pigments used, based on archaeological or historical context, limited technical archaeological studies, and previous literature studies perpetuate incorrect classification of

materials. This may be due to a lack of accessible analytical technologies or realization of the complexity with which archaeological materials may represent in their production. However, it devalues the true significance of the painting and prevents a proper understanding of their technologies, as well as the ancient craftsmen/artists who produced them. This is another important motivation for establishing scientific materials characterization as a routine component in the analyses of archaeological objects.

Scientific analyses of archaeological paintings are also of great significance to their conservation. Their long lifetime has left them exposed to detrimental influences such as weather, natural disasters and physical devastation by anthropogenic effects, causing discoloration or concealment of decoration, chemical and physical alterations of their constituent materials, and fragmentation. Condition assessments, including identification of degradation processes, evaluation of present damage and stability, and proposed interventions for protection of the painting can only be properly informed by scientific investigations. The development of effective, reversible consolidation materials requires a robust understanding of the chemical nature of the intended target. Furthermore, consistent, rapid and reliable analytical monitoring of the treatment to assess the chemical and structural integrity of the painting over time must be performed to evaluate the effectiveness of the applied conservation material.

Forensic investigations for archaeological objects benefit greatly from the application of scientific technologies. Undocumented objects under investigation can be analyzed to reveal important fingerprint markers diagnostic of their cultural and chronological context, establishing strong evidence for authentication and classification.

Furthermore, archaeological wall paintings are amongst the most complex of works of art to analyze, the challenges of which will be detailed in the following section. Scientific characterization and documentation of large-scale, decorated and hierarchically-complex wall paintings that remain on its architectural foundation drives the development of robust high-chemical specificity instrumentation that can then be translated to address the analysis of other cultural heritage and archaeological targets of significance.

1.2 Challenges in archaeological sciences for field studies and the need for portable, high specificity instrumentation

The significance of archaeometry for the recovery of insightful data from archaeological paintings and sites cannot be overstated; however, such studies are faced with several challenges, especially for materials that remain in situ or are not in a stable laboratory environment. Archaeological paintings that have been excavated and stabilized in laboratories or museums are able to undergo longer and more extensive analytical investigations. However, those remaining on site stay at risk of further harmful environmental and anthropogenic effects, and analytical access to them are complicated by time-sensitive restrictions as well as challenges of the natural environment, such as humidity conditions, uneven terrain, dust and dirt, poor lighting, small enclosures, out-of-reach decoration, and lack of power. Examples of on-site locations featuring these experimental conditions are presented in Figure 1.1.

The stability of the paintings, i.e. the fragility and friability of the surface (including the pigmented decoration), the amount of weathering and discoloration suffered, and the overall remaining amount of material also pose challenges for archaeometric analyses (Figure 1.2). Additionally, because archaeological objects are unique and irrepleaceable, sampling is often limited or altogether prohibited. This prevents invasive and destructive analyses from being repeatable and exhaustive, preventing a holistic understanding of its production and condition. Furthermore, sites have been re-purposed and therefore those which feature wall paintings may have multiple layers of re-plastering and re-painting, concealing the earlier decoration and creating complex hierarchical painting systems. Figure 1.3 is a schematic of the type of stratigraphy present in a wall painting, especially if re-plastering has occurred.

Figure 1.1: **(a)** Tomb 3882, located near the city center of Paphos, Cyprus, and **(b)** Tomb Silver House 1, excavated from the western necropolis of Nea Paphos. **(c-d)** The painted Cell and Bema from within the Enkleistra of St. Neophytos, near Tala, Cyprus.

Figure 1.2: **(a)** A degraded imitation marble pattern on the dado level of a room in the Villa of Theseus (Paphos Archaeological Park). **(b)** Imitation architectural blocks and a degraded egg and dart pattern on the arch of an arcosolium in Tomb Roma 1 (Kato Paphos).

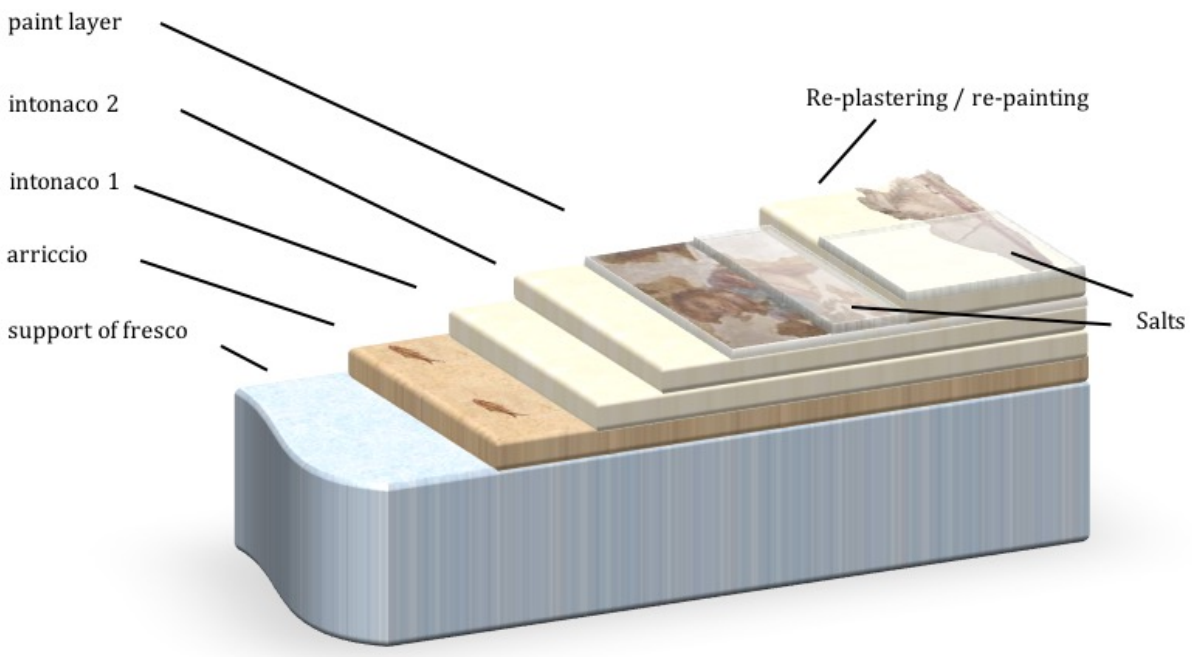

Figure 1.3: In this schematic of a wall painting stratigraphy, two layers of intonaco are shown as preparatory layers. However, as many as five have been found in real ancient wall paintings (i.e. in homes or villas) to prepare the wall surface for decoration.

Ultraviolet-induced fluorescence (UVF) photography, infrared reflectography (IRR), and X-ray radiography (XRR) have a long history in painting diagnostics [3, 55]. UVF is applied to reveal past conservation interventions or the presence of organic painting materials, while IRR can detect pentimenti (previous depictions or changes to the present composition), underdrawings, and preparation lines in the near-surface layers of works of art (Figure 1.4). X-ray radiography provides structural information as well as visualization of high atomic number pigments (i.e. lead-based pigments or mercury sulfide (HgS, cinnabar)). The contrast produced by images from X-ray radiography are dependent on the initial photon energy. However, these applications have several limitations. IRR as a near-surface technique can penetrate top paint layers but features limited-to-no signal capture from the ground layer or beyond. X-ray radiography requires a high level of precaution for both the user and the artifact, and the penetration depth is difficult to control, leading to uncertainty where fea-

tures lay within the structure of the painting. Furthermore, as it is a transmission imaging technique, this is not applicable for in situ analysis of wall paintings. UVF photography provides limited information to separate the multitude of potential fluorescent signatures caused by UV-induced excitation (i.e. dye-based pigments, binding media, glues and adhesives, or other conservation treatment materials). Additionally, the broad emission of binding media and white pigments into the visible, once excited, induces excitation of other pigments in the paint layers, causing false UVF signals. At best, it is only a very preliminary mode of imaging diagnostics for the presence of organic materials.

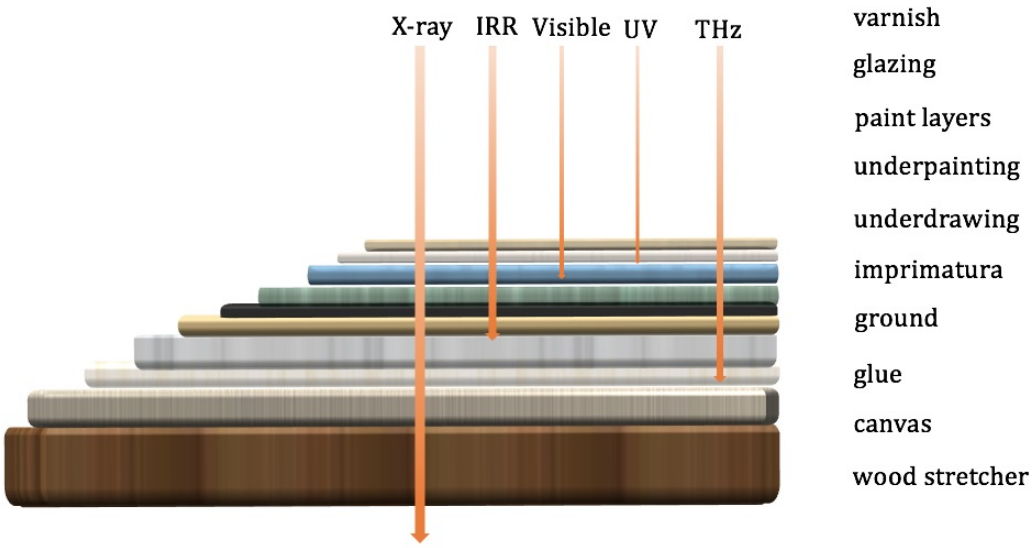

Figure 1.4: The penetration depths at different wavelengths of electromagnetic radiation incident on a canvas painting.

These analytical challenges can be mitigated by scientific instrumentation that are field-deployable, non-invasive, and feature high chemical specificity analyses with fast acquisition and feedback, meanwhile increasing the number of data points collected compared to minimally-invasive sampling. The diversity and complexity of ancient paintings necessitate this in order to develop a macroscale picture of material use, value, and function. Thus, advanced imaging spectroscopy (IS) and direct-detection terahertz (THz) imaging were proposed for field investigations. Hyperspectral imaging (HSI) is an image collection technique

where hundreds of images are collected in narrow spectral bands, producing contiguous spectral profiles in each spatial pixel of the image scene. Different materials' excitation and responses can be explored in HSI through diffuse reflectance imaging spectroscopy (RIS) and luminescence imaging spectroscopy (LIS) to perform chemical materials characterization, i.e. the identification of pigments and binding media, and these different material responses can be mapped across the image scene using multivariate statistical analysis [50, 129]. THz imaging is an imaging modality that can visualize features in stratified media due to the long penetration wavelength of the THz pulse ($\sim$ 450–750 μm). Each material it interacts with gives a characteristic response based on the material's THz refractive index. Thus, different materials will reflect the THz pulse uniquely, and this recorded signal allows hidden features such as concealed painting and structural defects to be identified [69, 52].

While IS and THz imaging applications for works of art in museums and research laboratories have been successfully demonstrated, field applications for wall paintings are highly underrepresented, indicated by the low number of reported scientific field campaigns [11, 36, 185, 130]. Of these applications, reflectance imaging spectroscopy was the only mode of materials analyses performed by commercial or custom-built IS systems. Meanwhile, research and application of THz imaging applications for scientific fieldwork appear to have stalled, due to the high cost and user expertise needed to implement the instrumentation and data analysis, as well as the limited information thus far recovered from the highly scattering media that comprise wall paintings, especially those which have concealed decoration.

Furthermore, the inherent layering and heterogeneous nature of paintings produce challenges for interpretation of the data in IS applications. Ancient artists painted with pure or mixtures of natural or synthetic colorants, in both single and multi-layered applications to produce distinct visual aesthetics, as demonstrated by the range of hues produced in a rare example of funerary figurative painting excavated from a tomb in Paphos, Cyprus (Figure 1.5). The identification and materials characterization of these colorants using RIS are the subjects of extensive research in cultural heritage. RIS datasets contain thousands of spectra that require data mining to establish the pigment diversity in the painting; novel extraction

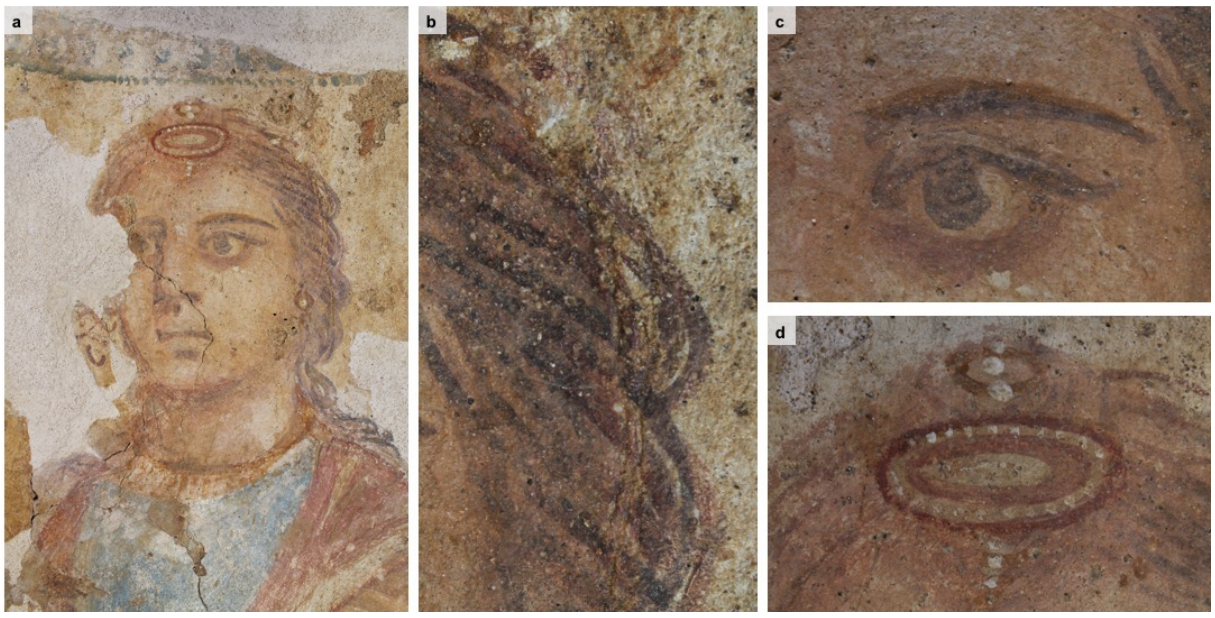

Figure 1.5: **(a)** Figurative painting from Tomb 3510, excavated near Tomb of the Kings in Paphos, Cyprus. **(b-d)** are close-up details of the figure's hair, eye, and diadem showing the fine details executed in a variety of hues.

methods are being explored to achieve this effectively. Upon producing a list of unique materials that constitute the chemical make-up of the painting, they must be interpreted. This is a significant challenge for pigment mixtures, otherwise known as intimate mixtures, and layered paint applications. For example, if a pixel records two pigments painted side by side (i.e. the figure's pink himation and blue chiton, Figure 1.6), their signals are mixed as a linear sum of the normalized areas for each pigment in the pixel, and straightforward linear un-mixing can be applied to identify each pigment. Intimate mixtures, however, due to scattering, produce spectral signatures with non-linear dependence on pigment concentration in the HSI datasets, as do mixed signals recorded from multiple layers. Advanced computational tools such as neural networks use adapted Kubelka-Munk radiation transfer models to estimate reflectance spectra from pigment mixtures. However, paint layers with glazes or those semi-transparent to the ground layer feature additional contributions to the recorded signal that complicate the deconvolution. Therefore, additional a priori information about the paint layers' composition is required to perform the un-mixing [187, 168]. The diversity

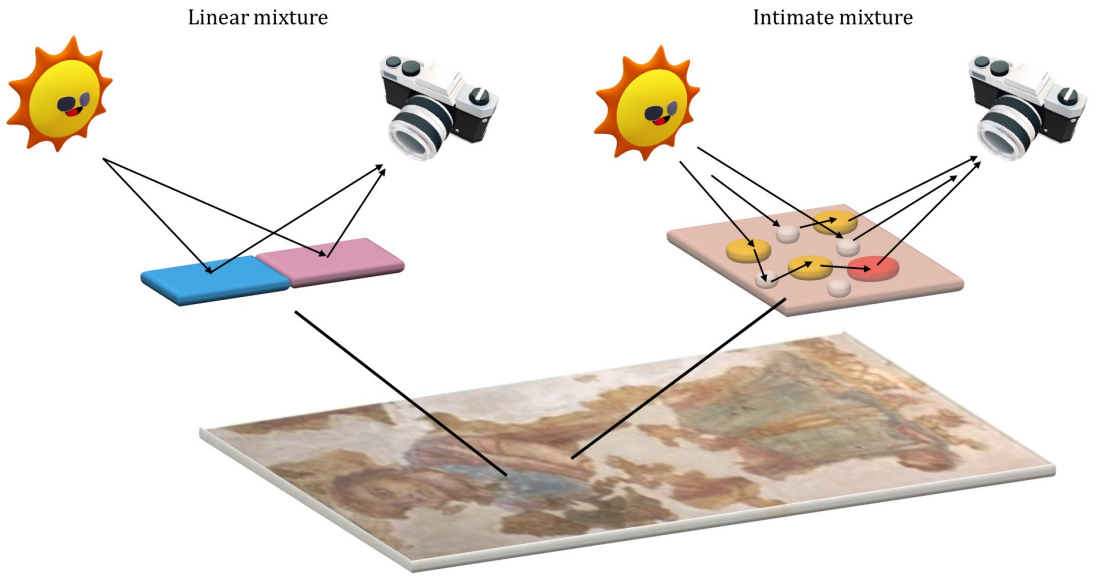

Figure 1.6: Linear mixtures produced in a signal, i.e. by the blue and pink pigments captured side by side, versus intimate mixtures, i.e. the flesh tone made of yellow, white, and red pigment particles.

of pigments across ancient and historical paintings makes this extremely difficult to accomplish. Without effective extraction and material assignment of the painting materials used by the ancient artists, archaeological interpretation of the paintings and their manufacturing are extremely limited.

1.3 Outline of this research

Noting the challenges encountered in the analyses of archaeological and historic wall paintings, this research utilized advanced imaging spectroscopy techniques and chemical sensing tools for non-invasive, in situ materials characterization. The analytical studies presented here demonstrate field applications of complementary and novel characterization techniques, and explorations of data analysis processing, revealing new insight in ancient paintings materials and techniques.

In Chapter 2, an integrated analytical methodology using forensic and RGB photography,

X-ray fluorescence spectroscopy, fiber-optic reflectance spectroscopy, and photomicrography were applied on site to an extensive collection of ancient Cypriot wall paintings to explore their raw materials selection and production sequence, reveal technological choices by the ancient artists, and use this information to provide a context for these paintings within the ancient Mediterranean world. The portable spectroscopic techniques facilitated multiple spot collections with complementary electronic, molecular and elemental data and supplemented forensic imagery that provided preliminary chemical mapping on the wall paintings of fingerprint markers of an ancient pigment.

Wall paintings, as demonstrated by the schematic in Figure 1.3, are hierarchically-complex multi-layered systems. Over the course of their extended lifetimes, wall paintings such as those found in both ancient archaeological sites and historical Byzantine churches have featured multiple painting phases due to re-use of the sites, whether motivated by political, religious, or aesthetic motivations, or destruction by natural disasters or human influence. Accessing hidden paintings and internal structure through strongly scattering layers such as chalk or lead white has been highly evasive for non-invasive imaging modalities. Chapter 3 presents preliminary studies of a direct detection THz imaging system, adopted from biomedical imaging research, for probing stratified painting media of cultural heritage targets and to assess the system's capability for field applications to reveal concealed imagery and hidden structural defects in multi-layered paintings.

Chapters 4 and 5 present novel applications of imaging spectroscopy. In Chapter 4, laboratory and field applications of reflectance and luminescence imaging spectroscopy were conducted on archaeological paintings using commercial hyperspectral imaging systems to reveal material use and technological applications by artists throughout the ancient world through materials characterization and chemical mapping. In Chapter 5, adapting the application of a portable spectroradiometer to a scanning system using a 'robotic' arm yielded a novel high spectral resolution scanning reflectance spectroscopy system for in situ studies capable of producing high chemical specificity datasets with an extended analytical range compared to conventional hyperspectral imaging systems. Furthermore, the datasets acquired from

both imaging spectroscopy systems employed derivative analyses for the identification, extraction, and mapping of the unique pigments employed. The use of the derivative spectrum is effective in enhancing small fluctuations in the reflectance profile, reducing the continuum background signal, and providing separation of closely spaced absorption signatures, and therefore was used to target the analysis of reflectance spectra of intimate pigment mixtures found on the paintings.

In Chapter 6, the analytical methodologies and instrumentation demonstrated in Chapters 2, 4, and 5 are discussed through the presentation of case studies exploring ancient Cypriot paintings, Byzantine Cypriot paintings, and Greco-Roman funerary portraits from Egypt. The adoption, adaptation, and implementation of advanced techniques to obtain chemical data of the paintings was a primary objective, which facilitated the secondary objective to improve interpretation and visualization of this data. This research explored progressive analytical and visualization approaches to produce insightful 2D chemical maps of painting materials, conservation materials, and degradation through derivative analyses, diagnostic material luminescence mapping, and 3D modeling.

Finally, Chapter 7 presents a technologically accessible and streamlined methodology to produce 3D models of objects featuring photoluminescence texture of ancient pigments and conservation materials.

1.4 Objects, materials, and locations of study

The first set of target materials analyzed in this research were wall paintings from Cyprus, an island with a rich history and archaeology, located in the easternmost part of the Mediterranean Sea. Ancient wall paintings from the Hellenistic and Roman periods were excavated from various funerary (tombs) and domestic (houses, villas) sites in the district of Paphos in the southwest region of the island (Figure 1.7).

Figure 1.7: **(a)** The Paphos Archaeological Park, containing the excavated ancient houses and villas from Nea Paphos. **(b)** Tomb Roma 1 and **(c)** Tomb 3882 (Paphos, Cyprus).

This region was known in the ancient world as Nea Paphos ("New" Paphos) and served as the economic and administrative capital during these time periods [106], making the decorative arts recovered a valuable source of information for artistic practices and cultural exchange. Unfortunately, this region was also damaged several times by earthquakes, thus diminishing potential remains. Some paintings have been recovered in fragmented form and are held in storage or are on display at the Cyprus Museum and Paphos Archaeological museum. The remaining paintings are left on site. This collection of paintings was analyzed throughout a multi-year campaign using the non-invasive, field-deployable instruments discussed in the previous section. Cypriot Byzantine wall paintings were also analyzed from the Paphos district from two historically-significant religious sites: the Enkleistra ("place of reclusion") of St. Neophytos, originally built in the late twelfth century and located in the hills above the village of Tala, and the Church of St. Paraskevi in the village of Yeroskipou, one of the earliest churches built in Cyprus, dating to the eighth century (Figure 1.8). Both sites contain multiple phases of re-painting with intermediate plastering, making them valuable cases to explore material use at different time periods, as well as motivate imaging studies for features' recovery from depth.

This rich collection of Cypriot wall paintings, ranging in pigment diversity, location, stability, and decorative schemes, presented compelling case studies to build, demonstrate, and evaluate the in situ scientific methodology produced by this research.

Figure 1.8: **(a)** The church of St. Paraskevi in Yeroskipou, Cyprus. **(b)** The Enkleistra of St. Neophytos, near Tala, Cyprus.

The second set of paintings analyzed was comprised of a collection of Greco-Roman funerary portraits excavated from burial sites in ancient Roman Egypt (first – fourth century AD) (Figure 1.9). These portraits 'merged' Hellenistic painting traditions with Egyptian fu-

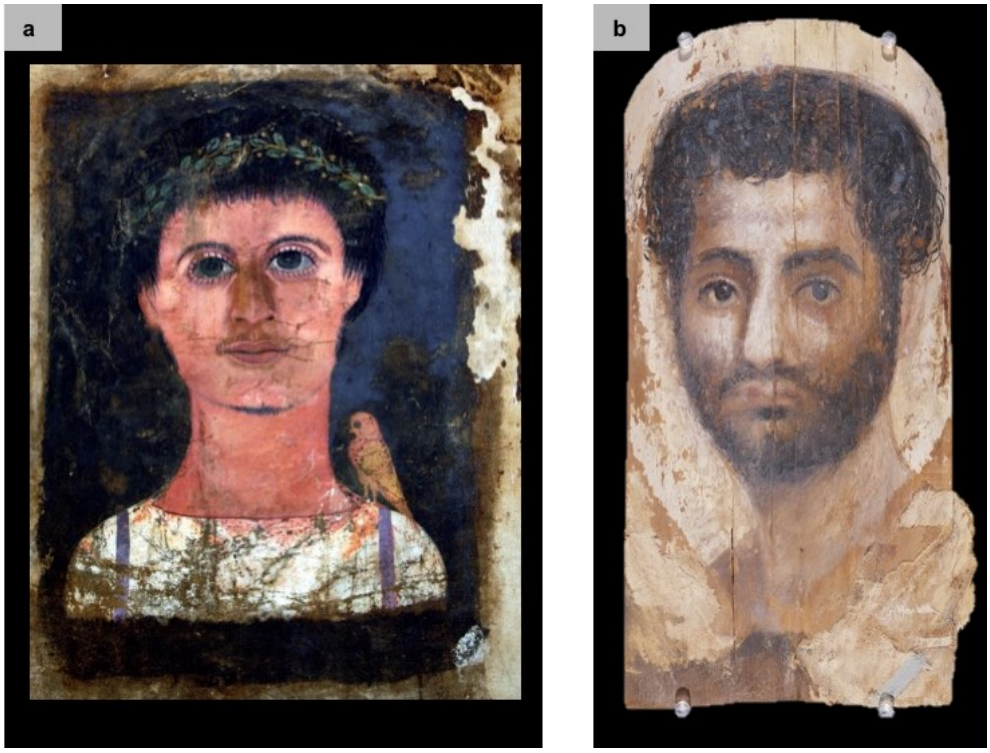

Figure 1.9: Funerary portraits from the J. Paul Getty Museum collection, painted on linen (**(a)** accession number 75.AP.87) and wood (**(b)** – accession number 73.AP.94).

nerary beliefs by depicting naturalistic representations of ancient Egyptians on thin wooden panels or linen shrouds, using wax, tempera, or oil-based binding media, and set over the faces of the deceased using linen wrappings [26]. As these portraits represented real members of society, they provide ethnographic records of social class and culture of Egypt in the Roman period. Chemical analysis of the paintings revealed important information on artist applications, technological choices, and potential markers of artisan workshops. The portraits analyzed in this research come from the collections of the J. Paul Getty Museum (Malibu, Ca, USA) and the Walters Art Museum (Baltimore, MD, USA).

Additionally, a decorated Hellenistic terracotta funerary head vase (Figure 1.10) produced from the Canosa workshops in Apulia, Italy, an object also from the J. Paul Getty Museum collection, was the target of the 3D modeling study in this research to demonstrate a new methodology for the integration of luminescence data as chemical texture in 3D visualizations.

Figure 1.10: Funerary Canosa terracotta vase from the J. Paul Getty Museum collection (accession number 81.AE.157).

In the ancient world, artists used a variety of natural (Figure 1.11a-c) and synthetic pigments (Figure 1.11d,e) to decorate wall paintings and statuary. These materials were applied relatively purely, in mixtures, and/or layered for various intentional visual aesthetics.

Figure 1.11: Natural and synthetic colorants found in the excavated materials from the House of Orpheus in the Paphos Archaeological Park: **(a)** jarosite; **(b)** red ochre; **(c)** realgar; **(d)** madder lake; **(e)** Egyptian blue.

Depending on the pigment used, the application technique (secco, painting onto dry surfaces, or fresco, painting into wet plaster), and the desired visual effect, the pigments were applied to the painting substrates using binding media such as water, oil, wax, or egg tempera. However, due to passage of time and weathering, binding media on wall paintings are extremely difficult to identify.

The identification of painting materials, the application methodology, and the decorative scheme on the paintings, within their respective contexts, were characterized using novel imaging spectroscopy techniques, forensic photography, and portable chemical sensing tools. The following chapters will present the investigations that demonstrate how these instruments produced new chemical and pictorial visualizations that revealed artistic choices, identified technical practices and unique painting markers, and revived imagery that will aid in conservation interventions and archaeological interpretation.

CHAPTER 2

Field applications of X-ray fluorescence, reflectance spectroscopy, and forensic photography for the investigation of ancient Cypriot wall paintings

Chemical analyses of archaeological wall paintings that remain in situ (i.e. still intact in the excavated site) face significant limitations. As the paintings are immobile, they cannot be brought to a laboratory to be placed in a stable, observational environment, nor can they be used with bench-top, laboratory, or museum-based instruments. Because the paintings are rare and non-renewable, minimally-invasive sampling is destructive and as only limited sampling from damaged areas are often allowed, it does not give an appropriate representation of their condition and material use. The appropriate solution is to bring instruments on site that are highly portable and robust to field conditions which can facilitate extensive data points collection with rapid and reliable feedback in real time.

These analytical requirements have spurred the application and development of various portable spectroscopic and imaging protocols for in situ analyses of wall paintings. Imaging is the first step in wall painting diagnostics to evaluate the condition of the painting, get preliminary information on constituent materials, and guide subsequent spectroscopic spot analyses. RGB photography (visible photography performed between 400-700 nm) with proper color correction and white balancing of the images provides fundamental documentation of the paintings. Ultraviolet (UV) reflectography (photography that captures reflected UV light off of the art work, $\sim$ 300–400 nm) (UVR), UV-induced visible luminescence, visible-induced infrared (IR) luminescence, and infrared reflectography (IRR) contribute to the identification of some organic materials, synthetic inorganic and inorganic-organic hy-

brid pigments, underdrawings, and changes to or differences within a painting's composition due to the different materials' absorption and emission properties [48]. These applications of 'forensic' photography normally employ a digital single-lens reflex (DSLR) camera modified to have sensitivity to UV and near IR wavelength ranges, and therefore do not provide spectroscopic data to confidently identify materials captured in the image data.

Portable chemical sensing tools such as X-ray fluorescence spectroscopy (XRF) and X-ray diffraction (XRD) [172, 199], fiber-optic reflectance spectroscopy (FORS) [39, 155], Raman spectroscopy [152, 132], Fourier-transform infrared spectroscopy (FTIR) [181, 82], and nuclear magnetic resonance (NMR) [94, 23] are materials characterization techniques that have been applied for non-invasive in situ analyses of wall paintings. Each of these methods probe a material's chemistry for different diagnostic signatures (i.e. elemental, crystal structure, molecular vibrations, band gap transitions, nuclear responses to magnetic field perturbations). A robust characterization of pigments, used purely, in mixtures or layered applications, degradation products, or conservation materials from past interventions necessitates the identification of more than one diagnostic signature, thus a thorough investigation requires complementary analysis by different spectroscopic tools [110, 111, 13, 125, 79, 148], integrated with the results from forensic imaging. The value of portable spectroscopic instrumentation for field studies is acknowledged by the creation of formalized mobile laboratories such as MOLAB (Mobile LABoratory) [32], a European multi-national network of laboratories developed under the Integrated Platform for the European Research Infrastructure ON Cultural Heritage (IPERION CH), with field and laboratory instrumentation dedicated to aid art and archaeological scientific investigations internationally.

Figure 2.1: Canosa terracotta vases **(a)** 81.AE.156 and **(b)** 81.AE.157 from the J. Paul Getty Museum collection.

2.1 Case study: scientific investigation of polychrome decoration using forensic photography and portable spectroscopy techniques

The UCLA Molecular and Nano Archaeology Laboratory employs an integrated analytical methodology utilizing portable, hand-held spectroscopic and forensic imaging tools to characterize archaeological objects, within the laboratory and in the field. This was demonstrated in the analytical case study of a pair of Hellenistic Canosa funerary terracotta vases from the J. Paul Getty museum collection (accession numbers 81.AE.156 and 81.AE.157) (Figure 2.1) [113]. The polychrome vases were decorated with blue, pink, red, and black pigments, and featured clay slips. Based on the time period these objects were attributed to, and previous literature on Canosa terracotta vases analyses, it was believed that the blue and pink pigments most likely were comprised of the ancient pigments Egyptian blue and madder lake, respectively.

Forensic photography was first performed to identify the luminescent fingerprint markers of Egyptian blue and madder lake on the Canosa vases, as each pigment has distinct photophysical properties that produce diagnostic photoluminescence (light emission from excitation). Egyptian blue (cuprorivaite, $CaCuSi_4O_{10}$) is the earliest engineered pigment in history ($\sim$ 2500 BC) and most prolific of blue pigments used in antiquity [20, 108]. Egyptian blue is a high-fired semi-vitreous pigment derived from a mixture of quartz (i.e. sand, SiO_2), calcium (i.e. chalk, $CaCO_3$), and copper (i.e. mined metallic copper, or Cu-containing pigments such as malachite, $Cu_2(CO_3)(OH)_2$). Though the production of Egyptian blue appeared to cease in the first few centuries AD (knowledge of its manufacturing lost over time [140]), the longevity of the pigment, due to its stable silicate matrix composed of layered structures of SiO_4 rings, allowed for its identification and renewed interest in modern times.

The characteristic photoluminescence of Egyptian blue is caused by three $d \rightarrow d$ electronic transitions of the Cu^{2+} ions situated in square planar CuO_4^{6-} complexes, also responsible for the blue color of the pigment. The reflectance spectrum of Egyptian blue (Figure 2.2a) shows the three diagnostic absorptions in the visible wavelength range at 560 nm ($^2A_{1g} \rightarrow {}^2B_{1g}$), 630 nm ($^2E_g \rightarrow {}^2B_{1g}$), and 790 nm ($^2B_{2g} \rightarrow {}^2B_{1g}$) [78]. Optical excitation in this region induces the $d \rightarrow d$ electronic transitions, causing a near-infrared (NIR) luminescence at $\sim$ 910-950 nm (Figure 2.2b) [6, 159].

Madder lake is a synthetic organic-inorganic hybrid pigment used extensively in antiquity (dating back to $\sim$ 2000 BC [127]). Madder is a natural dyestuff from the *Rubiaceae* family. To produce the red lake pigment, dye molecules were extracted directly from the madder root or from dyed textiles, using hot water or alkaline solutions, precipitated with a metal cation, typically Al(III) (usually sourced from potash alum, $Al_2(SO_4)K_2(SO_4)_3{\cdot}12H_2O$) and mixed with alkaline salts to facilitate chelation to the potash alum, producing a hydrated alumina. Madder consists of two hydroxyl anthraquinone (HAQ) dye compounds, alizarin (dihydroxy-9,10 AQ; 1,2 HAQ) and purpurin (trihydroxy - 9,10 AQ; 1,2,4 HAQ) [42]. Studies have shown that madder lake formulations with higher concentrations of purpurin-Al(III) compounds feature a structured double absorption in the reflectance spectrum at $\sim$ 515 and

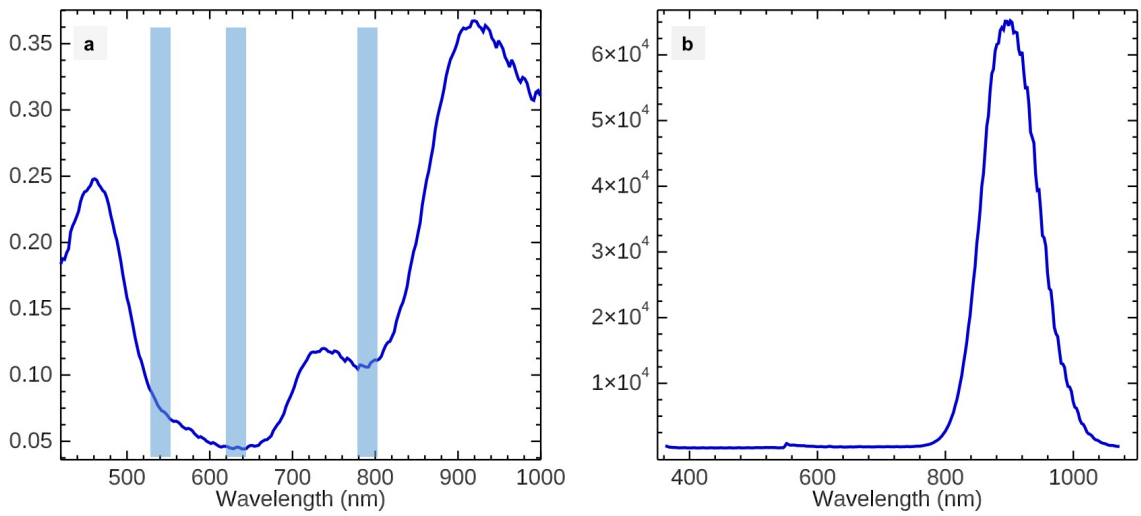

Figure 2.2: **(a)** The characteristic reflectance spectrum of Egyptian blue, painted on a mock-target with an acrylic binder, featuring absorptions at 560, 630, and 790 nm. **(b)** Optical excitation at the absorption bands produces a luminescence emission peak of Egyptian blue in the NIR. The peak maximum here is $\sim$ 900 nm.

545 nm (Figure 2.3a) and a higher quantum efficiency [90] for its characteristic photoluminescence (Figure 2.3b). Excitation of madder lake in the visible range at the structured double absorption induces the π-π^* excited singlet state and subsequent luminescence with maximum peak emission values reported at 596 - 625 nm [42, 90].

To induce the photoluminescence of Egyptian blue and madder lake on the Canosa vases, an alternate light source (ALS) utilized in forensic crime scene investigations, a Mini-Crimescope® MCS-400, was applied. It features a UV-visible metal halide lamp and two detachable tunable filter wheels with various bandpass ranges, which allowed excitation of Egyptian blue at 600 nm (red light) and madder lake at 535 nm (green light). A DSLR camera with the internal hot mirror removed, giving the camera sensor access to the UV and NIR wavelength ranges ($\sim$ 350–1000 nm), was filtered with a PECA 908 filter for NIR capture ($\sim$ 900–1000 nm) of Egyptian blue's photoluminescence, and with a Red 25 Tiffen filter ($\sim$ 580–700 nm) for the capture of the photoluminescence of madder lake. The imaging results successfully produced 2D chemical maps of Egyptian blue (Figure 2.4a) and madder lake (Figure 2.4b), showing the use and distribution of the two pigments in the Canosa

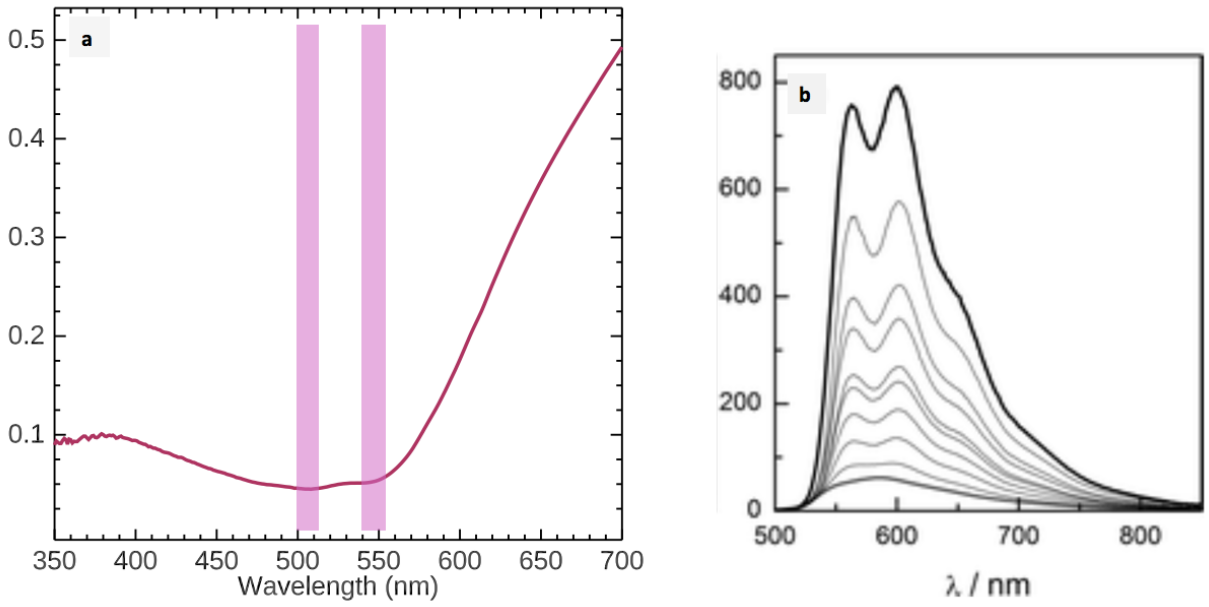

Figure 2.3: **(a)** The characteristic reflectance spectrum acquired from a powder sample of madder lake (Kremer pigments) with the diagnostic structured double absorptions at 515 and 545 nm. **(b)** The emission of purpurpin (1,2,4-HAQ) in a dimethyl sulfoxide (DMSO)-water solution, with and without Al(III), which is a main constituent of the madder lake pigment and responsible for the double absorption feature in **(a)** [**(b)** adapted from [90]].

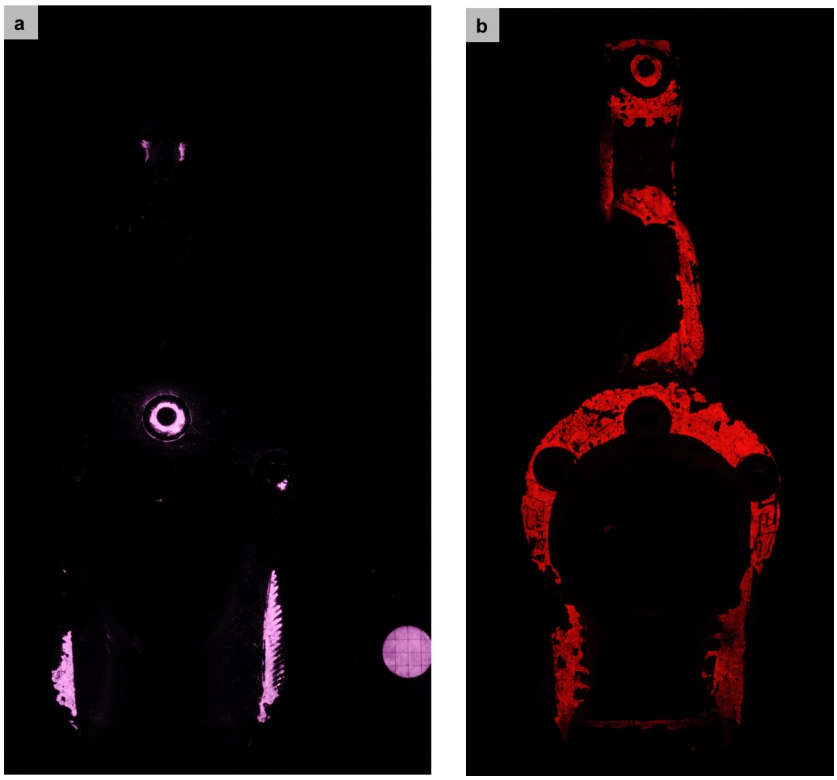

Figure 2.4: Forensic photography of Canosa 81.AE.156 produced a visible-induced NIR luminescence map of Egyptian blue (with an Egyptian blue standard in the lower right corner) **(a)** and a visible-induced visible luminescence map of madder lake **(b)**.

vases. This was also the first demonstration of isolating madder lake's photoluminescence in polychrome decoration through macroscale imaging. While the photophysical properties of Egyptian blue are well known and utilized by researchers through NIR luminescence imaging to identify the pigment in polychrome objects and wall paintings [200, 145], madder lake had not yet been targeted through forensic imaging as exclusively. Previously, UV-induced visible photography was used as a way to hint to the presence of madder lake in ancient polychrome objects and wall paintings. However, the UV-induced visible luminescence of other common materials present in these objects, such as glues, binders, and restoration materials, prevent any robust identification of madder lake. This study [113] established one of the first imaging protocols to isolate and capture madder lake pigment luminescence through visible-induced excitation.

False color analysis was applied to visualize the distribution of the two pigments over

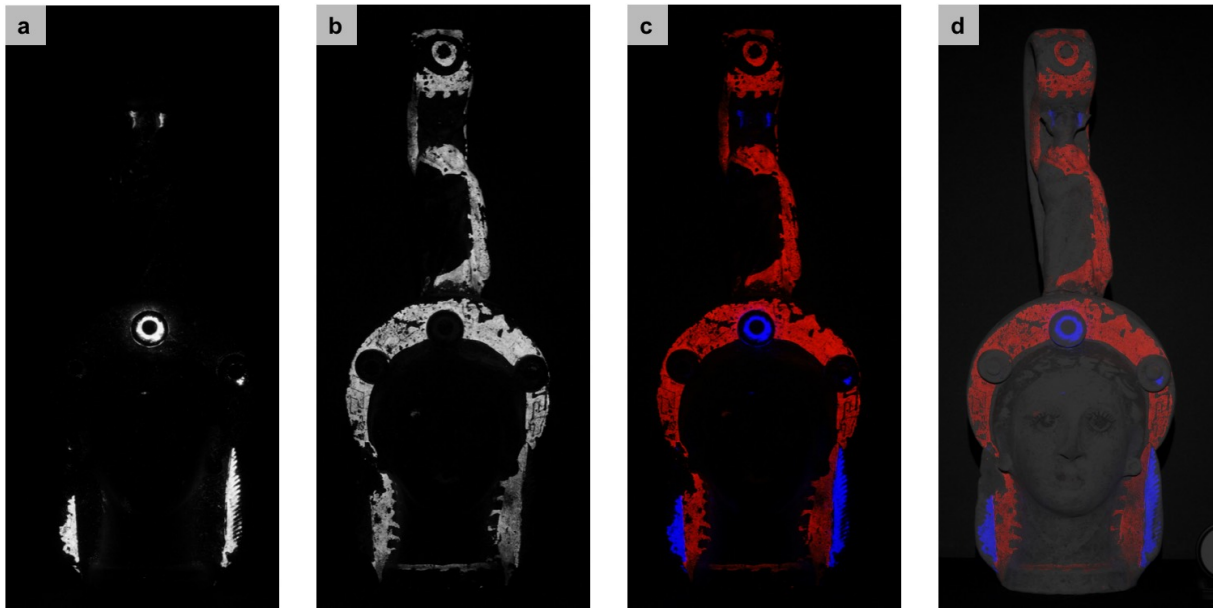

Figure 2.5: Single-channel luminescence maps of Egyptian blue and madder lake luminescence (**(a)** and **(b)**, respectively), are integrated into a false-color composite image **(c)** and overlaid onto a gray-scaled image of Canosa vase 81.AE.156 **(d)**.

the figurines. The digital luminescence images were separated into their single R, G, and B channels in Adobe Photoshop. Figure 2.5a and Figure 2.5b are the R channels of the Egyptian blue and madder lake images, respectively. A false color image was produced with the madder lake image inserted into the R channel, assigning an artificial red color to the luminescence, and Egyptian blue into the B channel, assigning an artificial blue color (Figure 2.5c). The false color image was overlaid onto a gray-scaled image of the Canosa vase (A.N. 81.AE.156) to visualize the application of the two pigments, simultaneously (Figure 2.5d).

Portable fiber-optic reflectance spectroscopy (FORS), operating in the wavelength range 350 – 2500 nm, and X-ray fluorescence (XRF) spectroscopy were also applied to characterize the pigments of the Canosa vases. FORS, also referred to as UV-Visible-NIR (UV-VIS-NIR) spectroscopy or diffuse reflectance spectroscopy, excites the sample with a UV-VIS-NIR light source and measures a material's reflectance, i.e. the material's interaction with the incident light. The recorded reflectance spectrum, such as those seen in Figure 2.2 and 2.3, presents diagnostic absorptions caused by electronic transitions, charge transfer, conduction

processes, and/or vibrational overtones of fundamental modes of molecular vibrations from the light illumination [41, 22, 196, 43], which is powerful for the identification of various painting materials such as natural pigments, synthetic inorganic and inorganic-organic hybrid pigments, as well as binders, restoration, and painting preparatory materials [7]. XRF provides complementary elemental information by measuring the energies of characteristic X-rays emitted from inner electron orbitals after the painting materials are excited by high energy X-rays. Together, FORS and XRF confirmed the presence of Egyptian blue through the collection of a reflectance spectrum similar to that in Figure 2.2a and significant elemental abundances of Cu, identified by its characteristic K_α energy emission at 8.05 keV, respectively. The luminescence of madder lake in the forensic images was further validated in the FORS spectra, attributable to the presence of the structured double absorption at 515 and 545 nm. Additional materials on the vase were identified such as an Fe-based pigment, most likely a hematite (Fe_2O_3)-rich pigment, used for the regions of bright red decoration, and kaolinite, a white clay mineral, for the clay slip of the vases.

This integrated methodology was applied in a year-long analytical campaign (2016-2017) to analyze ancient Cypriot wall paintings in Paphos, Cyprus, the first extensive non-invasive, scientific investigation of ancient Cypriot wall paintings [161]. Those results are presented in this chapter. Data collection using FORS, XRF and imaging techniques(RGB and forensic photography, photomicrography) gave access to the wall painting materials' chemistry, providing insight into the production technology and practices of ancient artists.

2.2 History of ancient Cypriot wall paintings

Hellenistic and Roman Cypriot wall paintings, which decorate residences, public spaces and tombs in the areas of ancient Nea Paphos ("New" Paphos), the eastern and western necropoleis, the Tomb of the Kings funerary complex and tombs in modern day Paphos city center (Figure 2.6), have been systematically analyzed using a protocol of combined field-deployable imaging and spectroscopic techniques. In 320 BC, the last king of Palaepaphos ("Old" Paphos) Nicocles founded the city of Nea Paphos to serve as the administrative and economic

center for the island during the Hellenistic and Roman periods [106]. Following the death of Alexander the Great, the Ptolemies, who ruled ancient Egypt at the time, took control over Cyprus [93] and established Paphos as the new capital of the island. Nea Paphos continued to be a strong economic center when the Ptolemies lost control in 58 BC and Cyprus was annexed to the Roman empire, under which it remained until the fourth century AD. The thriving signature of the ancient city can be seen in the remains of the domestic spaces, where beautiful mosaics adorned the floors of wealthy residences such as the Villa of Theseus, residence of the Roman governor of Cyprus.

As Cyprus underwent transitions of power, infusions of Hellenistic and Roman political, philosophical and artistic traditions became integral to the culture of Cyprus [149]. The expansion of Alexander the Great's kingdom produced a Macedonian empire of multiculturalism; his death, marking the start of the Hellenistic period, saw the split of his kingdom and the subsequent extensive exchange of wealth, people and materials across the old empire [139].

Hellenistic painting tradition can be characterized by three major categories: the Masonry Style, the Relief Architectural Style, and the Painted Architectural Style. Evidence of Hellenistic paintings in domestic, civic and funerary monuments varied regionally. The best surviving domestic paintings are those of the Stuccoed House of Pella, though presently there is a lack of evidence for figurative paintings in Macedonian domestic spaces. Furthermore, there is little remaining evidence of palatial wall decoration in the Hellenistic period [139]. Funerary monuments, on the other hand, being mostly subterranean, are well preserved. Tomb architecture and surviving wall painting decoration provide excellent examples to establish connections between Cyprus, Macedonia, and Alexandria. Alexandrian tombs characteristically featured open-air peristyle courts, while Macedonian tombs were sealed formed chambers; the latter feature also appeared in Alexandrian monuments, and both types of structures can be found in the necropoleis of Nea Paphos. Common decorative motifs from Alexandrian tombs such as fictive architectural elements, that is, false doors and isodomic masonry blocks, as well as floral garlands with ribbons appeared throughout

Figure 2.6: Contextual photographs of archaeological sites analyzed from ancient Nea Paphos: (**a**) The Paphos Archaeological Park; (**b**) The location of Tomb Roma 1, under the present-day Roman Boutique Hotel; (**c**) The Tomb of the Kings.

the Hellenistic and Roman Cypriot tombs in this region [93].

The death of Cleopatra in 30 BC marked the end of the Hellenistic period and the start of the Roman empire. At this time, the Roman influence over Greek territories was already evident, with elements of both Greek and Roman culture, seen in key locations in Greece (i.e., Delos) and Italy [139]. There was a significant effort by the new Roman leaders and citizens to lay claim to Hellenistic lineage by incorporating elements of the Hellenistic culture and art into their homes through the inclusion of ideas and imagery by importation, smuggling and reproduction of artworks [149]. More importantly, they understood the artistic techniques from which the paintings and objects were derived, thus cementing Hellenistic influences into Roman decorative arts. Roman wall paintings are today characterized according to the four Pompeian styles, successive in time ranging from the 4th century BC to 79 AD. The First Style is the most closely linked temporally and stylistically to Hellenistic art and seems to show similar themes to those found in ancient Cypriot paintings in their depictions of imitation marble, architectural elements and geometric shapes. There is not enough remaining decoration intact to comment on potential representations of the Second, Third and Fourth Style.

Hellenistic and Roman paintings in Cyprus also reflect access to, and use of, economic minerals such as ochres, umbers and green earth, knowledge of production methods and the trade from and to Cyprus of natural and synthetic pigments. The geology of Cyprus (Figure 2.7) and its richness in copper, umbers, ochres and green earth [166] have not only influenced the economic status of Nea Paphos but also its artistic culture. These resources were readily available, easy to extract and process, and provided the raw materials in paintings and an invaluable economic resource through trade [109, 12]. The gossans of the sulfide ores of the Troodos mountains and its ophiolitic rocks are particularly rich in colored rocks and minerals, such as hematite, goethite, and umber (iron oxide and manganese oxide) and celadonite [100, 114, 106, 44]. In the Mesaoria basin, the weathering of umbers from the sedimentary rock produced pyrolusite (MnO_2), which served as a black pigment in the paintings [106, 67]. The Lefkara formation in the southwest region of the island was the major

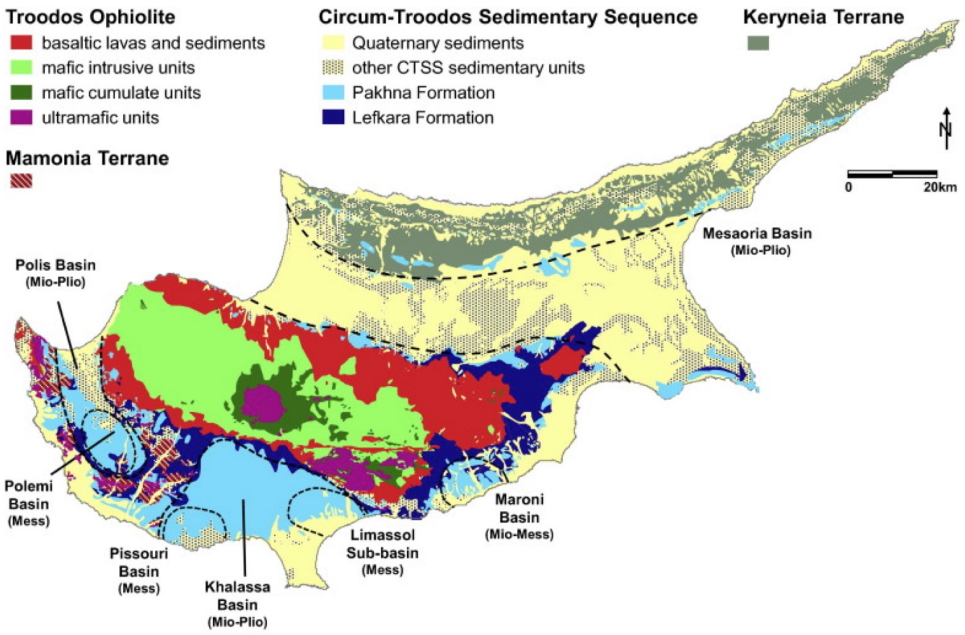

Figure 2.7: A map showing the geological formations of Cyprus. The Troodos Massif, the Mesaoria basin, and the Lefkara formation provided the natural resources that ancient artists used to prepare their pigments and plasters layers for wall paintings (image adapted from [166]).

source of chalk used as aggregate in the preparatory plaster layers of the paintings [107, 109]. Ancient artists in Paphos used the natural and synthetic pigments, pure or in mixtures, to achieve particular hues and aesthetic effects such as translucency, transparency and three-dimensionality achieved by *chiaroscuro* (*skiagraphia*), innovations that characterized the painting of these periods.

Attribution and absolute dating of the Hellenistic and Roman Cypriot paintings face several challenges. Cypriot funerary and domestic built heritage shows evidence of multiple construction phases (most likely linked to severe damages by earthquakes and other events), re-use and re-painting of the walls. The physical and 'restoration' history of these monuments make the dating and attribution of the wall painting fragments to specific time periods unreliable. Reconstructions of fragmented paintings from the Roman villas in Nea Paphos have provided a glimpse into the stylistic and technical approach towards decorative and

figurative representations in Roman Cyprus. Figurative paintings in particular, from both domestic and funerary contexts, provided valuable findings elucidating our understanding on local technical trends in the treatment of painting (artistic techniques) and/or artists/or workshops' organization.

This research aimed to address the challenge of attributing contextual information and providing a global understanding to the paintings by looking deeper into their chemistry and production technology. This study presents the first systematic non-invasive scientific survey on the polychromy of Hellenistic and Roman Cypriot monumental wall paintings, with the objective of: (1) identifying, mapping and interpreting the extent of polychromy and imagery through the characterization and imaging of the spatial distribution of pigments; and (2) exploring the function and use of pigments in the making of the wall paintings, thus obtaining new insight into the artistic expression and technical skills of the artists from the fourth century BC to the fourth century AD.

Our knowledge of the materials used in Cypriot funerary and domestic wall paintings thus far is only based on a few previous micro-analytical investigations, employing selective sampling to provide the first characterization of wall painting materials (pigments and plasters) and technology [16, 206, 107, 106]. Building on these previous researches, this study aimed to mitigate this knowledge gap on ancient Cypriot wall paintings by applying a new methodology, harnessing the capabilities of field deployable and high specificity imaging and spectroscopic technologies, enabling a detailed analysis of monumental painted surfaces without the need for taking samples. This investigation was important in expanding our understanding of the artists' palette, function of pigments and extent of painting decoration.

2.3 The Hellenistic and Roman Cypriot Wall Paintings and Their Contexts

The study of Cypriot wall paintings included the analysis of fragments from funerary and domestic contexts, either still surviving in situ or stored in museum collections. The sites

Figure 2.8: Satellite images: (**a**) satellite map of the southern half of the island of Cyprus, with the region of Nea Paphos highlighted in the red box; (**b**) map of present day Paphos showing the locations of the sites analyzed.

under study and their locations are listed in Table 2.1 and the spatial mapping of the sites is found in Figure 2.8. Paintings analyzed included fragments from five villas in Nea Paphos, located within the Paphos Archaeological Park (Figures 2.9 and 2.10); six tombs excavated within the western and eastern necropoleis; two tombs located in the modern day of Paphos; and two tombs located within and near the Tomb of the Kings funerary complex (Figures 2.11 and 2.12).

2.3.1 Paphos Archaeological Park: Hellenistic and Roman Residences

From the center of Nea Paphos, several villas of ancient wealthy citizens were excavated dating back to the Hellenistic (Hellenistic House) and Roman periods (Houses of Orpheus, Aion, and the Four Seasons). One of the more impressive residences is the Villa of Theseus, a palatial-style residence of the Roman governor of Nea Paphos, built over the foundations of earlier Hellenistic structures.

Nea Paphos suffered from the devastation of several earthquakes from the late 1st century BC to the 4th century AD [146, 106], leaving little of the walls and their polychrome decoration intact, resulting in thousands of fragments such as those seen in Figure 2.9f. The

Table 2.1: A list of the sites with wall paintings analyzed and their location. A painting ID (letter) is assigned for reference in the Results and Discussion section where the pigments are discussed. Numbers following the ID letter refer to a specific location, painting or collection of fragments from the site.

Site	**Period**	**Location**	**Paintings ID**
House of Four Seasons	Roman	Nea Paphos	A
House of Orpheus	Roman	Nea Paphos	B
Hellenistic House	Hellenistic	Nea Paphos	C
Villa of Theseus	Roman	Nea Paphos	D
House of Aion	Roman	Nea Paphos	E
Tomb at Glyky Nero (P.M. 2518)	Roman	Western Necropolis	F
Tomb Annabelle 47 (P.M. 3005)	Roman	Eastern Necropolis	G
Tomb at Costis Palamas Sq.	Roman	Pano (upper) Paphos	H
Tomb 3510	Roman	Tomb of the Kings avenue	I
Tomb Roma 1	Roman	Western Necropolis	J
Tomb Roma 2	Roman	Western Necropolis	K
Tomb Silver House 1 (P.M. 2902)	Roman	Eastern Necropolis	L
Tomb Silver House 2 (P.M. 2892)	Roman	Eastern Necropolis	M
Tomb 3882	Roman	Pano (upper) Paphos	N
Tomb 6 (P.M. 1983)	Hellenistic	Tomb of the Kings	O

best surviving paintings from the domestic sites, each named after the mosaics found within their respective contexts, were discovered in the Villa of Theseus and the House of Aion, the latter being the only residence where figurative paintings were found [105]. Ten figurative paintings were recovered in fragments from the same room in the House of Aion—one example can be seen in Figure 2.9c. Due to fragmentary nature of the domestic wall paintings, it is difficult to reconstruct the entire image scence, though from in situ surviving fragments, in addition to figurative paintings, the decoration consists mostly of geometric patterns and bands, imitation marble revetment, and monochrome paneling (Figure 2.10).

Evidence of re-use and re-plastering for new decorative scenes were evident from remaining walls on site as well as recovered fragments (Figure 2.10d); due to the multiple layers of wall paintings and the successive earthquakes that have destroyed the residences, attribution of the fragments' time period is extremely difficult.

Figure 2.9: Examples of figurative paintings, colored fragments, and pigment pellets excavated from the residences of Nea Paphos, designated now as the Paphos Archaeological Park: (**a**) madder lake pellets; (**b**) Egyptian blue pellets; (**c**) figurative painting E9, from the House of Aion; (**d**) fragments from House of the Four Seasons; (**e**,**f**) colored fragments from the House of Orpheus.

Figure 2.10: Examples of domestic in situ wall paintings in the Paphos Archaeological Park: (**a**,**b**) Imitation marble revetment and geometric designs in the Villa of Theseus; (**c**,**d**) the Hellenistic House.

2.3.2 Tomb of the Kings, the Western and Eastern Necropoleis, and Tombs in Modern-Day Paphos

Owing to the subterranean construction of tombs, Hellenistic and Roman funerary complexes survived the major earthquakes, and they preserve today much of the original wall painting imagery featuring floral decoration, isodomic bands, garlands, household utensils, animals and birds, and figurative paintings. The wall paintings decorating these tombs (Figures 2.11 and 2.12) follow conventions of contemporary paintings in northern Greece (Vergina, Pella, Demetrias), Alexandria and other parts of the empire [139, 149, 109, 203]. A notable Cypriot example of funerary wall painting decoration is found in Tomb Ammoi A with imitation of masonry, garlands and a unique ceiling carpet similar to that of the tomb of Lyson and Kallikes at Lefkadia and the Anfushi II Tomb (within loculus 5 of Hypogeum 5) in Mustafa Kamel necropolis in Alexandria [93, 112, 171, 138].

Most characteristic imagery in the tombs features geometric patterns (diamonds, triangles, bands); *trompe l'oeil* architectural elements, such as marble revetment, doors, and masonry blocks outlined with painted incised lines. Similar features are seen in Tomb Roma 1 and 2 (Figure 2.12e,f), as well as the tomb at Glyky Nero. The Hellenistic Tomb 6 from the Tomb of the Kings funerary complex (Figure 2.11e) shows a painted door above the loculus. These monumental tombs compare to the Macedonian tombs and Alexandrian Hypogea [138]. All tombs except for Tomb 6 display examples of vegetal and floral decoration. Tomb Roma 1 also shows depictions of animals and birds, as well as furniture (chest, chair), at the dado level of the central arcosolium. Other consistent motifs include egg and dart patterns, as noted in Tomb Roma 1 and fragments recovered from Tomb 3882 (Figure 2.11c).

Human figures are also found in funerary contexts, though less frequently in Cypriot tomb pictorial programs; one full figure was found on a large limestone slab in the Tomb 3510 (Figure 2.11a), the centerpiece of a triptych of limestone slabs that was used to seal an ossuary [163]. Two other paintings with surviving faces with floral decoration in the background were also reconstructed from fragments in the tomb discovered in the Costis Palamas square (Figure 2.11b) [164]. The personification of one of the four seasons (Summer)

Figure 2.11: Examples of funerary decoration featuring figurative paintings, fragments and in situ paintings featuring common decorative motifs: (**a**) a figure painted on a limestone slab from Tomb 3510; (**b**) two faces reconstructed from fragments from the tomb in Costis Palamas square; (**c**) a fragment displaying an egg and dart pattern, recovered from Tomb 3882; (**d**) a fragment with garlands recovered from Tomb Annabelle 47; (**e**) painting of a door in Tomb 6; (**f**) floral decoration in the tomb at Glyky Nero.

Figure 2.12: Examples of tombs and their funerary paintings, found in the western and eastern necropoleis, as well as modern-day upper Paphos: (**a**) Tomb Silver House 1; (**b**–**d**) Tomb 3882; (**e**) Tomb Roma 1; (**f**) Tomb Roma 2.

also survives in one of the pendentives in fragmentary condition in Tomb Annabelle 48.

Similar to the domestic sites, the tombs were re-used. The structure and material finds of numerous tombs indicate Hellenistic origin, but continuous construction and modification to the tombs' architecture as well as decorative schemes point to use well into the Roman periods [164, 138]. Notable examples showing evidence of multiple painting phases are found in Tombs Roma 1 and 2, Tomb 3882, and Tomb Ammoi B. Compared to the domestic wall paintings, the tombs show a greater extent of intact decoration remaining in situ. However, tombs throughout the city such as 3882 have suffered from environmental and anthropogenic effects. The most disastrous from the latter group are due to modern-day construction projects, making recovered fragments difficult to date to specific painting phases.

2.4 Instrumentation and data collection

An integrated approach using non-invasive, non-destructive scientific portable technologies was applied in this investigation. The ease of field-deployment and point collection with real-time feedback on the data with these instruments facilitated extensive data collection spanning across the surface of the paintings, as well as amongst the sites, not only providing materials characterization but also insight into the spatial distribution of the materials used. The high sensitivity of the chemical sensing instruments and photomicrography also revealed materials that were not easily detected by the naked eye. Forensic imaging also facilitated visualization and spatial mapping of Egyptian blue through the capture of its diagnostic luminescence.

2.4.1 Fiber-optic reflectance spectroscopy (FORS)

Two instruments were employed for analysis of Cypriot paintings and natural minerals using principles of reflectance spectroscopy.

1. A field-deployable spectroradiometer, the ASD Inc. Fieldspec 3 from Malvern Panalytical, operating between 350–2500 nm, was used to collect reflectance spectra of Cypriot

paintings, pigment pellets, and natural minerals. The spectroradiomter has three internal diffraction gratings and three detectors, all of which operate during a single measurement. For data collection in the visible-to-NIR (VNIR) range, the instrument operates a silicon photo-diode array. The short-wave infrared (SWIR) analytical range utilizes two InGaAs photo-diode detectors to collect from 1000 – 1830 nm and 1830 – 2500 nm. The Fieldspec 3 has a hand-held contact probe with a flexible optical cable that provided spot size collection of 10 mm diameter. The high spectral resolution (3 nm at 700 nm, 10 nm at 1400/2100 nm) allowed material identification of minerals in relatively pure applications as well as separation of constituents in pigment mixtures in the surface decoration of the wall paintings by analysis of diagnostic absorptions in the reflectance spectra.

2. A hand-held Miniscan EZ Colorimeter from Hunterlab, operating from 400–700 nm, was used for the characterization of standard red and yellow earth minerals from Cyprus used as pigments.

Analysis of the Fieldspec 3 data was performed in Viewspec Pro, the accessory software to the Fieldspec 3, as well as ENVI ('Environment for Visualizing Images', L3Harris Geospatial), and the data from the Miniscan EZ colorimeter was analyzed in Matlab (Mathworks). The 1st and 2nd derivatives of the reflectance spectra were also calculated to precisely identify inflection points, absorption minima and reflectance maxima in the spectral profiles for material identification. While the original reflectance spectra provided straightforward characterization of materials present in relatively pure applications (for materials with diagnostic UV-VIS-NIR signatures), analysis of the differential changes of the reflectance profile with respect to wavelength provided reliable absorption, peak maxima, and inflection values that indicated the presence of multiple materials by the quantitative deviation from expected spectral signatures. This allowed for the identification of individual constituent materials in multiple pigment layers and mixtures by comparing the values to reference spectra of natural minerals and synthetic pigments. A list of reference spectra with their VNIR reflectance profiles and respective 1st derivative calculations, as well as their spectral feature assignments,

can be found in Appendix A.

2.4.2 X-Ray Fluorescence Spectroscopy (XRF)

Elemental analysis was performed by a hand-held Thermo Scientific Niton® XL3t GOLDD$^+$ X-ray fluorescence (XRF) spectrometer with a silver anode (50 kV, 200 μA). Data was collected using the soil and mining modes at 90 s and 120 s, respectively, with a spot size of 8 mm diameter. Analysis utilized internal pre-set Fundamental Parameter and Compton Normalization calibrations. While quantitative measurements were not achievable with the portable XRF instrument, elemental identification from the characteristic X-ray peaks in the emission spectra, visualized in the Niton XRF NDT software, provided important, complementary information for the characterization of painting materials, especially for sample locations where the FORS spectra could not provide a diagnostic reflectance signature.

2.4.3 Optical Microscopy (OM)

Optical microscopy was performed with a Plugable USB2 Digital Microscope. This portable, lightweight, hand-held microscope was attached to a laptop and provided imaging at maximum magnification of 250x, allowing visualization of large mineral grains and preliminary assessment of pigment mixtures.

2.4.4 Forensic Photography (FP)

The identification and mapping of Egyptian blue on the paintings was conducted using the same imaging protocol used for the Canosa funerary terracotta vases [113]. Optical excitation was performed by a narrow-band red light illumination using an Optimax ™ Multi-Lite™ forensic LED flashlight ($\lambda_{ex,max}$ = 600 nm) and capture in the NIR (between λ ∼900 and 1000 nm) was achieved with a modified Fujifilm DSLR camera filtered by a PECA 910 filter.

2.4.5 Color (RGB) Photography

RGB photography was performed using a Canon T3 Rebel DSLR camera. QP color cards and an X-Rite Color Checker Passport were placed within the image scene to white balance and color correct the images for proper documentation and subsequent image processing.

2.5 Results

The composition and application of the painting materials through pigment mixtures and layering was significant in providing specific aesthetic qualities, tonal variations and three-dimensionality to the paintings. Unique shades of green were attained by combining green and blue pigments, applied directly over white plaster or layered over a uniform application of yellow, as well as by mixtures of green and yellow and black pigments. Purple hues were created through mixing and layering of blue and red pigments. Various tones of red and orange were also featured through the application of different red pigments and mixtures of reds and yellows.

Paintings of this period used a variety of natural inorganic mineral pigments such as green earth (celadonite, $(K(Mg,Fe^{2+})(Fe^{3+},Al)[Si_4O_{10}](OH)_2)$), goethite (FeO(OH))-rich yellow ochre (ochre refers to a natural earth pigment containing ferric oxide minerals, clay, and sand), hematite (Fe_2O_3)-rich red ochre, cinnabar (HgS), umbers (iron oxide with manganese oxide), pyrolusite (MnO_2) and synthetic inorganic pigments such as Egyptian blue $CaCuSi_4O_{10}$ and red lead (Pb_3O_4), applied over a single or multiple plaster layers [16, 106]. The arsenical compound realgar (A_4S_4), the hybrid organic-inorganic pigment madder lake, and jarosite ($(K,Na)Fe_3^{3+}(OH)_6(SO_4)_2$) were identified as 'raw' materials (prepared as powders and pigment pellets) in museum storage containers containing excavation materials from the House of Orpheus. It is unknown if these were intended for painting or if they fulfilled other functions, such as medicines and/or cosmetics [109, 173, 167].

2.5.1 Preparatory drawing and setting out techniques

Previous studies on ancient Cypriot paintings revealed that plaster preparation in the domestic spaces was more complicated than those found in funerary settings. Plaster layers in wall paintings feature two types: the *arriccio* and the *intonaco*. The *arriccio* layer is the first preparatory layer, the coarsest and thickest of a wall painting's stratigraphy. The subsequent layers are the *intonaco* layers, which are thinner and built up layer by layer to prepare for a smooth painting surface. The Cypriot paintings in the domestic spaces featured up to four *intonaco* layers applied over the *arriccio* layer [106]. The tomb paintings seemed to have only one or two plaster layers, which included the *arriccio* layer. Plaster layers closer to the wall are hydraulic (set by hydration) with hydrophobic properties, providing more strength and insulating the walls from moisture. The successive superimposed plaster layers are aerial (set by the carbonation of the calcium hydroxide–lime) and were used to provide optimal support for fresco painting. At the macroscale, several of the plasters layers in Cypriot paintings still preserved evidence of the original application technique, as can be seen in other parts of the Hellenistic and the Roman world. One such example are the herringbone incisions as seen on the *arriccio* in the remaining structure of the House of Orpheus (Figure 2.13), a technique known to roughen the *arriccio* layer to receive the successive *intonaco* layer. Similar features can also be seen in the Hellenistic Houses of the island of Delos and elsewhere in the empire [109, 16].

Figure 2.13: Herringbone incisions in the *arriccio* layer (base plaster layer) as preparation for subsequent plaster layers, from the House of Orpheus.

Preparatory techniques for painting include incised lines to guide geometric decoration as seen in Tomb 3882 (Figure 2.14), isodomic bands as seen in Ammoi A and figural outlines, unique to the figurative painting from Tomb 3510 (Figure 2.14d–f). Incised inscriptions have also been found in Tomb Silver House 2 and below the figurative painting from Tomb 3510 (Figure 2.14b,c).

Figure 2.14: (**a**) Geometric and line incisions in Tomb 3882; (**b**) Tomb Silver House 2 funerary inscription; (**c**–**f**) Figurative painting from Tomb 3510. A partially legible funerary inscription is found below the feet of the figure (**c**) and incision lines in the wet plaster created outlines of the face, arms, and garments (**d**–**f**).

Finally, amongst the fragmentary paintings analyzed, several from the House of Orpheus feature a pink wash in the plaster, most likely due to red ochre, as the basis for the top red paint layer (Figure 2.15).

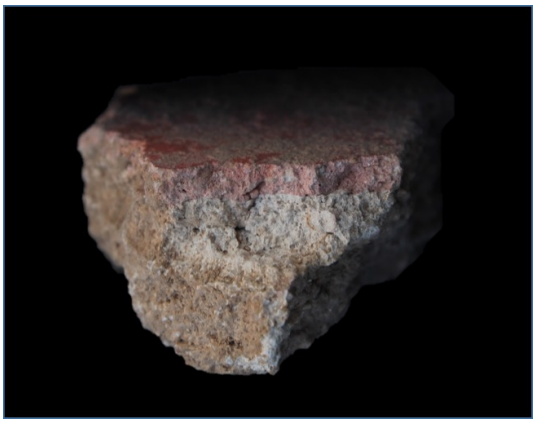

Figure 2.15: Wall painting fragment from the House of Orpheus. From top: dark red paint layer over a pink plaster layer, possibly a red ochre wash to increase the brilliance of the top red paint layer through light scattering, over a white plaster layer.

2.5.2 Pigments and Methods of Application

Pigments included a variety of natural minerals that can be found abundant in Cyprus, as well as a few synthetic pigments. These were used pure or mixed in single paint or multiple paint layers fulfilling different functions, for example, for shading creating the effect of *chiaroscuro*, or to create different hues and tonal variations. A list of pigments identified at the various sites showing the extent or limited use of a pigment is provided in Table 2.2; each pigment's application (in pure form or mixtures), the hues they produced, and their context is summarized in Table 2.3. In Appendix B, a detailed list of hues found throughout the sites is provided; for each hue, the main colorants and minor phases were identified, as well as the application, location, and function of the pigment in each painting's context. See Table 2.1 for site identification.

Table 2.2: Pigments identified on the paintings at each site.

	Egyptian blue	Green earth	Red ochre	Yellow ochre	Red lead	Cinnabar	Umber
House of the Four Seasons	x	x	x		x		
House of Orpheus		x	x	x		x	
Hellenistic House			x	x	x		
Villa of Theseus		x	x	x			
House of Aion	x	x	x	x			x
Tomb Glyky Nero	x						
Tomb Annabelle 47	x	x	x	x			
Tomb Costis Palamas	x	x	x	x			
Tomb 3510	x		x	x			
Tomb Roma 1	x	x	x	x			
Tomb Roma 2	x	x	x	x			
Tomb Silver House 1	x	x	x	x			
Tomb 6			x	x			
Tomb 3882	x	x	x	x			

Table 2.3: The hues, application methodology, and function of pigments identified in the ancient Cypriot wall paintings. The main hues listed here were found in shades of light to dark applications.

Main Pigment	Other Phases	Hues	Location/Function
Egyptian blue	Green earth; red ochre; $CaCO_3$	Blue; bluish-purple; gray-blue; bright ('cold') white	Background shading; tunic shading; animals; geometric patterns; floral decoration
Green earth	Egyptian blue; yellow ochre; Mn-compounds; $CaCO_3$	Green; green-blue; olive green	Wreaths; tunic shading; geometric patterns; floral/ vegetal decoration; architectural elements ; imitation marble revetment
Red ochre	Yellow ochre; Egyptian blue; $CaCO_3$	Red, purple; red-purple; pink; pink-red; orange-red; dark brown	Hair; geometric patterns; clothing; background; flesh tones; animals; architectural elements; imitation marble revetment
Red lead	$CaCO_3$	Orange	N/A
Cinnabar	Red ochre; Pb-based compounds	Bright pink-red	Uniform (*monochromata*)
Yellow ochre	Red ochre, $CaCO_3$	Yellow; red-yellow; orange-yellow; cream; white-yellow	Hair; geometric patterns; clothing; background; flesh tones; architectural elements; floral/vegetal decoration; imitation marble revetment; preparation layer for blue/green paint
Umber	Egyptian blue	Brown-black	Wreaths

2.5.2.1 Blue

Egyptian blue was the sole blue pigment identified in Cypriot paintings. It was identified either pure or in combination with other pigments (Table 2.3, Table B.1).

Egyptian blue is the oldest known synthetic pigment [20, 96, 104, 91, 108] and the most common blue coloring compound among the ancient Mediterranean world during the Hellenistic and Roman period. Indigo was another synthetic pigment used during this period, though its use was mainly on panel paintings as indicated by its frequent occurrence in

Greco-Roman funerary portraiture [162, 169]. While Cyprus was known for its rich copper resources with copper named as 'Aes Cyprium' by the Romans [114], to date, there is no archaeological evidence of Egyptian blue production on the island. However, pellets of the 'raw' pigment (ingots) have been found in different archaeological sites on the island.

The identification of Egyptian blue was established by FORS, XRF and forensic photography [113]. Using FORS, the pigment was identified by its diagnostic absorptions at 560, 630, and 790 nm (Figure 2.16a) (Appendix A.2.1). XRF also indicated characteristic energy emissions of copper (Cu K_α and K_β peaks at ~8.05 keV and ~8.90 keV, respectively), providing additional evidence of the pigment.

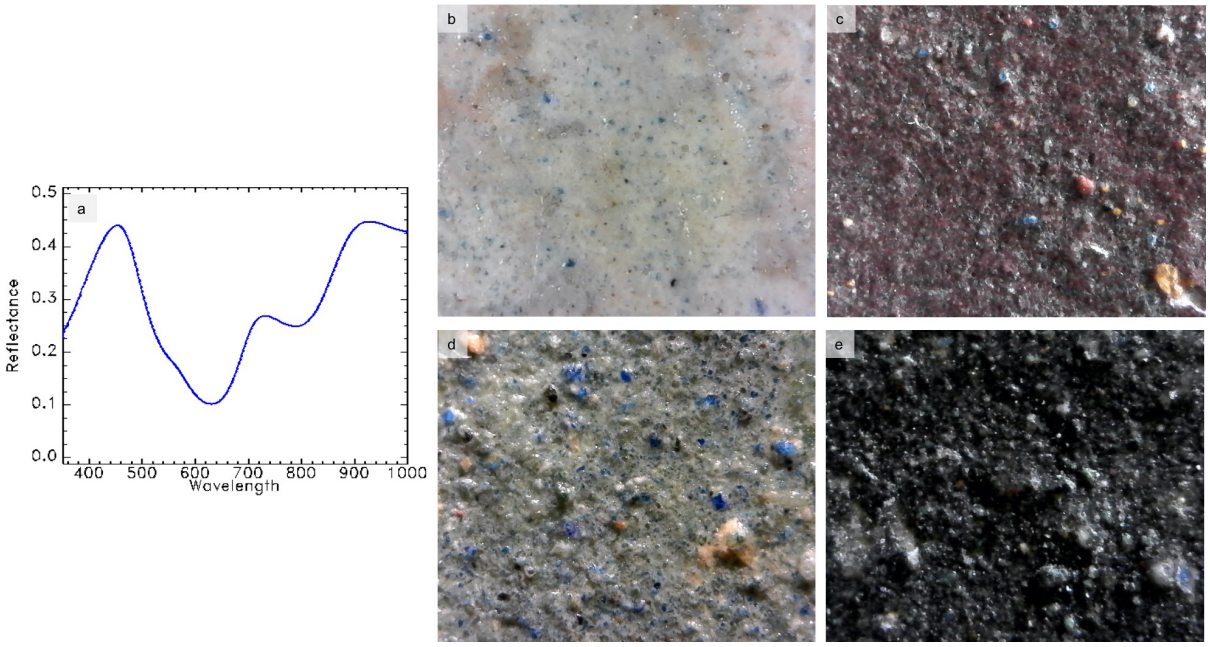

Figure 2.16: (**a**) Reflectance spectrum of Egyptian blue, featuring characteristic absorptions at 560, 630, and 790 nm. Photomicrographs (250x) of different wall painting fragments containing Egyptian blue: (**b**) Egyptian blue in a white paint (E5); (**c**) Egyptian blue in a purple paint mixed with hematite (E5); (**d**) Egyptian blue and green earth mixture applied over yellow ochre (N2); (**e**) Egyptian blue in a black paint (E5).

In painting, Egyptian blue was used undiluted and in mixtures (at different ratios) with other pigments, producing different hues and tonalities (Table 2.3 and Table B.1). When mixed in small concentrations with white pigments scattered in a white paint matrix it pro-

duces 'colder' white tones creating specific optical and aesthetic qualities to the paint. This 'colder' white tone was encountered in the coloration of the white of the eyes in sculptures and figurative paintings, as well as in decorative elements (Figure 2.16b) [201, 28]. This mixture was also applied as the backdrop for the figurative paintings in the House of Aion and in accessory items of the figures such as headpieces. Egyptian blue was further mixed with green earth and hematite to create light to dark blue-green and purple hues, respectively (Figure 2.16c,d), as well as with goethite, green earth, and pyrolusite (manganese dioxide) to produce olive green and gray-blue tones and for tunic shading. Black wreath leaves in a House of Aion figurative painting (E5) were found to be a mixture of black, green and Egyptian blue particles.

Forensic photography confirmed the presence of Egyptian blue in mixtures and unique shading applications based on its characteristic visible-induced NIR luminescence, and also aided in the mapping of this pigment providing important information not previously known on the function of this pigment in *skiagraphia*. This constitutes a new discovery on this unique application and function of Egyptian blue, appearing as wash on a muse's face from the House of Aion.

2.5.2.2 Green

Green earth, consisting of the mineral celadonite ($K(Mg,Fe^{2+})(Fe^{3+},Al)[Si_4O_{10}](OH)_2$), was the only green pigment identified in Cypriot wall paintings. It was discovered in different paintings either pure or in combination with other pigments (Table 2.3, Table B.2).

The presence of celadonite in Cypriot paintings is not surprising, as Cyprus is one of the major Mediterranean sources of this mineral [100, 75, 12, 106]. In this research, the identification of green earth was based on its characteristic reflectance spectrum, featuring asymmetrical reflectance peaks ranging from 544 – 564 nm and two absorptions at 750 nm and a broader one further into the near-infrared ($\sim$ 1000 nm) due to electronic transitions from crystal field effects (Appendix A.3.4), resulting in a diagnostic reflectance peak at 830 nm. Absorptions in the SWIR specific to celadonite ($\sim$ 2257, 2302, and 2346 nm) due to

hydroxyl (OH)-combination bands arising from the effects of the metal cations Al, Fe, and Mg helped to distinguish it from the mineral glauconite (Figure 2.17b).

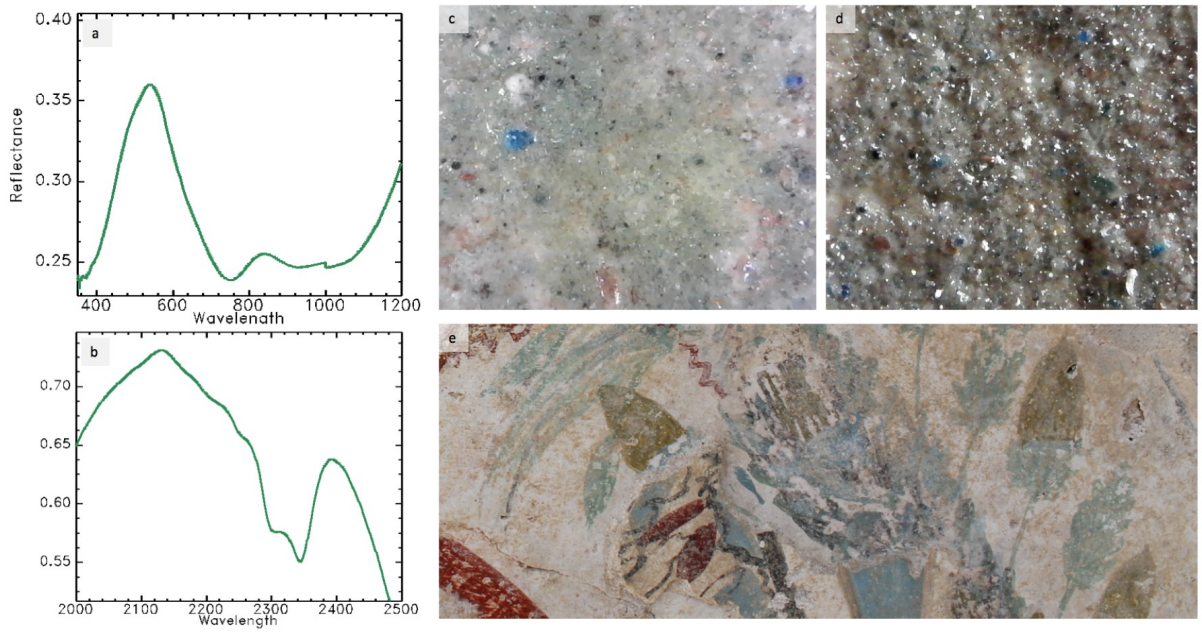

Figure 2.17: (**a,b**) Reflectance spectra featuring diagnostic absorption features of green earth (celadonite) in the visible range (400–1200 nm) and the short-wave infrared (2000–2500 nm) of a green painting fragment from the House of Orpheus. The following are photomicrographs (250x) of different wall painting fragments containing green earth: (**c**) light green hue consisting of green earth and Egyptian blue (E5); (**d**) dark olive green tone consisting of green earth, Egyptian blue, goethite, and a manganese-containing compound (E5); (**e**) example applications of various shades of green applied in Tomb 3882 (N1).

Its application was versatile, as a wide range of hues was noted containing green earth (Table 2.3 and Table B.2), including light and dark blue-greens (mixed with Egyptian blue), light and dark olive greens (mixed with goethite and sometimes pyrolusite), and other tones of green in mixtures with white or carbon black (Figure 2.17). Mixtures of green and blue were also applied over yellow ochre to create a bright blue-green tone.

In Cypriot paintings, green earth was used in imitations of marble revetment, geometric bands, floral motifs, and in the wreaths of figures. Additionally, the dark olive green tones were used in the shading of the tunic of figures.

2.5.2.3 Red

Three distinct red pigments were identified within the paintings: a hematite-rich red ochre, red lead and cinnabar (Table 2.3, Table B.3).

Hematite

Hematite (Fe_2O_3) is a mineral found abundantly in the gossans (iron cap) of the sulfide deposits of the Troodos mountains (e.g., Skouriotissa mine) in Cyprus [114]. The dominant red colorant in the paintings was a hematite-rich red ochre pigment, applied pure or in mixtures to produce tones of red, reddish orange, pinks, purples, and flesh coloration (Table 2.3 and Table B.3). It was used as the main pigment in geometric patterns, animals, furniture, floral decoration, marble imitation, and in figurative paintings (flesh and garments) (Figure 2.18a,b). It also most likely served as the colorant in the pink wash of the plasters of decorated fragments from the House of Orpheus.

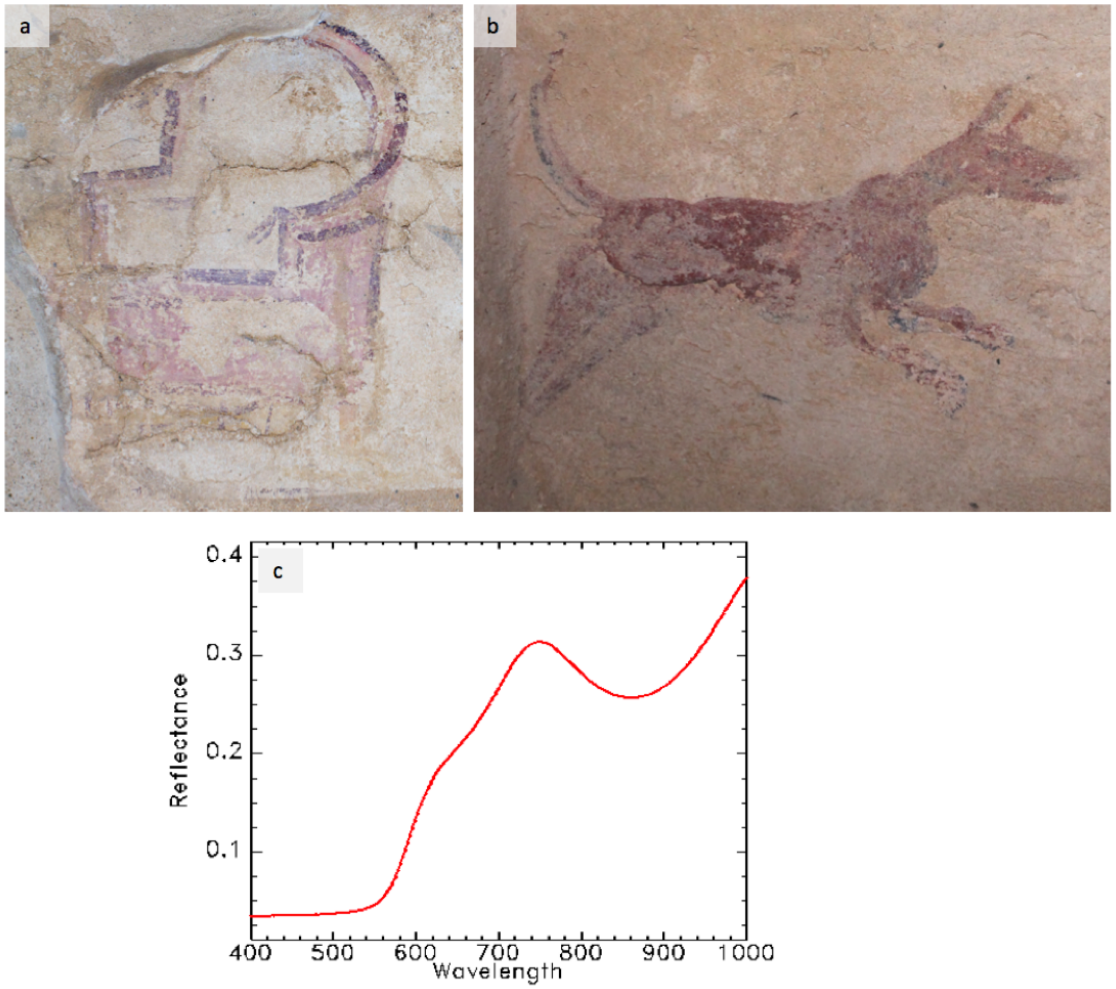

Figure 2.18: (**a**) Depiction of an arm chair featuring light and dark purple hues painted on the northern end of the dado of the central arcosolium in Tomb Roma 1 (J); (**b**) A red painted dog on the southern end of the dado of the arcosolium (J); (**c**) reflectance spectrum of hematite.

Red ochre was confidently identified by FORS, as XRF alone could not distinguish between different Fe compounds, namely goethite and other iron oxyhydroxides. Its reflectance spectrum features a UV charge transfer absorption band, responsible for the red hue of the mineral, and the characteristic inflection point in the visible region at 575 nm, arising from crystal field transitions of the Fe^{3+} ($^6A_{1g}(^6S) \rightarrow {}^4T_{2g}(^4G)$), as well as the local maxima at 749 nm and a broad absorption at 885 nm due to the Laporte-forbidden transitions ($^6A_{1g}(^6S) \rightarrow {}^4T_{1g}(^4G)$) (Figure 2.18c). While the mineral hematite is reported to have an

inflection point of 585 nm (Appendix A.1.1), the red ochre sites sampled with FORS consistently showed an inflection at 575 nm. A measurement collected from a powdered red ochre rock sample in Cyprus (Appendix A.3.1) also features an inflection at 577 nm; a small shoulder at $\sim$ 450 nm and the slightly shifted inflection indicates that the sample was abundant in hematite, but most likely contained other minerals.

Cinnabar

Cinnabar (HgS) was identified in painting fragments from the House of Orpheus. It was mixed with red ochre and produced a bright pink-red hue (Table 2.3) (Figure 2.19a), applied over a pink plaster most likely colored with red ochre. XRF data showed photon emissions of characteristic X-rays of Hg and S, at 9.89 and 11.82 keV (L_α and L_β of Hg) and at 2.31 keV (K_α of S) respectively. Emissions of characteristic X-ray of Fe (with K-lines at 6.40 keV and 7.06 keV) (Figure 2.19b) may derive from the pink plaster layer and/or from the top red paint.

The presence of cinnabar in Cypriot paintings constitutes an interesting finding, as cinnabar is not native to Cyprus. The procurement and processing of natural resources of cinnabar was described by Greek philosopher, Theophrastus (4th–3rd century BC), in his treatise *On Stones* [*De lapidibus:* 58–59][194]). Whether the cinnabar detected here is natural or synthetic cannot be determined non-invasively. The lack of geological resources and evidence of production in Cyprus suggest that cinnabar was imported and used in specific commissions.

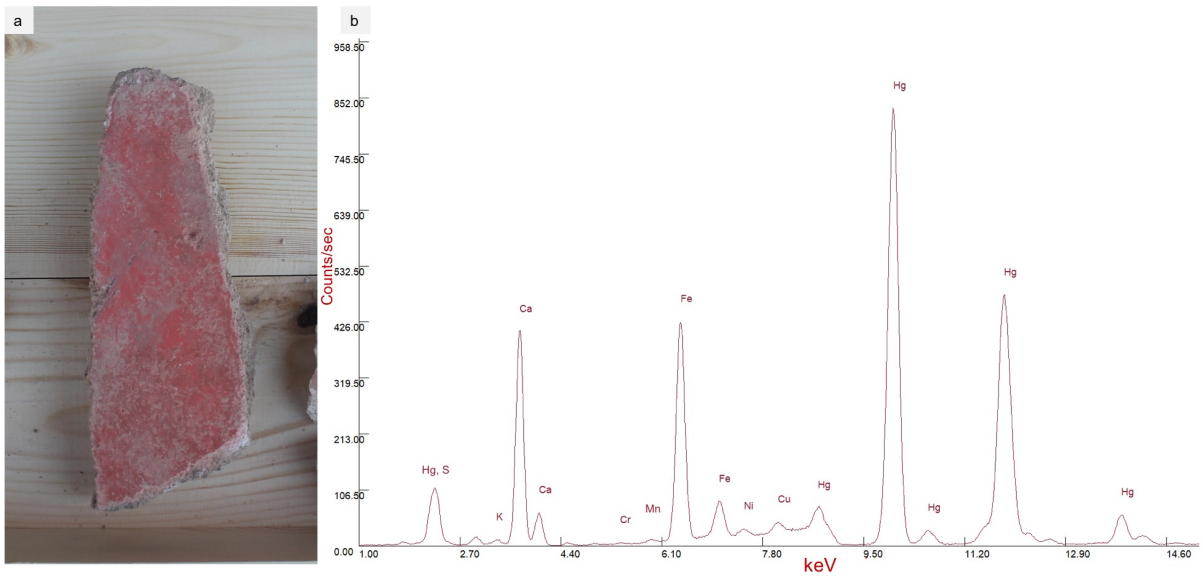

Figure 2.19: (**a**) A wall painting fragment decorated with cinnabar and red ochre from the House of Orpheus (B2); (**b**) an X-ray fluorescence (XRF) spectrum of the cinnabar-rich paint layer with elemental abundances from the preparation layers. The presence of Cr in the spectrum may be indicative of provenance.

Red lead

Red lead (Pb_3O_4), also known as minium, is an artificially-produced semiconductor pigment with an orange-red color. In a mostly pure application, it has a bright orange hue and is quite distinguishable from other orange hues produced from mixing red and yellow earth pigments (Figure 2.20a,b). This unique color was noted in several painting fragments excavated from the House of the Four Seasons and the Hellenistic House, which prompted spectroscopic analyses to confirm its chemical structure. Red lead was identified by XRF from its characteristic Pb photon emissions at 10.55 and 12.61 keV (L_α and L_β, respectively) (Figure 2.20d), complemented by FORS which showed a sharp reflectance transition, due to electron excitation across the conduction band, with a band gap at $\sim$ 2.1 eV. The band gap (and therefore color) of red lead is influenced by the presence of impurities such as PbO (lead oxide) (Figure 2.20c)(Appendix A.2.3).

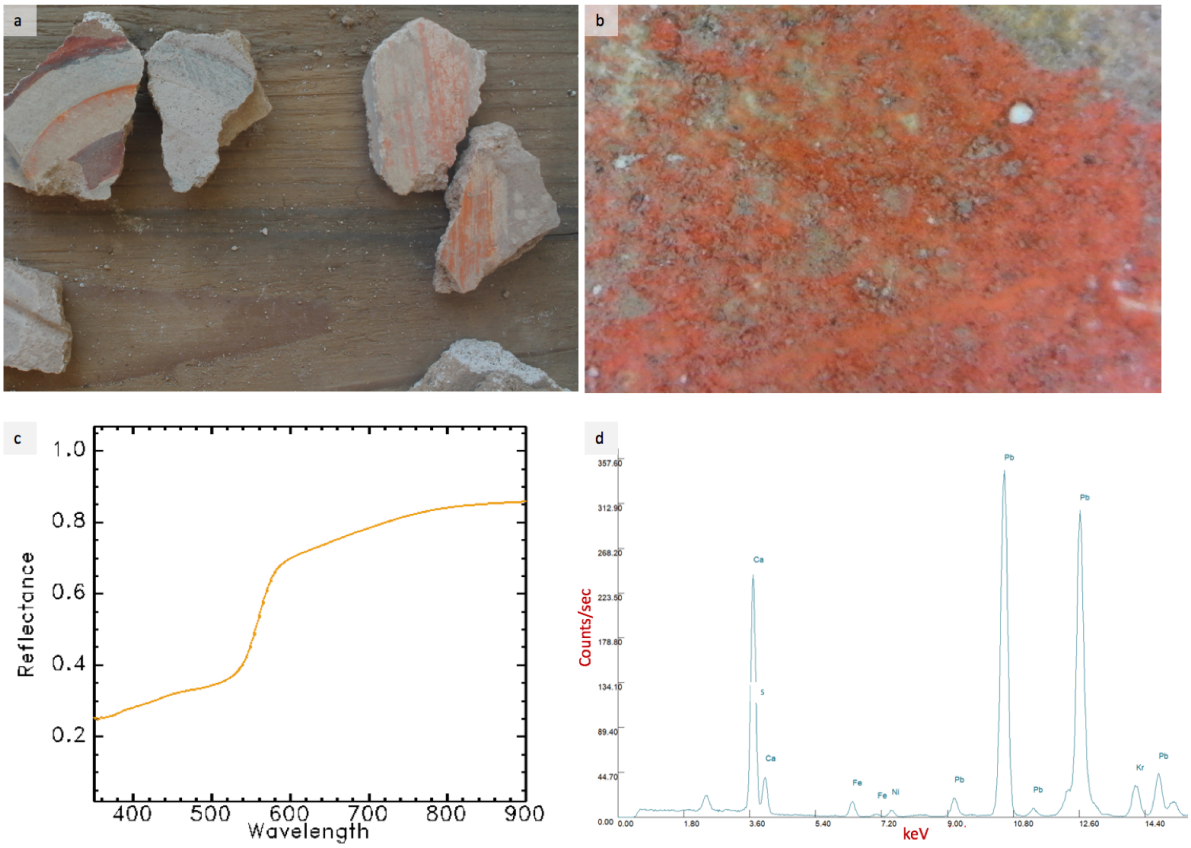

Figure 2.20: (**a**) Fragments featuring red lead from the House of the Four Seasons (A1); (**b**) Micrograph (250x) of a fragment from the Hellenistic House (C5); (**c**) reflectance spectrum and (**d**) XRF spectrum of a fragment from the House of the Four Seasons (A1).

While the production of this synthetic pigment in Cyprus cannot be excluded, the lack of Pb ores available on the island and the absence of any archaeological evidence points to an imported pigment, most likely as red lead powder. From the surviving painted fragments, it seems that its application in the paintings was limited to geometric designs and monochrome decorations.

2.5.2.4 Yellow

In the set of paintings analyzed in this study, only a goethite-rich yellow ochre was detected, used either pure or in mixtures with other colors (Table 2.3, Table B.4). As with hematite, goethite (FeO(OH)), a hydrated ferric oxide, is another abundant mineral in the gossans

of sulfide ores in Cyprus. Mixtures of yellow ochre with red ochre produced reddish and orange-yellow hues, as well as flesh tones. It was also mixed with green earth and umber or pyrolusite to produce shades of olive green. Like red ochre, the application of this yellow earth pigment was found in both funerary and domestic contexts and employed in both decorative motifs, as well as figurative paintings.

The reflectance spectrum of yellow ochre identified in the paintings is characteristic of goethite (Figure 2.21c). Its yellow hue is attributed to the UV charge transfer absorption band, crystal field transitions cause the absorptions giving rise to the shoulder at $\sim$ 450 nm ($^6\mathrm{A}_{1\mathrm{g}}(^6\mathrm{S}) \rightarrow {}^4A_{1\mathrm{g}}, {}^4\mathrm{E}_{\mathrm{g}}(^4\mathrm{G})$), the inflection point at 550 nm ($^6\mathrm{A}_{1\mathrm{g}}(^6\mathrm{S}) \rightarrow {}^4T_{2\mathrm{g}}(^4G)$), and the broad absorption at $\sim$ 900 nm due to the Laporte-forbidden transitions $^6\mathrm{A}_{1\mathrm{g}}(^6\mathrm{S}) \rightarrow {}^4T_{1\mathrm{g}}(^4G)$.

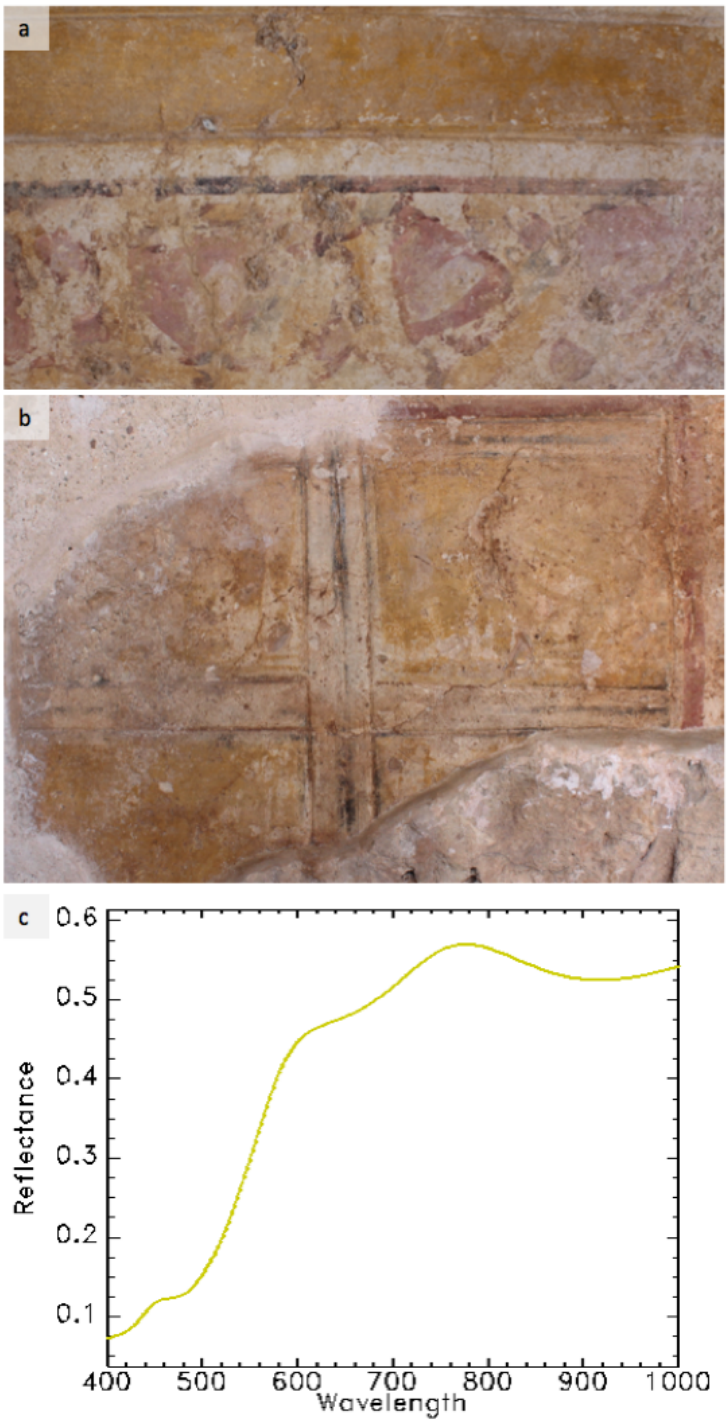

Figure 2.21: (**a**) A yellow band in the thalamos chamber of Tomb 3882 (N3); (**b**) A false door in Tomb 6, painted with yellow ochre (O); (**c**) The reflectance spectrum of goethite.

2.5.2.5 White and Black Pigments

White pigments were mixed with colored minerals and compounds in various concentrations to adjust the intensity of the hues and provide lighter tonal variations. This can be seen in the figurative paintings of the House of Aion where white was mixed with other pigments to produce facial highlights and more naturalistic flesh tones, as well as in the pink tones within the imitation marble revetment patterns in tombs such as Tomb 3882. Calcium carbonate ($CaCO_3$) was identified by its absorption feature at 2340 nm, as well as by Ca characteristic K_α lines at 3.69 keV. Previous micro-analytical studies also identified the presence of $CaCO_3$ in the paintings [106, 16].

White pigments mixed with Egyptian blue served as the backdrop for the figurative paintings in the House of Aion. Several examples of intentional bright white hues in geometric and pattern decorations also appear in the thalamos chamber and the northwest arcosolium of Tomb 3882, as well as in the accessory items in the figurative paintings of the House of Aion (Figure 2.22).

Figure 2.22: Details of paintings from Tomb 3882: (**a**) white geometric patterns alternating with blue geometric patterns (N1); (**b**) A brushstroke of white pigment is applied over a pink triangle (N3). From a figurative painting recovered from the House of Aion, (**c**,**d**) earrings and a central decorative headpiece are produced with white pigments on the figurative painting (E5).

Black pigments were also found in mixtures to create unique tones and dark shades in the paintings. XRF analysis of the black hues such as the wreath leaf of figurative painting E5

showed X-ray emissions of Mn and Fe, suggesting the use of umber (iron oxide and manganese oxide) (Figure 2.23). Carbon black may also have been used based on observations from in situ photomicrography.

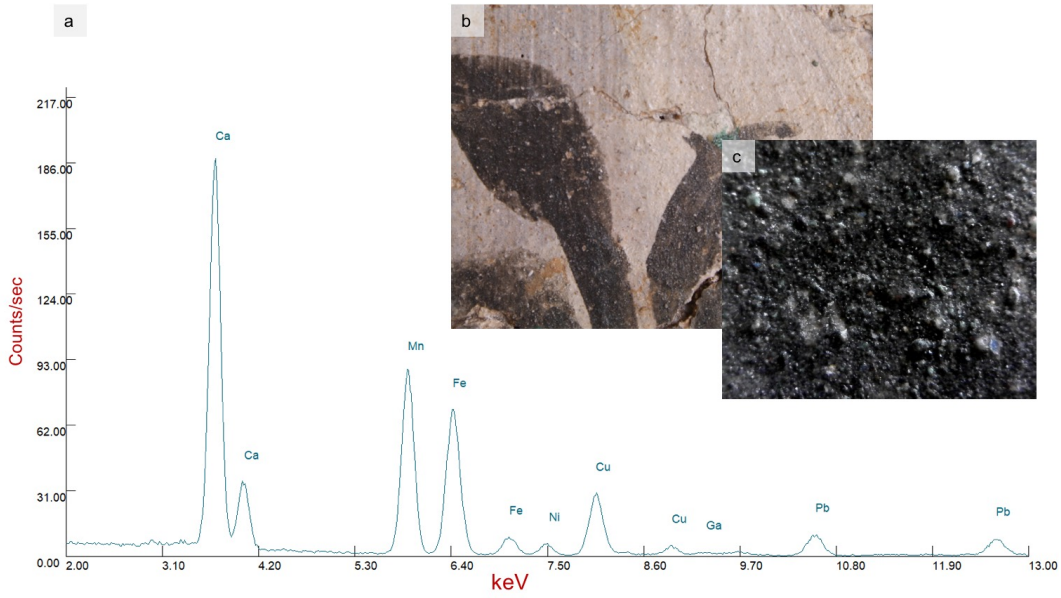

Figure 2.23: From a figurative painting from the House of Aion (E5), (**a**) an XRF spectrum taken of a black wreath leaf shows characteristic X-ray emission of Mn; (**b**) detail and (**c**) photomicrograph (250×) of the wreath leaf shows blue particles within the black matrix, most likely Egyptian blue, the source of the Cu peaks in the XRF spectrum.

Black paint was used to mark incised architectural lines, as well as in tunic shading (Figure 2.24a), and in the wreaths of the figurative paintings. It was also applied as outlines for different colorful geometric patterns in Tomb 3882 (Figure 2.24b).

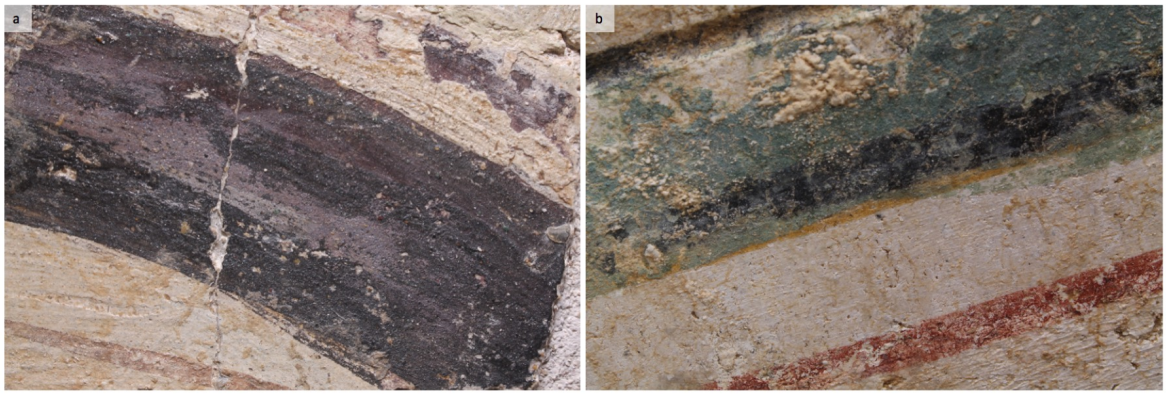

Figure 2.24: (**a**) Details of a figurative painting from the House of Aion: tunic shading is achieved using layers of purple and black to produce optical effects of light and dark purple hues (E5); (**b**) From Tomb 3882, a black pigment was used for outlining geometric bands (N2).

2.6 Discussion

2.6.1 Significance of Technical Applications to Painting Aesthetics

The analysis of ancient wall paintings indicated that a variety of pigments, either natural minerals or synthesized compounds, comprised the palette of the Cypriot painter during the Hellenistic and Roman periods. Most common natural minerals included celadonite, yellow and red ochres (goethite and hematite, respectively), umber (iron oxide and manganese oxide) and calcium carbonate. Cinnabar and realgar (the latter identified in the XRF data by S K_α and As K_α and K_β lines, only found in a preparatory state) were also present. Synthetic inorganic and inorganic-organic hybrid pigments include Egyptian blue, red lead and madder lake (the latter identified by FORS, only found in a preparatory state). While analyses conducted non-invasively were limited in providing data necessary to geosource the natural minerals, it is most probable that green earth, yellow and red ochres and umber are of local origin, owing to their abundance on the island and their known use in antiquity as pigments. As with copper, timber and asbestos, these natural resources were part of an extensive trade and communication network that provided great wealth to Cyprus during the Roman period. Cypriot green earth (celadonite mineral) provided one of the most

important economic minerals during antiquity. Evidence of its trade is indicated by the identification of this pigment on Mediterranean wall paintings outside Cyprus [12]. Cinnabar, one of the most celebrated pigments in ancient times, was most likely brought from Spain and/or Ephesos (modern-day Turkey) as these were well-known sources of cinnabar in the ancient Mediterranean world [Pliny (*Naturalis historia XXXIII: 37*)[158]][Theophrastus (*De lapidibus:* 58–59) [194]] [83]. The use of cinnabar seems to be in line with practices described in ancient texts, as it was applied in a mixture of red ochre, most likely to balance the 'harsh' tone of a pure application [Pliny (*Naturalis historia XXXIII: 39*) [158]]. Only found in the House of Orpheus, its limited application implies that it was valued and employed for specific applications such as 'monochromata' (single-color painting) of important commissions.

Red lead was most likely imported to Cyprus as a prepared pigment. Its use in Cypriot paintings is rare; it was only found in two sites (the House of the Four Seasons and the Hellenistic House). However, as red lead is known to blacken to form other lead compounds when used in wall paintings [14], its rare use in this form of painting may not be surprising. Realgar (arsenic sulfide) has not yet been identified in Cypriot wall paintings; as it is not a local resource, it was most likely imported. Madder lake (an inorganic-organic hybrid pigment) could have been produced locally as the plant from the Rubiacae family was cultivated on the island since ancient times.

Egyptian blue is not known to have been produced in Cyprus, but the copper mines of Skouriotissa served as an important resource for the production of Egyptian blue in Egypt [Theophrastus (*De lapidibus:* 55) [194]]. Its use in Cypriot wall paintings presents an original application in delineating facial outlines an in *chiaroscuro*. The ancient artists used this core palette of locally-inspired resources, mixed with black and white pigments, to produce an impressive range of hues in the wall paintings.

The most diverse range of hues present in the ancient Cypriot paintings were found in shades of green, purple and flesh tones. Changing the relative concentrations of the constituent pigments in mixtures, or by layering relatively pure pigments or pigment mixtures over other paint layers, as well as grinding and using pigments of variable grain sizes, influ-

enced the optical properties of the paint layer through light scattering and produced different perceived colors. Light and dark olive green hues whose tones shifted between a deeper green and yellow-green, were produced by various combinations of green earth, yellow ochre, Egyptian blue and a Mn-based black pigment (most likely umber or pyrolusite). For example, an olive-green color representing a plant stem (N2) was produced by mixing a relatively small amount of Egyptian blue into a green earth matrix, and then applied over a base layer of yellow ochre. Nearby, a strong yellow-toned olive green was present in the plant decoration, which was produced by a mixture of green earth and yellow ochre (N3). In regions of paintings where the application of multiple pigment layers is not obvious, the presence of yellow ochre may be due to an intentional mixture of yellow and green, or due to a partial alteration of green earth in its natural environment [109]. In other wall painting fragments, a larger relative concentration of Egyptian blue mixed with green earth and applied over yellow ochre produced a bright blue-green hue (B, Figure 2.25a).

Figure 2.25: (**a**,**b**) Fragments recovered from the House of Orpheus (B); (**c**) photomicrograph (250×) from Tomb 3882 (N2).

Mixtures of green earth and Egyptian blue have been reported in ancient Roman paintings [175, 131, 153, 106, 109], as well as ancient Cypriot polychrome sculptures [80]. Theophrastus discussed how different hues were produced by Egyptian blue based on the state of its preparation, with larger grains producing darker blue hues, and finer grains producing light or pale blue hues [Theophrastus (*De lapidibus:* 55) [194]]. Figure 2.25b shows an example of significant density of large-grained Egyptian blue crystals applied over a matrix of green

earth containing a low concentration of finer-grained Egyptian blue particles, applied over an undercoat of yellow ochre. This seems to be the first documentation of this extensive mixture/application process with these three core pigments by artists in antiquity.

One of the most valuable materials for producing the color purple was the organic dye known as Tyrian purple, derived from mollusk shells. Pliny described the process of using this dye and how to produce the intended optical effects by applying different undercoats such as sandyx (a lead white and red ochre mixture heat-treated to produce a red-orange hue) to produce a cinnabar-type hue, or Egyptian blue as a base coat to produce a deep purple hue [Pliny (*Naturalis historia XXXIII: 26*)[158]] [57]. The high cost and demand of natural resources to produce Tyrian purple meant that other means were used to achieve purple hues in ancient painting. This included mixtures and layering of Egyptian blue or indigo with madder lake, a red lake dye pigment and one of the most prolific synthetic pigments in the ancient world [107, 27]. In ancient Cypriot wall paintings, however, no evidence for the presence of red or purple dye pigments has been found. Though madder root is easily accessible in Cyprus and found in the decoration of pottery and votive shards [40], pellets of prepared madder lake pigment have been found in archaeological excavations, and it is one of the most ubiquitous red dye pigments in antiquity, its use did not seem to extend to Cypriot wall painting applications.

Ancient Cypriot painters predominantly used mixtures and layering of red ochre and Egyptian blue to produce purple tones, most of which were found in the figurative paintings from the House of Aion. Two exceptions were the faint purple lines used in the shading of the blue tunic of the figurative painting from Tomb 3510, and the outline of the chair found at the dado level of the central arcosolium in Tomb Roma 1 (Figure 2.18a). Purple tones were also mixed and layered with black pigments to give the effect of shading in the tunic of figure E5 (Figure 2.17c). Finally, similar to the light blue background washes produced by mixtures of white pigments with Egyptian blue, mixtures of low concentrations of red ochre with Egyptian blue and white pigments produced faint purple background washes and architectural features.

Mixtures and layering of pigments also helped to develop the flesh tones of the figurative paintings in the funerary and domestic spaces. The artistic skill and technological creativity of ancient Cypriot painters are showcased in the figurative paintings recovered from the House of Aion [105], Tomb 3510 [163], and the tomb from Costis Palamas square [164]. The garments, accessories, flesh tone and facial shading applications, as well as surrounding floral decorations highlighted the application of complex pigment mixtures and layering to produce a wide variety of hues, as well as the artful rendering of the figures' facial features, jewelry, and clothing (Figure 2.26).

Figure 2.26: (**a**) From Tomb 3510, a funerary figurative painting exhibits fine brush strokes with juxtaposition of different colors in small details such as the eyebrows and hair and the blending of ochres to produce naturalistic shading in the face are a testament to the skill of the artist (I); (**b**) From the House of Aion, a figurative painting features extensive color mixing and shading to produce multiple tones in the skin and a heavy *skiagraphia* effect (E9); (**c**) A funerary figurative painting from the tomb in the Costis Palamas square shows a simpler depiction of facial features; there is less skin tone variation than the other two figures, and shading mostly appears with the application of a red wash around the face (H1).

To produce the flesh tones of the figurative paintings and give a naturalistic effect to these faces, red and yellow ochres were mixed together with white pigments. The relative concentrations of each pigment produced tones that ranged from dark pink to a soft cream-colored tone; additionally, the artists used these pigments to create highlights in the face along the bridges of the nose and the forehead, complemented by shading around the eyes,

chin and neck, to give the effect of *skiagraphia* (Figure 2.26a,b). This technique was developed by Apollodorus, a 5th century BC painter from Athens, who Pliny referred to as "*lumen artis*" and lauded him as the first to achieve realistic figurative painting through his *skiagraphia* [115]; [Pliny (*Naturalis historia XXXIII: 36*)[158]]. Theophrastus also discussed in his treatise how red ochre was used to create flesh tones, a practice clearly seen in the Cypriot paintings [Theophrastus (*De lapidibus:* 51) [194]]. However, with the aid of forensic photography, an important discovery was made in the technological approaches to figurative paintings that are not noted in ancient records. Egyptian blue was found to be mixed with the flesh tones to create regions of brighter hue. Thus, the well-known practice of mixing Egyptian blue with white pigments to create a 'cold' white tone, an effect previously noted in background washes of the figures and a practice applied throughout the ancient world, was applied in facial shading to enhance naturalistic features.

In one of the two faces recovered from the tomb in the Costis Palamas square, forensic imaging revealed Egyptian blue in the outline of the cheeks (Figure 2.27b). This provided a brighter foundation to lighten the hue of subsequent layering of a red ochre wash, creating a shading effect around the face. This practice of using Egyptian blue with white pigments to build up the flesh tones in ancient figurative painting for naturalistic appearances was also discovered in the Greco-Roman Egyptian funerary mummy portraits from the 1st–4th century AD [162, 77]. From the House of Aion, figurative paintings E3, E5, and E7 all showed the use of Egyptian blue to enhance facial tones as well as 'cold' white accents to the eyes, while paintings E1, E3, and E9 had Egyptian blue appear in white jewelry and head accessories (Appendix C.1).

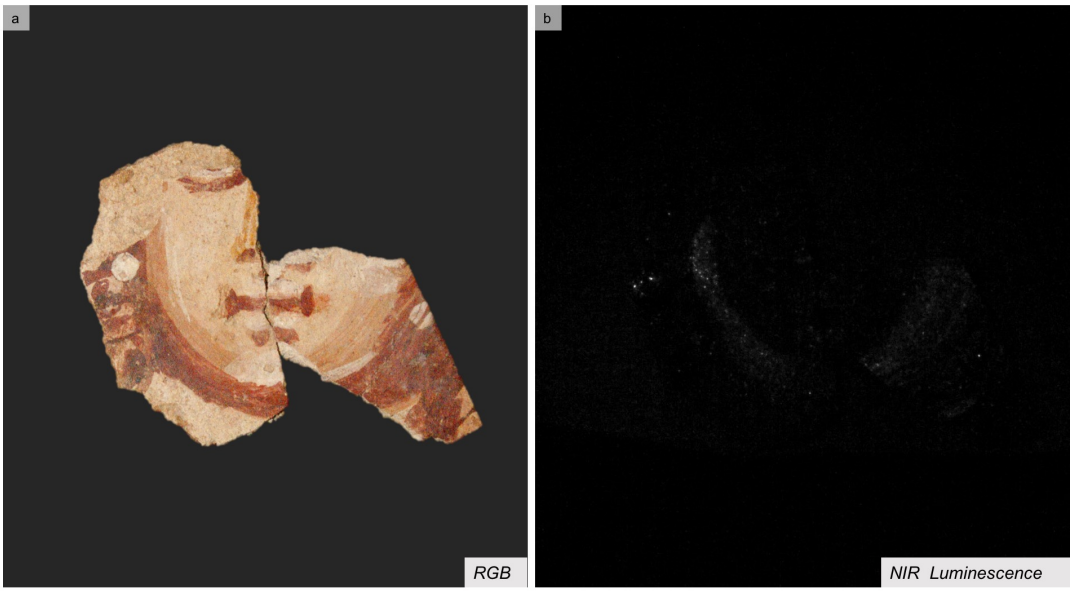

Figure 2.27: (**a**) A color (RGB) image of a reconstructed face from the painting fragments recovered in the tomb in the Costis Palamas square (H2); (**b**) Forensic imaging shows near-infrared (NIR) luminescence of Egyptian blue in the cheeks, indicating a mixture of Egyptian blue with white pigments to facilitate brighter tones in the shading of the cheeks.

In figurative painting E9 from the House of Aion, a unique approach to facial shading with Egyptian blue was discovered. Near-infrared luminescence imaging and microscopic observations revealed a dense wash of Egyptian blue over the eyebrows and around the cheeks of the face (Figure 2.28). Egyptian blue was further detected within the flesh tones, a practice similar to the paintings previously discussed and the funerary mummy portraits. However, the blatant outline of the face using a wash of Egyptian blue, a truly unique technique in the art of shading, is the first example noted amongst figurative paintings, and the only one found amongst the Cypriot collection. The application of Egyptian blue in this manner provides new insight into artistic practices and a characteristic marker for attribution to a specific artist, or group of artists.

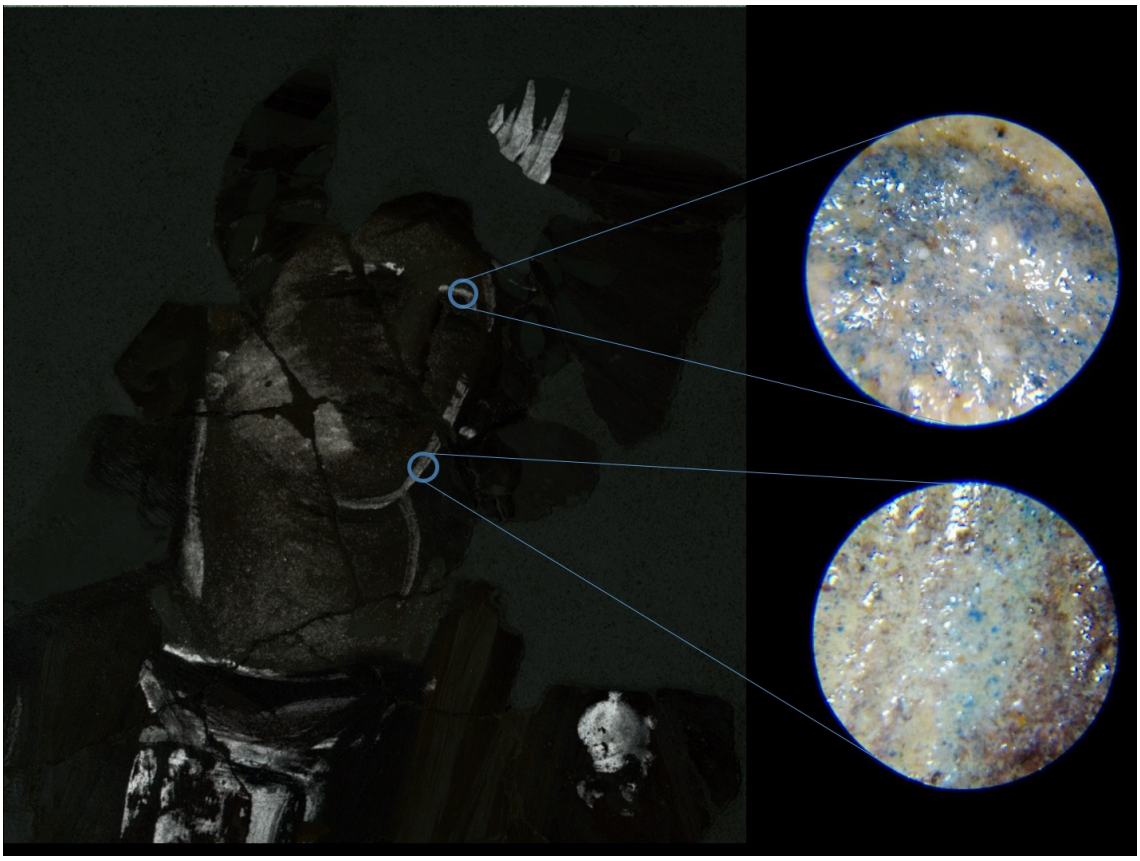

Figure 2.28: The NIR luminescence image of figurative painting E9 from the House of Aion, overlaid onto the color (RGB) image of painting E9, reveals different uses of Egyptian blue to enhance facial features. In the flesh tones, it was mixed with white pigments to promote brighter tones to contrast the shading of the skin, while along the eyebrows, cheeks, and neck, a dense wash of Egyptian blue was applied for outlining, as noted in the micrographs.

Due to the limited availability of figurative paintings in funerary spaces and the discovery of figurative paintings in domestic spaces only coming from the House of Aion, it is difficult to identify specific technological patterns and isolate trends between the two settings to classify approaches in ancient figurative painting on Cyprus. However, even amongst this set, a wide variety of technological approaches and artistic skill is observed amongst the paintings. This suggests that the artists were developing and testing new methodologies in their paintings. This raises the question whether external influences and/or adaptations contributed to this creative use of color.

2.6.2 Contributions of Non-Invasive Technology to Art Historical Interpretations and Preservation of Ancient Paintings

Analytical forensic photography aided to identification and mapping of Egyptian blue, based on its luminescence. When excited by red light, Egyptian blue 'glows' owing to its high near-infrared luminescence quantum yield, even when it only survives as ghost paint, or is concealed by salt encrustations and is rendered invisible to the naked eye. Harnessing this property of Egyptian blue, it was possible to recover partially lost and hidden decoration. In Tomb Roma 1 (Figure 2.12e), visible-induced NIR luminescence imaging recovered the partridge's head painted on the dado of the central arcosolium, which in its present state is almost completely indiscernible. Egyptian blue's quantum yield of 10.5% and lifetime luminescence of ∼138 µs allows forensic imaging to reconstruct these images [6, 45] (Figure 2.29. The tail and legs, both heavily weathered, were also decorated with Egyptian blue. Micrographs show a base layer of red and yellow pigment, and it appears that Egyptian blue particles were mixed into this base layer. A top layer of black pigment defines the legs.

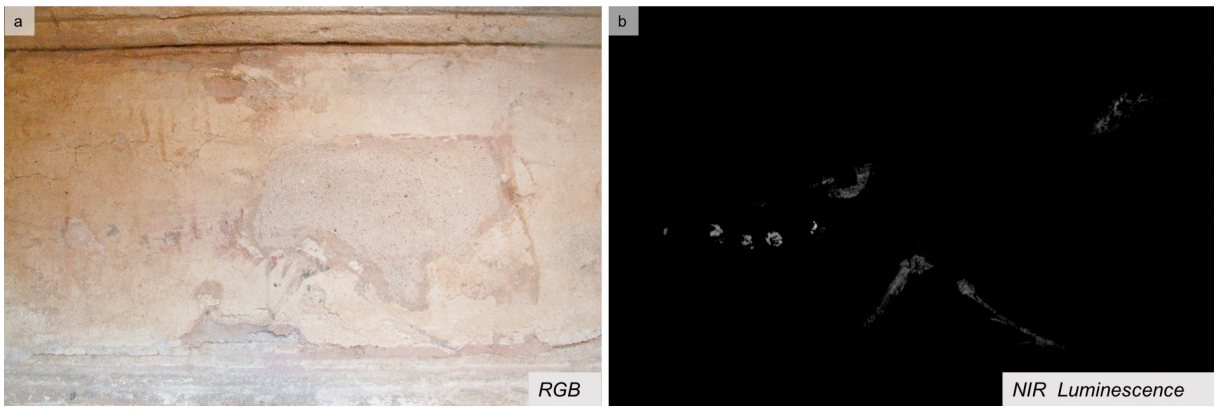

Figure 2.29: (**a**) A color (RGB) image of a partridge painted on the dado of the central arcosolium (J); (**b**) The NIR luminescence image identifying the blue dots on the tail as Egyptian blue and providing recovery of the leg, tail, and head details that have disappeared due to deterioration.

At the north end of the dado, a smaller bird in gray-blue hue was only partially visible. The center part of the bird's body seems to be completely weathered away. Using visible-

induced NIR luminescence imaging, it was possible to recover much of the bird's figure (Figure 2.30).

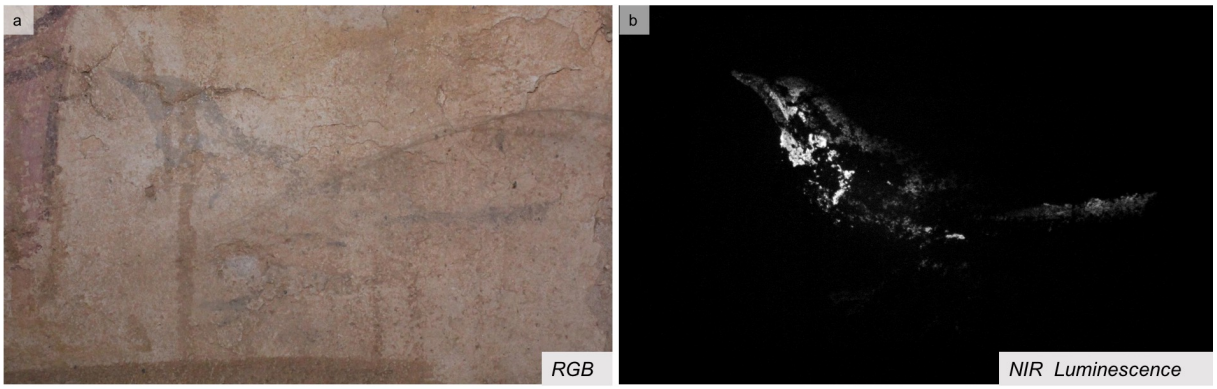

Figure 2.30: (**a**) A color (RGB) image of a small, faded gray-blue bird on the dado of the central arcosolium (J); (**b**) The near-infrared luminescence image identifies Egyptian blue as one of the major pigment constituents for the hue and recovers the figure of the damaged depiction.

In Tomb Roma 2 (Figure 2.12f), analytical imaging was able to revive decorative patterns under the heavy salt encrustation on the stone slab concealing a loculus (Figure 2.31). Visual observation gave no indication of the outlines and dot patterns revealed by the luminescence of Egyptian blue. This is an extremely important finding as it will provide vital information for wall painting conservators in developing their approach to treating the slab. These results confirm the efficacy of this non-invasive and field-deployable technique to reveal unknown, degraded and/or concealed imagery painted with Egyptian blue.

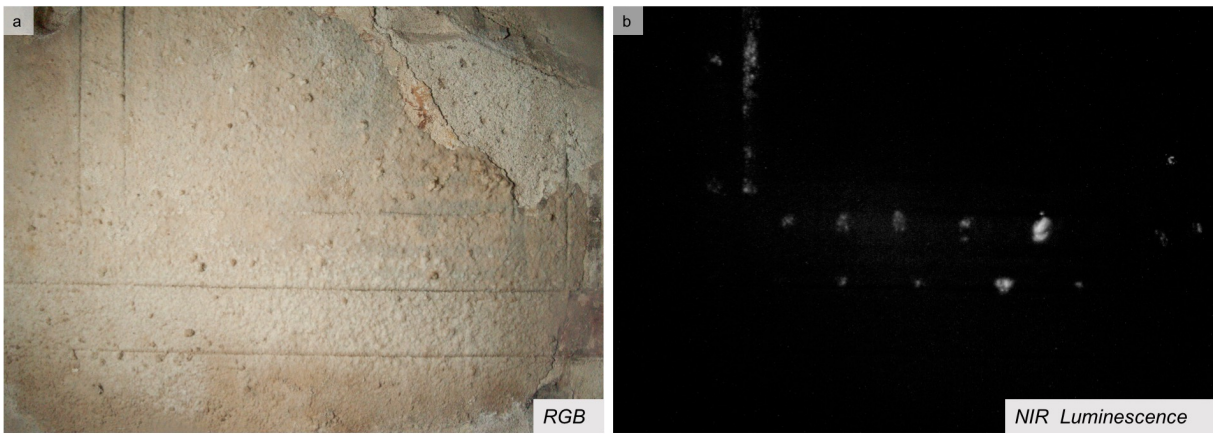

Figure 2.31: (**a**) A color (RGB) image of the painted slab sealing the loculus in Tomb Roma 2 (K). The heavy gypsum salt encrustation covers much of the surface and leaves only incision lines noticeable. (**b**) The NIR luminescence of Egyptian blue capture reveals patterns of dots and lines under the crust.

These investigations, representing the first comprehensive non-invasive scientific field study of ancient Cypriot wall paintings, provided new insight into the material use and technical practices by ancient artists. The integrated analytical methodology established a new list of pigments used for wall painting decoration, and the forensic images helped to identify the presence of Egyptian blue in challenging analytical conditions where the pigment was concealed or in trace amounts (a comprehensive list of paintings identified with Egyptian blue using forensic photography can be found in Appendix C). Furthermore, it established the diverse uses of this pigment in figurative wall paintings and provided the discovery of a new technical marker to potentially identify ancient artists and workshops in Cyprus and the ancient Mediterranean world.

CHAPTER 3

Terahertz imaging studies for cultural heritage

3.1 Motivation

One of the most significant challenges of studying a painting is looking "within". Paintings, whether built up on panels or over walls, can feature a complex stratigraphy comprising of multiple ground/preparatory layers, preparatory drawings, and subsequently the pigments and binding media that produce the decoration. These paintings can be further complicated by being over-painted, usually driven by the need for re-purposing of the canvas or wall, or possibly fueled by religious or political reasons. In this case, a complete pictorial program may be completely concealed by a newer one. For panel paintings, this may be accomplished by a thin layer of whitewash. Wall paintings are more complex, however. Evidence in archaeological investigations of ancient Cypriot wall paintings show thick re-plastering of the walls for new decorative schemes (Figure 3.1a,b).

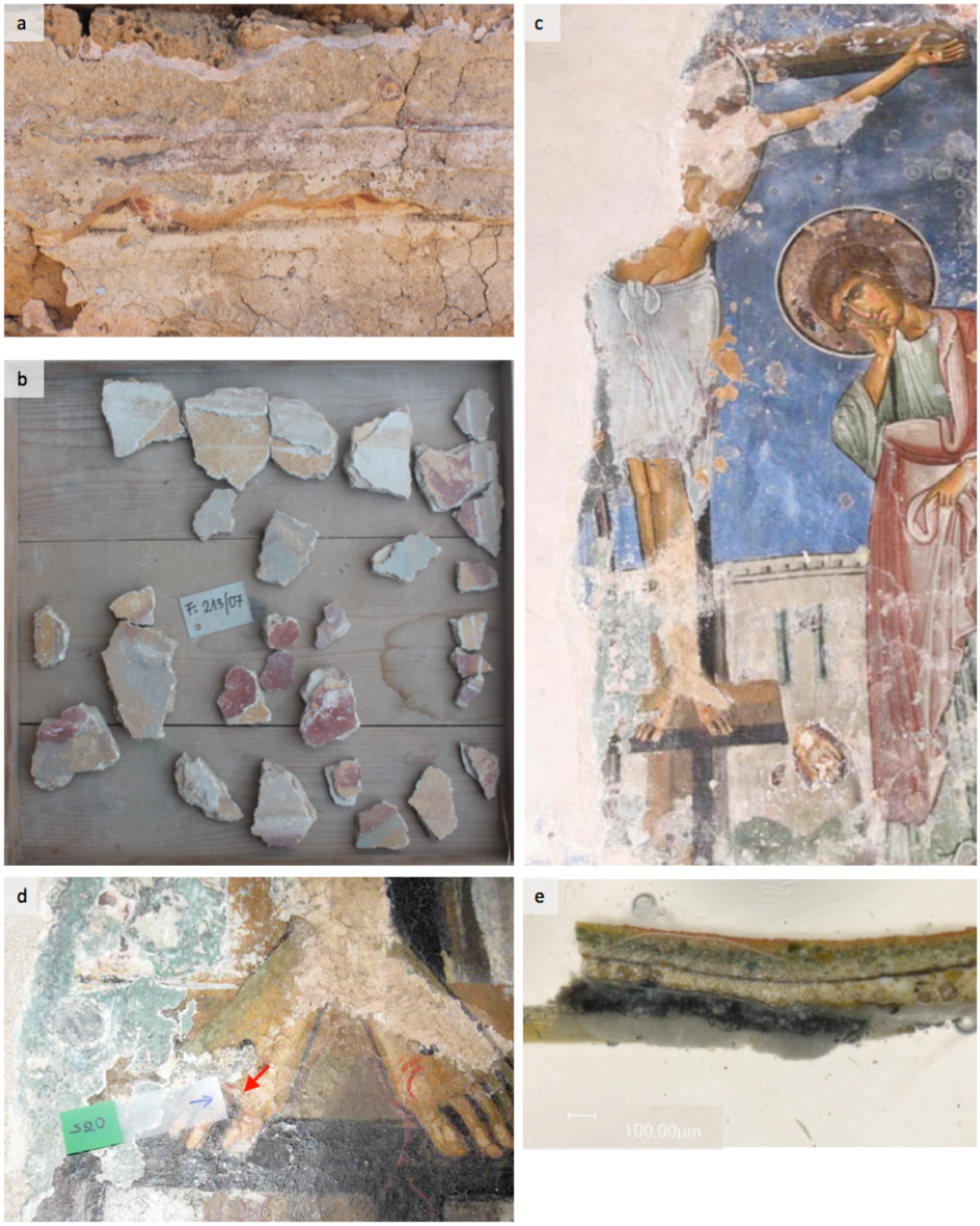

Figure 3.1: Examples of multilayer paintings from Paphos, Cyprus: **(a)** House of Aion, room 7; **(b)** fragments from the House of Aion; **(c)** depiction of Christ on the cross in the cell at the Enkleistra of St. Neophytos, with the older painting noticeable by the exposed foot just below the cross. A sample taken from Christ's proper right foot **(d)**, viewed in an embedded cross-section **(e)** reveals multiple layers in the painting's build-up.

For the historically-significant wall paintings of the Enkleistra ("place of reclusion") of St. Neophytos, both heavy re-plastering and thin whitewash layers were used to conceal earlier iterations of painting (Figure 3.1c-e). The Enkleistra was the motivation in this research to explore a new type of imaging to access the multiple layers found on the walls. The Enkleistra is a treasure for those seeking knowledge on the cultural history of Cyprus in the Middle Ages. Initially hewn out of rock by a single monk seeking a place of solitude [133], the Enkleistra has developed into an extensive place of worship reflecting the island's complex history marked by its devastation by Raynald of Châtillon in 1155/6 and the cruel and scandalous administration of Isaac Comnenous just before the Latinization of Cyprus. The wall paintings in the Enkleistra reflect individuality, unique for Byzantine art, as well as stylistic influences expressing local and Constantinopolitan traditions. The technology, materials, and provenance of the pigments are of particular interest and motivated this research. The walls of the Enkleistra feature several painting phases spanning from the twelfth to the sixteenth centuries [133, 110]. The various painting phases are separated from each other by a thin plaster layer or a lead white ($2PbCO_3{\cdot}Pb(OH)_2$) concealant, and, due to degradation of the later phases, earlier paintings have become partially visible (an example can be seen by the two pairs of feet in Figure 3.1c. In order to thoroughly visualize what underlies the foremost layers on the Enkleistra's walls, a non-invasive and non-destructive technology is required to image through the later painting phases. Recalling the schematic from Chapter 1 (Figure 1.4), X-ray radiography penetrates deeply into the painting with no depth resolution, and is not a viable option in the case of wall paintings. IRR is most effective for near sub-surface imaging to identify features such as pentimenti, underdrawings, and preparatory lines, but cannot penetrate deeper or thicker layers. To approach this challenge, the use of terahertz (THz) imaging as a new alternative for controlled, penetrative imaging of multi-layered structures was explored.

THz imaging is an investigative technique that has gradually captured the interest of the cultural heritage research community. The THz frequency band appears between the microwave and infrared region of the electromagnetic spectrum; its borderline behavior provides

several unique characteristics: a) similar to microwaves, it can penetrate non-conducting and opaque materials such as ceramics and plastics and b) the approach in which THz imaging can be conducted is a blend of technology and concepts from quantum and classical treatments of wave behavior [38]. THz imaging has found application in areas such as security intelligence, materials quality inspection, astronomy, and biomedical studies [38, 103, 141, 189]. The low frequency, non-ionizing characteristics of THz radiation and its ability to penetrate opaque materials make THz imaging an extremely appealing tool to conservators and cultural heritage scientists to probe hierarchically-complex structures with hidden features [5]. This includes, but is not limited to, objects with multiple painting layers applied over time, structural defects such as cracks, de-lamination of layers, and air gaps, preparatory drawings, and masked artist signatures.

The interaction between THz radiation and a material is dependent on the material's refractive index, n, a measure of a material's optical density and a function of its dielectric constant, κ, or relative permittivity:

$$n = \sqrt{\kappa} = \sqrt{\frac{\epsilon}{\epsilon_0}} \tag{3.1}$$

A THz image of an object that is made of different materials with n_1, n_2, n_3, etc. will present a contrast-based image that shows the variation of THz interaction with those materials. The first THz image, presented by B.B. Hu and M.C. Nuss in 1995 [101], was acquired by a THz time-domain spectroscopy (THz-TDS) system (Figure 3.2). Due to the sensitivity of water's dielectric constant to THz frequencies, Hu and Nuss were able to show the changing water content in a leaf over time.

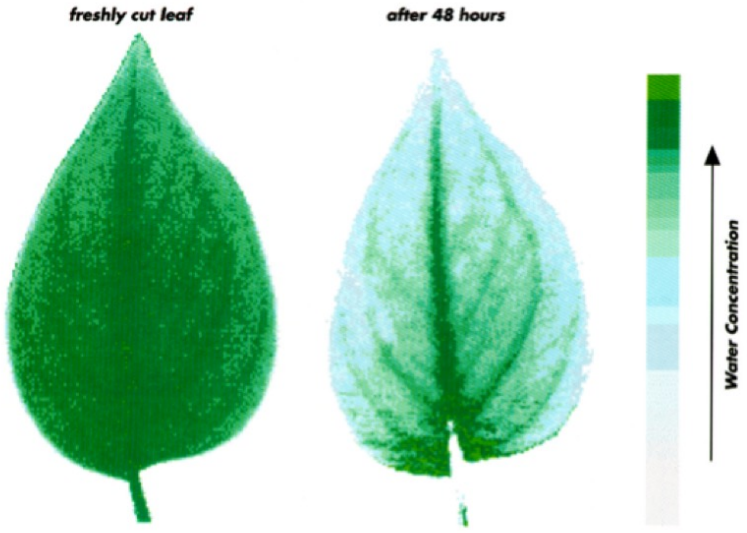

Figure 3.2: First THz image produced by THz-TDS. The water content was effectively mapped over the course of two days because of its high sensitivity to THz radiation [101]

THz systems utilize a photoconductive switch or non-linear crystal, which is pumped by an ultrafast laser to produce the THz signal. A polyethylene lens is used to focus the beam and mirrors propagate the signals through an optical train of mirrors to the target. The reflected signal is subsequently detected by a photoconductive antenna or electro-optic crystal. For the relatively few cultural heritage applications reported of panel and wall paintings imaging, only THz-TDS systems, also known as THz time-domain imaging (TDI), were used. These systems were mostly commercial and rather expensive, as THz device research is still considered in early development and production is costly, making these systems elusive for cultural heritage use. In THz-TDI applications, a portable scanning system is applied; the THz emitter and receiver uses a pitch-scanning configuration to send and receive the signal as it raster-scan over the surface of the painting. The reflected signal is a convolution of the incident signal's interaction with the multi-layered target (Figure 3.3).

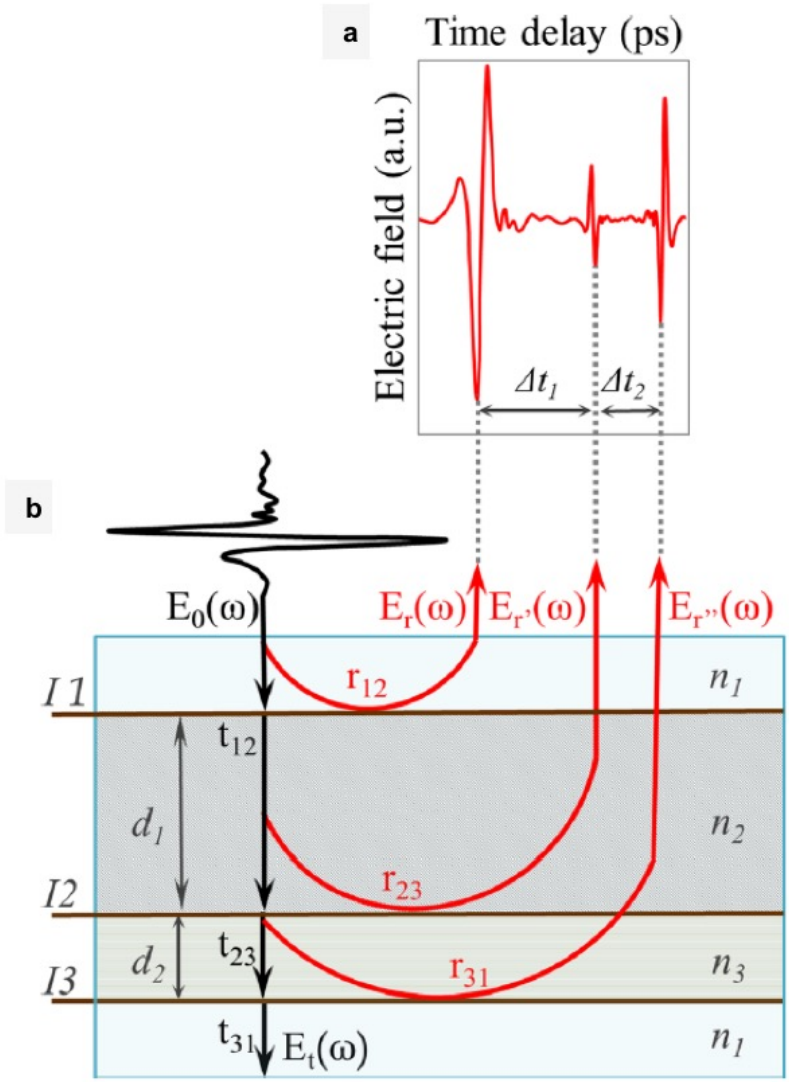

Figure 3.3: **(a)** The measured THz signal reflected from the multilayered target **(b)**. The distance between peaks in the convolved pulse from the successive reflections gives an indication of layer thicknesses in the sample. [Image adapted from [52]]

In-depth post-processing of the resultant data cube of THz signals can provide visualizations of a painting's stratigraphy in the form of a virtual cross-section (B-scans). Extracting specific layers from the virtual cross section can provide 2D images (C-scans) at different depths of the painting. This requires extensive noise filtering and signal deconvolution to effectively separate and extract the different interactions from a single pulse, which has also

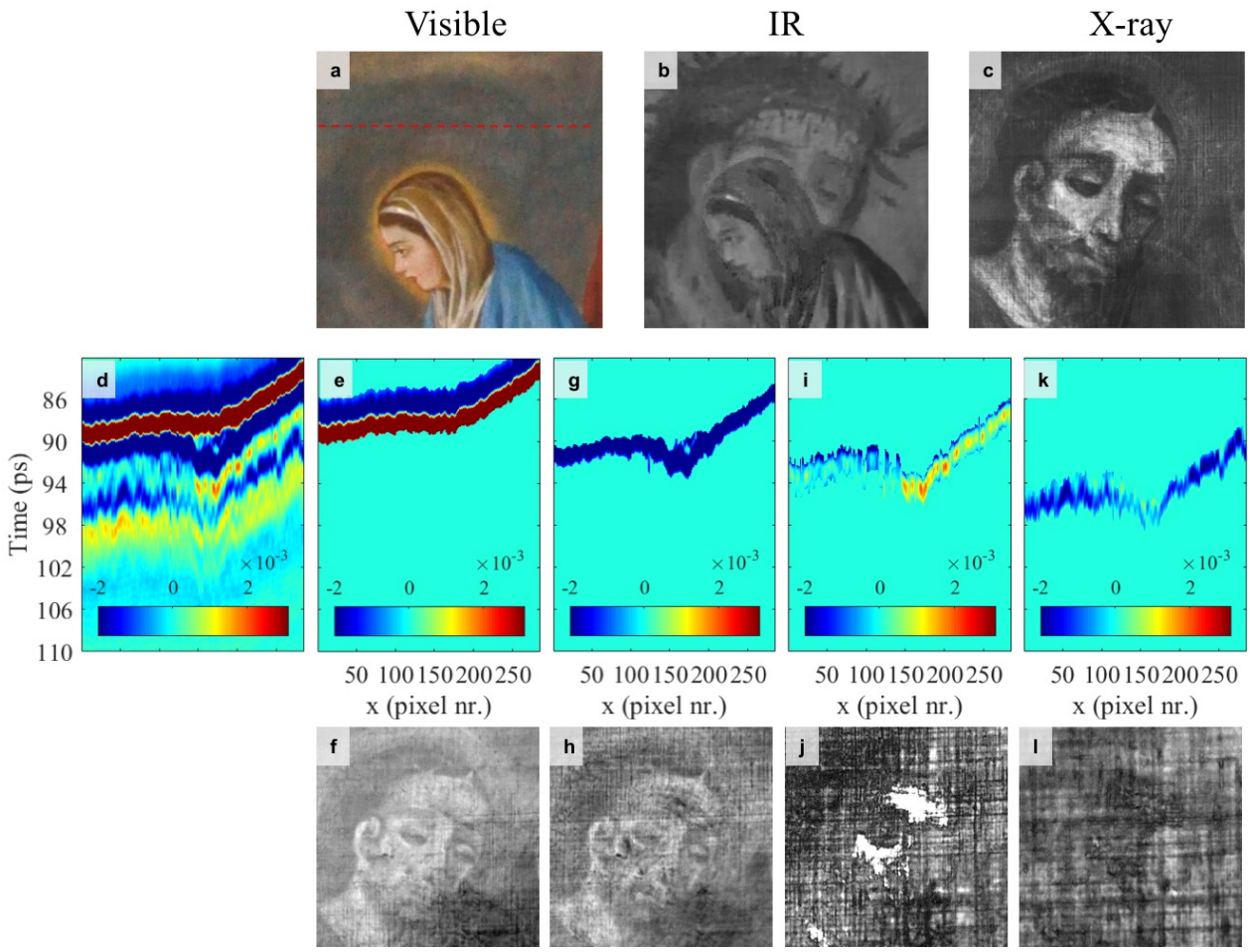

Figure 3.4: **(a)**, **(b)**, and **(c)** are the visible, IRR, and X-ray images of *Jesús se encuentra con su madré*. **(d)** shows the full denoised and filtered B-scan (virtual cross-section) along the red dotted line in **(a)**. **(e-f)** are the extracted top layer from the B-scan and its respective C-scan (THz image). The next pairs **(g-h)**, **(i-j)**, and **(k-l)** represent the deeper layers of the painting. [Image adapted from [87].]

made the use and effectiveness of THz-TDI limited in cultural heritage.

An example of THz-TDI applications can be seen in Figure 3.4, which was performed on an altarpiece painting, *Jesús se encuentra con su madré* from a parrish in the town of Purísima del Rincón, Mexico (a select region of interest is shown in Figure 3.4a) [87]. Figure 3.4d shows a virtual cross-section (B-scan) extracted along the red dotted line in the painting. The separation of the B-scan's layers produces THz images (C-scans) of the painting at various penetration depths (Figures 3.4e-l), which reveals the hidden face and the

subsequent build-up of the face down to the canvas preparation layer. Figures 3.4b-c provide comparisons of the THz images to conventional IRR and X-ray applications, respectively, which show residual features from different depths of the painting.

It was suggested in 1999 that THz imaging could be used to look for hidden layers in paintings [141]. Only in 2008 did THz begin to be actively explored for this purpose [73, 76, 103]. Most applications have been used for panel or canvas paintings [156, 117, 87]. Few applications have been focused on sub-surface imaging of wall paintings to search for hidden imagery [202] and to assess internal structure [52, 71], though no decorative imagery has been confidently recovered from sub-surface. These applications strictly used THz-TDI in their investigations. Such investigations have been challenged by standard wall painting configurations: re-plastering with thick layers using highly scattering materials such as chalk and sand; uneven painting layer applications on the walls; and porosity of the layers due to long term environmental weathering. These inherent characteristics affect the signal penetration, producing significant scattering and additional non-relevant peaks in the reflected THz pulses, which interferes with deconvolution and interpretation of the spectral data.

This research approached sub-surface imaging for *in situ* wall painting applications using a novel THz medical imaging system based on direct detection of signal power reflected from a target. The system was originally developed by the UCLA Biophotonics Laboratory. The main objective of this system's design was to take advantage of water's strong dielectric response to THz radiation by mapping hydration sensing to perform biomedical diagnostics, such as cornea imaging, burn wound patterns, identification of cancerous cells, etc [190, 31, 19]. Instead of working in the time domain and recording high spectral resolution signal pulses, the power of the THz signal reflected back from the target is directly measured by a Schottkey diode, which ideally maximizes the contrast resolution within the reconstructed image. Figure 3.5 demonstrates the hydration maps of partial and full thickness skin burns over a three-day period [193]. The high contrast sensitivity shows the flow of hydration in the cross-shaped burns, marked by the brighter regions due to higher THz reflectivity. At

the end of 8 hours and over the course of the next two days, a distinct difference in hydration behavior of the skin occurs in the partial versus full thickness burns occurs as the skin aims to heal itself. This rapid feedback of burn wounds provides doctors with a monitoring tool to assess the severity of the damage and potential treatment for patients.

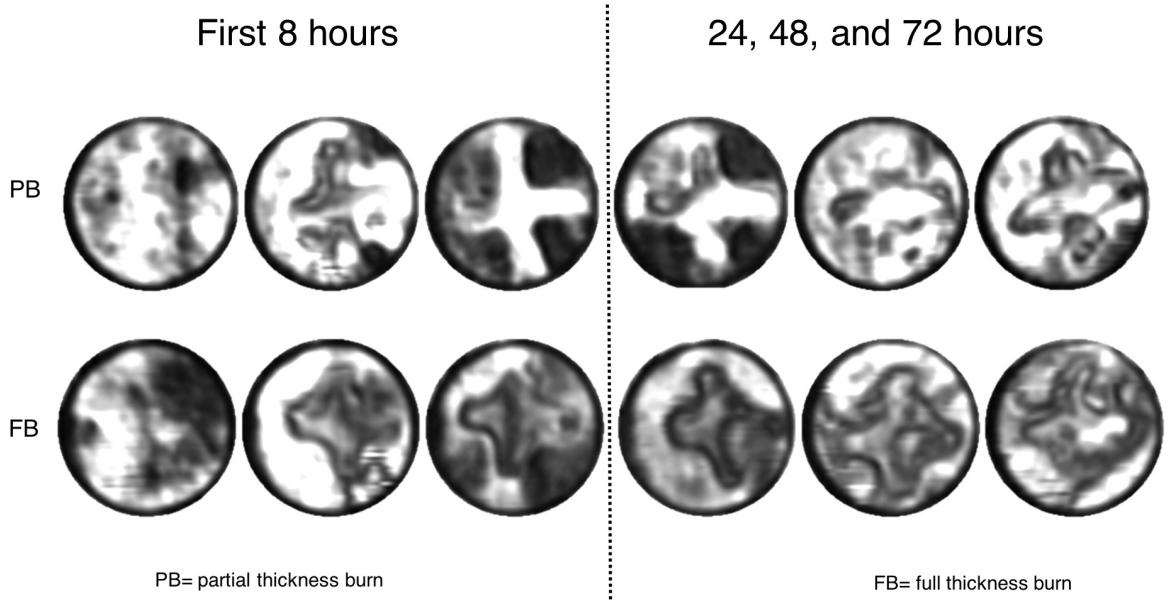

Figure 3.5: THz images from partial (PB) and full (FB) thickness burns, collected from the UCLA Biophotonics Laboratory's THz medical imaging system. Hydration monitoring and mapping over the course of three days showed the skin's response to the burn wounds. The white regions (high THz reflectivity) show that in the partial burns, the water rushed to the immediate region of the burn wound (in the shape of a cross), while the water mostly surrounded the wound in the case of the full burn [Image adapted from [193].]

This research used the same THz imaging system to acquire high contrast imagery of cultural heritage-inspired experimental models (mock-ups). Imaging challenges that multi-layer painted architectural structures present motivated these mock-ups. The aim was to demonstrate the capability of this imaging system's novel optical design to probe beyond the visible surface to identify hidden painting and structural defects such as voids, cracks, and delamination within hierarchically-complex paintings and polychrome objects.

3.2 Instrumentation

The setup of the UCLA THz imaging system and its block diagram can be seen in Figure 3.6. The THz source is a photoconductive switch [184, 188] pumped by a 780 nm femtosecond (fs) laser with a 230 fs pulse width, 20 MHz repetition rate, and $\sim$ 8 mW of average power. At high DC-bias fields (200 V/9 μm gap = 222 kV/cm) the source produces average powers of up to 46 μW across 1 THz of bandwidth [188]. The THz beam is directed to the target through a series of off-axis parabolic mirrors (OAP) and the reflected illumination is focused into the feed horn of a 0-bias Schottky diode detector mounted in a WR1.5 waveguide. Pixels are generated by raster scanning the target in the x and y directions, using stepper motors. Additional technical details are available in references [190, 178, 191, 192, 31, 19, 18, 179].

The effective center frequency and bandwidth of the system are defined by the switch power spectral density (PSD) and the detector spectral responsivity. These curves are displayed in Figure 3.7 [189]. Convolving these traces yields a center frequency of $\sim$ 525 GHz with $\sim$ 125 GHz 3 dB bandwidth. The direct detection methodology implemented in this architecture provides a DC voltage proportional to the total area under this convolved curve without the need to coherently sample the THz beam.

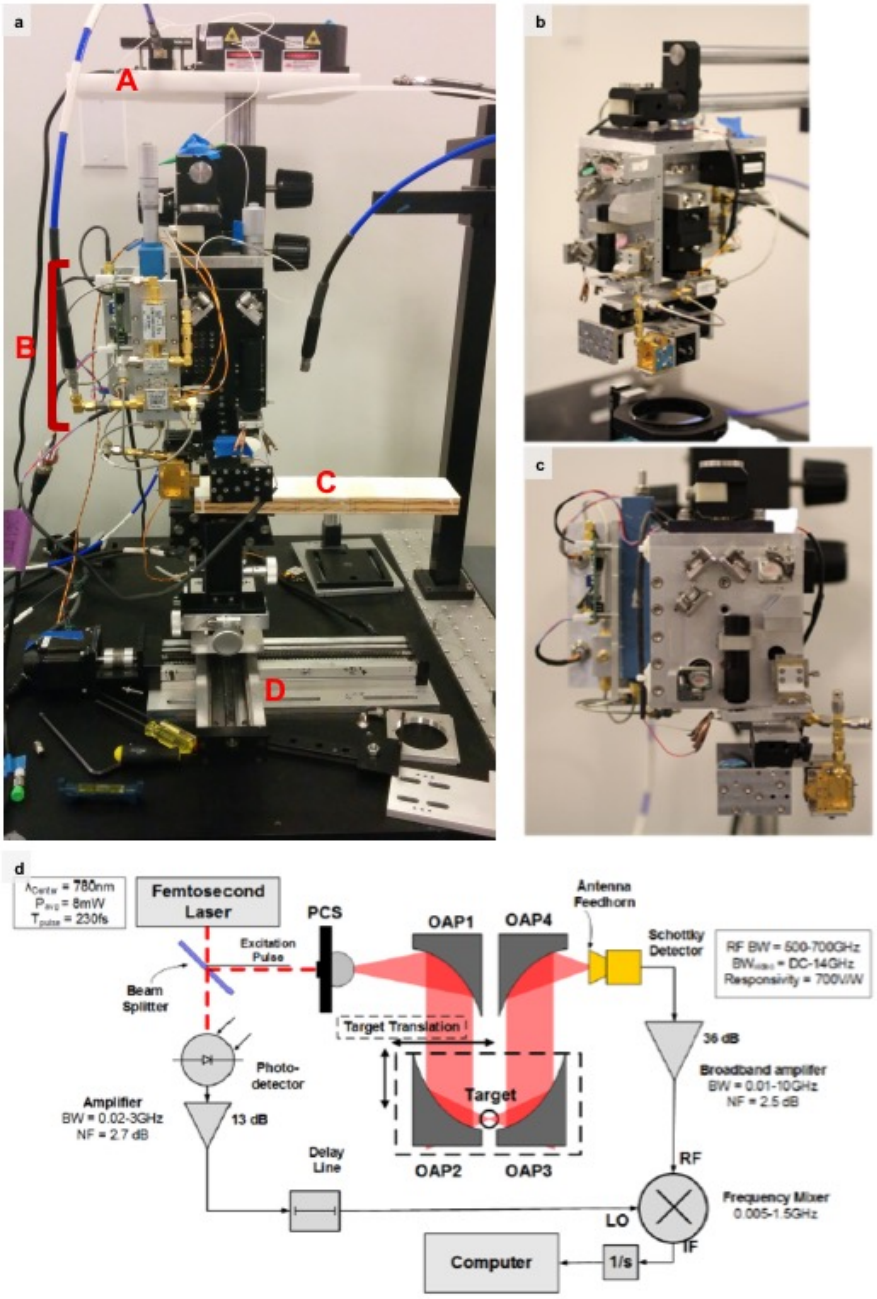

Figure 3.6: **(a)** The THz imaging system developed by the UCLA Biophotonics laboratory. 'A' indicates the THz source. 'B' represents detector, amplifier, ad optical path for the THz signal, with close-up images in **(b)** and **(c)**. A panel target ('C') is positioned in place for imaging, which is raster scanned within the optical path between off-axis parabolic (OAP) mirrors 2 and 3 by the motarized stages marked by 'D'. **(d)** Block diagram of the THz system [186].

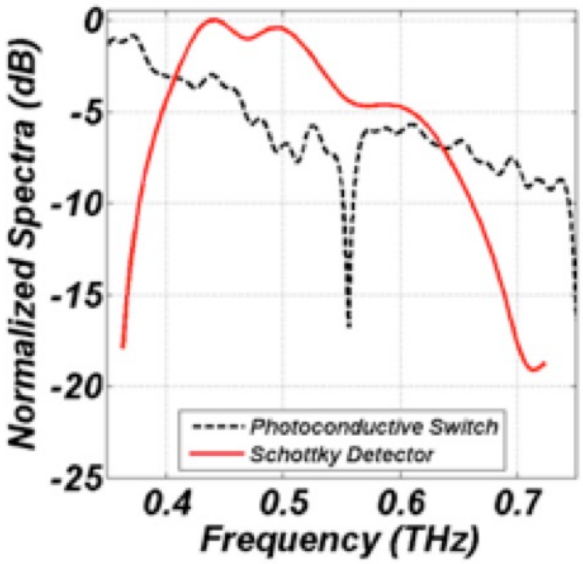

Figure 3.7: The normalized power spectral density curve (dotted black line) for the photoconductive switch and the normalized spectral response for the Schottkey diode (solid red line). The total area under the convolution of these spectral curves parameterizes the system's sampling capability under direct detection of the reflected THz signal [189].

The train of off-axis parabolic (OAP) mirrors is designed to maximize spatial resolution and minimize depth of focus (Figure 3.6d). The beam is collimated by OAP 1 and focused onto the target by OAP 2. The reflected beam is re-collimated by OAP 3 and focused down to the detector by OAP 4. This arrangement of parabolic mirrors offers a number of advantages over existing designs. First, OAPs 2 and 3 form a matched pair that accept and transmit collimated beams. Therefore, the focal length of these mirror pairs can be changed with minimum optical realignment enabling straightforward comparison of varying optical parameters. Second, the oblique angle of incidence reduces the overlap of the focused beam's Rayleigh length leading to a significant reduction in the depth of focus. This, coupled with the wavelength-order dimensions of the source antenna and detector waveguide, result in confocal-like optical performance in terms of spatial and depth resolution. Measurements of the THz system's optical performance yield a spot size of $\sim$ 700 μm and depth of focus of $\sim$ 800 μm; both only fractions larger than the freespace wavelength at 525 GHz.

3.3 Test targets

3.3.1 Panel No.1 - hidden writing

A mock-up target inspired by medieval panel painting, made by the Getty Center Institute (GCI), was provided for THz imaging tests. The target was a painted wooden panel with a multi-layered structure, measuring 10 x 2 x 0.75 in. The panel (Figure 3.8), initially sanded and covered in gesso, was separated into five parts that was further sectioned for different configurations of covering paper, parchment, gesso, lead-white pigment with a binder, ink, and charcoal. One section of the panel, marked out in the red box, was of particular interest: over the initial layer of gesso, the words "Getty" and "GCI" were written in charcoal and iron-gall ink (iron-based salts and tannic acids), respectively. These words were written in a 3 x 3 matrix with each column covered by parchment, covering paper, or canvas and then subsequently covered uniformly with gesso and lead-white paint with different binding media (egg tempera, linseed oil).

The various types of pigment mixtures, concealant materials, and layering applications provided a succinct set of signal penetration challenges to recover hidden features often found in panel and canvas paintings.

3.3.2 Plaster samples

Experimental wall painting targets inspired by archaeological and historical wall paintings, such as those found in the Enkleistra, and imitating the chemistry and surface roughness of the substrates and surface paint layers were reproduced the UCLA/Getty Conservation Program. The targets were prepared in both fresco (pigments applied with water as the binding medium while the calcium hydroxide rich binder of the plaster was still moist) and secco (pigments applied with an organic binding medium on a dry plaster layer) applications. Figure 3.9 displays cross-sectional and schematic diagrams of the test targets, which measured 50 x 50 x 25 mm. Inorganic and organic pigments including titanium white (titanium dioxide (TiO_2) - white), natural umber (iron oxide with manganese oxide (Fe_2O_3/MnO_2) -

Figure 3.8: Mock-up provided by the GCI for THz imaging analysis. The wooden panel was sectioned and prepared with various configurations of words, writing materials, and concealants. The subsequent build-up of the target is viewed from the right to left.

brown), cinnabar (mercury(II) sulfide (HgS) - red), minium (lead (II,IV) oxide (Pb_3O_4) - orange), and graphite were applied directly over the plaster layer. Lead-white and chalk (calcium carbonate-rich) layers up to 4 mm of thickness were used as concealing coatings to cover the painted features. Results of plaster samples will specifically focus on samples painted with minium obscured by chalk and cinnabar obscured by lead-white, with linseed oil as the binding medium. The concealants selected are notoriously difficult to penetrate both with IR and visible light and have until now demonstrated extremely limited penetration with THz illumination [8, 72, 70, 102]. The hidden decoration depicted a simple cross in order to be distinguishable by THz imaging.

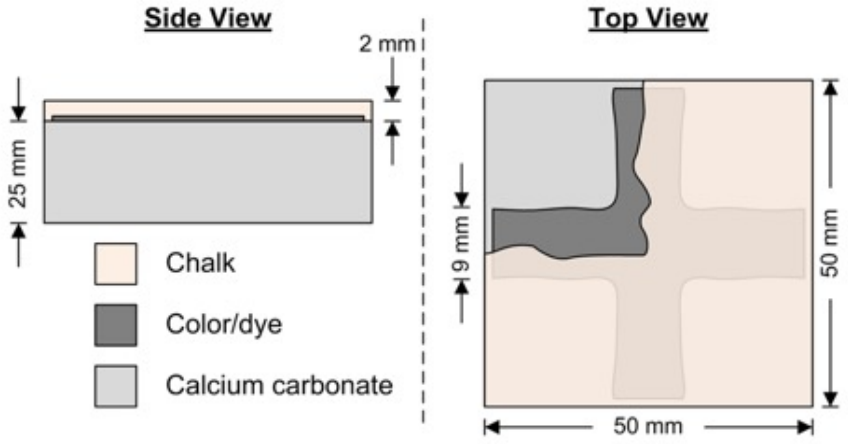

Figure 3.9: Schematic for mock-ups of calcium carbonate substrate with painted crosses and concealant layers (chalk or lead-white).

3.3.3 Panel No.2 - hidden defects

To test the detection capability of the THz system of underdrawings, voids and delamination of a painting's layers, a wooden panel was prepared with a variety of defect/underdrawing configurations. The panel was prepared in a similar style as late medieval and early Renaissance paintings to mimic their materials, features, and defects. Underdrawings and air gaps were created under and between layers of gesso (Figure 3.10). The underdrawings were produced using a charcoal pencil. Due to the grain orientation of the wood, certain parts of letters required repeated application (to be discussed further in the imaging results). A thin layer of mylar plastic film, transparent to THz radiation, was used to cover the hand-made defects to prevent the gesso layer from filling the gaps ($\sim$ 5 mm in depth). Textile was also applied in certain parts of the panel, as this was part of the preparation technique of medieval paintings. Small strips of aluminum tape were used in the hidden words to produce a bright reflection in the THz image as a location guide and indication of the signal intensity (Figure 3.10b). The panel imaging results will focus on the region with the hidden writing "UCLA" and "THz!". As seen in Figures 3.10d-e, part of the concealing gesso layer broke

over one of the air gaps, which provided an interesting comparison to the fully covered air gap in the imaging test.

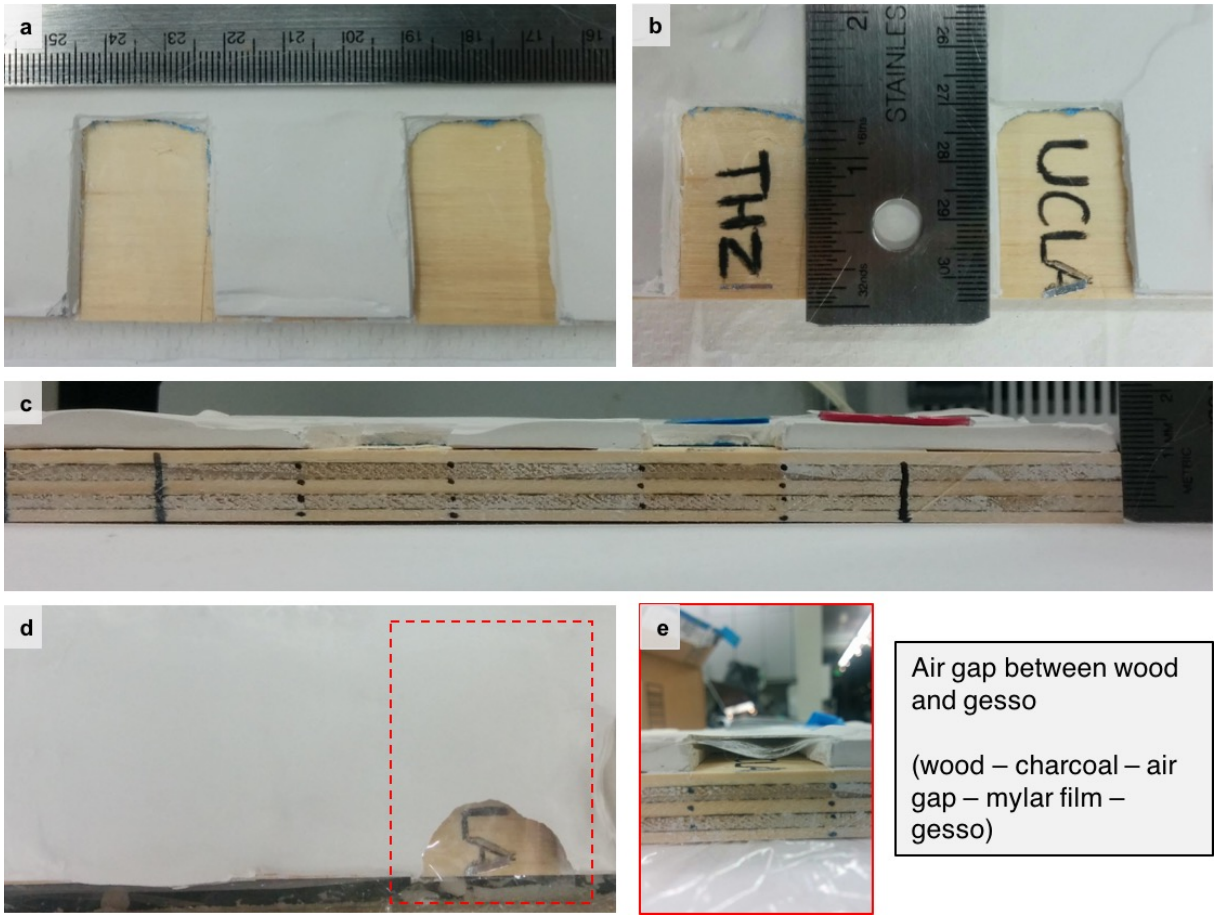

Figure 3.10: **(a)** Gessoed wood panel with two gaps ($\sim$ 5 mm in depth) to serve as defects. **(b)** "UCLA" and "THz!" written with charcoal pencil in the gaps, directly onto the wooden panel. The right side of the "A" and the "!" are lined in aluminum tape for increased reflectivity. **(c)** Side view of the wooden panel. **(d)** Top view of the wooden panel after a concealing layer of gesso is placed over the top. The two air gaps were sealed by mylar. There was a small break in the top layer of one of the defects. **(e)** Side view of the broken defect, where the warping of the mylar film is also visible.

3.4 Data collection

The samples were imaged in reflection as this method would be applied in a real case scenario. However, the configuration of the THz system keeps the THz emitter and detector stationary,

while the target is raster scanned. The scan time for each target took approximately 10–12 minutes.

To observe features below the surface of the targets, the focal points of the OAP mirrors must be focused at the obscured layers, though the precise depth of the decoration is generally unknown. The system was initially focused at the top of the target by placing on the surface a thin, flat aluminum plate in the optical path and adjusting the height of the target until the maximum reflected THz signal was recorded. Then, taking advantage of the confocal-like behavior of the system, the height (z) of the sample mount was adjusted for different imaging tests. At incremental sub-millimeter z changes for each acquisition, a THz image (C-scan) is obtained by rastering the target in the x and y directions at 0.5 mm steps under the THz signal. Thus, rather than acquiring a single image at a particular depth, a set of images were collected within the focal range of the mirrors to visualize the sub-surface structure of the samples at different depths.

To conduct a comparison of THz and X-ray imaging on the visualization of hidden defects, X-ray radiography on panel No.2 was kindly performed by Jane Bassett at the Getty Conservation Institute.

3.5 Data Analysis

Data collection, file structuring, image processing and visualization was performed in Matlab. Select subsequent image processing was also performed in ENVI ("Environment for Visualizing Images", L3Harris Geospatial).

As multiple images at different depths (z values) were acquired, various image processing methods were explored to identify or enhance hidden features, include interactive histogram stretching and addition and subtraction of images. In the gray-scale THz images, brighter areas indicate higher reflectivity.

3.6 Results and discussion

3.6.1 Panel No.1 - hidden writing

The THz imaging results of panel No.1 are in Figure 3.11. In Figures 3.11a-b (the latter using red circles to highlight the hard-to-discern features), the "Getty" words written in the first two rows of the left column, obscured by covering paper, are most distinguishable. It appears that the penetration of lead white and recovery of the THz signal was not a challenge in this layered configuration. The middle column with the parchment paper featured partial recovery of the "Getty" words. In the second column, the "Getty" letters are less distinguishable due to the presence of the parchment layer. In the final column, none of the letters are particularly distinguishable and only vague outlines suggest the presence of the charcoal letters. Covered with canvas, this column is the least favorable with the THz signal. None of the "GCI" letters throughout the 3 x 3 matrix written in iron-gall ink were seen. This writing medium appears to be elusive to the THz signal.

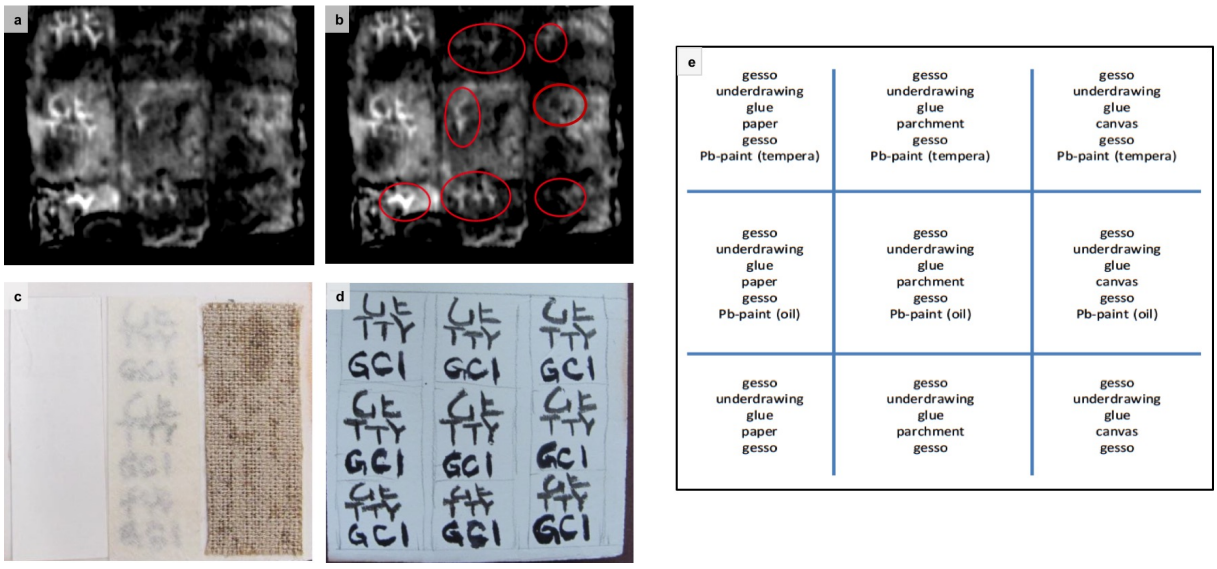

Figure 3.11: **(a)** THz image produced from imaging of the concealed 3 x 3 matrix. **(b)** The THz image with red outlines for the more difficult-to-discern features. **(c-d)** are close-up images of the 3 x 3 matrix, after and before concealment by covering paper, parchment paper, and textile. **(e)** Layout and layering schematic of panel No. 1. [160]

3.6.2 Plaster samples

Two imaging results of plaster samples are presented here: (1) a chalk-obscured minium-decorated target, and (2) a lead white-obscured cinnabar-decorated target.

3.6.2.1 Chalk-obscuring sample

Chalk is a significant scatterer of THz signals and poses a challenge for non-invasive imaging in a cultural heritage environment. A secco plaster sample with a cross painted in orange minium (Pb_3O_4, also known as red lead) (Figure 3.12a), was uniformly coated with a layer of chalk (Figure 3.12b). The THz images in Figure 3.12c-d were taken at different z heights. The image in Figure 3.12c showed the horizontal band of the cross and its texture more clearly, as well as some definition to the upper part of the vertical band. While the horizontal band in 3.12d was less defined, the upper part of the vertical band showed more reflectivity. As for the the downward component of the cross, there is a lack of definition in this region. Instead, the appearance of an indentation suggested the location of the bottom part of the cross. The lack of contrast could be due to an uneven application of the paint or uneven plaster surface, which is often a problem with real wall paintings.

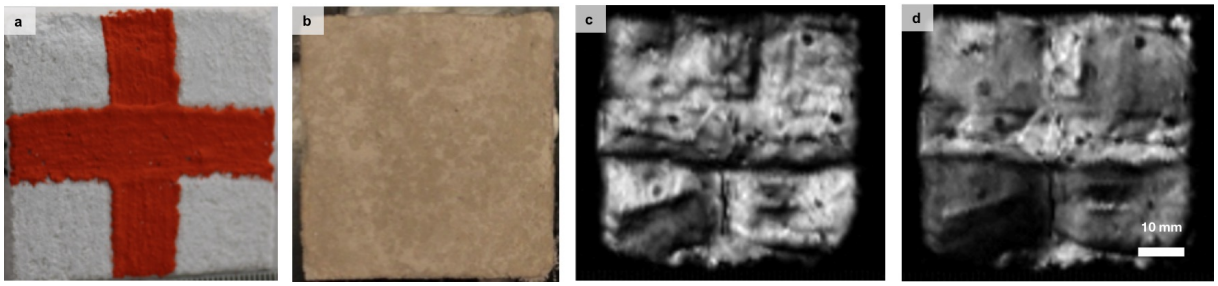

Figure 3.12: **(a)** The uncovered orange minium cross. **(b)** The plaster sample covered in chalk. **(c)** The THz image of the sample at z_1. Note the clear definition of the horizontal bar of the cross, as well as the upward component. The downward portion of the cross was not defined. **(d)** The THz image at z_2. There was less definition but more reflectivity of the horizontal and upward components of the cross and a dark indentation where the downward component of the cross was expected to be [160].

3.6.2.2 Lead white-obscuring sample

A plaster sample developed as a secco mock-up with cinnabar, painted in a cross figure using linseed oil as the binding medium (Figure 3.13a), was imaged with the THz system. The red cross was covered with a layer of lead-white (Figure 3.13b), in imitation of the situation at the Enkleistra, which also feature obscuring lead-white layers over earlier painting phases. Unlike painting a wooden panel, plastered-over and natural rock surfaces present greater difficulty to paint uniform pigmented layers, and therefore are much more difficult to image. A series of C-scans were collected of the plaster sample (Figures 3.13c-e); progressing through the sequence corresponds to images acquired at higher z values (i.e. closer to OAPs 2 and 3 (Figure 3.13g)). At each incremental z height, only partial images of the cross were visible. This is most likely due to the uneven surface and/or application of the paint layers. The multiple z scans were combined in post-processing to produce Figure 3.13f, where a more complete THz image of the cinnabar cross was visible. This was feasible as in each of the THz scans, portions of the cross visible had clearly distinguishable edges. Using the confocal-like nature of the imaging system to collect at various depths proved extremely useful in situations of uneven texture or orientation with respect to the optical path.

3.6.3 Panel No.2 - hidden defects

The results of the THz imaging tests on panel No.2 to assess detection of voids and hidden underdrawings are in Figure 3.14. The thin gesso layer over "UCLA" broke, leaving part of the letters and the mylar exposed (Figure 3.14b). This created an interesting comparison between the two voids, as their preparation was the same except for the hidden words. In Figure 3.14c, the unprocessed THz image clearly identified the voids. Additional structural details visible were the orientation of the wood grains and a distinction between the original gesso layer and the concealing layer (marked in the dotted blue lines in Figures 3.14b-c). In the area of the broken gesso cover, the right arm of "A" shows a bright reflection due to the aluminum tape. The left arm, on the other hand, is much darker than the wooden panel. During the preparation of the panel, when the word "UCLA" was written, applying charcoal

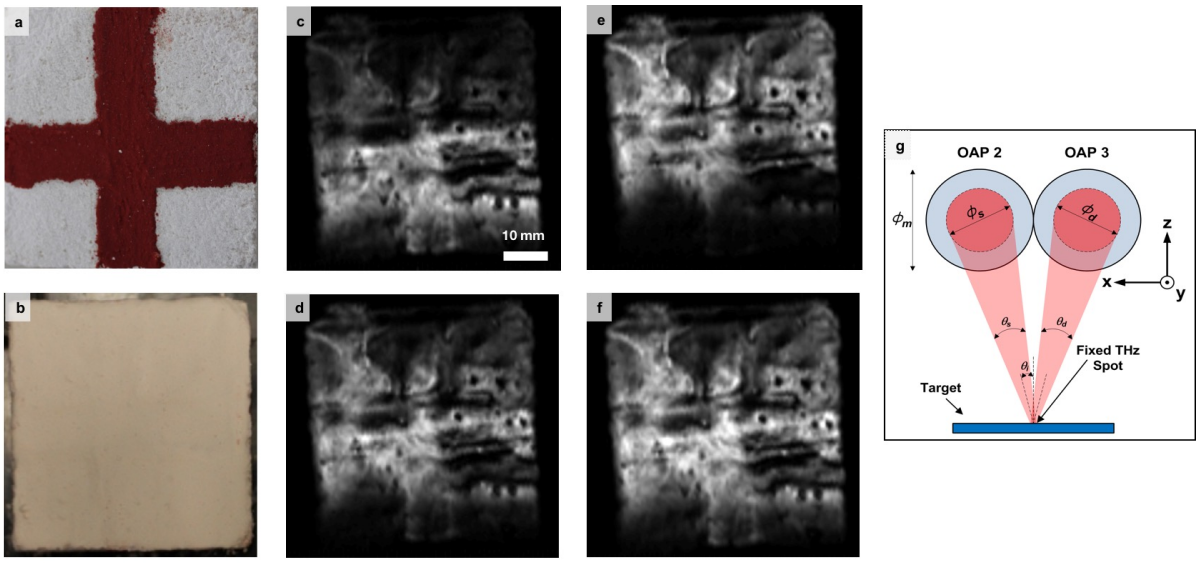

Figure 3.13: **(a)** The visible cinnabar cross. **(b)** The plaster sample covered with lead white paint. **(c)-(e)** are THz images acquired at different z values (with the signal focused at the sample as demonstrated in **(g)**). Due to the tilted surface of the sample, only part of the cross was visible at the different stage heights. Adding the images together produced a more complete reflectivity of the cross in **(f)** [160].

in the orientation of the wood grains was difficult. Significant pressing into the panel caused indentation in the wooden surface. The sensitivity of the THz system to the z height of the target showed the depression in the wood. Once this was understood, the left side of the "U" and the vertical part of the "L" was more obvious in the THz image. The brighter parts of these letters correspond to the orientation perpendicular to the wood grain, such as the bottom of the "U" and the bottom of the "L". For the completely covered "THz!", the letters "T" and "z" show some reflection. The "H", on the other hand, suffered the same issues as "U" and "A" as indentations were pressed into the wood to form the letter, thus appearing darker. Slight deformations into the wood, marked by the yellow lines in Figure 3.14a, were also visible in the THz image (Figure 3.14c), similarly outlined.

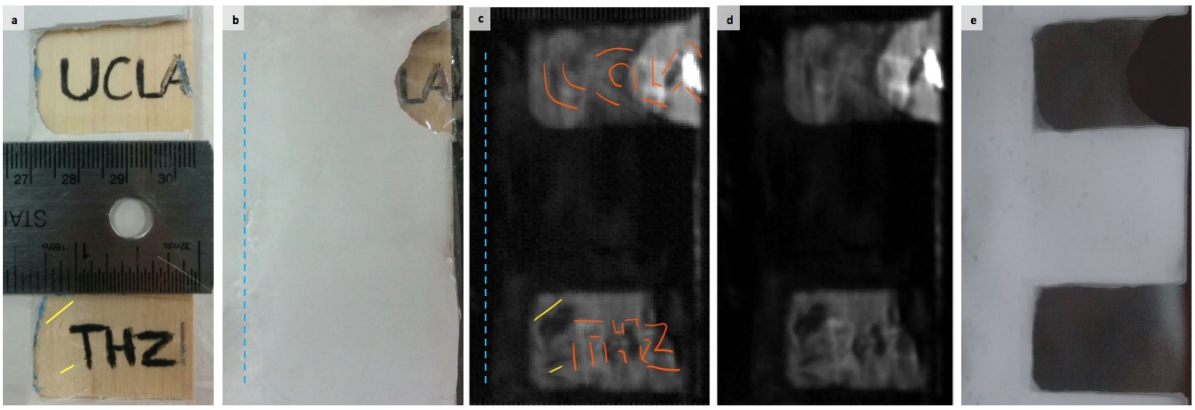

Figure 3.14: **(a)** Visible image of the voids before concealment. **(b)** The concealed defects, with the partial break over "UCLA". **(c)** Original THz image produced. The orange lines show the outline of the faint letters in the image. The yellow lines indicate the wood impressions, also noted in **(a)**. The blue line corresponds to the edge of the top concealing layer of gesso, also noted in **(b)**. **(d)** The filtered THz image for clarification of hidden features. **(e)** X-ray radiograph of the panel.

In comparing the filtered THz image (using a median filter in ENVI) to the X-ray radiograph, the difference in sensing capabilities is quite stark. The radiograph showed no indication of the letters or the wood grain, nor a distinction between the lower and top layers of gesso. On the other hand, the X-ray showed a clean outline of the air voids.

Further processing of the THz image in ENVI through interactive histogram stretching showed that different parts of the image's histogram (Figure 3.15d), representing the intensity distribution of the reflected THz signals, corresponds to different depths from which the signals were reflected. Figure 3.15a was produced from the rising edge of the left part of the histogram, corresponding mainly to the entire defect regions (the 5 mm air gaps) and some of the concealing gesso layer. The small Gaussian shape in the histogram strictly visualized the defects (Figure 3.15b), specifically the hidden surface and decoration of the air gaps. The higher intensity in the image represented the broken gesso cover. The remaining leg of the histogram corresponded to this exposed region as well as a small spot of the concealed "T" in THz, indicating the high reflectivity of this letter (Figure 3.15c).

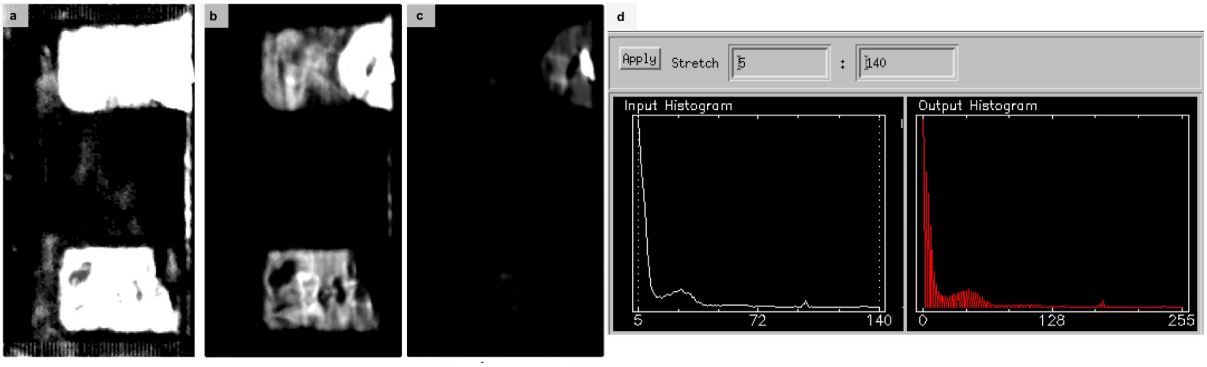

Figure 3.15: **(a)-(c)** corresponds to new visualizations of the original THz image (Figure 3.14c) over different regions of its histogram **(d)**

These results confirm the advantage of acquiring THz images using the UCLA THz biomedical imaging system. By utilizing the system's confocal-like features to acquire images at different depths below the surface, it was possible to visualize hidden decoration and defects in the samples, especially for uneven, non-uniform applications. The contrast sensitivity allowed robust detection of textured surfaces and differences in materials with similar refractive index. Furthermore, the system's ability to image through lead-white paint in both panel No. 1 and the plaster sample was a significant step in addressing the research question of whether the obscured paintings in the Enkleistra can be revealed using THz [160].

CHAPTER 4

Reflectance and Luminescence Hyperspectral Imaging (HSI) for the Analysis of Archaeological Paintings

"The current level of problems involving the loss of archaeological information, particularly within historic buildings, and the lack of financial aid to undertake recording work, present severe difficulties. Ground-based remote sensing allows relatively low cost, rapid survey and permits the recovery of information which might otherwise be lost"

— C.J. Brooke (1987)

4.1 Motivation

Research presented in Chapter 2 demonstrated the significance of portable hand-held spot collection analytical techniques for in situ non-invasive scientific field investigations of archaeological paintings. Combined field-deployable X-ray fluorescence (XRF) spectroscopy for elemental characterization and fiber optic reflectance spectroscopy (FORS) for molecular analysis, together with analytical (forensic) photography, provide versatility in the analysis and essential, complementary data that aid in the identification of materials. However, a holistic understanding of a painting – a binary system consisting of the colorants (pigments) and the binding medium or media – is limited through this approach, as photography alone cannot provide unbiased characterization of materials and qualitative/quantitative measurements using spot analysis is restricted only to the points analyzed.

Hyperspectral imaging spectroscopy (HSI), using remote sensing and materials characterization principles and methods, takes the in situ analysis of paintings and painted surfaces

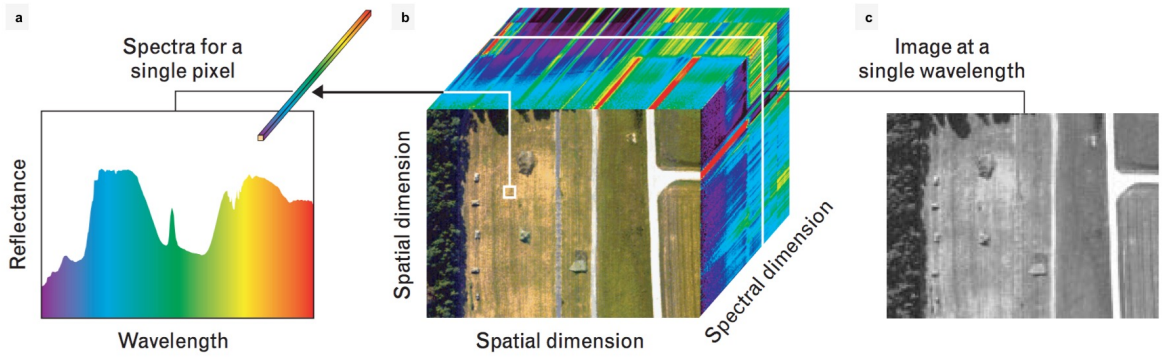

Figure 4.1: The ROI scanned by the aerial HSI imager constitutes the $x - y$ axis, or the spatial plane of the dataset **(b)**. At every spatial pixel there is a reflectance spectrum **(a)**. The spectral data provides the third dimension in the 3D cube. To visualize how materials in the ROI absorb or reflect at a different wavelengths, images can be extracted at specified spectral bands **(c)** [134].

further and provides robust identification of materials, both constituent and foreign surface materials and alteration products, on the macroscale. The application of ground remote sensing methods in the analysis of the paintings facilitates rapid and reliable chemical mapping of the paintings' materials at the surface and subsurface. These chemical data provide not only reliable identification, but also spatial information on the distribution of materials across the surface analyzed. These are essential elements for the attribution and even authentication of works of art as well for an assessment of their state of preservation.

HSI is a powerful remote sensing imaging modality that collects spectral data over a spatial plane. The spatial plane constitutes the scanned region of interest (ROI) by the IS system in pixels. Each spatial pixel contains a reflectance spectrum (Figure 4.1a); the resulting set of reflectance spectra collected within the detector's field-of-view (FOV) produces a three-dimensional (3D) data cube (Figure 4.1b) by which the spatial data forms the $x - y$ plane and the spectral data constitutes the z axis [134].

Analysis of the spectral cube provides feedback on the types and distribution of materials detected within a scene of interest, typically by using classification techniques from multivariate statistics, to extract a set of unique spectral profiles or "endmembers" for char-

acterization and mapping. Furthermore, 2D images can be extracted from the 3D cube to visualize absorption and reflectance characteristics of materials at specific wavelengths (Figure 4.1c). The capability to identify individual materials and obtain detailed imagery along with high specificity classification maps is a function of the radiometric resolution (the bit depth of a pixel), spectral sampling (number of spectral bands accessible) and spatial resolution (spatial sampling) of the IS system [174].

Since their development and deployment in the 1960s, multispectral (MSI) and hyperspectral imaging spectrometers have been predominantly employed for space and airborne land surveys of the Earth, notable examples including JPL's Airborne Imaging Spectrometer (AIS) [121] and NASA's MODIS (Moderate-resolution Imaging Spectrometer) [144]. However, it was AVIRIS (Airborne Visible Infrared Imaging Spectrometer), developed in 1984 at JPL, that revolutionized the application and became the pioneer of advanced reflectance imaging spectroscopy for remote sensing [123, 86].

The late 1980s and early 1990s marked the beginning of applications of remote sensing principles to paintings in the search for faded and hidden imagery and for identification of differences in material absorption at different wavelength bands to distinguish between painting materials [2, 9]. Two main research trends motivated the growth of multiband imaging techniques in cultural heritage science: 1) the objective to acquire color accurate images of paintings with high resolution details [170] and 2) exploration of image processing methods to extract new painting details through false color analysis with images acquired from conventional imaging techniques such as RGB photography, infrared reflectography, and X-ray radiography [9, 98]. In the latter case, with the acquisition of different types of imagery, statistical approaches began to play an important role in data reduction and feature extractions from stacks of images [17].

In the past ten years, the application of MSI and HSI in cultural heritage has taken on new dimensions due to the wealth of information available through large datasets produced by advanced and improved field-deployable, non-destructive analytical techniques that have been integrated into the field of archaeological materials science. By using different types

of excitation sources and having access to hundreds of spectral bands in a wide spectral range (from the UV to the short-wave infrared (SWIR)) numerous painting materials could be identified and mapped by probing electronic properties and molecular-level interactions. Thus, imaging spectroscopy (IS) allows chemical characterization of pigments, binding media, restoration treatments, and degradation products [60, 63, 62, 50, 53]. High resolution spectra facilitate accurate identification of materials with similar spectral profiles or closely-spaced absorptions. High spatial sampling over the image plane means smaller spot size, translating to more data points, thus effectively providing materials' distribution after performing multivariate statistical analyses. Applications of IS in a luminescence mode (luminescence imaging spectroscopy, LIS) have also been used to map and study the behavior of the emission of semiconductor and fluorescent organic pigments found in paintings [195, 46]. LIS is becoming a powerful alternative to forensic photography for diagnostic studies on luminescence behavior. Using the recorded emission profile can (a) more confidently attribute or differentiate between the source of a luminescence instead of solely relying on excitation and capture settings or the color of the recorded luminescence, and (b) help to map multiple emission signatures separately within a single 3D data cube by isolating each emission through subsetting the dataset (cropping the spectral data to specific wavelength ranges).

While these studies have revolutionized how cultural heritage objects are being examined in the laboratory, the application of IS in the field, especially to analyze rock art and in situ wall paintings remained limited, primarily due to cost, accessibility, and portability of these instruments. However, there are a few examples of IS-demonstrated applications beyond the laboratory. One of the earliest examples of ground remote sensing applied in historical buildings to analyze wall paintings was performed by Brooke (1987), who recognized early on the value, as well as the challenges, of macroscale, non-invasive imaging investigations in archaeological fieldwork [30]. Cucci et al. (2015) employed remote sensing using an avionic HSI imager to analyze large scale mural paintings outside of a museum context [51]. Alfeld et al. (2018) applied RIS and XRF mapping on polychrome frieze sculptures and funerary wall paintings to recovery polychromy and identify pigments used in their

decoration [11, 10]. HSI applications have also been demonstrated in situ on Chinese mural paintings to assess the degree of flaking and recover faded mural patterns using multivariate statistical analyses [185]. For long range remote sensing of wall paintings that are out-of-reach for spot spectroscopic measurements, Liang et al. (2014) developed a portable MSI system that performs spectral imaging for pigment identification and image enhancement and 3D topographical mapping [130].

A recent exploratory study pushing the capabilities of HSI investigations on archaeological paintings was conducted on a Greco-Roman funerary mummy portrait (Figure 4.2a) by imaging scientists at the National Gallery of Art (NGA) in Washington, D.C and researchers from the UCLA Archaeomaterials Research Group, using an integrated application of RIS, LIS, and XRF imaging spectroscopy (MA-XRF) [57]. Data cubes acquired by each imaging modality were registered, providing for each pixel of the painting XRF, reflectance, and luminescence data (obtained at specific excitation and capture conditions) (Figures 4.2b-h). This multi-modal HSI technique revealed important information on the production of the portrait (i.e. production sequence and material choices), as well as societal practices being reflected into the artist's technical choices. The XRF map for Cu (Figure 4.2d) and the green reflectance endmember (Figure 4.2f) identifying a green organometallic compound confirmed that copper carboxylate, most likely derived from verdigris (copper acetate) and beeswax following alchemical practices of the period to imitate colored precious stones [35], was used to create the green gemstones of the woman's necklace. Madder lake was identified as the coloring material for the woman's tunic. By mapping the luminescence endmember (Figure 4.2h), it was shown that the same pigment was used for producing the various shades of purple and pink in the tunic. The application of madder lake again mimicked ancient practices, as madder extract was used to dye the yarns for textiles in antiquity; this technical choice has also been found throughout the other funerary portraits from the Greco-Roman period and will be further demonstrated in Chapter 6. The study was the first application of luminescence imaging spectroscopy (LIS) to map the emission of an ancient pigment on archaeological paintings and provided a strong foundation to apply LIS on other

archaeological objects and for other types of pigments with known diagnostic luminescence (i.e. Egyptian blue).

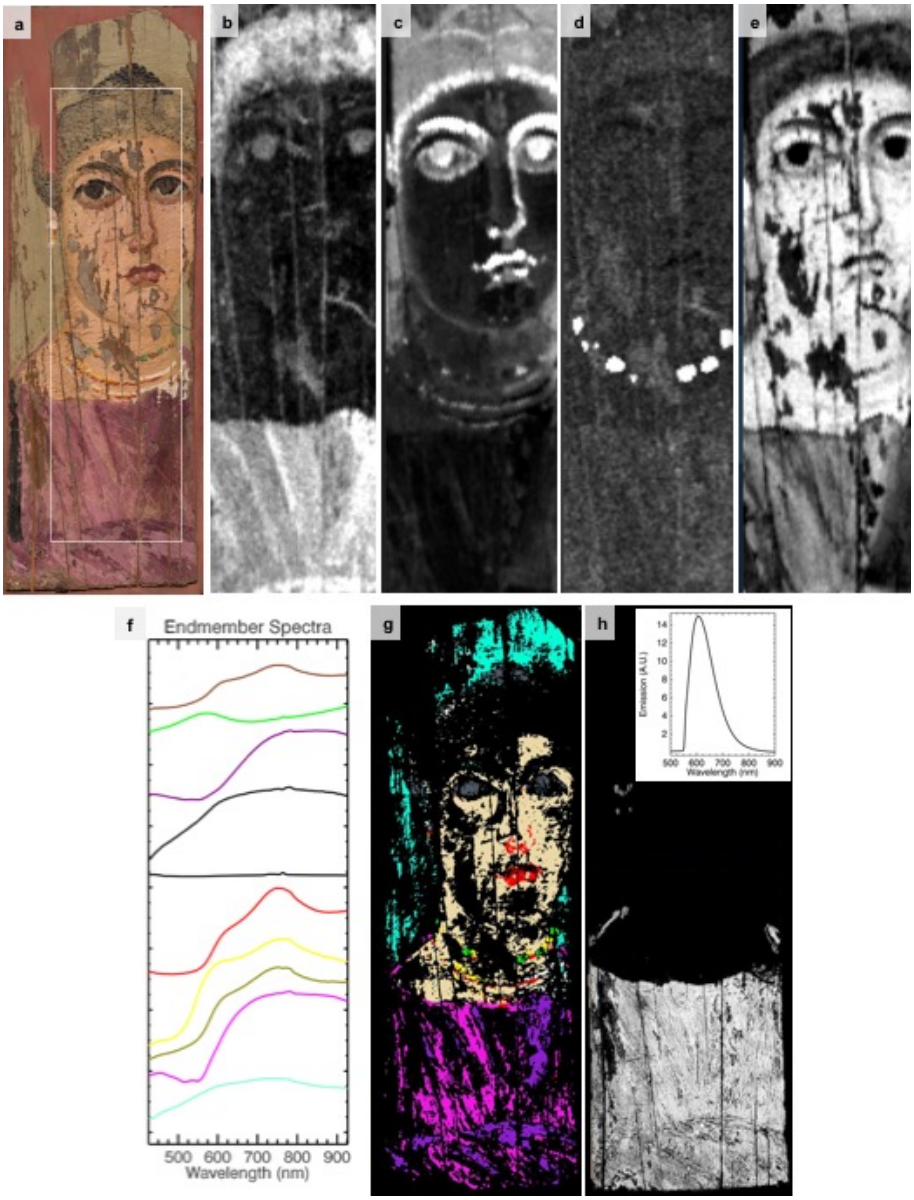

Figure 4.2: **(a)** RGB image of the funerary mummy portrait from the National Gallery of Art, Washington D.C. (A.N. 1956.12.1). **(b-e)** are the elemental maps from the macroscale XRF scanning of Ca, Fe, Cu, and Pb, respectively. The endmembers extracted from the reflectance dataset **(f)** were mapped in **(g)**. From the luminescence cube, the corrected luminescence endmember in the inset figure **(h)** was mapped, demonstrating the application of the same madder lake material throughout the tunic and jewelry [57].

The success of this research on the funerary mummy portrait, as well as the previously highlighted examples of fieldwork IS applications motivated this research to continue extending the capabilities of current HSI systems for the characterization of archaeological and historic objects and monuments, with the objective to (1) provide a holistic understanding and context of ancient and byzantine paintings, (2) recover faded and concealed imagery, and (3) advance in situ IS applications.

4.2 Instrumentation

Two HSI systems, both operating in the VNIR range (400-1000 nm), were employed for the imaging of archaeological and Byzantine paintings. The first HSI system, belonging to the NGA, is an SOC-730VNIR assembled at Surface Optics using an N10E transmission grating spectrometer from Specim Corporation for wavelength dispersion and a high sensitivity EM-CCD detector array from Princeton Instruments, customized for cultural heritage imaging at lower light levels. The second system, an instrument used by the UCLA/Getty Program and the Molecular and Nano Archaeology Laboratory at UCLA, is the Specim IQ, a compact, highly portable commercial HSI camera from Specim Corporation featuring a CMOS sensor [49]. Both systems operate imaging spectrometers in a push-broom (line scan) configuration for data collection (Figure 4.3). Data storage formats in IS systems follow band-interleaved-by-line (BIL) (all spectral bands are stored in a line of pixels before continuing to the next line), band-sequential (BSQ) (entire first spectral band is stored before progressing to the next band), or band-interleaved-by-pixel (BIP) (all spectral bands in pixel are stored before progressing to next pixel) (Figure 4.3) [81].

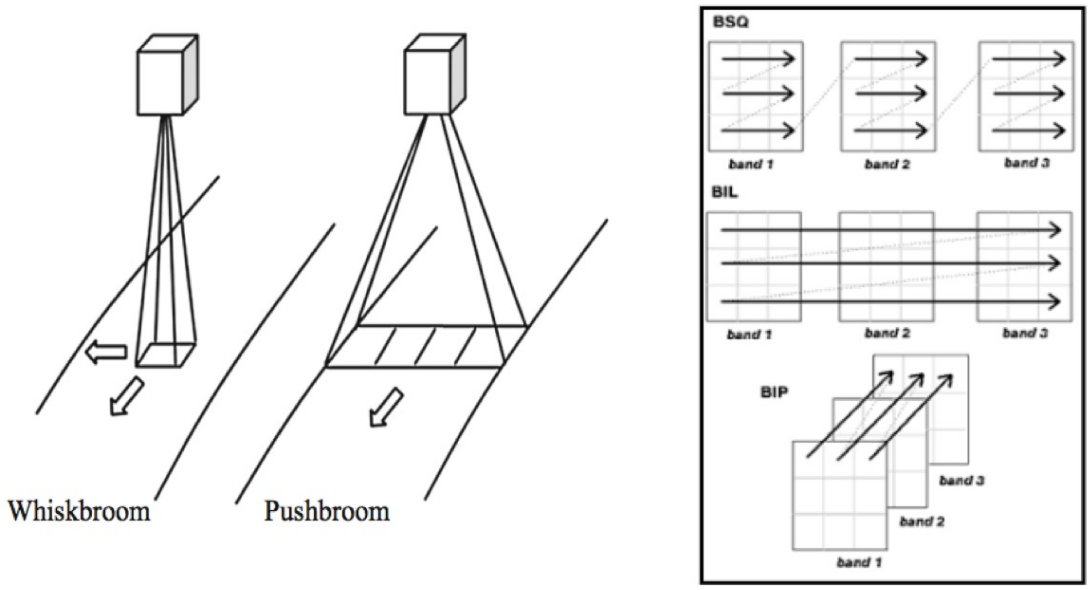

Figure 4.3: Imaging spectroscopy scanning techniques (whisk-broom and push-broom scanning) and the image storage data formats [81].

The Surface Optics system has a 2.5 nm sampling and 240 spectral bands comprising the VNIR range; the Specim IQ camera features 3 nm sampling, providing 200 spectral bands (Table 4.1). IS systems have several noise susceptibilities that affect their signal-to-noise ratio (SNR). The main limitation is shot noise due to photon counting, intrinsic to the quantum nature of light. The photons collected follow a Poisson distribution, and the shot noise is proportion to the square root of the collected signal. Other limitations arise from the residual non-uniformity response of pixels in the focal plane arrays after two point (gain and offset) correction, as well as random detector noise [59].

Table 4.1: IS system specifications for the NGA and UCLA systems.

	Surface Optics	**Specim IQ**
Image Size	1024 x 1024 pixels	512 x 512 pixels
Spectral Range	400 - 1000 nm	400 – 1000 nm
Spectral Sampling	2.5 nm (240 bands)	3 nm (200 bands)
SNR	400:1	180:1

The SNR of the Surface Optics system was previously reported in [61] to be 400:1 (Table 4.1). To calculate the SNR of the IQ camera (Equation 4.1), a 3D data cube was collected containing a white diffuse reflectance standard (usually 99% reflectance) in the image scene.

$$SNR = \frac{\mu}{\sigma} \tag{4.1}$$

where μ is the average signal of raw counts from the white standard in a select region of interest (here, a region of interest (ROI) of 16 pixels), and σ is the standard deviation of the signal. The average SNR for the IQ camera is 180:1. While large absorptions in the reflectance spectra can be easily distinguished at this level of system performance (noise is $\sim 0.5\%$ of the total signal), subtle spectral features will be more difficult to resolve. The IQ performance can be evaluated visually by looking at the spectrum of a single pixel extracted from the white reflectance standard's data cube (Figure 4.4).

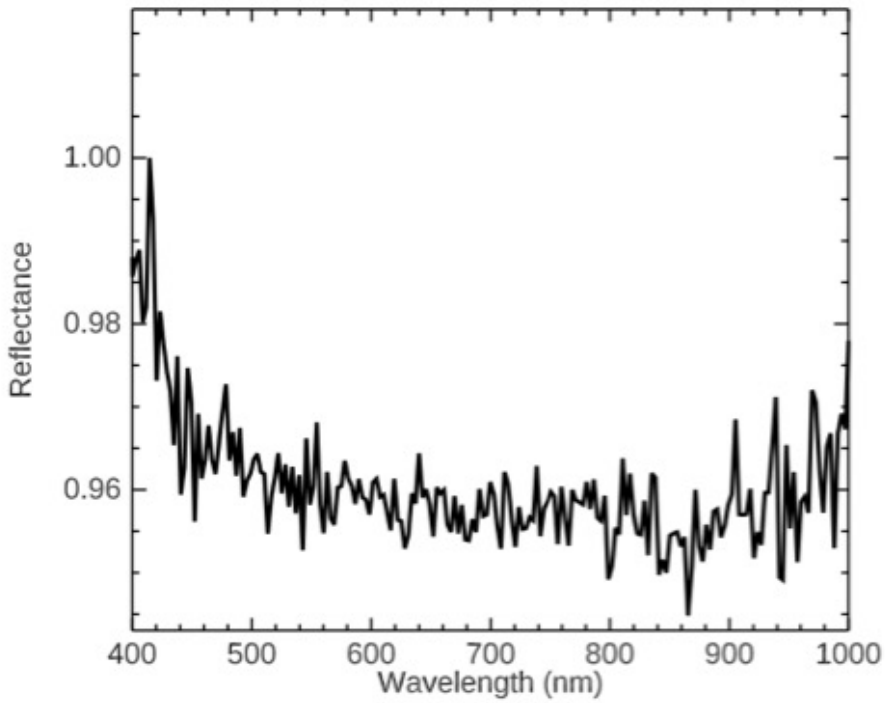

Figure 4.4: A single pixel in the image scene recorded of a white diffuse reflectance standard. The average SNR calculated between 500–900 nm is 180:1.

4.3 Archaeological/historical materials: case studies

The Surface Optics and Specim IQ systems were applied for RIS and LIS studies of ancient and historical paintings situated in various settings, including museum galleries, storerooms, and in situ funerary and religious contexts. The first case study is of an ancient Greco-Roman funerary mummy portrait (accession number 32.4) from the Walters Art Museum in Baltimore, Maryland, which was examined using the Surface Optics system. The IQ camera had been applied in various archaeological sites and historical Byzantine sites in Cyprus, resulting in over 20 data cubes comprising reflectance and luminescence spectral data. As the IQ is a relatively new HSI camera, only a few studies have been reported on its application to cultural heritage materials [49]. This research is the first demonstration of the IQ camera's capability for scientific archaeological fieldwork. The second case study presented here are the RIS and LIS investigations of Tomb 3882 from Paphos, Cyprus.

4.4 Data collection

Data collection was structured to acquire all the necessary information for image post-processing and spectral analyses. Each painting was uniformly illuminated with a source specific to the RIS or LIS analyses, thus the IS systems are active sensors. First, dark frames were acquired for the image calibration process. Second, an image scene consisting of only an illuminated diffuse white reflectance standard panel (99% reflectance) was collected. Coupled with the data from the dark frames, this was used for flat-fielding the image and to address pixel non-uniformity issues. Black and white reflectance standards (Labsphere Inc, NH) were also placed within the scene to calibrate the data to reflectance factor and perform noise analysis.

4.5 Data analysis and results

Spectral data analysis is performed in ENVI, a geospatial analytical software from L3Harris Geospatial used to perform statistical analysis on 3D imagery datasets. The objective of the data analysis is to extract unique endmembers from the set of reflectance and luminescence spectral profiles that represent the constituent materials comprising the painting's makeup. Each material has its own unique reflectance spectrum caused by inherent electronic and vibrational processes induced by light excitation. In the experimental setup, the spectral radiance measured from a target, L_f, is the product of the reflectance spectrum, ρ, with the excitation source's radiance on the target, L_i, [174]:

$$L_f(\lambda) = \rho(\lambda) L_i(\lambda) \tag{4.2}$$

With respect to 3D data cubes, by dividing $L_f(x, y, \lambda)$ by the $L_i(x, y, \lambda)$ measured off of a large white 99% reflector, the apparent reflectance, $\rho(x, y, \lambda)$ can be recovered. This was achieved through flat-fielding and dark noise correction of the data cubes using equation 4.3.

$$\rho = \frac{R - B}{W - B} \tag{4.3}$$

$R = Reflectance\ cube$

$B = Dark\ frame\ (noise)\ cube$

$W = White\ panel\ reflectance\ cube$

For paintings with multiple captures, the reflectance and luminescence 3D data cubes were registered and mosaicked together with a high-resolution RGB image using common control points, performed by an automatic Matlab image registration/mosaicking script developed by Conover et al. (2015), to produce a single reflectance data cube and a single luminescence data cube [47].

Some of the most significant challenges for characterizing pigments in paintings based on

their reflectance profiles are that the pigments are often in intimate mixtures of two or more different materials of inorganic and/or organic origin, or are applied in layers in such a way that reflectance signatures of top-most and lower layers (surface and subsurface) are both collected as a single signal. For example, a 'flesh' coloration (hue) in archaeological (Classical) paintings is often produced by mixing hematite-rich red ochre (Fe_2O_3), yellow ochre (mainly goethite, FeO(OH)), and calcium carbonate ($CaCO_3$). In Byzantine paintings, the flesh tone was a build-up using a greenish preparatory paint layer known as *proplasmos* made of a mixture of pigments, mainly green earth ($(K(Mg,Fe^{2+})(Fe^{3+},Al)[Si_4O_{10}](OH)_2)$), superimposed by a yellow and red paint layer (of FeO(OH) and Fe_2O_3 respectively). Therefore, unlike in most remote sensing applications, the final reflectance spectrum, ρ, does not necessarily represent a pure material. The complexity of the artist's application is further increased by introducing shading and variations in hues to produce intentional effects of darker/lighter areas and different colors as noted in Chapter 2. This makes traditional approaches to the mapping of reflectance endmembers a limiting factor in understanding the production process of a painting, as the subtle mixtures produced in the painting are accounted for by a widening of the mapping tolerance. To properly explore the artistic techniques employed and address the complexity of these admixtures, derivative analyses were applied to the reflectance cube, where the 1st derivative of the cube was calculated ($\frac{\delta\rho(x,y,\lambda)}{\delta\lambda}$), and the 1st derivative of the reflectance spectral endmembers were mapped. Analyzing the reflectance features of pigments in the 1st and 2nd derivative has been applied in remote sensing and for FORS data; it has proven extremely helpful for identifying the maxima of absorptions, inflection points, and other diagnostic spectral features to distinguish materials of similar spectral profiles, such as earth minerals and semiconductor pigments [198, 15, 7]. The derivative spectra also makes it possible to identify subtle features in the original reflectance spectra more reliably. In rare cases it has been used to map specific uses of a material based on a diagnostic spectral feature [74]. However, it has not been applied as a method to improve extraction and map endmembers to interpret artistic applications in ancient polychromy and paintings. In this study, 1st derivative cubes were used to identify and separate different pigment mixtures in the VNIR range and map their presence more robustly. 2nd derivative

calculations of the cubes ($\frac{\delta^2 \rho(x,y,\lambda)}{\delta \lambda^2}$) were used for targeted mapping of specific absorption features of interest in the SWIR. The 1st and 2nd derivative calculations were performed in Matlab and the resulting data cubes were analyzed in ENVI.

Two methods were utilized to extract endmembers from the 3D data cubes. The first method was the Spectral Hourglass Wizard (SHW), a built-in ENVI tool. It is an operational process that begins with data-dimensionality reduction to manage the high volume of data produced. A Minimum Noise Fraction (MNF) transform is applied to noise-whiten and reduce the data, using two separate linear principle component transforms, and therefore produce a set of coherent eigenimages (Figure 4.5).

Figure 4.5: **(a)** Minimum noise fraction (MNF) image no. 2, from the 1st derivative cube of portrait A.N. 32.4. **(b)** MNF image no. 5. **(c)** MNF image no. 7.

The number of eigenimages with discernible features provides a first look at the classes of materials within the dataset. It also determines the data dimensionality; as only the eigenimages with content are selected for clustering, this reduces the number of dimensions in the subsequent data processing steps to the number of useful eigenimages. Next, using

a convex geometry framework, the Pixel Purity Index (PPI) are calculated. Each pixel is projected multiple times onto various unit vectors, and the extreme pixels are noted and counted, determining the pixel purity [24]. The pixels are then put into an n-D space visualizer, n corresponding to the number of spectral channels. Endmembers are selected from the extreme pixels in the clusters appearing in the n-D visualizer (Figure 4.6).

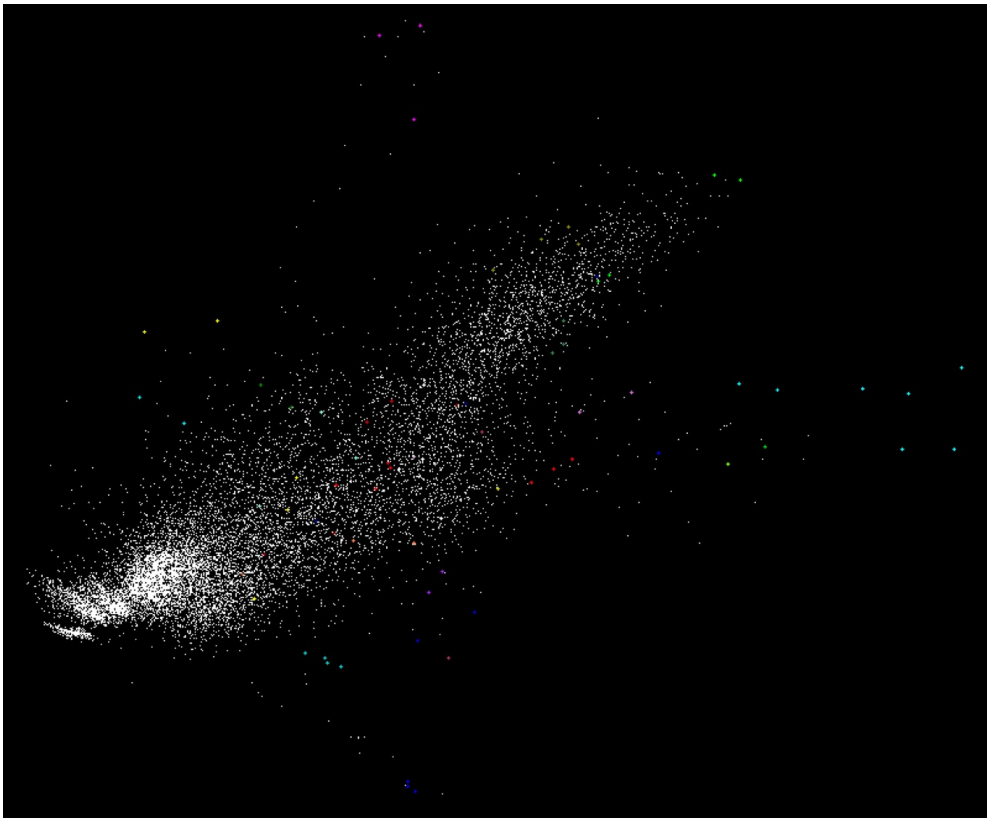

Figure 4.6: n-D visualizer for 1st derivative data from portrait A.N. 32.4. The different colored pixels represent pixels chosen for endmember extraction. A selection of extreme pixels in a cluster will be averaged for the resultant endmember.

A secondary advantage to the MNF transform is that once the data dimensionality is determined, an inverse MNF transform selecting only MNF bands with coherent data can be performed, which reduces the noise in the spectra.

The second extraction method is the Sequential Maximum Angle Convex Cone (SMACC) [92], also part of ENVI's endmember tool set. This is an attractive alternative for datasets

where clear cluster separation is difficult to achieve in the n-D visualizer and key endmembers may be missed. SMACC utilizes a convex factorization approach to extract extreme vectors (pixels). First, the two most extreme vectors in the dataset form a convex cone. In a sequential process, each endmember found is evaluated based on the angle it forms with the convex cone. Vectors with the maximum angle are selected as an endmember. This process continues until the dataset has no vectors remaining outside of tolerance limits.

The final sets of endmembers extracted from SHW and SMACC are then input into ENVI's Spectral Angle Mapper (SAM) to evaluate whether (1) there are sufficient endmembers to describe the painting's materials, and (2) the endmembers are applicable with a reasonable tolerance level (i.e. the spectral angle). The SAM is a classification tool that determines spectral similarity between pixels in the data cube with the set of endmembers extracted, by calculating in n-D space the spectral angle between the pixel vectors and endmember vectors [207]. Smaller spectral angles correspond to higher spectral similarity, i.e. better matches. The evaluation is performed by looking at the individual maps for each endmember, also known as 'rule' images. By adjusting the histogram of a rule image, thus modifying the spectral angle, and comparing the spectra of the pixels visualized in the image to that of the associated endmember, the final spectral angle is determined. Redundant endmembers are discarded in the process. Mixed-tuned matched filtering (MTMF) can also be applied to give feasibility scores to the endmembers and mapping results [25]. The final spectral angle map represents the integration of rule images for the chosen set of endmembers at their designated spectral angles.

4.5.1 Funerary Portrait A.N. 32.4 – The Walters Art Museum

The funerary Greco-Roman portrait analyzed is from the collection of the Walters Art Museum (accession number 32.4, Figure 4.7a) and dates to 130 – 200 AD and is provenanced to the region of Antinoopolis, the city founded by the Emperor Hadrian [26]. These types of portraits offer important glimpses into the Greco-Roman society that flourished in Egypt, as they were painted in the likeness of real people that lived during this period. More im-

portantly, they are the only examples of portrait painting remaining from the ancient world. Though it is not known with certainty whether the portraits were painted before death or posthumously, they were placed over the mummy's face and wrapped within the linen that surrounds the body. As these portraits represent real people, the imagery and the materials choices and production technology provide important information on how these people lived and how they organized themselves (additional background on the funerary portraits can be found in Chapter 6).

Portrait 32.4 represents a woman of high wealth and social status. She wears a white tunic and veil, and gold jewelry. In the foreground, she appears to have a floral garland with pink flowers and green leaves. This portrait is rather unique for the high-relief gilded applications used for her crescent-shaped earrings and torc (Figure 4.7b). Additionally, pieces of gold foil decorate the garland across her chest. The medallion of her torc most likely represents a gold coin. Her jewelry and the sun-shaped pattern of the bole (a reddish-brown clay used as a preparatory layer for gilding) bear a striking resemblance to a female portrait in the Detroit Institute of Arts (accession number 25.2), also from Antinoopolis, dating to the early-mid 2nd century AD [65], though stylistically they appear to be by the hands of different painters.

The intricate details in this portrait of the hair, the variations in flesh tones, the decoration of her veil (Figure 4.7c), and the shading effects used to produce a 3D effect for her tunic are a tribute to the craftsmanship of the ancient artist and suggest that a highly skilled painter was hired for this portrait commission. Despite the weathering and degradation of the portrait, it shows the rich commission and depiction of a noble woman. The painting complexity of this portrait made it an ideal case study to demonstrate the potential of imaging spectroscopy to characterize archaeological paintings, as well as provide new insight into funerary portraiture from Roman Egypt.

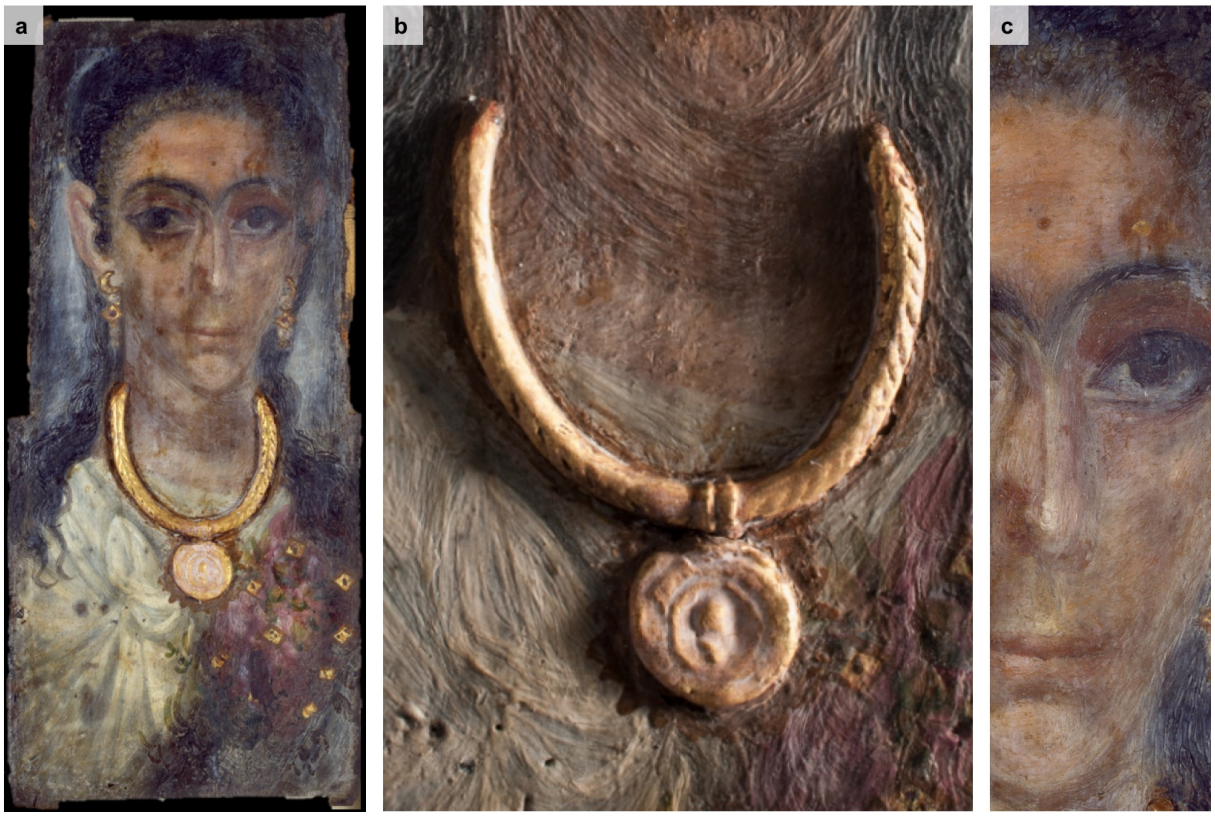

Figure 4.7: **(a)** Funerary portrait A.N. 32.4 from the Walters Museum of Art. **(b)** Raking light image of the high-relief gold necklace. **(c)** Close-up of the face, showing the highlights of her chin, upper lip and nose, as well as variations of her flesh tone and the details in her hair braid

The funerary portrait was first analyzed using the HSI system in reflectance mode (Figure 4.8a-b). The painting was illuminated using four Solux lamps (4700 K, Tailored Lighting, Inc.) mounted onto two light stands, projected approximately 45 degrees to the surface of the painting. A light meter was used to assess the illumination distribution and maintain that the lux level at the painting's surface was $\sim$ 1200 lux, for the safety of the object. Two image scans were collected of the painting (250 ms integration time), with a small degree of overlap for registration in post-processing, to acquire 3D cubes with high spatial resolution. The final registered cube featured a spatial resolution of 0.7 mm/pixel.

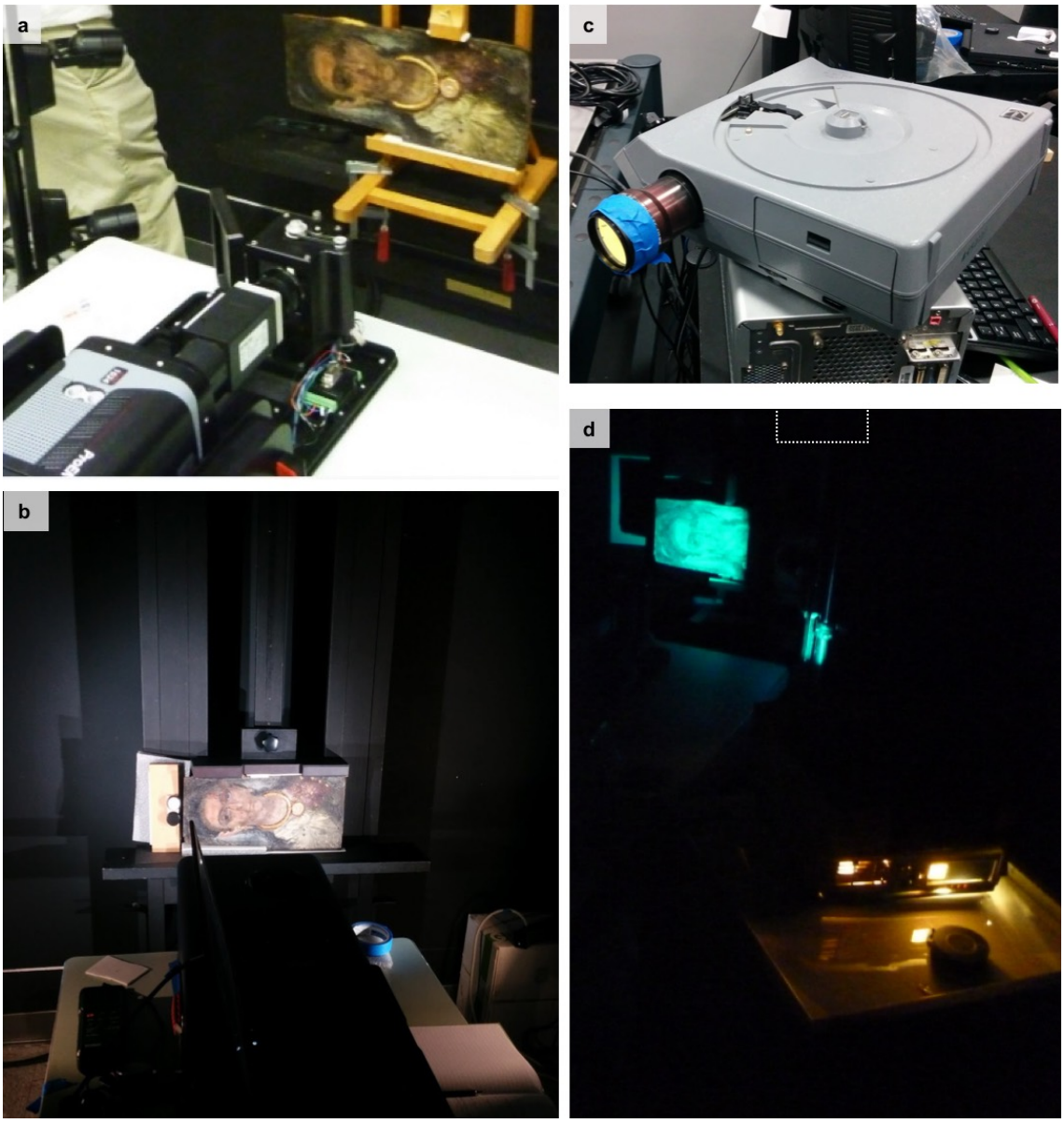

Figure 4.8: **(a)** The VNIR camera of the NGA used for the analysis of the Greco-Roman portrait A.N. 32.4. The collection was acquired in a dark room to minimize stray light **(b)**. **(c-d)** To record the luminescence datasets of the funerary portrait, a light projector was filtered to illuminate the painting with a blue-green light (450-550 nm).

In luminescence mode, the identification and capture of madder lake and Egyptian blue, both luminescent in the VNIR with no emission overlap, were targeted. Due to madder lake's absorption maximum between $\sim$ 505 and 545 nm (with characteristic sub-bands at $\sim$ 510 and $\sim$ 540 nm) and Egyptian blue's broad absorption between 560 nm and 630 nm,

and luminescence emissions at $\lambda_{em,max} \sim 620$ nm and $\lambda_{em,max} \sim 930$ nm, respectively, the two pigments can be excited simultaneously using a green light. A filtered light projector (Figure 4.8c) was used to illuminate the portrait from 430 – 540 nm, and the lens of the VNIR system was filtered to capture from 540 – 1000 nm. Image collection was performed in a dark environment to prevent stray light from interfering with the emission signals, which was an especially significant concern for the visible luminescence of madder lake (Figure 4.8d). Two luminescence image scans were collected at longer integration times ($\sim$ 500 ms) to record the emission signals.

Before progressing with the SHW and SMACC methods for extracting endmembers from the 1st derivative cube of portrait A.N. 32.4, an additional step to mask the gold necklace and earrings and the non-painting background from the image scene was applied. This process removed those pixels to provide a 'cleaner' dataset for clustering and extracting pixels representing pigments. The final 1st derivative endmember set can be found in Figure 4.9d, with their corresponding reflectance endmembers in Figure 4.9c. The SAM results of the 1st derivative endmembers are visualized in in Figure 4.9b. The hues for each endmember, their tolerance level for the mapping, and the constituent materials identified from HSI analyses and supplemental FORS and XRF data collection providing supplementary information and validation of the results are listed in Table 4.2.

The endmembers represent relatively pure as well as intimate mixtures of a hematite (Fe_2O_3)-rich red ochre, a goethite (FeO(OH))-rich yellow ochre, natrojarosite ($(Na)Fe_3^{3+}(OH)_6(SO_4)_2$), madder lake, copper (Cu(II)) carboxylate, and lead white ($PbCO_3$). Hematite is an iron oxide with characteristic absorptions in the VNIR wavelength ranges due to spin-forbidden ligand field transitions (Appendix A.1.1). It features a characteristic inflection point at 585 nm and absorption at 660 nm ($^6A_{1g}(^6S) \rightarrow {}^4T_{2g}(^4G)$), and a peak maximum at 750 nm and broad near-infrared (NIR) absorption at $\sim$ 870 nm ($^6A_{1g}(^6S) \rightarrow {}^4T_{1g}(^4G)$). Goethite, an iron oxyhydroxide, is identified by a shoulder at 445 nm ($^6A_{1g}(^6S) \rightarrow {}^4A_{1g}, {}^4E_g(^4G)$), an inflection at 550 nm and absorption at 670 nm, as well as a peak maximum at 765 nm and a broad NIR absorption centered at 925 nm (Appendix

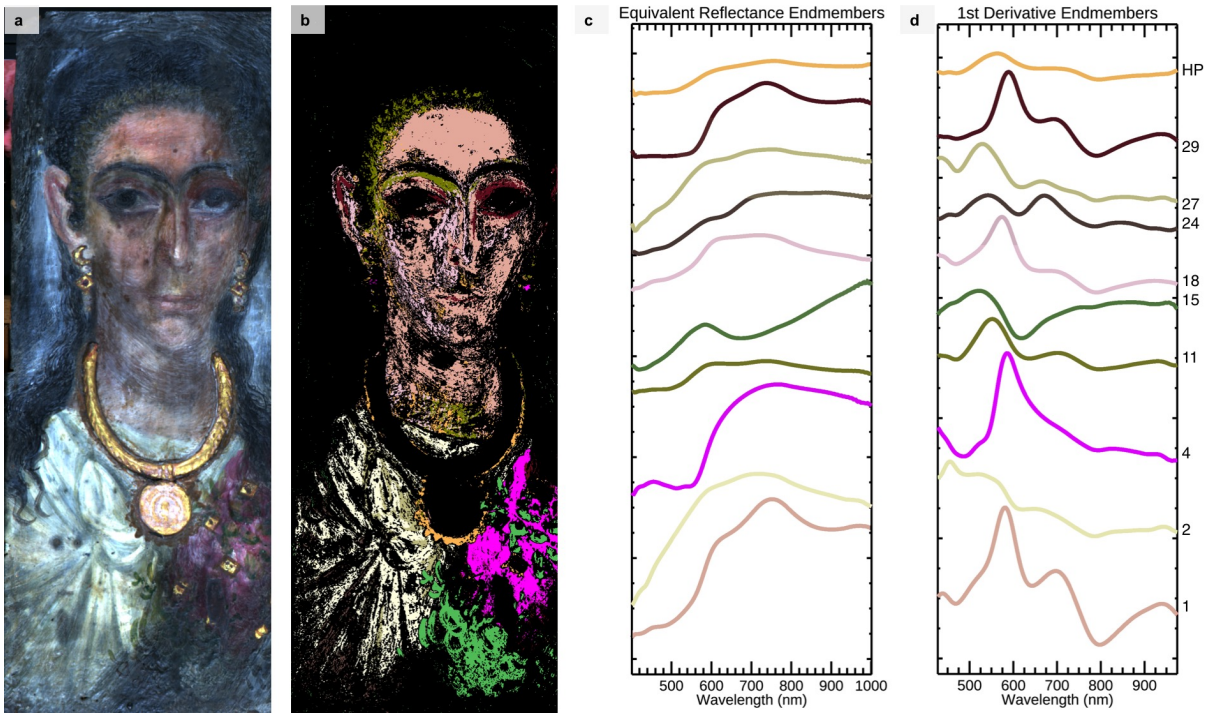

Figure 4.9: **(a)** RGB image of portrait A.N. 32.4 extracted from the reflectance cube. **(b)** Spectral angle map of 1st derivative endmembers extracted **(d)**. The equivalent reflectance spectra are in **(c)**.

Table 4.2: 1st derivative endmember results from the RIS studies.

Endmember	**Spectral angle**	**Region**	**Hue**	**Material(s) ID**
1	0.2	Flesh (forehead, facial shading)	Light pink	Red ochre Yellow ochre Lead white
2	0.2	Tunic (bright areas)	White	Natrojarosite Lead white
4	0.35	Earrings, Garland	Pink/Purple	Madder lake
11	0.35	Hair braid; eye line	Greenish yellow	Yellow ochre Natrojarosite
15	0.726	Garland	Green	Copper carboxylate
18	0.241	Flesh (skin tones, highlights)	White-pink	Yellow ochre Red ochre Lead white
24	0.288	Tunic lines	Black	Lead white Egyptian blue
27	0.195	Tunic lines	Yellow	Natrojarosite Lead white
29	0.241	Ear; eye line	Deep red	Red ochre
HP	0.21	Bole	Orange-red	Red ochre, yellow ochre

A.1.2). 1st derivative analysis helped classify endmembers representing different mixtures of ochre pigments used for the different flesh tone applications in the woman's face and neck. The large peaks' maxima from $\sim$ 550–590 nm correspond to the inflection points of the ferric oxide minerals in the pigments, which can be identified by comparison to reference reflectance spectra (Appendix A). The secondary peaks from $\sim$ 615–750 nm provide absorption information corresponding to the ${}^6\mathrm{A}_{1g}({}^6\mathrm{S}) \rightarrow {}^4T_{2g}({}^4G)$ from 660–670 nm in the reflectance spectra. Smaller secondary peaks can indicate high pigment concentration, causing an absorption saturation, or mixtures with a darker pigment (such as carbon black).

While the portrait has undergone some degradation and discoloration, it is apparent that the artist used various shading applications on her eyelids, the sides of her nose, her ears, and neck, as well as her forehead, tip of her nose, and chin. The hues in her face comprise deep red-brown, light pink, yellow, and white tones. 1st derivative endmembers 1, 11, 18, and 29 show varying concentrations of a red ochre, a yellow ochre, natrojarosite and lead white to decorate and accentuate certain areas of her face. Endmember 1 (applied for forehead and facial shading) has spectral features at 456 nm (shoulder), 582 nm (inflection), 670 nm (absorption), 752 nm (peak maximum), and 901 nm (NIR absorption), which clearly shows a mixture of hematite-rich red and goethite-rich yellow ochres. The white pigment was identified by XRF as lead white due to the presence of Pb L_α and L_β characteristic X-ray energies measured at 10.55 and 12.61 keV, respectively, and the M_α emission at 2.34 keV. This lead white pigment is believed to be cerussite ($\mathrm{PbCO_3}$), a natural lead carbonate mineral. Hydrocerussite ($\mathrm{Pb_3(CO_3)_2(OH)_2}$), which has been found in other portraits [57] and is identified in reflectance spectra by hydration absorption signatures at 1440 and 1900 nm, is a result of synthetic lead white production where metal lead sheets are placed above acidic baths (usually vinegar) and sealed for long periods of time to induce a corrosion process [84, 88, 158]. This procedure produces both cerussite and hydrocerussite phases, thus the absence of the latter's signature in the endmember spectra suggests that the portrait's lead white pigment was not synthetic. Natrojarosite, a Na-rich jarosite, was identified by a small characteristic absorption due to the electronic transition at $\sim$ 433-435 nm (${}^6\mathrm{A}_{1g}({}^6\mathrm{S}) \rightarrow {}^4A_{1g}$)

(Appendix A.3.3). FORS and XRF confirmed the presence of a Na-rich jarosite mineral due to the lack of K in the XRF spectra and the presence of the 1543 nm first O-H stretching overtone in the SWIR spectra [43].

Endmember 18 also contains red and yellow ochre, mixed with lead white, to produce a white-pink flesh tone but suggests a unique mixture based on the diagnostic spectral features' positions at different wavelengths compared to endmember 1: 456 nm (shoulder), 575 nm (inflection), 670 nm (a), 736 nm (peak maximum), 860 nm (NIR absorption). Endmember 11, which maps to the greenish yellow toned ringlets in the hair braid across her forehead and the proper right eyeline under her eyebrow, is a mixture of yellow ochre and natrojarosite. The final flesh tone, mapped by endmember 29 on her ear and proper left eyeline, is a deep red hue produced by a relatively rich application of red ochre.

Natrojarosite was also found in the tunic, in different pigment mixtures mapped by endmembers 2 and 27, mixed with lead white and Egyptian blue (the latter identified by luminescence mapping, to be discussed presently). Regions appearing brighter (noticeable brush strokes and dots by the artist) show stronger signatures of natrojarosite (endmember 2). Weaker signals were found sparingly in the veil and the earring of the woman. The tunic of the woman also features dark and yellow stripes, most likely to create shadows and highlights in the tunic imitating the appearance of the knot and folds in the tunic. The yellow stripes were mapped by endmember 27. The darker stripes were mapped by endmember 24, which has a $\sim$ 630 nm absorption in the reflectance spectrum. However, because the tunic hues were produced by a mixture of natrojarosite (which has an absorption at $\sim$ 640–650 nm), lead white, and Egyptian blue, the convolution does not permit the latter's identification based only on the reflectance signature.

The orange-red bole material, which was used as a preparatory layer and outline decoration for the gold jewelry (mapped by endmember HP), was identified as a mixture of red and yellow ochre, as well as a subtle presence of natrojarosite, by the endmember's spectral features at 434 nm (absorption), 562 nm (inflection), 670 nm (absorption), 755 nm (peak maximum), and 932 nm (absorption).

The portrait demonstrates similarities to the NGA funerary portrait [57] and a portrait of the J. Paul Getty Museum collection (to be discussed in Chapter 6) in that the green pigment in the floral garland is a copper carboxylate material, most likely produced by mixing copper acetate (the pigment verdigris) with heated beeswax [35]. Endmember mapping reveals traces of this pigment in the dark background (possibly due to brush contamination). This is one of the few confident identifications of a green copper carboxylate pigment used in funerary portraits, though a preliminary investigation from the Penn Museum of a female funerary portrait shows a copper green pigment in the gemstones of a necklace, very similar to the NGA portrait.

The gold jewelry and the lead white applications in the veil and eye were challenging to extract representative endmembers to map in the 1st derivative, which is sensitive to differential changes in the reflectance profile. The reflection off the gold, which was applied in high relief and does not have a characteristic VNIR profile, creates highly variable, non-identifiable signatures in the 1st derivative. The gold jewelry was more easily mapped by a reflectance endmember showing a broad reflectance (Figure 4.10a-b), and it was identified by XRF as an alloy (most likely electrum) of gold and silver. While spectral mapping was not effective for lead white, due to the semi-transparent application of the veil and mixtures with other pigments, an MNF 1st derivative image emphasized the applications of white in the portrait (Figure 4.10c), highlighting interesting features such as the proper left eye and revealed that the veil was in fact wrapping around the body of the woman at the bottom of the portrait, giving an enhanced sense of dimensionality to the painting. Additional details such as the fabric mesh of the veil are clearly visible, and it appears that the veil itself has small adornment features, appearing both on the top of her head and along the draped edge on her proper left side. In additional MNF images, the texture of her hair and the veil are also enhanced (Figure 4.10d).

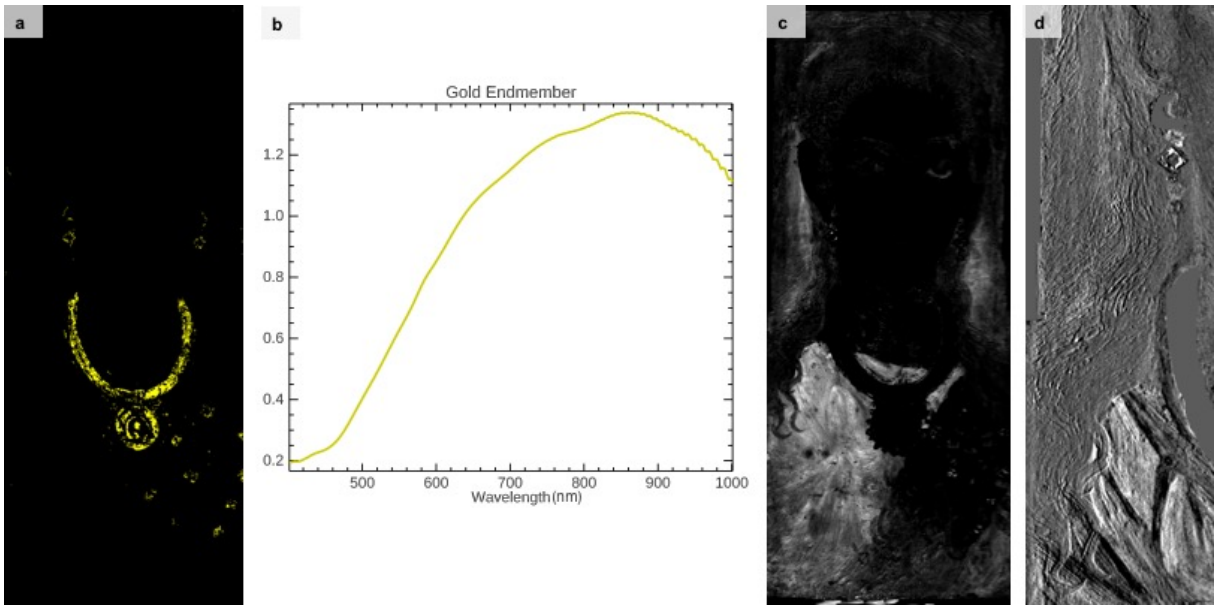

Figure 4.10: **(a)** Reflectance SAM image of the gold reflectance endmember **(b)**. **(c)** MNF image no. 2, which highlights the white applications in the portrait, most likely containing lead white. **(d)**) MNF image no. 8, showing textural details of the hair and veil.

Endmember 4, which identified madder lake by its double absorption at 514 and 547 nm, was mapped to the pink/purple floral garland, however, it will be shown that this did not map all applications of the pigment in the portrait. The LIS data cube was next analyzed to explore the distribution and application of madder lake and Egyptian blue through mapping of their luminescence profiles. To extract and properly identify the emission endmember of madder lake, a fluorescence correction was applied to the luminescence data cube. This was necessary as the double-structure absorption of the purpurin-Al(III) compound and the respective luminescence emission wavelength range of madder lake overlap [90], causing the emission of the madder lake pigment to be re-absorbed and then re-emitted, thereby causing a change in the shape of the spectral profile as well as a bathochromic shift in the peak emission [42]. The fluorescence correction is performed using principles of the Kubelka-Munk theory, a simplified model for the diffuse reflectance behavior of light considering absorption and scattering effects, under the assumption that the inorganic substrate used for the production of madder lake does not absorb in the excitation or emission wavelength

ranges for the dye pigment, and that the paint layer is optically thick. Lagorio et al. [124] developed a fluorescence correction factor, γ , for the original emission spectrum by solving the bidirectional differential photon flows from a uniform, optically thick luminescent media to find the true emission spectrum:

$$\gamma(\lambda, \lambda_0) = \frac{1}{1 + \sqrt{\frac{F(R_\lambda)}{F(R_\lambda)+2}}} \frac{1}{1 + \sqrt{\frac{F(R_\lambda)(F(R_\lambda)+2)}{F(R_{\lambda_0})(F(R_{\lambda_0})+2)}}} \tag{4.4}$$

where $F(R)$ is the remission function, or a ratio of the absorption to scattering coefficients of the media:

$$F(R_\infty^{\lambda_0}) = \frac{(1 - R_\infty^{\lambda_0})^2}{2R_\infty^{\lambda_0}} = \frac{k(\lambda_0}{s(\lambda_0)} \tag{4.5}$$

By dividing the luminescence cube by γ, taking into account broadband excitation (it should be noted that Equation 4.4 applies for a single excitation wavelength) [64], the corrected emission cube is obtained.

Three luminescence endmembers were extracted from the corrected emission cube (Figure 4.11). The Egyptian blue endmember features a true emission peak $\sim$ 910–950 nm [6, 159]; the emission peak at 600 nm is due to a background fluorescence from the tunic region where the endmember was retrieved, possibly due to the presence of the binder. Further analysis must be done to understand the source of this signal.

The rule images of the luminescence endmembers (Table 4.3) are presented in Figure 4.12. Madder lake shows two distinct emission profiles with maxima at 595 and 605 nm (Figure 4.11). The endmember with the peak emission at 595 nm maps to the earrings and a small feature in the eye (Figure 4.12a); these spectra are noisier than the those mapped in the pink garland (Figure 4.12b), corresponding to the second madder lake endmember with the peak emission at 605 nm. The spectral angle mapping of the Egyptian blue endmember produced poor results as it did not sufficiently map many of the areas that contained lower concentrations of the pigment. The three endmembers were linearly unmixed in ENVI's

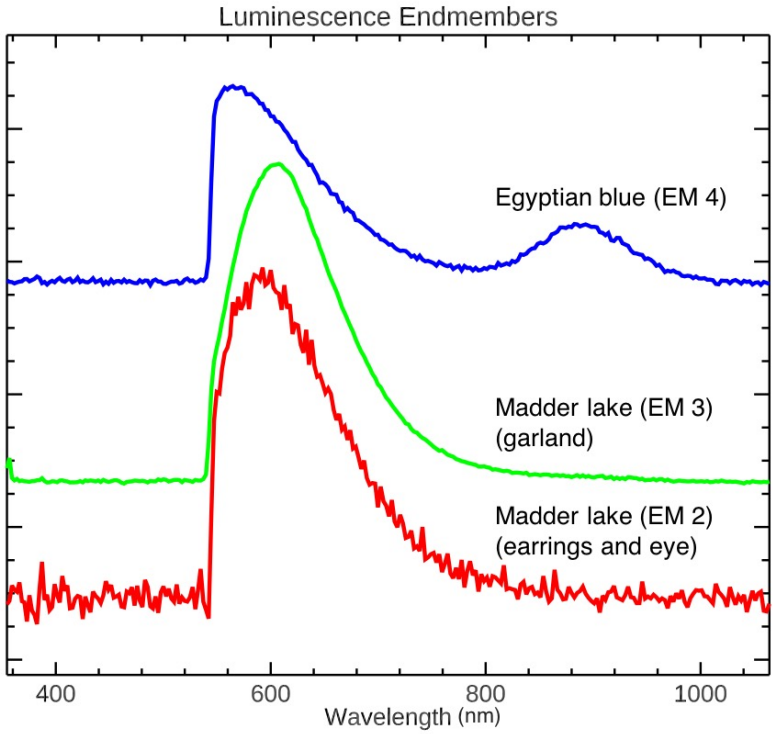

Figure 4.11: Luminescence endmembers extracted from the corrected emission cube.

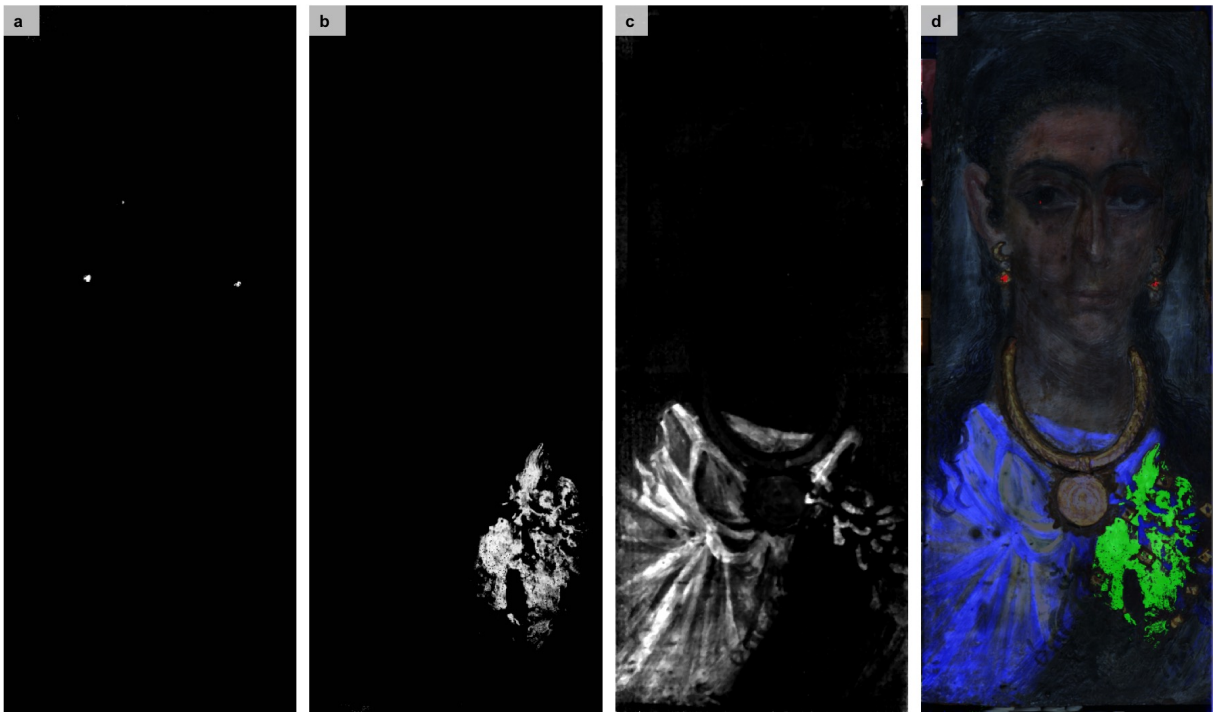

Figure 4.12: **(a)** Endmember rule image for madder lake emission from the earrings and proper right eye. **(b)** Endmember rule image for madder lake mapping emission from the garland. **(c)** The linear unmixing result of the Egyptian blue endmember, showing the distribution of the pigment throughout the tunic and the green leaves. **(d)** The false color image of the three endmembers, overlaid onto the RGB image of the portrait.

Linear Spectral Unmixing tool. The unmixed Egyptian blue endmember rule image, followed by an application of a median filter to remove the speckle noise, produced the map in Figure 4.12c. The integrated image of the three endmembers were overlaid onto an RGB image of the portrait to show precisely where madder lake and Egyptian blue were applied. The results establish that the emission cube provided a more robust identification for madder lake because the small feature in eye was not mapped in the 1st derivative analysis (this would have required a less strict, thus less accurate, spectral angle), as well as some of the pink garland decoration that seems to have been partially concealed by damage. Furthermore, the presence of Egyptian blue was more effectively identified and mapped using its diagnostic luminescence spectral signature.

LIS endmember 4 maps the relative concentration and distribution of Egyptian blue throughout the tunic, with the darker regions aligning similarly to regions mapped by the 1st derivative endmember 24 and unmapped regions of the tunic in the 1st derivative map (Figure 4.9b). The application of the mineral jarosite and Egyptian blue in admixtures with white pigments to provide warm tones and shading in the tunic are extremely interesting. Egyptian blue is well known for its use in white pigment mixtures to provide a 'cold' tone to the white color [201, 28]. This has been identified in the tunics of other figurative paintings analyzed from Greco-Roman Egypt and ancient Cyprus (Appendix C) as well as in facial shading, eyes, and accessories, suggesting a knowledge transfer amongst ancient workshops and artists [162, 161, 77]. However, the use of jarosite to produce warm white hues has not been explicitly noted in the scientific analysis of ancient painting. It appears that this was in fact another technological artistic practice that ancient artists employed; in Chapter 6 it will be shown that another funerary portrait contains jarosite in the warm tones of a white

Table 4.3: Endmember results from LIS studies of portrait 32.4.

Endmember	**Spectral angle**	**Region**	**Material ID**	**Peak wavelength**
2	0.085	Earrings, eye	Madder lake	595 nm
3	0.125	Pink garland	Madder lake	605 nm
4	–	Tunic	Egyptian blue	890 nm

tunic. This choice by the artists is not surprising, as jarosite has a brilliant, bright yellow hue in its mineral form, compared to yellow ochre.

The binding medium used to apply the pigments in portrait 32.4 was identified from the FORS spectra to be wax-based. The wax is identified by absorptions in the SWIR at 2312 and 2352 nm due to CH combination bands of CH_2 asymmetric and symmetric stretches and bending (Figure 4.13a). Additional absorptions from CH_2 overtones at 1730 nm ($2\nu_a$), 1763 nm ($2\nu_s$), and 1210 nm (3ν) confirmed the presence of a lipid-based binding media [63]. The raking light image of the portrait (Figure 4.13b) shows a highly-textured surface due to the use of the wax. Painted areas such as the tunic show less relief (not shown), suggesting the use of a brush, while regions of her face and her hair show repeated, scratched in lines of high relief, indicating that a pointed tool like a cestrum was used. The use of a wax-based binding media mixed with the pigments and molded with a heated tool to create texture is known as the encaustic ('burnt in') technique, a practice well known in the ancient world and has been identified in studies of other funerary portraits [65, 26, 57].

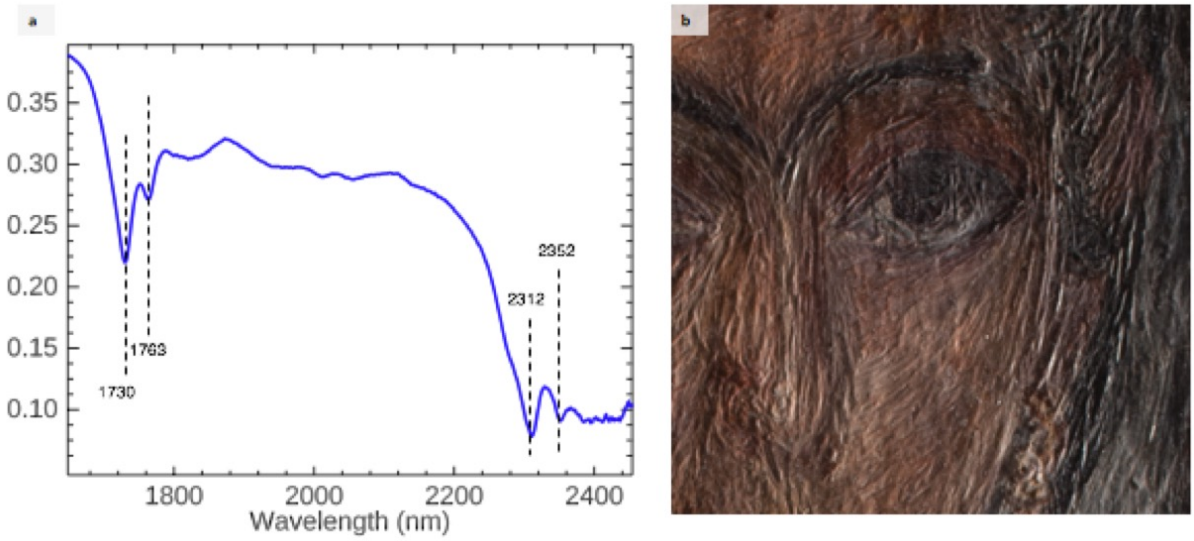

Figure 4.13: **(a)** The SWIR region of a reflectance measurement captured from the white tunic. CH_2 asymmetric/symmetric plus bending fundamental modes at 2312 and 2352 nm, as well as the 1st overtones of CH_2 asymmetric/symmetric stretching at 1730 and 1763 nm confirm the binding media as wax. **(b)** Raking light capture showing thin incised lines to texture the face and hair.

The combined analyses from RIS and LIS, supplemented with the FORS and XRF analyses, have allowed an in-depth analysis of the materials, production technology, and artistic choices by the ancient artist. The approaches used in the production of the portrait of this wealthy individual were reveaeled by analyzing the 1st derivative of the reflectance cube and the luminescence endmembers of important ancient synthetic pigments employed in the artist's palette. Additionally, the luminescence map of Egyptian blue is the first demonstrated application of LIS to detect and visualize its distribution in an ancient painting.

4.5.2 Tomb 3882 – Paphos, Cyprus

In Chapter 2, an introduction to the ancient sites of Cyprus was provided. In this chapter, analysis is focused on Tomb 3882 (Figure 4.14a), a Roman tomb (potentially originating in the Hellenistic period), excavated near the city center of modern day Paphos, Cyprus. It was uncovered by accident during a modern-day construction project, which resulted in the partial destruction of the tomb. A metal cage was built to cover and protect the now permanently exposed tomb. The painting of interest, located on the tympanum of the southeast arcosolium (Figure 4.14c) is an imitation marble revetment pattern within an incised lozenge design. The painting is degraded and also features surface discoloration. The HSI analyses were complemented by forensic photography, FORS, XRF, and photomicrography taken during previous analytical campaigns.

The UCLA IQ camera was used to collect RIS data of in situ wall paintings in Tomb 3882 (Figure 4.15a). A halogen lamp was used to illuminate the surface of the wall, and a light meter used to measure the lux levels ($<$ 2000 lux) and evaluate the light distribution. The camera exposure was optimized for the dynamic range of the camera sensor. For each collection the camera was calibrated using a diffuse white reflectance standard. A large Color-aid white paper (Figure 4.15b) was also placed on the surface of the painting to capture a white data cube, similar to the large white tablet collection used for flat-fielding the data of the mummy portrait. One reflectance data cube (100 ms integration time) was collected for this region of interest (Figure 4.14b). The final cube featured a spatial resolution of 3.4

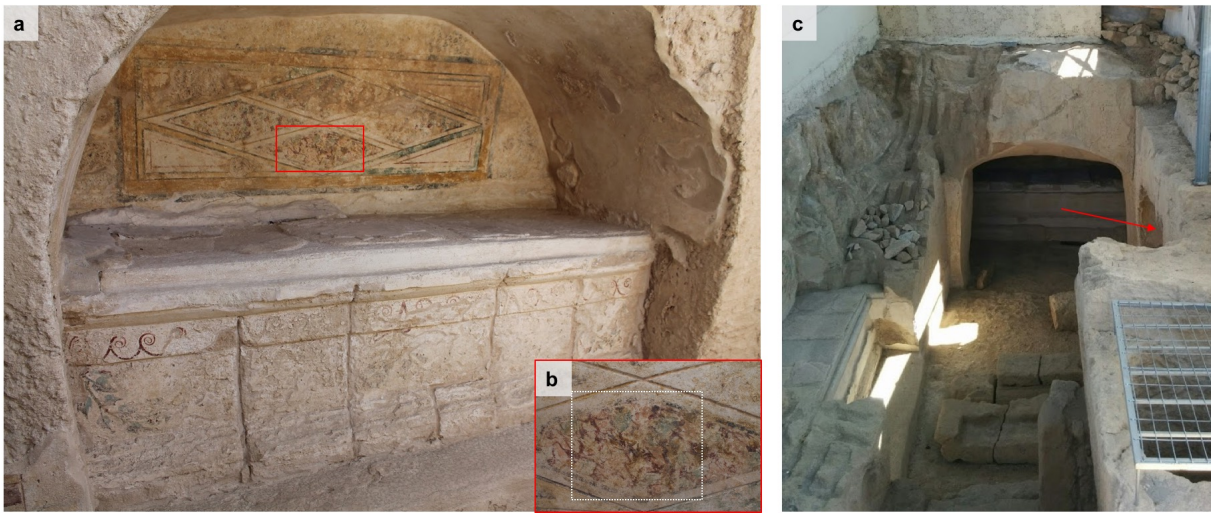

Figure 4.14: **(a)** The southeast arcosolium of Tomb 3882. The scene of interest is designated in the red box and the scan region is marked in white of the inset image **(b)**. **(c)** A pseudo-aerial view of the tomb shows the destruction of the tomb from modern-day construction. The northwest arcosolium was destroyed, leaving remnants of the tympanum intact. Most of the recoverable wall painting fragments were extracted and placed in storage. In the back is the thalamus chamber, which remained relatively intact. The arrow on the right indicates the location of the southeast arcosolium

mm/pixel.

One of the challenges of working in an open-air, high humidity environment was the presence of atmospheric effects in the spectral data from 900-1000 nm. While normally this could be overcome by bringing the camera closer to the target and increasing the illumination intensity, this would reduce the scene of interest and the increased incident light would saturate the sensor, not to mention pose a possible threat to the painting.

Previous analytical campaigns of the wall paintings at Tomb 3882 using forensic photography and FORS identified Egyptian blue as the only luminescent pigment present. Using the same FOV as the reflectance dataset, the IQ camera was filtered by a PECA 908 filter to capture NIR luminescence. Another challenge for the field collection was the requirement to work in the daytime, in order to have access to the tomb. A black sheet was draped across the arcosolium to create a darker environment with less light noise leakage into the camera (Figure 4.15d), although it was not possible to completely shield the painting from

all external light. A white LED panel was filtered with a transparent red gel sheet to excite the wall painting between 600-700 nm (Figure 4.15c). One luminescence cube was captured (300 ms integration time).

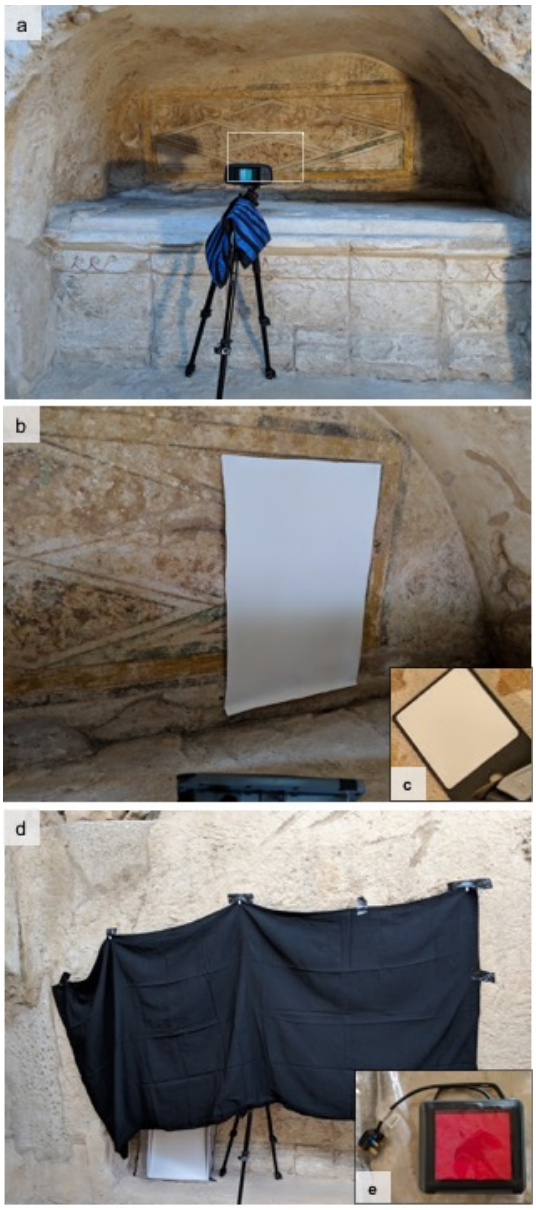

Figure 4.15: **(a)** The IQ camera in Tomb 3882, directed to the wall painting on the tympanum of the southeast arcosolium. A large white panel was not available for image calibration; instead, a large white Color-aid was used to fill the image scene **(b)**, supplemented by small reflectance standard from Specim **(c)**. **(d)** Unlike the controlled museum settings, Tomb 3882 required a shield to create a darker environment for luminescence imaging. A red light **(e)** was used for excitation of Egyptian blue.

Analyses of the RIS data on the lozenge imitation marble pattern (Figure 4.16a) revealed four main colorants: red ochre, yellow ochre, green earth, and Egyptian blue (Table 4.4). The 1st derivative endmembers (Figure 4.16d) mapped the dark red, dark yellow, light pink, and green-blue hues (Figure 4.16b). Endmember 2 represents yellow ochre by the first derivative peak at 550 nm and the equivalent characteristic yellow ochre profile in Figure 14d. Endmembers 3 and 4 both contain significant amounts of red ochre. The peak locations of endmember 3 and their relative intensities suggest the presence of a dark material mixed or overlaid onto the surface. RGB photographs of this region show thin layers of a black material over select areas of the red ochre application (Figure 4.17a). Endmember 4 corresponds to the light pink regions. The 1st derivative and reflectance spectra show characteristic features of red ochre, and supplementary FORS spectra reveal SWIR absorptions of calcium carbonate, indicating the artist mixed the two materials to produce the light hue. Endmember 5 mapped the blue-green regions in the marble pattern. The reflectance profile identifies the presence of green earth, the dominant mineral in this pigment. Based on the FORS studies of green earth pigments in Cypriot paintings discussed in Chapter 2, this was determined to be a celadonite-rich green earth.

Table 4.4: 1st derivative and luminescence endmembers for the painting from Tomb 3882

Endmember	**Cube**	**Spectral angle**	**Hue**	**Material(s) ID**
2	1st derivative	0.485	Yellow	Yellow ochre
3	1st derivative	0.64	Dark red	Red ochre, black
4	1st derivative	0.37	Pink	Red ochre, calcium carbonate
5	1st derivative	0.56	Blue-green	Green earth, Egyptian blue
L2	Luminescence	0.7	—	Egyptian blue

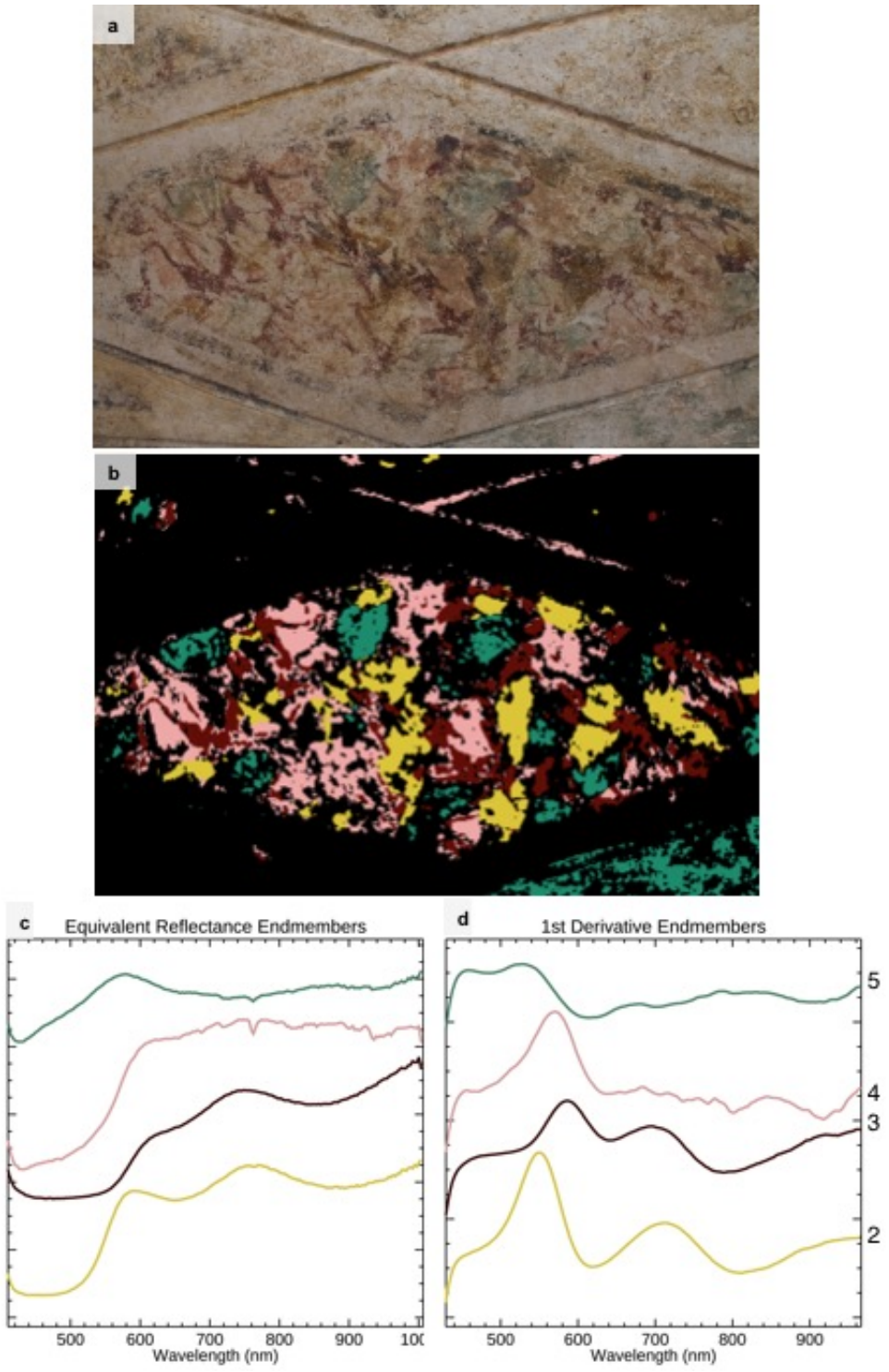

Figure 4.16: **(a)** RGB image of the imitation pattern in the lozenge diamond from Tomb 3882. **(b)** The 1st derivative spectral angle map produced from the 1st derivative endmembers **(d)**. The reflectance equivalent endmembers are in **(c)**.

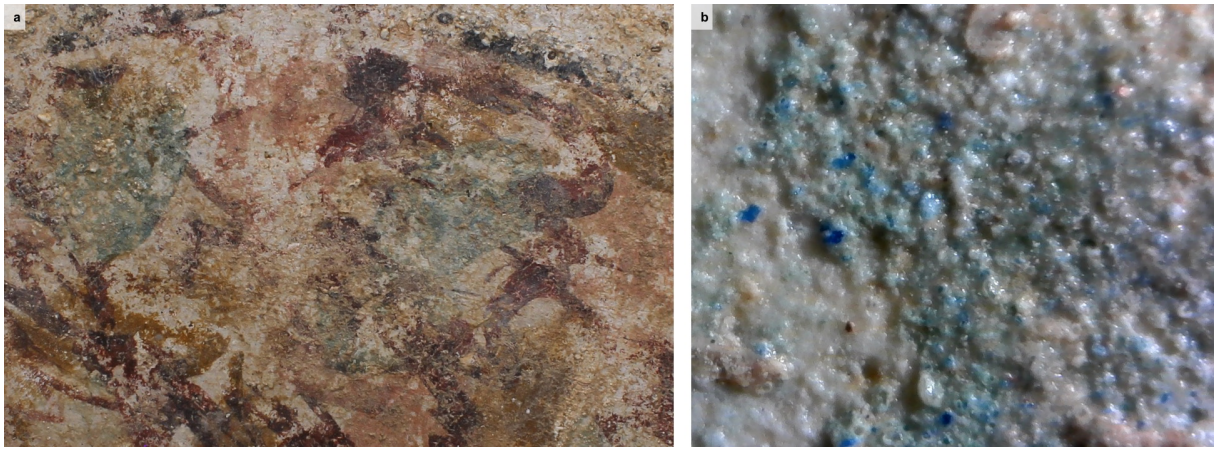

Figure 4.17: **(a)** RGB close-up of the imitation marble pattern. It clearly shows the layering process of the artist, including the black colorant that overlays onto regions of red ochre. The yellow and pink pigments were applied first, followed by the red ochre and black pigment. The blue-green pigment was the final application for the decorative features in this pattern. **(b)** Photomicrograph (250x) of the blue-green region, showing a mixture of green and blue particles.

Forensic photography and the LIS data, however, revealed an additional component to Endmember 5. Figure 4.18a is the map of a luminescence endmember (Figure 4.18c), at a tolerance of 0.0075) with a peak emission at 940 nm. This emission profile is attributed to Egyptian blue, the only luminescent pigment in the near infrared found in the ancient Mediterranean world. The feature at 954 nm in the data is a spectral artifact, either appearing as an upright or inverted spike. The maximum peak value noted here is significantly shifted from literature values reported for Egyptian blue at $\sim$ 910–950 nm [6, 159]. This may be due to the fact that the camera is not calibrated for luminescence. The LIS map, however, confirms the previous forensic photograph (Figure 4.18b) acquired of this painting using a modified DSLR and PECA 910 filter; the spectral data in the luminescence cube allowed a quantitative, and therefore more accurate, mapping. Looking back at the reflectance profile of Endmember 5, Egyptian blue cannot be reliably identified from the spectrum. Hence, the LIS approach provided a powerful method to find 'hidden' materials used in the painting's production. Photomicrographs (Figure 4.17b) also confirmed the mixture of green and blue particles to produce this pigment. Preliminary studies for the evaluation of LIS to identify

Egyptian blue in complex pigment mixtures and layers are in presented Appendix D.

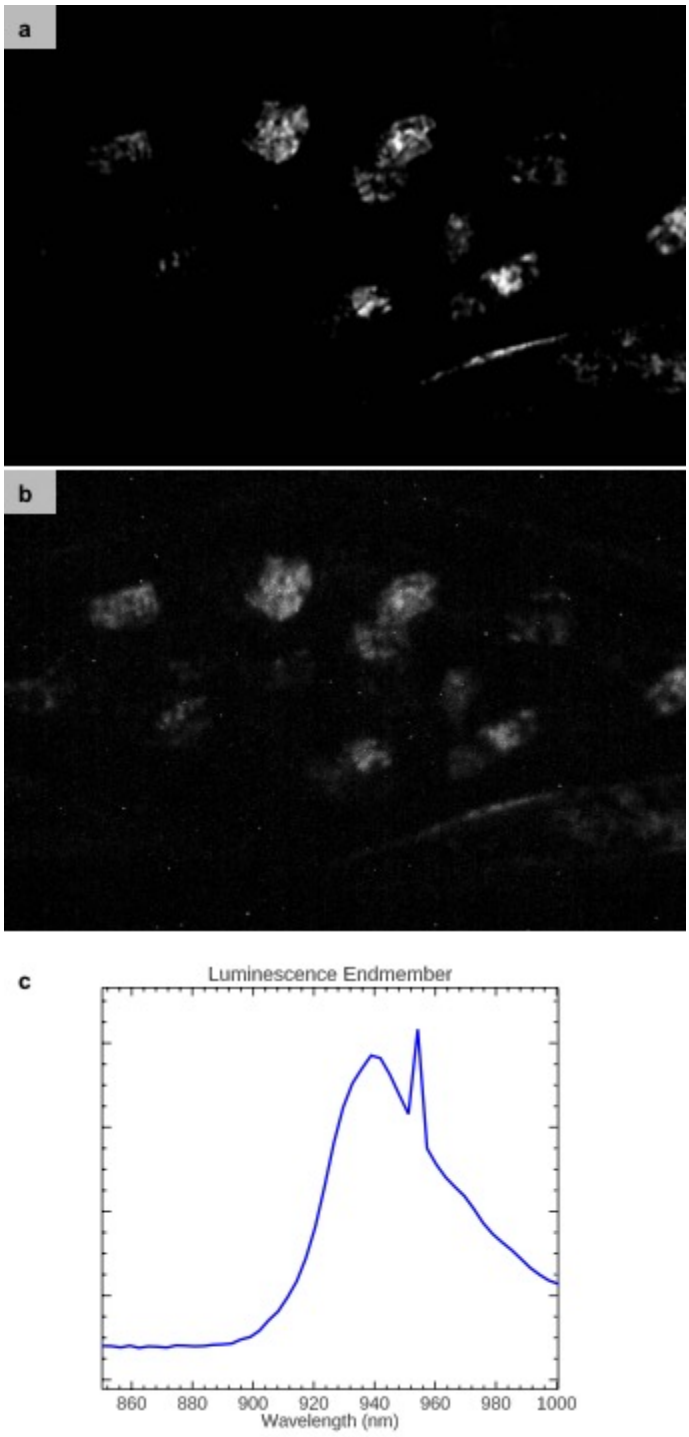

Figure 4.18: **(a)** The rule image for the luminescence endmember (**(c)**) corresponding to the application of Egyptian blue. **(b)** The visible-induced near-infrared forensic photograph of the same region.

The 1st derivative studies provided a powerful discrimination between the dark red and light pink hues, both containing red ochre mixed with different concentrations of light and dark pigments to change the tone. This not only produced a representative 2D chemical material map, it facilitated a re-visualization of the weathered and discolored painting. Additionally, it provided analyses to regions inaccessible by FORS, such as the incised lines above the lozenge decoration. Prior to the HSI analyses, it was not clear if and with what these incisions were painted. The 1st derivative and emission maps show that the light pink pigment was used for the upper right line, while the bottom right line most likely was painted with the blue-green pigment. The map provides a new interpretation on the original decoration by the ancient artist. The application of the highly portable IQ camera in reflectance and luminescence modes for scientific fieldwork studies provided material identification, insight into the production technology of the painting, and re-visualization of the degraded imagery.

CHAPTER 5

High Spectral Resolution Scanning Reflectance Spectroscopy (SRS)

5.1 Motivation

This chapter features the design of a new imaging spectroscopy system in response to the high cost of commercially-available imaging spectroscopy systems at a wide spectral range from the UV to the SWIR to support research on wall paintings found on site. Traditionally, field imaging has utilized analytical photography to document UV, visible, and near-infrared fluorescence and reflectance behavior of painting materials. The lack of spectral data from this imaging technique, however, affects the robustness of these results. The few examples applying imaging spectroscopy (IS) in the field, previously discussed in Chapter 4, have been limited between the ultraviolet (UV) and the near infrared (NIR) range. To reach the short-wave infrared (SWIR), an essential wavelength range for the characterization of organic and inorganic materials, in hyperspectral imaging spectroscopy (HSI), an additional imaging system is usually necessary. This increases significantly the cost. Furthermore, many existing HSI systems can be considered 'transportable' rather than portable as they are relatively heavy and/or large-scale, impacting transportation and setup. They also require reliable power sources, and are sensitive to environmental factors (dust, dirt, humidity, etc). Limited demonstration and accessibility of cost-effective, highly portable imaging spectroscopy systems in the field prevents this technique from becoming an integral component of analytical protocols in scientific fieldwork.

The system presented here was designed with the analysis of wall paintings as the objec-

tive, to be highly portable and produce spectra with high chemical specificity and mapping capabilities at a spectral range from the UV to the SWIR in a single instrument. The extended range from NIR to SWIR enabling the recording of overtones of fundamental vibrations in the mid IR and combination bands allows improved pigment identification, visualizations of underdrawings, identification of organic binding media, varnishes and restoration materials, as well as the presence of clays, minerals, and degradation products.

A commercial field-deployable spectroradiometer, increasingly applied for the analysis of material culture in scientific and conservation laboratories and was used for spot collection in fieldwork as discussed in Chapter 2, was adapted into a high-resolution (HR) scanning reflectance spectroscopy (SRS) system using an extremely low-cost scanner that facilitated acquisition of thousands of high resolution reflectance spectra that were subsequently built into 3D data cubes to perform materials identification and mapping.

5.2 Proof of concept study

The custom designed system integrating a UV-SWIR spectrometer and an $x-y$ scanner was conceptually designed in collaboration with the National Gallery of Art (NGA), Washington DC, inspired by their study of Georges Seurat's painting *Haymakers at Montfermeil* using stand-off molecular spectroscopic imaging [56]. That painting, placed on a motorized easel, was raster-scanned by a fiber-optic (FO) cable of an ASD FieldSpec 3, decoupled from its accessory leaf probe and mounted to an optical table, and pixel-by-pixel reflectance measurements over the surface of the painting were collected. Using trigger data from the easel system which contained position information of the painting per spot collection, the data were reconstructed into 3D hyperspectral data cubes using ENVI.

As in situ wall paintings are 'fixtures' of the architecture where they are found, the concept for the design of this hyphenated instrument was to adopt a scanning system that can support the FO probe to enable raster-scanning the surface of the painting. This concept was tested at the NGA using an ASD FieldSpec 4 with a 3 mm diameter bifurcated FO

(containing both the excitation source and optical collection fibers), mounted to the optical table. A test painting was raster-scanned across the surface of the probe using the motorized easel system, but triggering was disabled for this configuration (Figure 5.1). This meant the FieldSpec 4 was collecting spectra independently of the easel control and there was no positional information encoded into the data, making construction of 3D data cubes non-trivial.

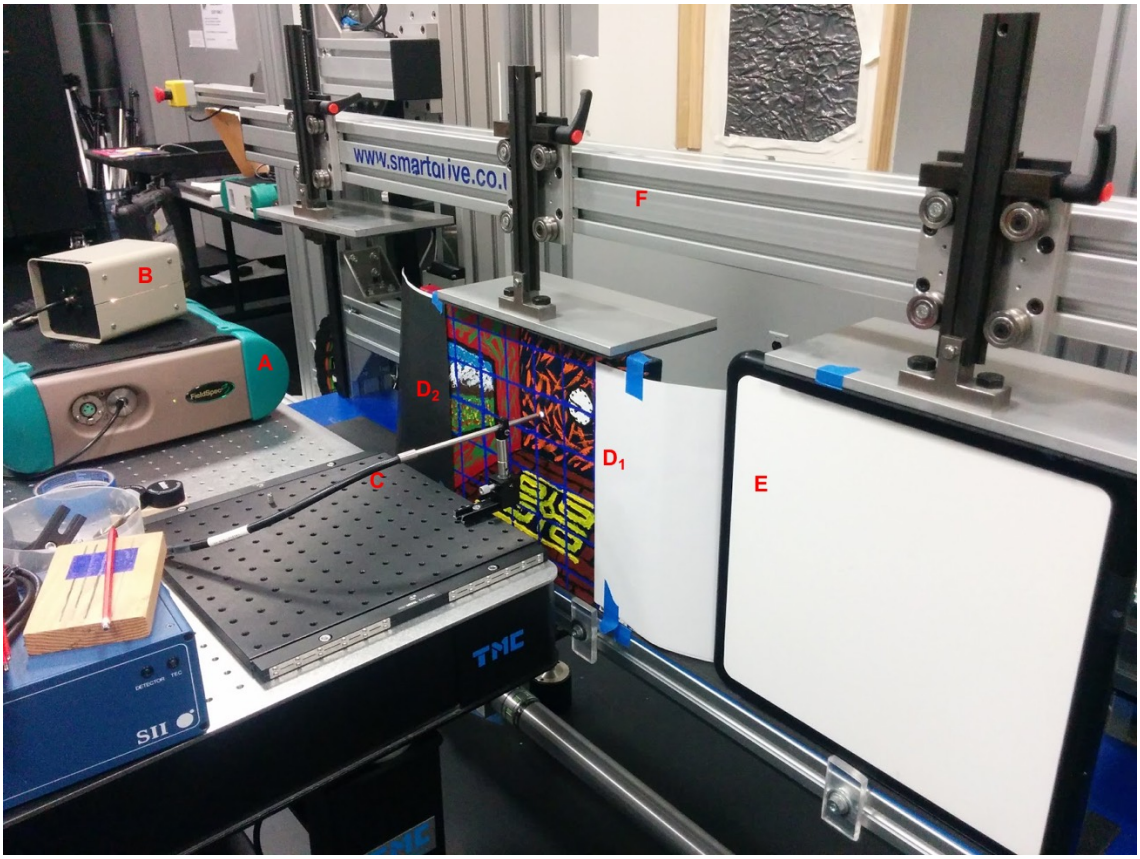

Figure 5.1: Experimental configuration for proof of concept study at National Gallery of Art, Washington D.C.: **(A)** The FieldSpec 4 spectroradiometer; **(B)** External lamp source; **(C)** bifurcated optical probe; **(D)** White (1) and black (2) paper marking end of line scans; **(E)** white tablet for optimization and calibration of the FieldSpec 4.

A method to define the end of a line scan had to be introduced into the data so that the spectra could be assembled into their exact spatial positions. To achieve this, white and black printed paper strips were placed at the edges of a target painting (Figure 5.1 - D_1 and D_2) to serve as spectral identifiers in the dataset. The 3D data cube was subsequently

built in Matlab (MathWorks) and exported to ENVI (image analysis software from L3Harris Geospatial). The reconstruction of the target painting (Figure 5.2b) yielded promising results. An RGB reconstruction of the painting was reproduced with relatively accurate spatial positioning, although it became apparent that there are small horizontal offsets. This was caused by the imprecise widths and alignment of the black and white markers bordering the scene, whose reflectance spectra marked the beginning and end of each scan line in the dataset. However, refining these markers and correcting their alignment would improve relative spatial positioning of the spectra.

Figure 5.2: **(a)** RGB image of test panel painting; **(b)** reconstructed RGB image from data cube of test panel painting.

Post-processing of the cubes can also be applied to improve the spatial resolution of the images. Despite the low spatial resolution conditioned by the hardware, the high spectral resolution data provides robust materials characterization in a wide spectral range including the VNIR and SWIR region (Figure 5.3). The results from this study provided a strong argument for developing and optimizing a field-deployable reflectance spectroscopy scanning system for in situ wall paintings studies.

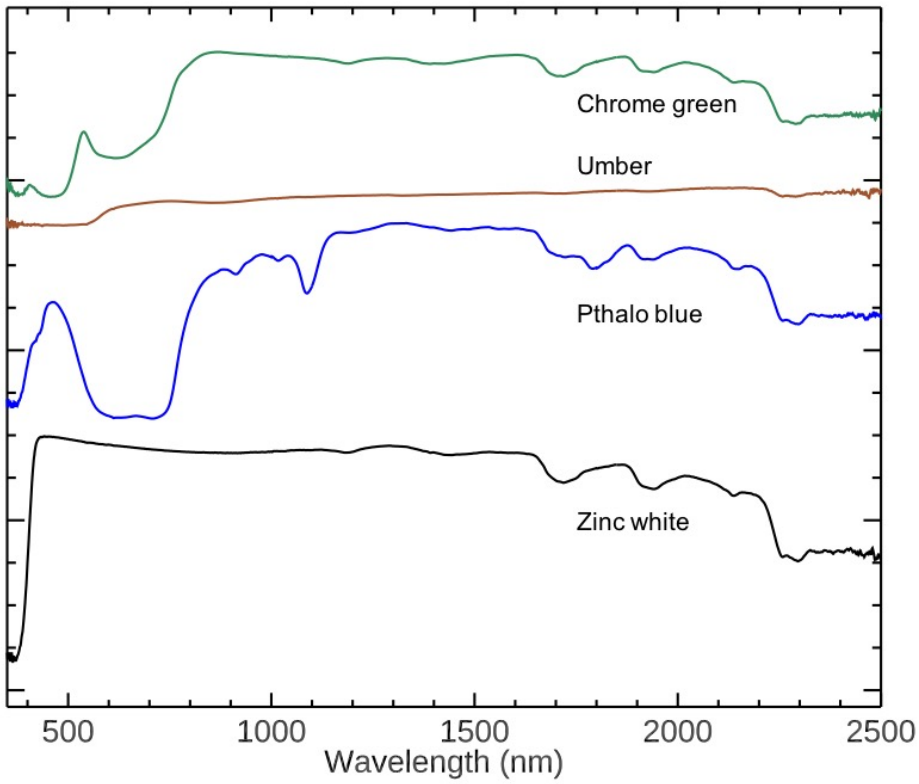

Figure 5.3: Examples of spectra extracted from the 3D data cube of the target painting. The spectra feature diagnostic electronic processes and vibrational absorptions from the UV to the SWIR, which aid in the identification of the constituent materials.

5.3 SRS system development

Driven by analytical limitations for the analysis of in situ wall paintings, a scanning system was developed that could move the excitation source and the acquisition/detection probe across the surface of the immovable paintings. The scanner's orientation had to be adjustable for vertical and horizontal applications, as well as for uneven surfaces of a certain topography. The scanner needed to be light weight such that it could be operated over a surface of a painting in a horizontal configuration (i.e. detached fragments of wall paintings on artificial supports or laying over a sand box), while at the same time, it needed to be robust and stable to support the weight of the system and for operation in challenging spaces, such as

in tombs, on scaffoldings, and in storage rooms.

Following the proof of concept study at the NGA the ASD FieldSpec 3 spectroradiometer was incorporated into the design of the SRS system. This presents two powerful advantages: (1) the instrument is highly portable and field-deployable; (2) the analytical range spans the UV to SWIR, thus providing access to materials with diagnostic signatures beyond the visible to NIR (VNIR), such as organics and clays, and eliminating the need for separate instruments.

To perform the raster scan over the surface of a painting, the fiber-optic (FO) cable of the FieldSpec 3, normally inserted into the accessory leaf probe for spot collection, was left decoupled and mounted onto the scanning arm of a modified motorized $x - y$ drawing instrument, the Axidraw V3 from Evil Mad Scientist, Inc. (Figure 5.4). The Axidraw V3 is a light-weight, structurally robust pen-plotter, with a range of motion matching the dimensions of a US letter size paper. The scanning arm responsible for the pen operation runs along an aluminum extrusion with wheels, driven by a universal-input power supply. During data collection, the system was instructed to 'draw' a raster scan pattern, now holding an excitation source and the FO instead of a pen. To accomplish this the Axidraw V3 was customized to have the motorized z-stage of the pen holder and associated electrical cables removed and replaced with a fixed mounting plate to accommodate the FO probe. This reduced the weight and size of the scanner, allowing it to be positioned closer to the surface of a painting.

Due to the fact that the leaf probe of the FieldSpec 3 containing the halogen lamp was too heavy to mount onto the Axidraw V3's scanning arm, an alternative lightweight light illumination source (such as the battery-powered incandescent mini Maglite) emitting radiation from the UV to SWIR was attached to the scanning arm. To record diffuse reflectance spectra, the FO and excitation source were mounted together using a proprietary mount, enabling the FO to be kept perpendicular to the surface and the light source projected on the surface at an angle of $\sim 45^\circ$ with respect to the FO. This was achieved by keeping the Maglite parallel to the FO and using a 1-1/4" mirror to direct the light to the surface. The

Figure 5.4: The Axidraw V3, a pen-plotting instrument customized for novel $x-y$ scanning operation to drive the FO cable over the surfaces of paintings.

mount was designed in SketchUp (Figure 5.5a), a free online 3D modeling software and 3D printed at the Digital Archaeology Lab at the Cotsen Institute of Archaeology (UCLA). Preliminary tests of the mount demonstrated that the walls needed to be thicker to support the clamping of the mirror's wand. The final model utilized a black 3 mm nGen filament by colorFabb. After printing, through holes were tapped in the UCLA machine shop to allow it to be fastened onto the Axidraw V3 mount (Figure 5.5b-c).

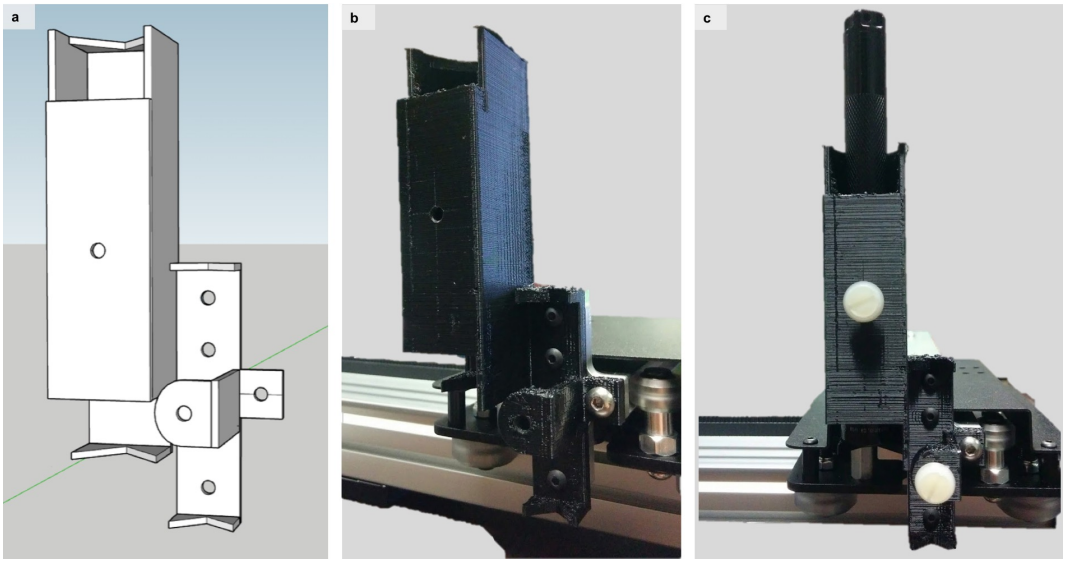

Figure 5.5: **(a)** The FO mount designed in SketchUp; **(b)** the 3D printed mount assembled onto the Axidraw V3 scanning arm; **(c)** the excitation source in the mount box, with plastic stabilizing screws for the light and FO cable in place.

The SRS system was mounted onto a Manfrotto tripod (MK190XPRO3) with a rotational ball head. An advantage of this tripod is the adjustable center column, which can be oriented vertically or horizontally; this feature, coupled with the ball head, allowed the SRS system to be mounted in vertical and horizontal scanning configurations and better match sloping surfaces of the paintings. A customized mounting tripod plate was made by Evil Mad Scientist, Inc. to attach the scanner to the quick release mounting plate on the ball head. To improve the stability of the tripod, sandbags were placed around the tripod legs and on the central column when in the horizontal configuration to counter balance the weight of the system (scanner and FO mount, $\sim$ 2.5 kg).

A close-up of the final configuration of the SRS system mounted on the tripod can be seen in Figure 5.6. Owing to the versatility of the SRS system design, it was successfully operated in various sites, including churches, museums, a tomb, and field storage rooms (Figure 5.7).

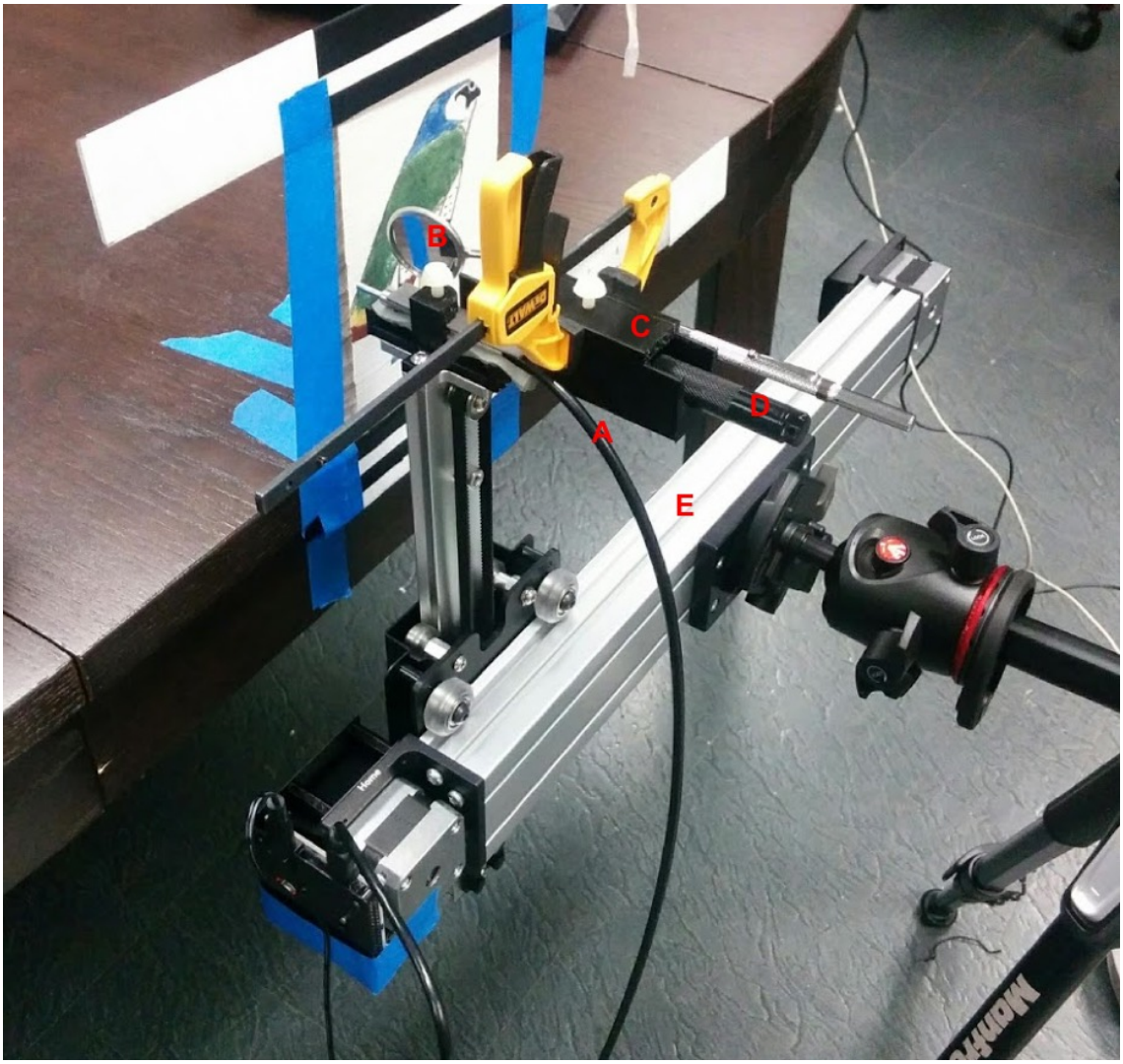

Figure 5.6: The complete assembly of the scanning system: **(A)** FO cable of the FieldSpec 3; **(B)** mirror, clamped to mount **(C)**; **(D)** excitation source; **(E)** scanner.

Figure 5.7: Various applications of the SRS system: **(a)** figurative painting from Tomb 3510, Paphos Archaeological Museum (PM); **(b)** figurative painting E6 from House of Aion, PM; **(c)** feet of Christ (on the cross), the Enkleistra of St. Neophytos; **(d)** wall painting in the thalamos chamber of Tomb 3882; **(e)** Painting of the Virgin Mary, the church of St. Paraskevi; **(f)** figurative painting E9 from the House of Aion, Cyprus Museum; **(g)** facial fragments from the Tomb in Costis Palamas Square, PM storeroom.

5.4 Data Collection

During data acquisition, the two components of the SRS system, the scanner and the spectro-radiometer, operate independently though in synchronization. The FieldSpec 3 is managed by the partner RS3 software from Malvern Panalytical, while the Axidraw scanner is driven, via USB, by the freely accessible vector graphic software Inkscape to 'draw' the raster pattern.

To build the raster pattern in Inkscape, the scan scene must be measured. Unlike commercial HSI systems where the system's lens and image sensor size sets up the fixed relationship between the field of view and the working distance, the SRS system's field of view is restricted to the scan range of the Axidraw V3. The scan scene includes two end-of-line black and white markers (Figure 5.8). The white markers are made of Tyvek tape, which features a high reflectance continuum, to mark the edges of the scan region. The black markers are made with electrical tape for strong absorption of the incoming light. The black and white reflectance signatures are used in the post-processing stage to confidently identify the beginning and end of the line scan, which determines the set of spectra per line in the constructed 3D data cube. Care was taken to ensure that the distance between the markers were uniform throughout the scan scene to minimize the horizontal offset in the reconstruction.

Figure 5.8: The boundary markers denoting the scan scene on a wall painting in the thalamos chamber of Tomb 3882.

The 'box' marked out by the position of the two markers is measured and the raster scan vector graphic, matching the dimensions of the 'box' measurement, is then built in Inkscape. Several factors are taken into consideration to determine the step size and scan speed of the raster pattern, including the total time of the scan, the proximity of the probe to the target surface, and the overhead time for spectral collection. Equation 1 is used to calculate the spot size (Y) of the 1 mm diameter FO probe of the FieldSpec 3.

$$Y = D + 2\,l\ \tan\frac{A}{2} \tag{5.1}$$

$D = Effective\ diameter\ of\ FO\ (1\,mm)$

$A = FO\ angular\ field\ of\ view\ (25°)$

$l = Distance\ from\ FO\ to\ target\ painting$

$Y = Spot\ size$

Working distance of 6 to 7 mm was established as optimal for safe operation of the SRS system over the painting, taking into account the slight unevenness in a painting's surface; at $\sim$ 7 mm, a spot size of 4 mm is measured. At this distance, it was determined that four spectral averages at an integration time of 136 ms was sufficient for high SNR.

The Axidraw V3 freely scans at a specified speed; Inkscape utilizes an extension developed by Evil Mad Scientist, Inc. to control the scanner's operating parameters. The scan speed for the raster was determined by the spot size, as the objective was to effectively collect one spectrum per 'step'.

$$Y = v\ t \tag{5.2}$$

$Y = spot\ size$

$v = scan\ speed$

$t = time\ for\ single\ spectrum\ collection$

The individual spectrum collection time was estimated from a test collection of 100 spectra after optimizing and calibrating the FieldSpec 3 with the desired experimental settings. Obtaining four average measurements per spectrum at 136 ms integration time, the collection of 100 spectra took 207 seconds, yielding 2.07 seconds per spectrum, t. This meant a scanning speed, ν, of 1.93 mm/s was necessary. Inkscape's Axidraw extension requires integer values for the speed input, thus 2 mm/s was selected. Returning to Equation 5.2, this would yield a 'step' of 4.14 mm. This value determined the step size (i.e. the spacing between the line scans) in the raster pattern (Figure 5.9).

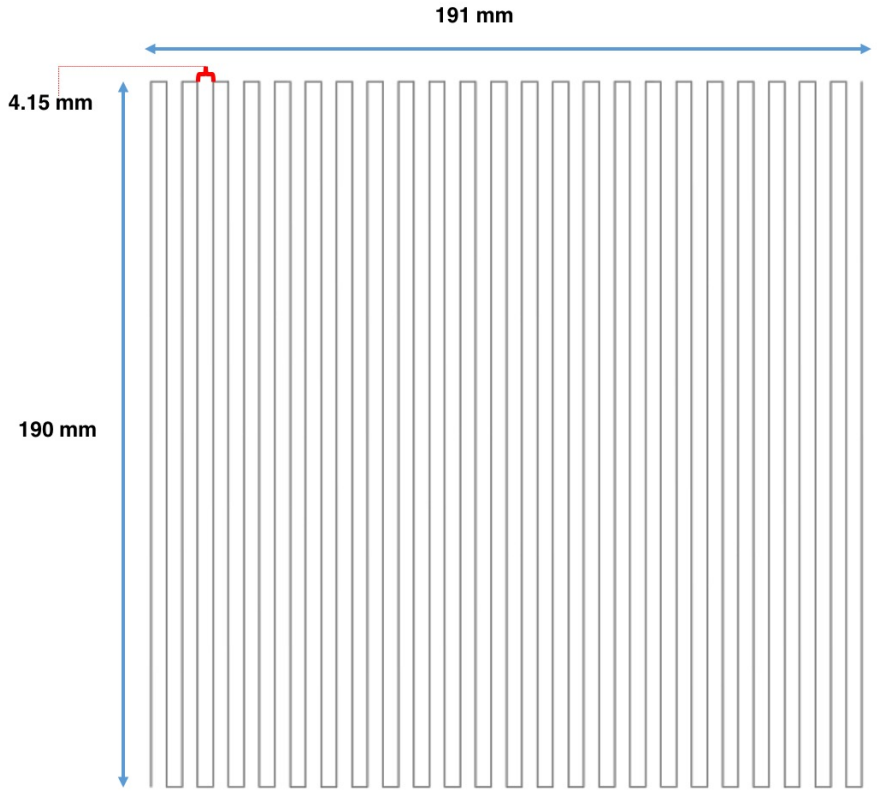

Figure 5.9: An example of a raster scan vector graphic drawn in Inkscape to guide the Axidraw V3. This specific graphic was used to drive the raster scan of the imitation marble pattern in Tomb 3882.

After the design of the raster pattern, a simulation of the scan was run in Inkscape. The software outputs the distance 'traveled' and the time estimate for the scan. With the individual spectrum collection time, t, this information was used to calculate the number of spectra to be collected by the FieldSpec 3 for the scan duration.

$$N = \frac{T}{t} \tag{5.3}$$

$T = Time\ duration\ of\ scan$

$N = Number\ of\ spectra\ collected$

The collection time for scans that utilized the maximum range of motion of the Axidraw took $\sim$ 1.5 hours at these experimental settings. Though a slower scan speed is desirable, this would have increased the scan time dramatically, which was not feasible due to time restrictions for site and object access, as well as the battery lifetime of the excitation source.

5.5 3D cube construction

Once the spectra were collected, the dataset was imported into the ENVI software (LS3 Harris Geospatial) to define the black and white boundary markers from their reflectance signatures. The boundaries for each line scan were input into an Excel file. The spectra were then exported into a text file and called into Matlab, where they were input into a 3D matrix; each line of the matrix was filled with the appropriate set of spectra according to the boundary values listed in the excel file. The matrix was then exported as an ENVI-readable 3D data cube (Figure 5.10).

Figure 5.10: **(a)** An RGB image of the face of a figurative painting recovered from Tomb 3510. **(b)** The 3D matrix constructed in Matlab from the individual spectra collected in the scan. **(c)** The extracted image from the final reconstructed 3D data cube in ENVI.

5.6 System parameters and noise evaluation

The SRS system specifications, based on the FieldSpec 3 technical performance and the operating conditions for data collection, are summarized in Table 5.1. These parameters are listed for comparison next to those of the commercial Specim IQ HSI camera. The noise was evaluated by collecting spectral radiance and reflectance measurements from a white reflectance standard using the bare FO cable under similar operating conditions (FO distance to surface, integration time, illumination) as the SRS system. Using Equation 4.1, the SNR was calculated across the UV to SWIR range in 50 nm intervals (Figure 5.11), showing highest performance in the VNIR range, specifically from 500–900 nm (>7000:1), with strong performance in the SWIR from 1100–1800 nm ($\sim$ 2000–5000:1). Table 5.1 reports the average SNR across the VNIR.

Table 5.1: Specim IQ and SRS system technical specifications

	Specim IQ	**SRS**
Spectral Range	400 – 1000 nm	350 – 2500 nm
Spectral Sampling	3 nm	1.4 nm (VNIR) – 2 nm (SWIR)
Spectral Response	7 nm	3 nm (VNIR) – 10 nm (SWIR)
SNR	180:1 (500-900 nm)	2800:1 (500-900 nm)
Spatial Sampling	1 mm/pixel at 1 m	4 mm/pixel
Collection time	∼1–5 minutes	∼1.5 hours
Scan region	>Min 2.7 x 2.7 inches	8.5 by 11.5 inches

In comparison to the Specim IQ camera, whose peak SNR performance (400:1) occurred at $\sim$ 625 nm (Table 4.1), the SRS system is the more powerful instrument for spectral analysis and characterization. Table 5.2 compares the average SNR performance of the SRS and IQ system; it also shows the average SNR over different analytical ranges of interest, including the UV, VNIR, and different portions of the SWIR.

The noise-equivalent spectral radiance (NESR) was also calculated, using the spectral

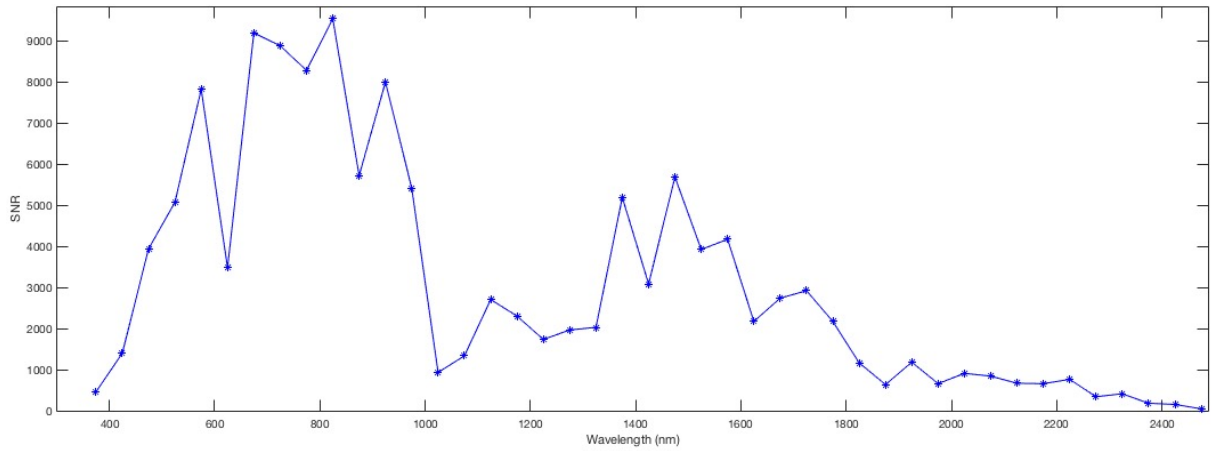

Figure 5.11: SNR calculated at 50 nm intervals to show system performance across the VNIR and SWIR ranges. The highest system performance for SNR is from $\sim$ 500–950 nm

Table 5.2: Average SNR for SRS and IQ systems

	Wavelength range (nm)	**Average SNR**
SRS system	350–400	470:1
	500–900	2800:1
	1420–1620	3800:1
	2000–2400	370:1
Specim IQ	500–900	180:1

radiance curve and the reflectance measurement from the white target. The NESR is a sensitivity parameter that is used to assess a sensor's capability to detect small variations in reflectance [85]. It is a measure of the amount of change in the spectral radiance needed in a measurement for the signal to match the noise level (i.e. to achieve an SNR of 1). Equation 5.4 was used to calculate the NESR per wavelength:

$$NESR(\lambda) = \frac{N_s(\lambda)}{SNR_R(\lambda)} \tag{5.4}$$

$N_s = Spectral\ radiance\ from\ target$
$SNR_R = SNR\ of\ the\ reflectance\ profile\ from\ white\ target$

$SNR_R(\lambda)$ was calculated as $\frac{\bar{R}}{\Delta R}$, where $\bar{R}$ and ΔR is the average and differential reflectance, respectively, at incremental wavelengths. R, in theory, should be a uniform (flat) reflectance profile. Thus, variations in the experimental reflectance values across the spectrum provide an indirect measure of the standard deviation as a function of wavelength. The NESR from 350–1700 nm is on the order of 10^{-6} ($\frac{W}{cm^2 \cdot nm \cdot sr}$) (Figure 5.12), while further into the SWIR it is more variable but on the order of 10^{-5}. The FieldSpec 3 reports an order of magnitude of 10^{-9}, also slightly increasing further into the SWIR. It should be noted that 1000 nm and 1800 nm marks the change in detector in the FieldSpec 3 for recording measurements at these wavelengths (Chapter 2.4.1), thus the rise in NESR is expected.

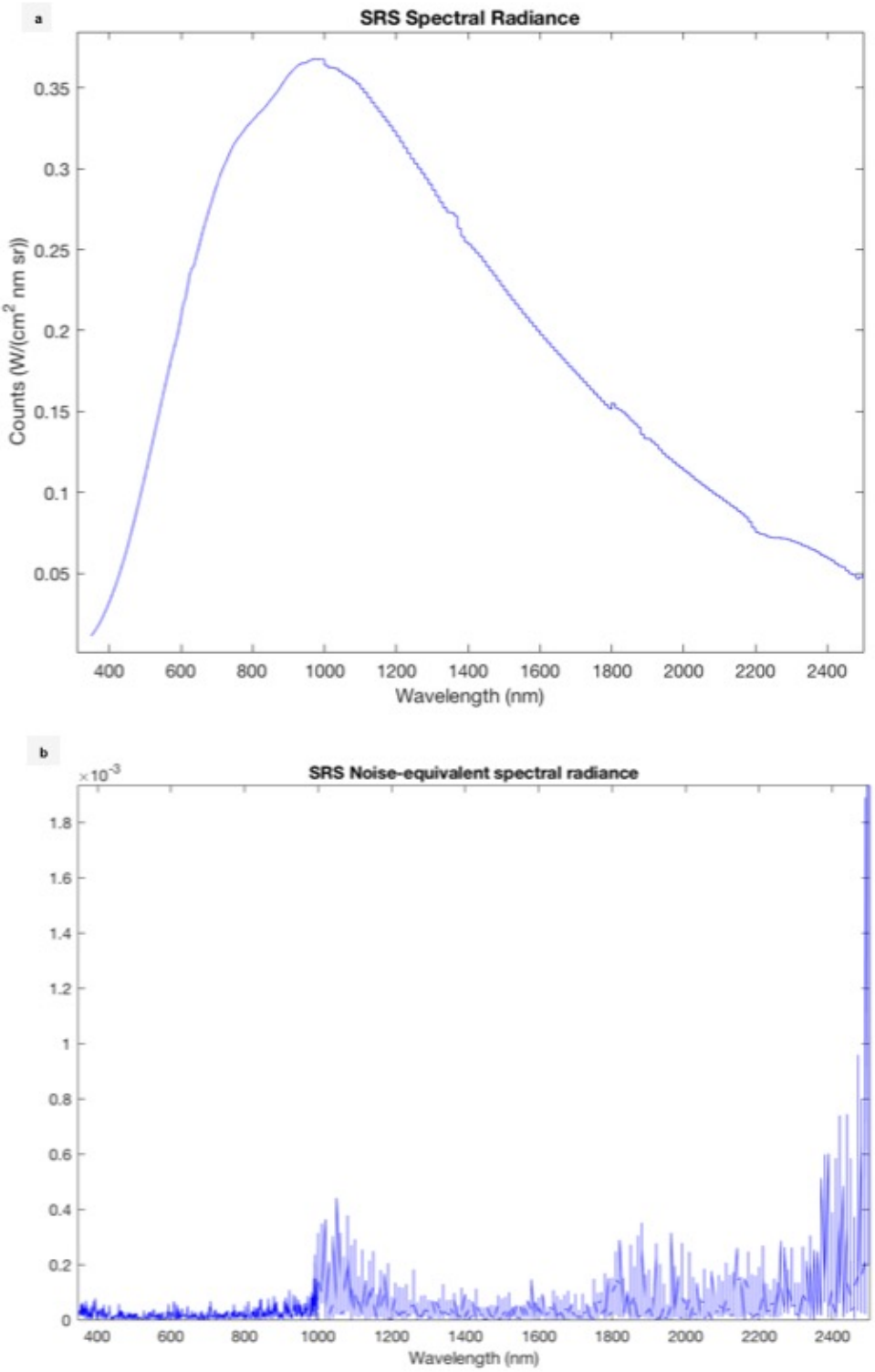

Figure 5.12: **(a)** Spectral radiance for an SRS pixel collection. **(b)** The noise-equivalent spectral radiance.

5.7 Data analysis and results

To demonstrate the performance of the SRS system, the imitation marble pattern from Tomb 3882 will be revisited. The same image scene analyzed by the Specim IQ camera in Chapter 4 was scanned using the SRS system (Figure 5.13). These datasets collected by the two systems will also be used to compare system performances.

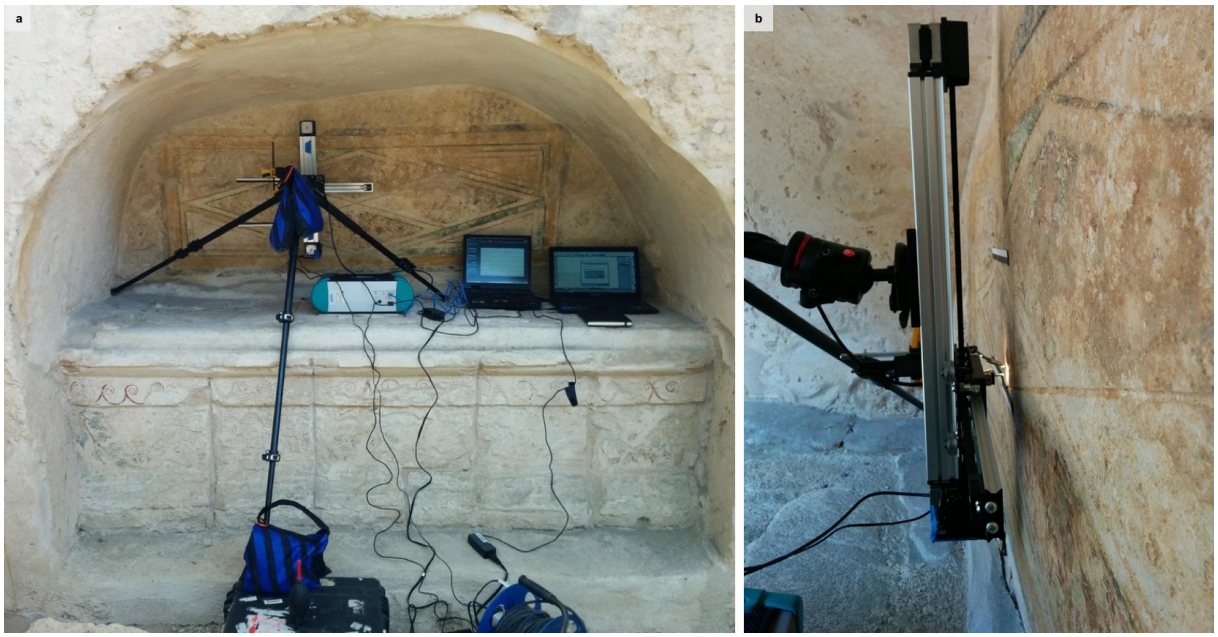

Figure 5.13: **(a)** The southeast arcosolium in Tomb 3882 with the experimental set-up of the SRS system. **(b)** Side view of the SRS system scan in progress.

A similar analytical protocol used for the HSI datasets described in Chapter 4 was also applied to SRS datasets. The Spectral Hourglass Wizard (SHW) and the Sequential Maximum Angle Convex Cone (SMACC) tools in ENVI were both used to extract endmembers from the data spectral cubes, while the Spectral Angle Mapper (SAM) was applied to produce maps of the endmembers. Because the cubes' spectral data range from 350 nm to 2500 nm, regions of the cube were 'cropped' to perform analyses in specific wavelength regions to target different types of materials. For pigment analysis, the cubes were subset from 400 nm to 1000 nm. To improve separation of endmembers with subtle shifts of inflection points in the visible and major absorptions in the NIR range, the 1st derivative of the VNIR spectral

cube was also calculated.

The analysis of spectral signatures from the imitation marble pattern in Tomb 3882 illustrates an example of this application, where four unique 1st derivative endmembers were selected in the extraction process (Figure 5.14a). These suggested the use of hematite-rich red ochre, yellow ochre (goethite), green earth, Egyptian blue, and calcium carbonate. The red and yellow pigments represent relatively pure applications of red and yellow ochre, respectively, while the pink pigment, indicated by a relatively high reflectance in the VNIR compared to the other pigments and diluted absorption features, was produced by combining red ochre and a white pigment, most likely calcium carbonate because this material has been identified as the white pigment in other ancient Cypriot wall paintings [106, 16] and was used in the preparatory layers of the paintings (Chapter 2.5.2.5). The blue-green pigment was an admixture of Egyptian blue in a matrix of green earth. Using forensic photography, the green pigment was shown to also contain Egyptian blue, which accounts for the $\sim$ 630 nm absorption in endmember 3. The SRS system's performance in the VNIR and SWIR, compared to the standard application of the leaf probe of the FieldSpec 3 (Figure 5.14c-d) show that the reflectance responses are essentially the same, not taking into account overall intensity between the two spectra. The sharp changes in the spectral profiles at 1000 and 1800 nm correspond to switching of detectors in the FieldSpec 3 system during the measurement (See section 2.4.1).

The distribution of each endmember, based on the spectral angle values recorded in Table 5.3, were mapped in Figures 5.15c-f. The visible pixels in the rule images represent the 1st derivative spectral profiles, calculated from the reflectance data cube, that match the 1st derivative endmember within the established tolerance (or spectral angle), and therefore the distribution of each unique pigment identified in the scanned painting. The spectral angle map (Figure 5.15b) essentially integrates this set of rule images into a composite to produce a chemical map of the ancient decoration. The high sensitivity of this instrument also maps to regions of the painting that appear to have pigment loss, providing a reconstructed visualization of the imitation marble pattern.

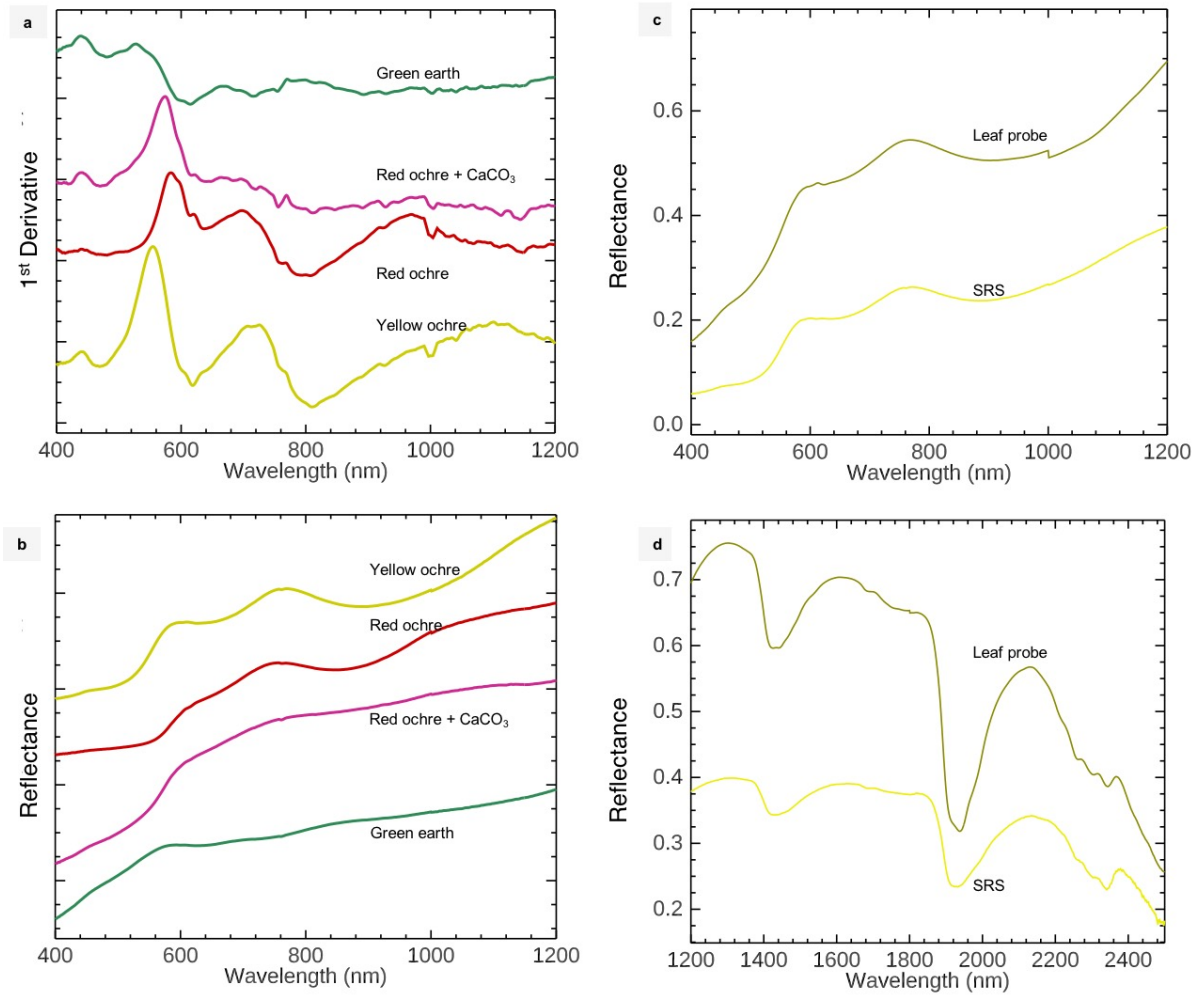

Figure 5.14: **(a)** The 1st derivative endmembers extracted from the SRS 3D data cube. **(b)** The corresponding reflectance spectra of the endmembers. Reflectance spectra in the VNIR **(c)** and SWIR **(d)** of a yellow ochre pigment on the wall painting, collected with the FieldSpec 3 leaf probe and the SRS system.

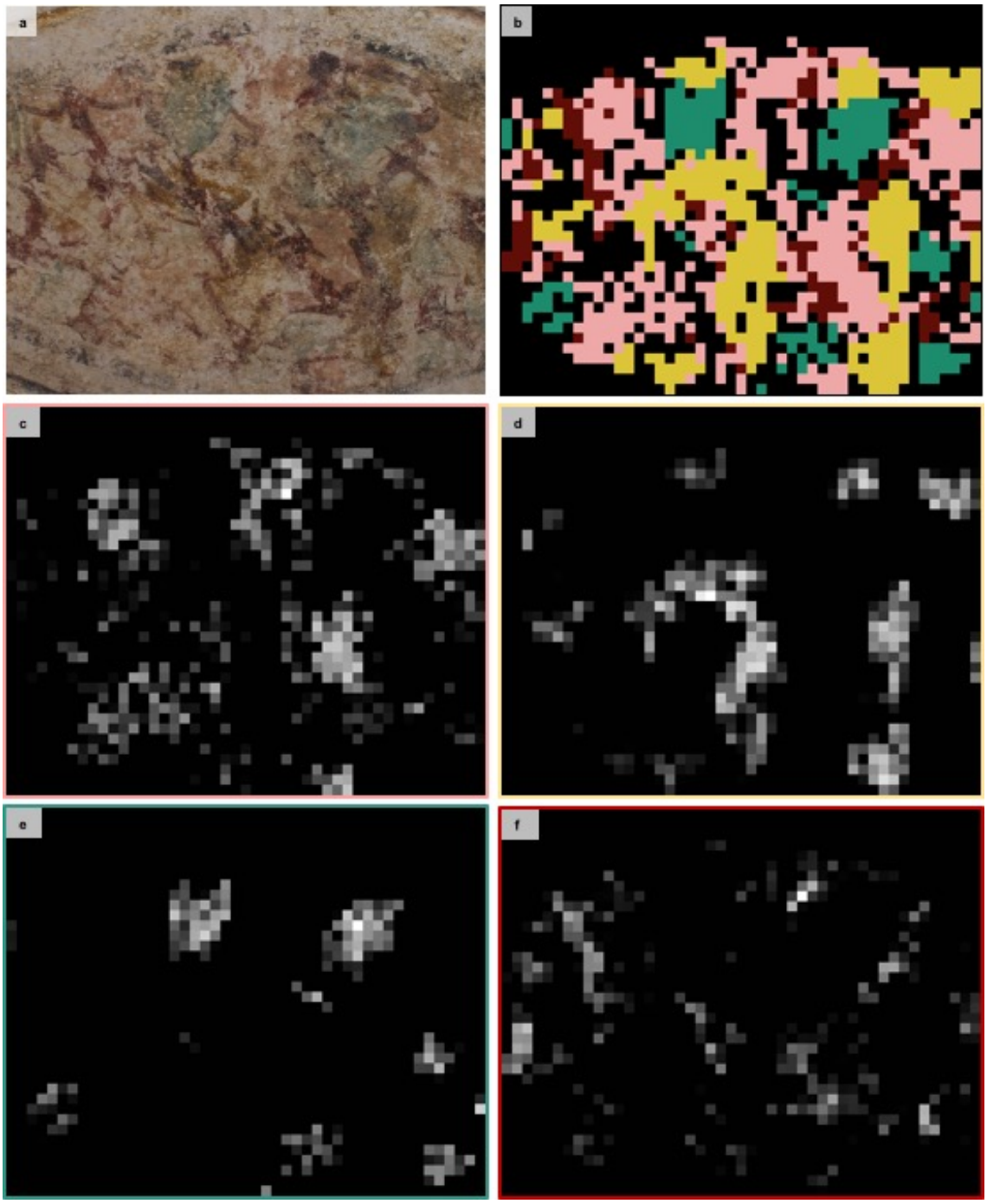

Figure 5.15: **(a)** An RGB image of the scanned scene from Tomb 3882. **(b)** The SAM map showing the distribution of the four endmembers. **(c)** The rule image of endmember 1 (red ochre with calcium carbonate). **(d)** The rule image of endmember 2 (yellow ochre). **(e)** The rule image of endmember 3 (green earth with Egyptian blue). **(f)** The rule image of endmember 4 (red ochre).

Table 5.3: 1st derivative endmembers, their spectral angle tolerances, and the materials identification.

Endmember	**Spectral Angle**	**Hue**	**Material(s) ID**
1	0.21	Pink	Hematite-rich red ochre, calcium carbonate
2	0.57	Yellow	Goethite-rich yellow ochre
3	0.33	Blue-green	Green earth, Egyptian blue
4	0.56	Dark red	Hematite-rich red ochre

To compare the spectral, spatial, and mapping results of the SRS system and the Specim IQ camera, two endmembers from each dataset, representing the blue-green and pink pigments, were selected and compared side by side (Figure 5.16). The IQ and SRS rule images for the blue-green pigment (Figures 5.16c,e, respectively) map in the same regions. The reflectance signatures from each system were compared to the reference spectra of Egyptian blue and green earth (Figure 5.16b). While the spatial resolution of the IQ camera is much higher than that of the SRS system, the noise/signal is higher in the IQ spectral data, making subtle absorptions difficult to discern. The noise level disparity is also present in the pink endmembers (Figures 5.17d,f), which also produced comparable rule images (Figures 5.17c,e). While the spatial mapping is more reliable based on a statistical analysis of the shape of the spectral profile, the material characterization based off the reflectance spectra is more challenging. The mapping between the IQ and SRS datasets are again comparable for the pink endmembers, while the material identification was more robust in the SRS dataset.

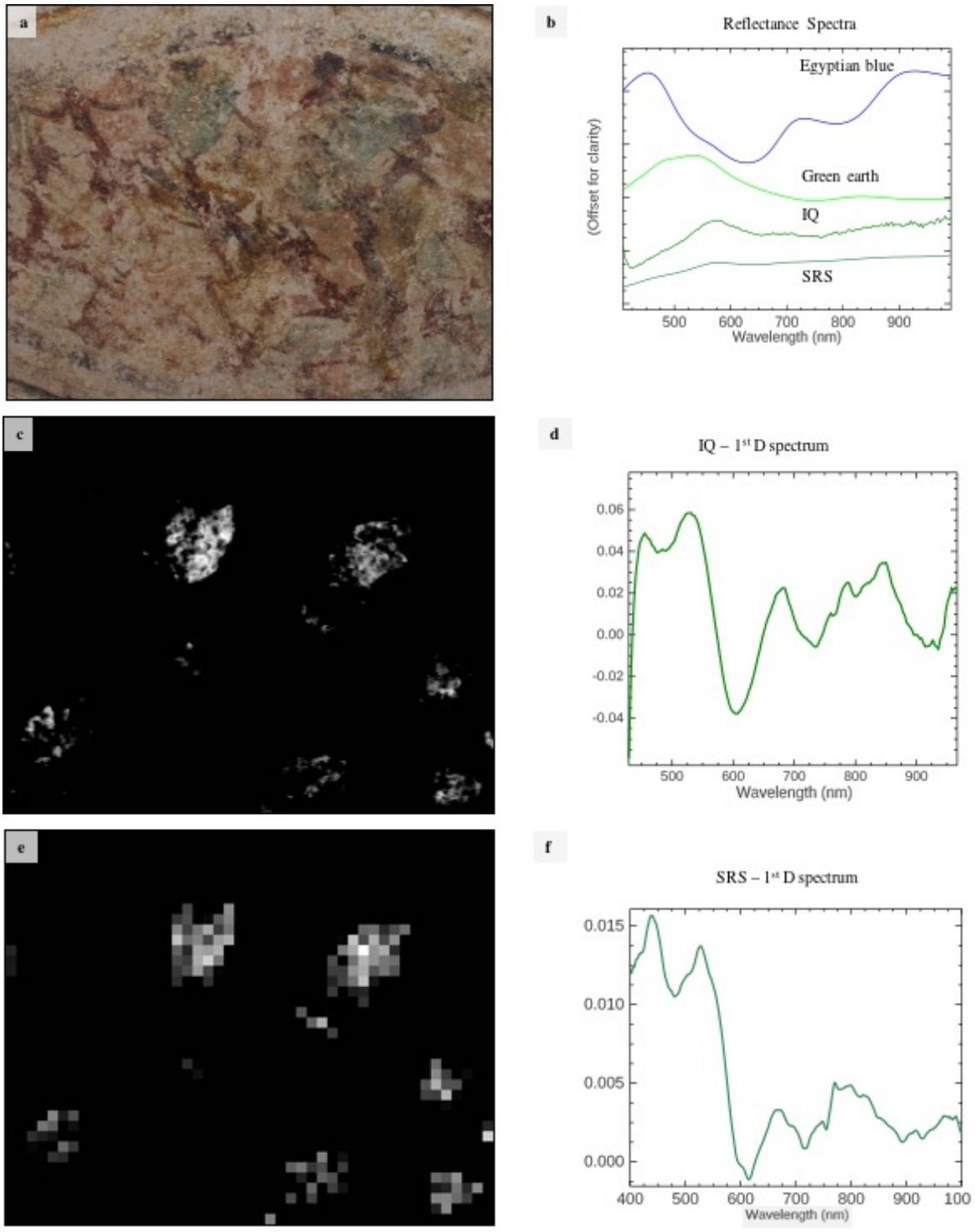

Figure 5.16: **(a)** RGB image of the imitation marble pattern. **(b)** Reflectance endmembers and reference spectra for the blue-green pigment. **(c)** IQ rule image for endmember 5 **(d)**. **(e)** SRS rule image for endmember 3 **(f)**.

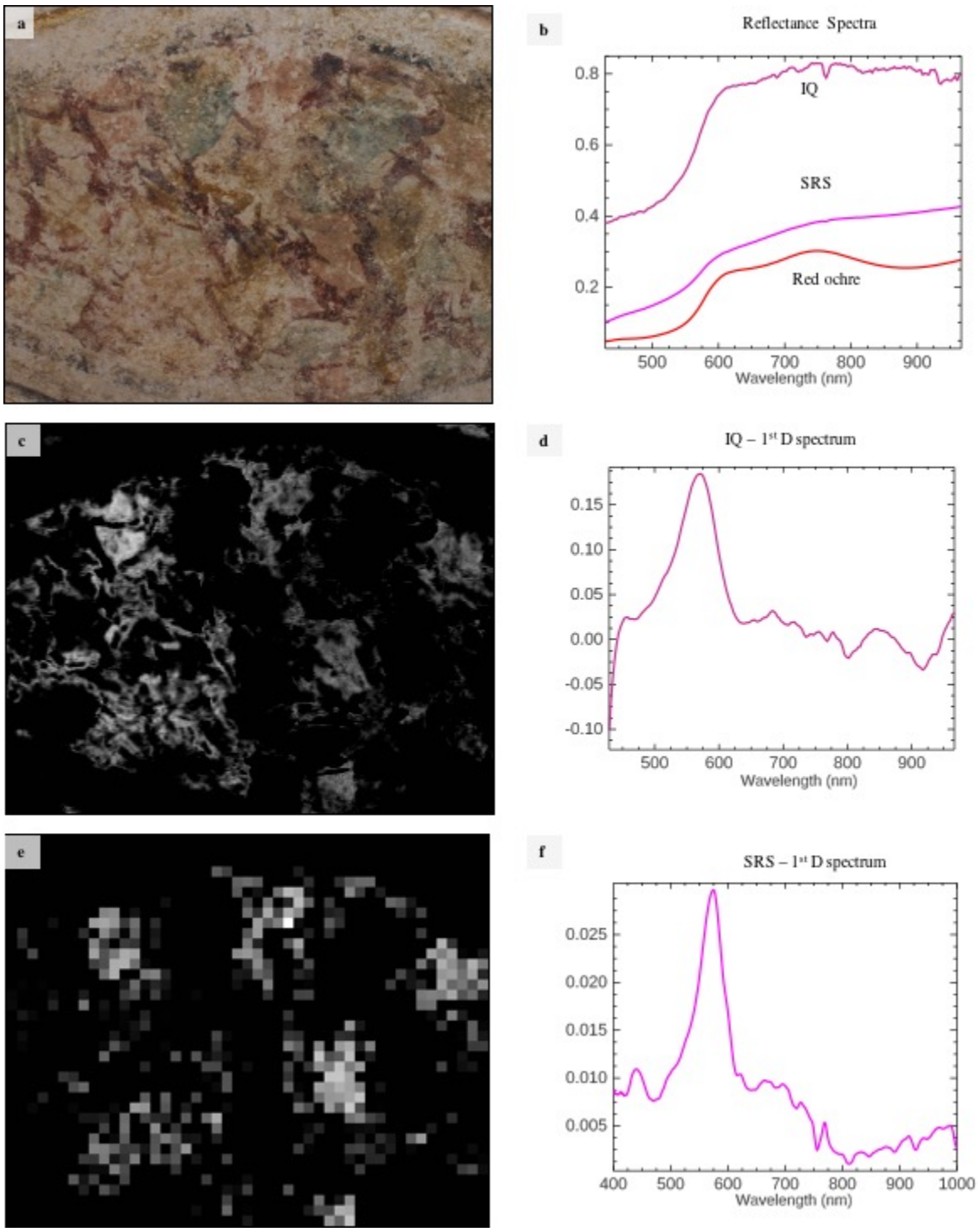

Figure 5.17: **(a)** RGB image of the imitation marble pattern. **(b)** Reflectance endmembers and reference spectra for the pink pigment. **(c)** IQ rule image for endmember 4 **(d)**. **(e)** SRS rule image for endmember 1 **(f)**.

With the extension of the analytical range to the SWIR, there is access to new absorptions that can be mapped for materials with distinct signatures outside of the VNIR such as clays and minerals binding media and organic conservation materials, like consolidants. The absorptions of a material in the SWIR are caused by overtones of fundamental vibration modes (in the mid IR) and combination bands. Due to the extended spectral range (1000–2500 nm), it is not feasible to extract endmembers from this large subset to target all of the previously mentioned materials. Instead, targeted analyses at specific absorptions are performed. To do so, one may extract an image at a specific spectral band to see the reflectance intensity at that wavelength throughout the scene (Figure 5.18a). This could be misleading, however, as it only represents a reflectance value and may not be indicative of an actual absorption. For example, a pixel with low reflectance (i.e. a dark material) but no distinct absorption feature at this band may be mistaken for a specific material behavior.

Three different analytical methods can be applied to study specific vibrational features and produce maps of their distribution. The first relies on creating a spectral subset of the data cube closely around a specific vibrational feature and performing the routine statistical analysis approach of endmember extraction and mapping. The second method integrates throughout the absorption feature to visualize the intensity of the absorption. The third method calls upon a 2nd derivative calculation of the cube, which effectively removes the background continuum, zeros the baseline and transforms the absorption minima into a peak. Methods two and three were applied to map the distribution of $CaCO_3$ by isolating the carbonate (CO_3^{2-}) absorption band around 2343 nm.

Figure 5.18a shows the overall reflectance of spectral curve at band 2343 nm (Figure 5.18b) per pixel. The white pixels indicate areas of higher reflectance. Figure 5.18c shows the integration of the absorption depth from the reflectance profile (method two). A convex hull correction from 2323 nm to 2360 nm is performed to isolate the region of absorption (marked in red), which contains the reflectance curve marked in blue dots (Figure 5.18d). By integrating through this region and performing this calculation across the cube, an absorption depth map of the CO_3^{2-} feature, where white pixels indicate greater absorption,

is produced, which is markedly different from the simple reflectance intensity at 2343 nm. However, visualizing the spectral band (Figure 5.18e) of the 2nd derivative peak (Figure 5.18f) of the CO_3^{2-} feature produces a highly comparable map to Figure 5.18c, where the white pixels correspond to a larger peak value, and therefore a greater amount of absorption (method three). The latter two methods are more robust alternatives to simply looking at the overall reflectance value, as the uneven surface and the surrounding environment may cause the overall reflectance profile to increase or decrease, which falsely informs the relative absorption.

In the SWIR region, signatures of polyvinyl acetate (PVA)-based material at 2257, 2300, 2368 nm could be identified. Polyvinyl acetate is synthetic polymer resin used as surface consolidant for wall paintings. This type of coatings seems to have been used in the conservation of different wall paintings, both detached fragments kept in the Department of Antiquities (of Cyprus) storerooms and in situ wall paintings. A spectral subset from 2252 to 2323 nm was analyzed in the first derivative to identify endmembers with reflectance absorption features at 2256 and 2296 nm. As seen in Figure 5.19b, three were produced showing relative shifts around 2285 nm and differences between peak intensity values. These endmembers were mapped, showing a roughly uniform application of PVA over the surface of the wall painting (Figure 5.19a).

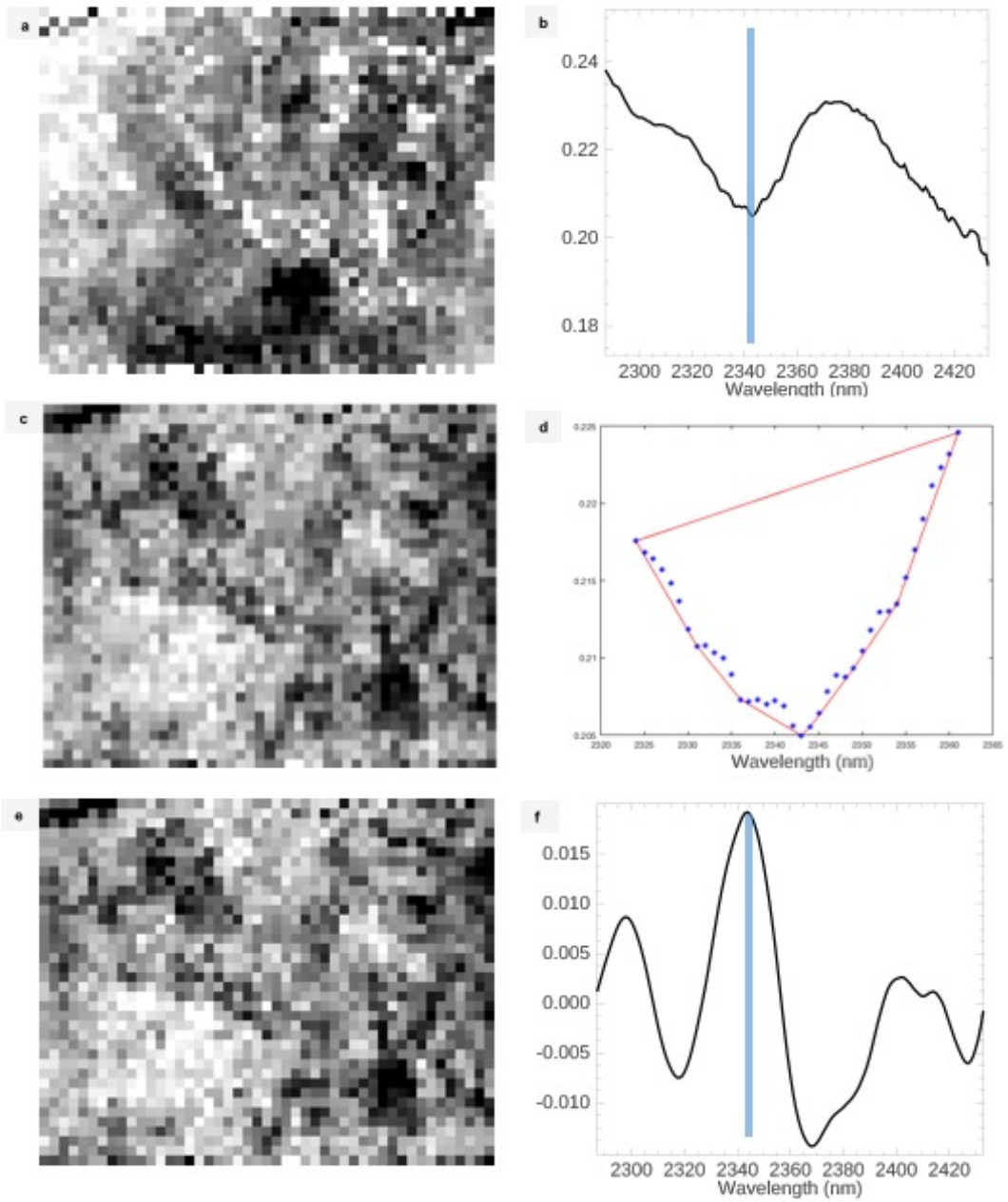

Figure 5.18: **(a)** A gray-scale map of spectral band at 2343 nm **(b)**; white areas indicate higher absorption at this band. **(c)** A gray-scale map of an integrated absorption centered around 2343 nm; white areas indicated higher integrated absorption. **(d)** The convex hull correction calculated for the absorption curve at pixel [17, 24] is outlined in red, designating the area for integration; the blue dots represent the reflectance curve in that spectral range. **(e)** A gray-scale map of 2343 nm absorption feature in the 2nd derivative **(f)**; white areas indicate higher peak values (greater absorption). The integrated absorption and the 2nd derivative peak reflectance show comparable results for the distribution map of the CO_3^{2-} absorption.

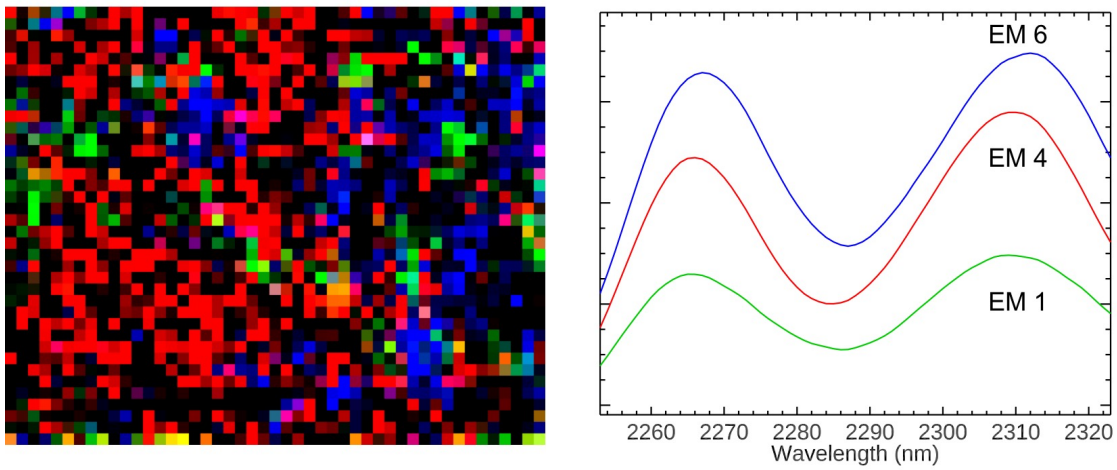

Figure 5.19: **(a)** The map of PVA application over the surface of the painting. **(b)** The endmembers of PVA extracted from the 1st derivative cube in the SWIR.

One of the major products of deterioration on the wall paintings are salts such as gypsum ($CaSO_4 \cdot 2H_2O$). Due to liquid moisture in the walls, mobilization and supersaturation of salts within the porous structure of the wall paintings at subsurface and surface has caused surface damage and encrustations. Gypsum has a diagnostic triplet feature from 1445 to 1540 nm (Figure 5.20), corresponding to the first overtone vibrations of the hydroxyl groups. To better identify more subtle absorptions from 1480 to 1550 nm, especially in regions where the gypsum concentration is lower, a spectral subset of the region of 1430 to 1563 nm was extracted from the 2nd derivative cube to visualize the absorptions as maxima, and the endmembers were extracted using the SHW and SMACC (Figure 5.20b). Mapping these signatures showed that the presence of gypsum was mostly widespread throughout the surface (Figure 5.20d), however the green endmember, corresponding to reflectance features with greater absorption, indicates regions with higher salt presence.

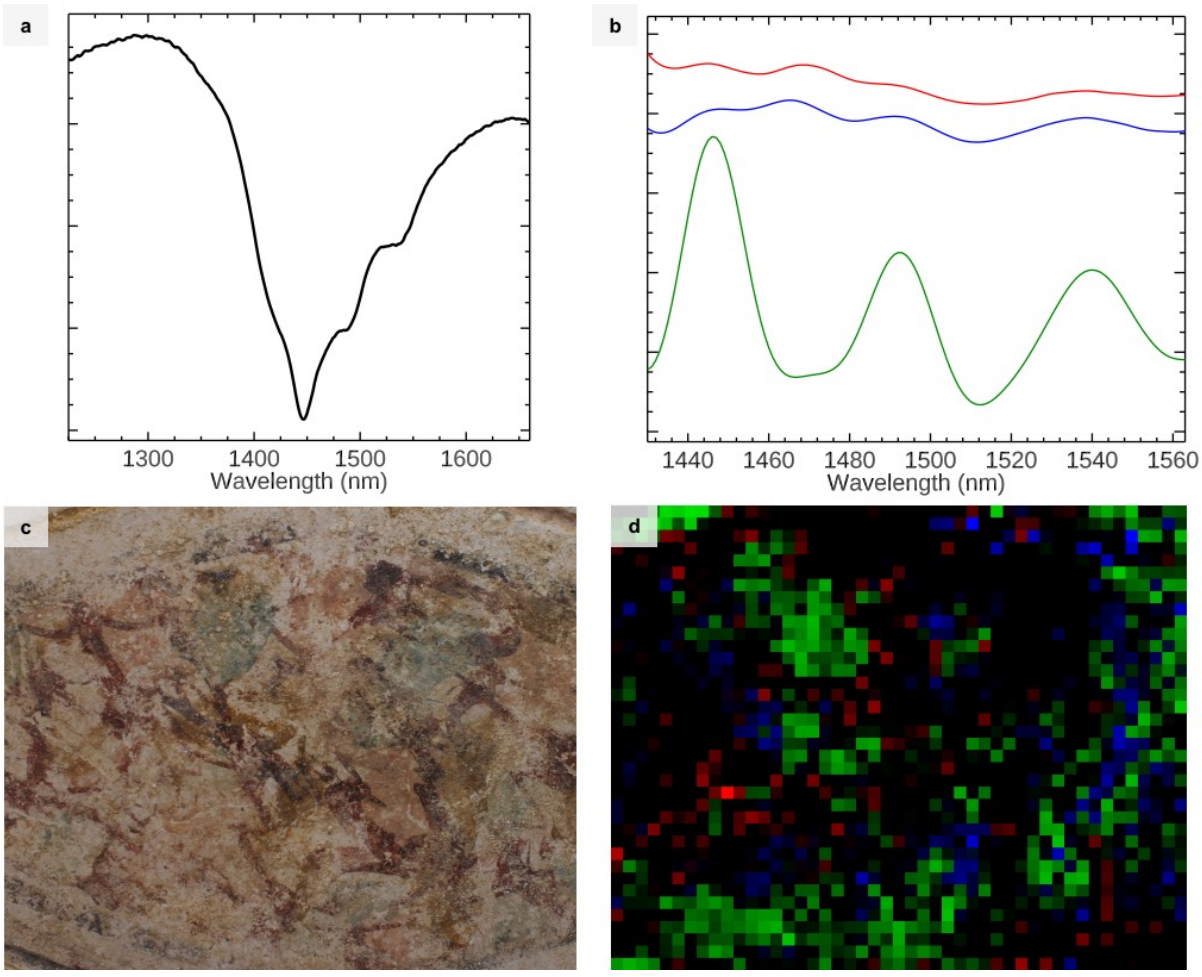

Figure 5.20: **(a)** The triplet signature of gypsum from 1445 to 1540 nm. **(b)** The endmembers extracted from the 2nd derivative cube from the wavelength ranges of the triplet absorption. **(c)** RGB image of the scan scene. **(d)** Map of the thee endmembers showing the distribution of gypsum.

Finally, MNF images of three large spectral bands in the SWIR helped to identify new principle component signatures in this region, a method adapted from applications of principles of stellar photometry utilizing astronomy interference filters J (1100–1400 nm), H (1500–1800 nm), K (2100–2400 nm) [58, 21], to emphasize signatures in the IR. From the SRS data cubes, discrete bands in the SWIR were summed in ENVI to produce three wide spectral bands, followed by an MNF transform on the three bands. This transform produced an image of principal components that represented the triplet SWIR infrared signature of green earth (Figure 5.21b), as it is clear that the dark regions in the image correspond closely

to the rule image of Endmember 3. This is an important demonstration of IR IS applications because confident attribution of the triplet absorptions in the SWIR from individual spectra was not possible due to the presence of PVA and $CaCO_3$.

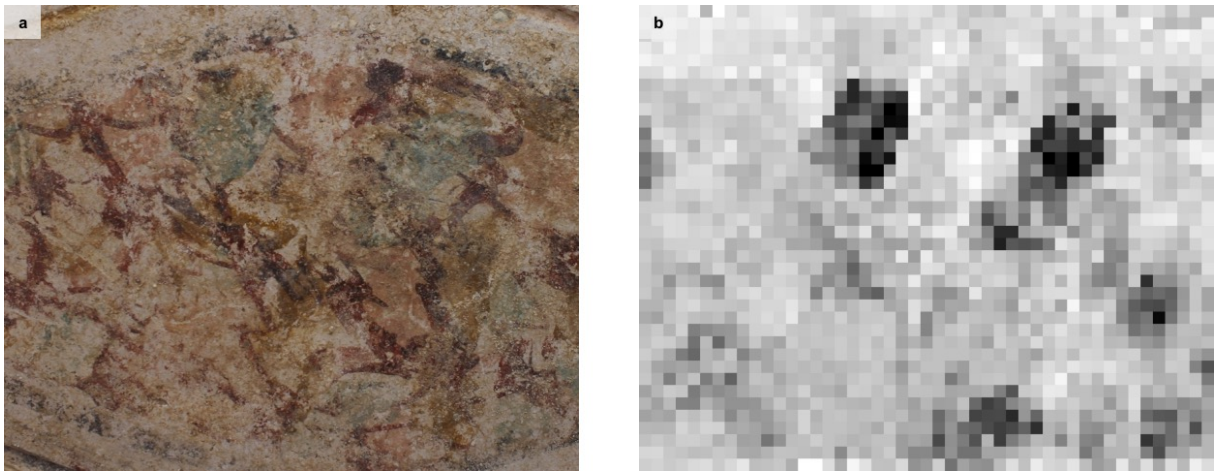

Figure 5.21: **(a)** RGB image of the scan scene in Tomb 3882. **(b)** MNF no. 1 image from the MNF transforms of the three wide IR bands. The dark regions correspond closely with the rule image of endmember 3, indicating these regions correspond to the SWIR signature of green earth.

The SRS 3D cubes have demonstrated that this unique field-deployable imaging spectroscopy system, with an extended analytical range to the SWIR compared to many commercial HSI cameras limited to the VNIR region, facilitates in-depth investigations by providing access to new absorption features that improve mapping of constituent materials. Using creative post-processing techniques, different visualizations can be produced to inform how materials were used, how conservation practices were applied, and deterioration processes occurring in the paintings.

CHAPTER 6

Case Studies

This chapter presents scientific investigations for materials characterization, production technology and assessment of the condition of important Greco-Roman paintings from Egypt and Hellenistic, Roman and Byzantine Cypriot wall paintings. The analytical protocol and characterization techniques included non-invasive and non-destructive spectroscopic and imaging technologies as described in Chapters 2, 4, and 5.

6.1 Greco-Roman funerary portraits

A group of Greco-Roman Egyptian funerary portrait paintings, also known as Fayum portraits (Figure 6.1) from the J. Paul Getty Collection, housed at the Getty Villa Museum in Malibu, CA, were analyzed. This work was initiated under the Ancient Panel Paintings: Examination, Analysis, and Research (APPEAR) project, a macroscale archaeological and technical analysis of Fayum portraits across global collections, initiated at the Getty Villa by antiquities conservator Marie Svoboda. The name Fayum portraits denotes the location of their origin, the Fayum oasis in Egypt, where many of these paintings were found in funerary context [26]. However, it is now understood that funerary portrait production occurred beyond the Fayum region; unfortunately, due to looting of burial sites, specifically for the illicit sale and trafficking of sarcophogi and portraits, the provenance of many portraits today are unknown. Presently, there are approximately 1000 portraits in collections across the world.

The portraits provide a rare look into Greco-Roman Egypt. In this period, Hellenistic art and culture were highly valued [149]. Though this art form flourished in Egypt, the naturalistic depiction seen in the portraits is a direct influence of Hellenistic painting tradition,

as flat and frontal stylized portrayals are more representative of Egyptian art [65]. Archaeological records indicate that many of the portraits recovered with known provenance come from cities where large numbers of Greek immigrants resided [26]. These portraits represent the intersection of Hellenistic painting traditions and Egyptian funerary beliefs, which were persistent in the Romanization of Egypt, and these beliefs are demonstrated through the inclusion of the Egyptian burial practices and decorative styles into the paintings.

The portraits also provide strong records of Greco-Roman society. First produced in the first century AD, the number of portraits increased in the second century. However, towards the mid-end of the third century AD, portrait production decreased significantly [26]. The highly-individualized nature tells us about the person depicted, as well as glimpses into social classes, fashion trends, occupation, and potentially age demographics. Additionally, a large-scale study of the portraits provides an insight into artistic trends, material use, and technical applications practiced by artists and workshops in Roman Egypt [143].

Most of the portraits in the group are painted on wooden panels, except for portraits 75.AP.87 and 79.AP.219, depicting male youths, which are painted on linen. Portraits 73.AP.94, 74.AP.11, 79.AP. 142, 79.AP.141 portray adult men, and 81.AP.29, 79.AP.129, and 73.AP.91 adult women. All of the male figures except of the figure in painting 73.AP.94 wear white tunics; The figure in painting 73.AP.94 may have been an athlete, who were often depicted naked in the portraits [65]. Of these figures, all but the individual in painting 79.AP.141 have pink or purple clavi (thin decorative bands) running along the length of their tunics. The women wear pink or purple tunics, with black clavi, and jewelry. The double strand of necklaces of gold and emerald-colored gemstones were commonly seen in female funerary portraits of women of status [65]. The two youths both have birds, possibly falcons, on their shoulders, while the portrait figure in painting 79.AP.219 has two additional winged, linen-wrapped figures hovering over his shoulders - these symbols clearly reflect Egyptian funerary beliefs. While there appear to be common decorative choices amongst the portraits, there are clearly a wide variety of artistic techniques and skill levels represented in this group, and the portrayal of the figures themselves are highly individualized in each portrait.

Figure 6.1: The set of funerary mummy portraits analyzed from the J. Paul Getty Museum collection

All portraits were first analyzed by forensic reflectance and luminescence photography to record the presence of any luminescent materials, i.e. madder lake and Egyptian blue, two of the most common pigments in ancient paintings of this period and culture, as well as other organic materials that may be present, including conservation materials from previous interventions. The Mini-Crimescope MCS-400®, featuring the alternate light source (ALS), was used to excite the paintings at different narrow bandpass wavelength ranges. A modified digital single-lens reflex (DSLR) camera (internal hot mirror removed) was used to capture the photon emission (luminescence) at longer wavelength (from that of the excitation source). Portraits 75.AP.87, 79.A.141, and 73.AP.94 were also analyzed using fiber-optic reflectance spectroscopy (FORS) and X-ray fluorescence (XRF) spectroscopy to provide supplementary information and confirm findings from the forensic photography.

The portraits were analyzed using three different excitation wavelengths (λ_{ex}) to induce luminescence emitted in longer wavelengths (λ_{em}): 1) UV-induced visible luminescence (ex-

citation with λ_{ex} = 300–400 nm, capture in λ_{em} = 400–700 nm; Figure 6.2), visible-induced visible luminescence (excitation at λ_{ex} = 535 nm, capture in λ_{em} = 580–700 nm; Figure 6.3) and visible-induced near-infrared (NIR) luminescence (excitation at λ_{ex} = 600 nm, capture in λ_{ex} = 900–1000 nm; Figure 6.5).

The UV-induced visible luminescence or fluorescence (as it is most commonly referred to in the visible range) images showed characteristic fluorescence corresponding to conservation materials such as glues or other adhesives (i.e. the light blue fluorescence and cracks in Figure 6.2a-b). The damage suffered by the portrait 73.AP.94 (Figure 6.2b) was more noticeable compared to its RGB image.

Figure 6.2: UV-induced visible luminescence photography of the portraits.

Beyond the visualization of conservation materials and weathering/damage, UV-induced visible fluorescence together with visible-induced visible luminescence and visible-induced NIR luminescence aided in the characterization of pigments. The distinctive bright orange luminescence in the UV-induced visible images also appearing bright white in the visible-induced visible luminescence in seven out of the nine portraits (Figure 2) suggests

the presence of an organic/inorganic hybrid red pigment such as madder lake, though the presence of cochineal and/or lac cannot be excluded as these three red colorants show similar luminescence behavior and have all been identified in Classical art [68, 66, 182, 135]. Consistent painting applications of the red colorant can be seen in this collection: facial shading and coloration, such as the distinct under-eye line in 75.AP.87 (Figure 6.3a), the cheeks of 79.AP.142 (Figure 6.3c), some subtle rouging of the face in 73.AP.91 (Figure 6.3g) and the lips of 79.AP.129 (Figure 6.3d); the pink and purple clavi and collar decoration of the male tunics; and the pink and purple tunics of the women. The red colorant was also used for different accessories that the youth in 79.AP.129 (Figure 6.3d) and the man in 79.AP.142 (Figure 6.3c) were holding; the linen wrappings on the small figures above the shoulders of the youth also had some subtle coloration with the red colorant. On the tunic of the youth in portrait 75.AP.87 (Figure 6.4a), the orange residue on his proper left shoulder does not fluoresce. FORS analyses of this spot revealed red lead (Pb_3O_4) by the sharp transition at $\sim$ 590 nm due to the pigment's band gap (Figure 6.4b).

Figure 6.3: Visible-induced visible luminescence (gray-scaled) photography of the portraits. The exceptionally bright regions correspond to the luminescence of madder lake.

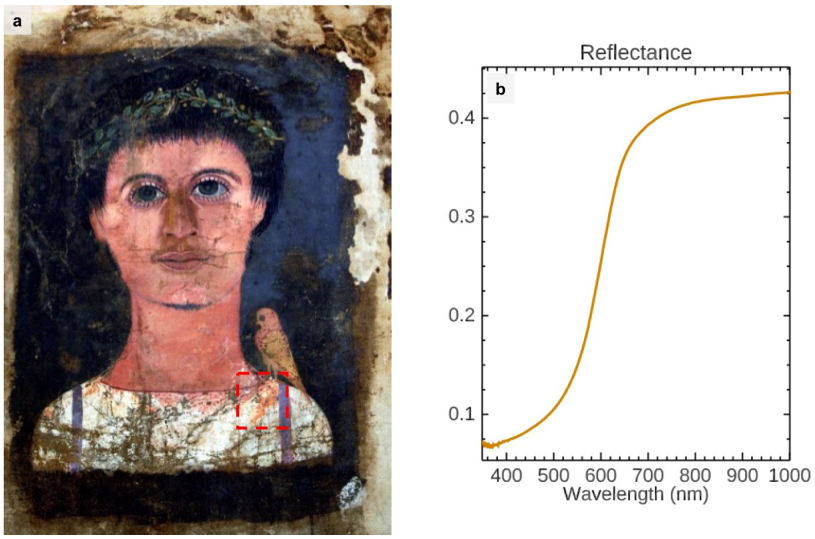

Figure 6.4: **(a)** The red dashed square on the proper left shoulder of portrait 75.AP.87 indicates the region where red lead was identified by FORS (**b**). The transition occurs at $\sim$ 590 nm.

Results of the visible-induced NIR luminescence photography (Figure 6.5) revealed that three portraits, 73.AP.94, 79.AP.141, 73.AP.91, contained a luminescent pigment, most likely Egyptian blue, the only known blue pigment used in this period with this unique property to emit light at λ_{em} = 910–930 nm [6, 200, 108] when excited by red light (λ_{ex} = 600 nm). In the first two portraits (Figures 6.5a,b), Egyptian blue was used not to provide a blue hue but was found dispersed in a white matrix to produce a 'cold' white tone. In portrait 73.AP.94 (Figure 6.5a), the Egyptian blue-containing white pigment was used to accent the skin tones of the man's face, ears, and along the neck.

The use of Egyptian blue pigment particles in white paint matrices (without changing the hue to blue) is quite common in Hellenistic and Roman painted sculpture and wall paintings [200, 28]. In portrait 79.AP.141 (Figure 6.5b), the Egyptian blue-containing white pigment was used for the tunic and the hazy white background. This practice was noted in both the Cypriot paintings (see Appendix C.1) and the funerary portrait (A.N. 32.4) (see Chapter 4, Figure 4.12) where this white pigment (enhanced with Egyptian blue) was used to produce shading effects. Egyptian blue was identified in portrait 73.AP.91 (Figure 6.5c) in the purple tunic, and in a white pigment to put highlights on her nose and lip. However, most interesting was the application of the blue pigment to shade her facial features including the shape of her face, eyes, nose, neck. This distinct technique of outlining has been identified in one funerary portrait from the Phoebe A. Hearst Museum of Anthropology [77], and it echoes the unique application identified in the House of Aion funerary painting E9 (Figure 2.28).

Further analyses using FORS and XRF of portrait 79.AP.141 (Figure 6.6a) revealed technical similarities to portrait 32.4 from the Walters Art Museum. The white tunic here was produced using Egyptian blue, lead white (identified by XRF), and jarosite (identified by FORS, Figure 6.6b). The warm white accents on the man's neck and the soft-toned halo around the man's head (spot analyses indicated by arrows in Figure 6.6a) were produced by a mixture of jarosite and a white pigment (either lead white or calcium carbonate, though most likely the former as it was identified in the tunic and other portraits have featured lead white use in flesh tone decoration [57]). The same white pigment mixture and the practice of

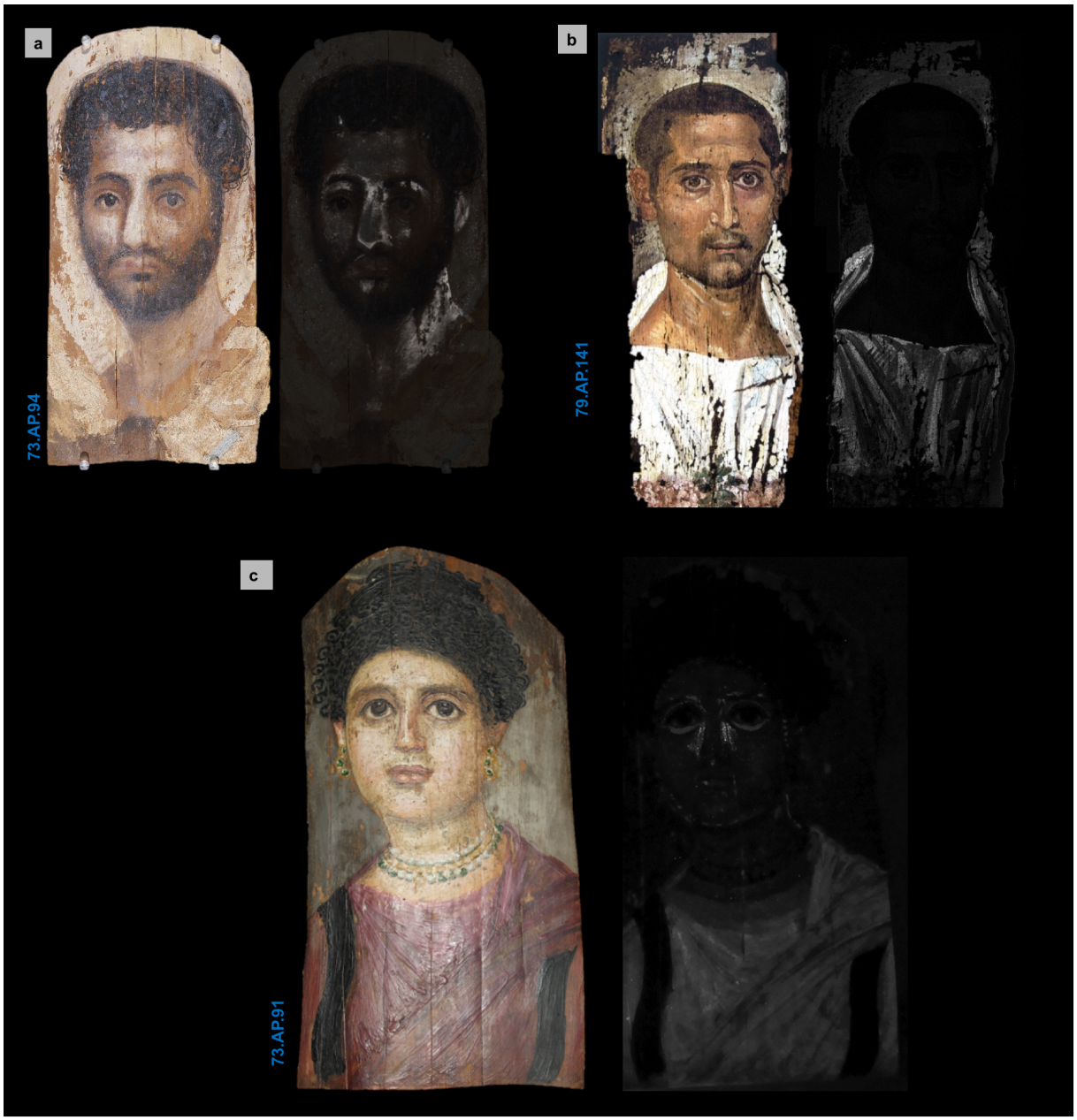

Figure 6.5: Visible-induced NIR luminescence (gray-scaled) photography of the portraits. The white luminescence corresponds to the presence of Egyptian blue.

using jarosite to make warm tones for the flesh highlights and in the tunic can be connected back to portrait 32.4 (Table 4.2). This suggests a technical application practiced amongst ancient Egyptian artists in the decoration of funerary portraits and can potentially serve as an identifying trait for a specific artists' workshop or group of artists. The green pigment found in portrait 79.AP.141 was identified by FORS as a green copper carboxylate, also used in the portrait from the National Gallery of Art and portrait 32.4.

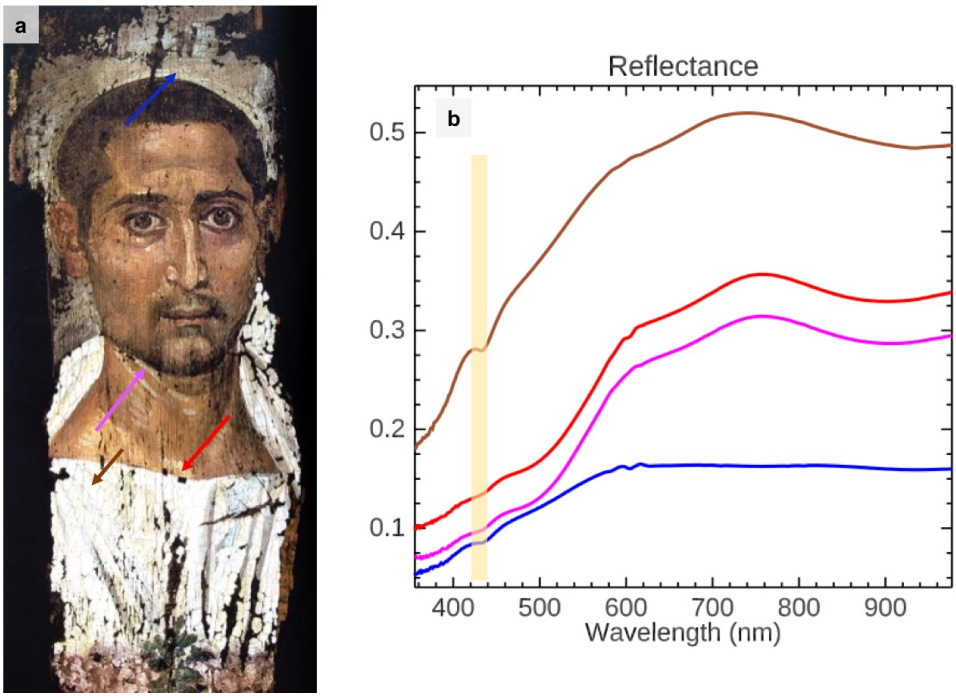

Figure 6.6: **(a)** Locations of FORS collection from 79.AP.141, indicated by the arrows, identifying the application of jarosite in the tunic, bright stripes along his neck, and the white background above his head. Their corresponding reflectance spectra **(b)** have an absorption feature at 433 nm that clearly indicates the presence of natrojarosite.

FORS analyses also gave insight into the binding media used for the portraits analyzed. Portrait 79.AP.141 shows the application of wax, due to characteristic absorptions of CH-combination bands (CH_2) stretching and bending) at 2312 and 2352 nm and νCH-1st overtone (of (CH_2) stretching) at 1730 and 1763 nm. In portrait 73.AP.94 (Figure 6.1b), two binding media were identified: wax and an oil-based binding medium. The latter featured characteristic absorptions of CH-combination bands at 2303 and 2345 nm and the νCH-1st

overtone at 1723 and 1753 nm. The oil, most likely linseed oil, was found in the light blue pigment (identified as indigo) on the linen wrapping, not as a part of the composition on the wooden panel. Similar binding media were also identified in the shroud portrait 75.AP.87 (Figure 6.1a). Wax was the primary binding medium. However, in the green wreath of the youth, the absorptions were at 2297 and 2343 nm, and 1723 and 1752 nm, suggesting the use of an oil. The green pigment requires further studies for its characterization; based on the reflectance profile it appears to not be a natural or synthetic green pigment, but perhaps a mixture of blue and yellow.

These analyses based on forensic imaging combined with FORS and XRF provided crucial information into technical trends practiced among artists in Greco-Roman Egypt. The Egyptian blue-containing white paints and how they were applied in Cyprus and Egypt may suggest knowledge exchange between these regions. Additionally, these results demonstrate the strength of ALS applications, whereby excitation of various fluorescent materials at different wavelengths from the tunable light source, coupled with capture by a UV to NIR sensitive camera with interchangeable filters, produces complementary scientific imagery that allows separation and identification of material signatures, as well as interpretation of their application in the paintings. The supplementary analyses by FORS and XRF allowed further characterization of the pigments in the portraits and identification of their binding media.

6.2 Ancient Cypriot Paintings

6.2.1 House of Aion

The figurative painting E9 from the House of Aion (Figure 2.9c) in Nea Paphos, Cyprus, previously discussed in Chapter 2, was analyzed with the SRS system and the Specim IQ camera in the 2018 and 2019 analytical campaigns, respectively. The region of interest imaged with the two systems was the figure's face (Figure 6.7a) due to the various shading, highlight, and color-mixing applications used to produce the hair and flesh tones. In this

scene, the figure's green wreath and blue and white headpiece are visible, and the backdrop of wide light and dark purple brushstrokes can also be seen.

The same analytical protocol presented in Chapters 4 and 5 were used on the original reflectance and luminescence data cubes collected. A 1st derivative calculation (performed in Matlab) was applied to the SRS-collected reflectance cube, subset to the visible/near-IR (VNIR), and a set of 1st derivative endmembers (Figure 6.7d) were extracted in ENVI (the image analysis software) to map the different pigment mixtures (Figure 6.7b).

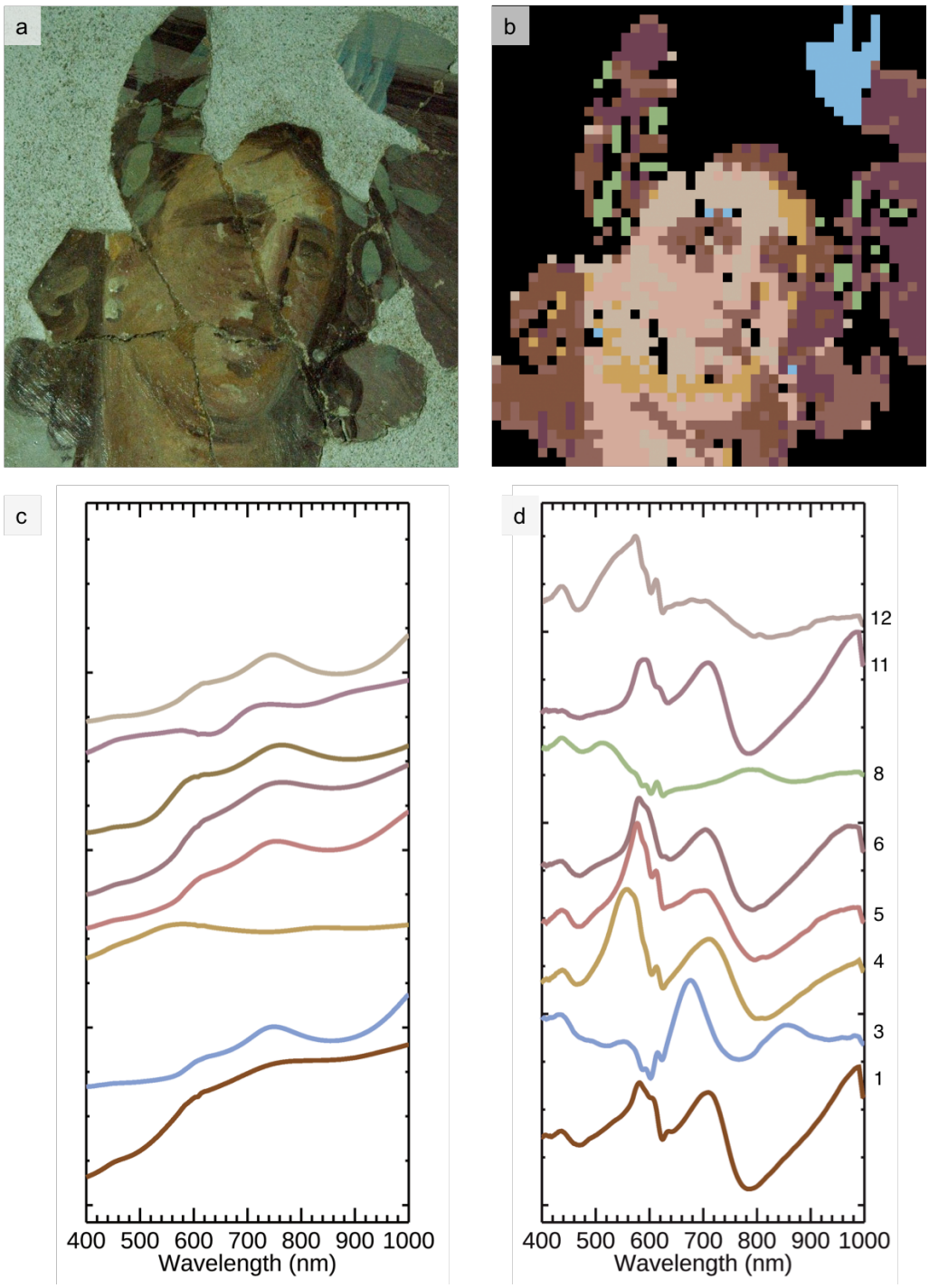

Figure 6.7: **(a)** Scan region of figurative painting E9, House of Aion (see Figure 2.9c for full painting). **(b)** The chemical material map produced from the SAM, using the extracted 1st derivative endmembers in **(d)**, whose reflectance equivalent endmembers can be found in **(c)**.

Table 6.1: 1st derivative endmembers applied for chemical mapping of figurative painting, E9. The last column contains the diagnostic spectral features used to identify the constituent materials.

Endmember	**Features and hues**	**Material(s) ID**	**Spectral features**
1	Brown hair	Red ochre	452 (s), 582 (i), 656 (a), 750 (m), 867 (a)
3	Blue head piece; facial outline	Egyptian blue Calcium carbonate	540 (a), 632 (a), 800 (a)
4	Yellow facial shading; hair strands	Yellow ochre	452 (s), 560 (i), 763(m), 890 (a)
5	Light pink facial shading	Red ochre Calcium carbonate	452 (s), 577 (i), 662 (a), 766 (m), 857 (a)
6	Light purple background	Red ochre Calcium carbonate	445 (s), 580 (i), 755 (p), 850 (a)
8	Green wreath leaves	Green earth	458 (s), 584 (m), 736 (a), 848 (m), 900 (a)
11	Dark purple background	Red ochre	452 (s), 590 (i), 750 (m), 870 (a)
12	Light flesh tone	Yellow ochre Red ochre Calcium carbonate	452 (s), 550/576 (i); 604 (s); 777 (p); 880 (a)

Eight unique endmembers were extracted from the 1st derivative cube (Figure 6.7d). The values of their diagnostic spectral features were extracted by analysis of the 1st derivative endmembers, and compared to reference reflectance spectra of minerals and synthetic colorants (Appendix A). The following materials were identified based on their characteristic absorption, maxima, and inflection features (detailed in Table 6.1): hematite-rich red ochre, yellow ochre (goethite), green earth (celadonite mineral), and Egyptian blue. From the tonalities of various hues produced in the painting, lighter tones were produced in admixtures with a white pigment and darker tones with a black pigment. XRF spectroscopy of the white pigment indicated characteristic X-ray emissions of Ca suggesting the presence of calcium carbonate ($CaCO_3$), the most common white pigment used in Cypriot Hellenistic and Roman wall paintings (references). The black pigment was carbon black.

The skin tones were mapped by endmembers 4, 5, and 12, representing mixtures with different relative concentrations of goethite and hematite-rich red ochre, with calcium carbonate white. This was determined by the shifts in the inflection points, peak maxima values, and near-infrared absorptions. Endmembers 4 and 12, of the light yellow flesh tones, show absorptions shortward of 550 nm ($^6\mathrm{A}_{1g}(^6\mathrm{S}) \rightarrow {}^4T_{2g}(^4G)$), indicative of the presence of goethite. Endmember 5 is a pink flesh tone with strong absorption shortward of $\sim$ 577 nm, and absorptions at $\sim$ 662 nm and $\sim$ 857 nm, characteristic of hematite. However, the peak maxima at 766 nm corresponds to that of goethite. The background stripes of light purple (endmember 6) and dark purple (endmember 11) were produced with hematite-rich red ochre, as was the brown hair with subtle yellow strands (endmember 1). The differences in the spectra between the purple and brown hues are due to the different pigment mixtures. The green wreath leaves were painted with celadonite mineral (endmember 8), and Egyptian blue (endmember 3) was used in the head piece of the figure and the outline of the face. These outlines were first seen in the forensic image in Chapter 2 (Figure 2.28). Here, the endmember was not able to robustly map the outlines, applied as a blue wash, or its presence in the flesh tone mixtures, as visualized in the luminescence photography; the concentration of Egyptian blue in these applications was not sufficient to be detected by the instrument employed.

The luminescence data cube collected by the Specim IQ camera was able to overcome this challenge. The luminescence endmember extracted (Figure 6.8a) produced a chemical map of Egyptian blue application throughout the image scene in the field of view (Figure 6.8b), owing to the strong luminescence quantum yield of the pigment (ϕ_E = 10.5% [6]). Similar to the image produced in Figure 2.28, the map here confirms that Egyptian blue was used in the flesh tones and to outline the face and neck. Luminescence imaging spectroscopy using an HSI system thus serves as a powerful diagnostic tool for the identification and quantitative spectral mapping of luminescent pigments with high luminescence quantum yields like Egyptian blue, conventionally mapped by their luminescence glow in forensic photography.

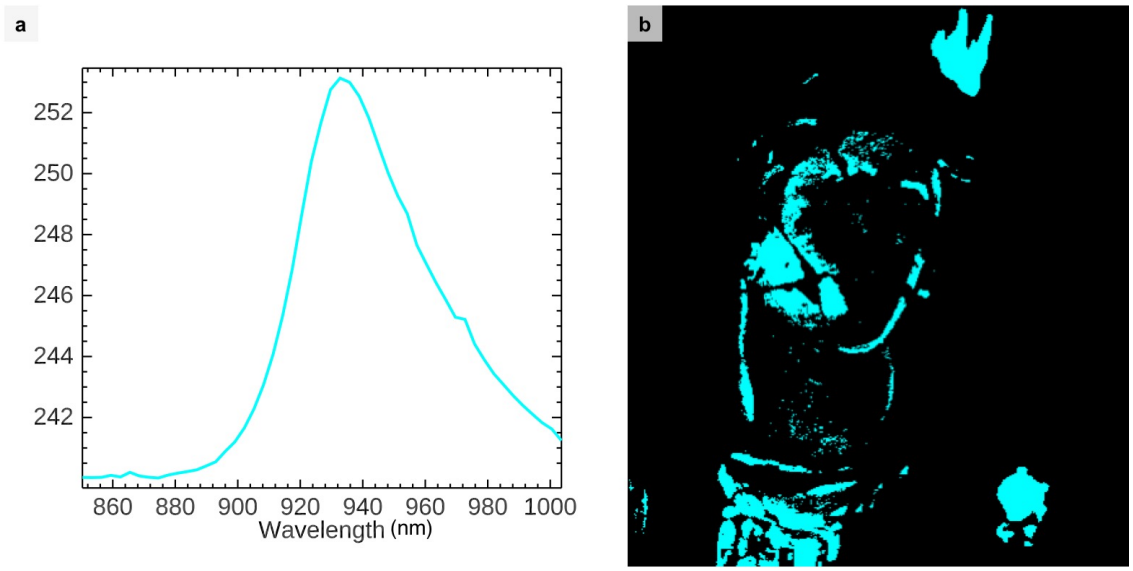

Figure 6.8: **(a)** The emission endmember extracted from the luminescence data cube (peak location $\sim$ 935 nm). **(b)** The chemical map of Egyptian blue over the figurative painting E9 confirms the forensic photograph captured of the same scene in Figure 2.28. Luminescence imaging spectroscopy is a robust alternative to forensic photography by employing quantitative spectral mapping of the diagnostic emission peak.

SWIR analyses of the SRS data cube identified the use of a polyvinyl acetate (PVA) material for the consolidation of the painting. Furthermore, MNF analyses of the J, H, K-simulated wide infrared bands produced an MNF eigenimage clearly identifying the green leaves in the black regions (Figure 6.9), due to the triplet signature of celadonite from 2250-2350 nm corresponding to vibrations of OH-combination bands. This demonstrates again that SWIR MNF analyses can provide a better chemical map for materials whose VNIR reflectance signatures are more challenging to visualize through spectral angle mapping due to low concentration or masking effects.

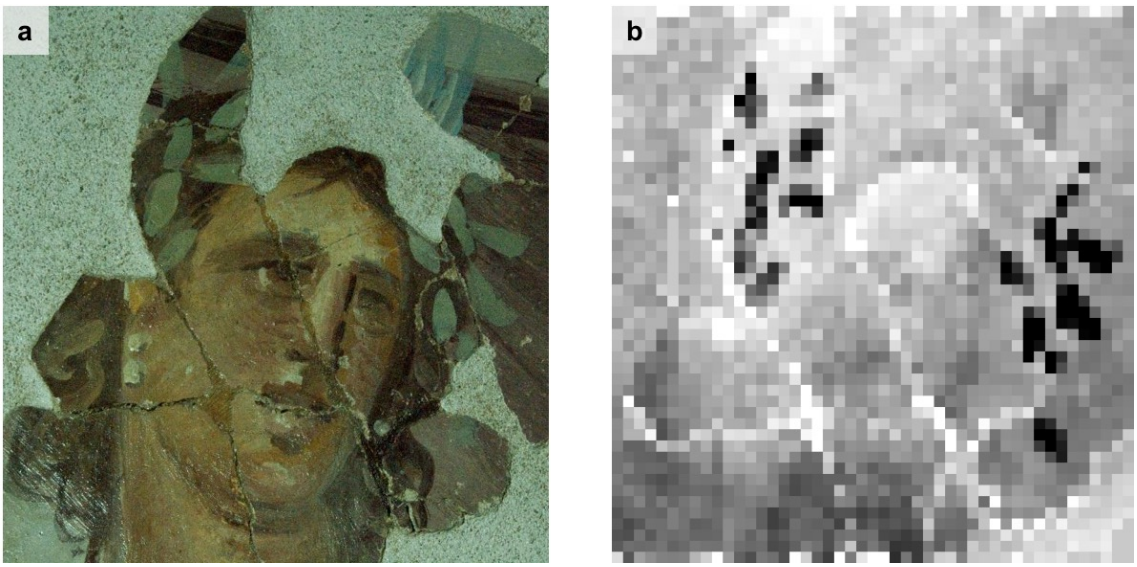

Figure 6.9: **(a)** RGB image of figurative painting E9. **(b)** The third MNF eigenimage produced from the J, H, K bands in the SWIR. The intense black regions correspond to the green earth-painted wreath.

The analysis of the data from these investigations show that when the hyperspectral Specim IQ camera and the SRS system are used in tandem, they provide complementary information necessary for the identification of materials and an understanding of the technical practices of the ancient artists, mainly on the application of pigments and their function. 3D data cubes provide a new avenue to identify and deconstruct the pigment mixtures applied by ancient artists, and facilitate chemical mapping of the painting applications. Additionally, novel processing methods allowed various signatures to be probed that were challenging to identify in the original reflectance profiles.

6.2.2 Tomb Roma 2

Forensic photography and luminescence imaging spectroscopy using an HSI system was applied in Tomb Roma 2 to recover concealed decoration. A stone slab in Tomb Roma 2 sealing a loculus (Figure 6.10) features two layers of different decorative schemes. In the lower left region of the slab, a layer of heavy gypsum salt encrustation, identified by FORS, covers the decoration (Figure 6.11a,c). Red light excitation ($\sim$ 600 nm) was applied to the surface of

the slab and the cameras (a modified Fujifilm DSLR and the Specim IQ) were filtered with PECA NIR filters to capture luminescence from $\sim$ 900–1000 nm. An IQ luminescence data cube was collected of the region marked in red. Extraction and mapping of the emission endmember produced the map in Figure 6.11b.

Figure 6.10: The decorated limestone slab of Tomb Roma 2.

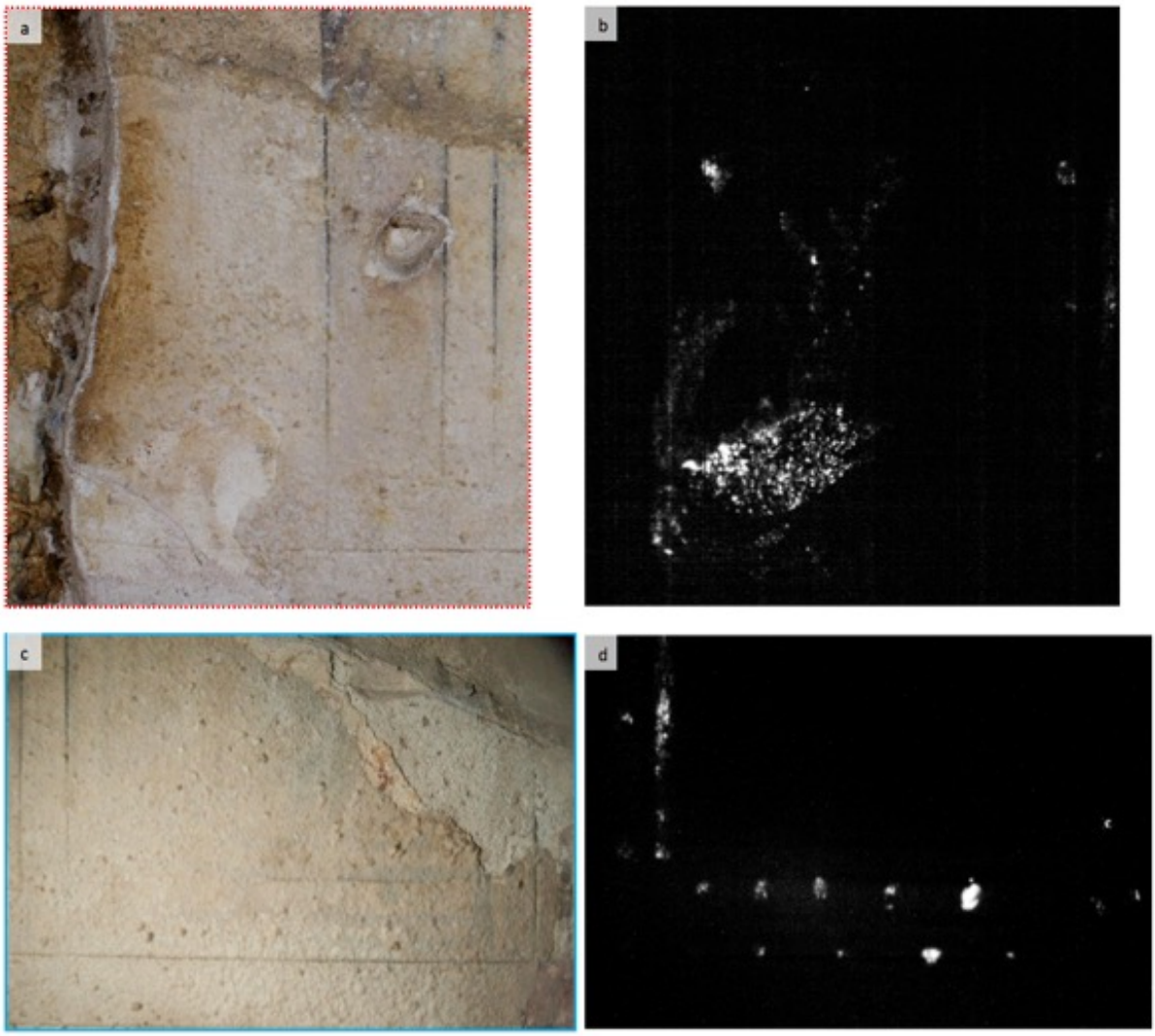

Figure 6.11: The red **(a)** and blue **(c)** dotted regions of interest from Figure 6.10. **(b)** and **(d)** are the visible-induced NIR images produced from LIS and forensic photography studies, respectively.

The style of imagery is presently indistinguishable but the intensity and distribution suggest a non-geometric motif, and the shape of the decoration is inconsistent with the remaining visible decoration in the rest of the slab. It should be noted that the brightest region towards the bottom of the image corresponds to a removal of the gypsum crust layer, but there is no visible indication of pigments (only present in trace quantities identified by photomicrography). Forensic photography produced the NIR luminescence photograph

in Figure 6.11d. There is a clear pattern of dots running along the bottom of the slab and two dots are visible next to a vertical solid line. Though these regions of the slab covered with salt crust feature barely-to-no visible hints of any decoration, the luminescence imagery has provided a new visualization and understanding of the hidden painting for future interpretation by archaeologists, and the maps will provide conservators with a guide for their intervention protocol to protect the slab.

6.3 Byzantine Cypriot Paintings

6.3.1 The Church of St. Paraskevi

The five-domed basilica church of St. Paraskevi (Figure 6.12a) is located in the village of Yeroskipou in the district of Paphos, Cyprus. It is one of the oldest churches in Cyprus, dated to the eighth century AD. This has been suggested for two reasons: (1) a reddish-brown apotropaic (ability to ward off evil) cross painted directly on the stone foundation of the church, which was typical of eighth and ninth century early Christian churches and have been seen in the Eastern Mediterranean [95]; (2) a decorated cross in the eastern-most dome along the nave of the church is also typical of Early Christian churches and comparisons with contemporary churches at the time with similar iconography suggests an eighth century origin [183]. Since its construction, the church of St. Paraskevi has undergone multiple repainting. In 1974–1977, conservation work undertaken by the Department of Antiquities of Cyprus revealed older wall painting phases, and it appears that there are four phases of repainting, dated to the tenth, twelfth, fourteenth and fifteenth centuries [95, 1].

Figure 6.12: **(a)** The church of St. Paraskevi. **(b)** The wall painting above the north aisle's arcade. **(c)** Close-up image of the paintings. The Virgin Mary dates to the twelfth century painting program, while the figure to her proper left, a Roman soldier, belongs to the fifteenth century painting program. **(d–e)** The SRS system, on top of the scaffolding, scanning the face of the Roman soldier.

Until now, no material analysis has been performed on the church's wall paintings. This is the first scientific study of the wall paintings, providing the new technical insight into the painting materials used. Details of two wall painting programs, overlaying each other with the twelfth century program painted below the fifteenth century one, were analyzed. These are located on the north aisle wall above the arcade on the tympanum (Figure 6.12b). The SRS system (Figure 6.12d–e) was applied to collect data cubes of two figures' faces: the Virgin Mary, from the twelfth century program, and a Roman soldier, immediately adjacent to the proper right of the Virgin Mary, from the fifteenth century program (Figure 6.12c). As the paintings were painted high on the wall, the SRS system had to be placed upon a scaffolding to scan the figures.

6.3.1.1 The Virgin Mary (twelfth century phase)

The scan of the twelfth century painting presents the scene of the Dormition of the Virgin, with Mary lying on her bier, surrounded by figures in mourning that are now difficult to discern. Mary wears a dark brownish-purple mantle and has a dark yellow halo surrounding her head. Thin white lines detail her mantle as well as lines on her face. On her mantle and halo parts of the painting have broken off, and small areas of chipped-away painting can be seen throughout the painting. In the scan scene, the bright red bier can be seen towards the right as part of the background, as well as part of the beard of a mourner (Figure 6.13a).

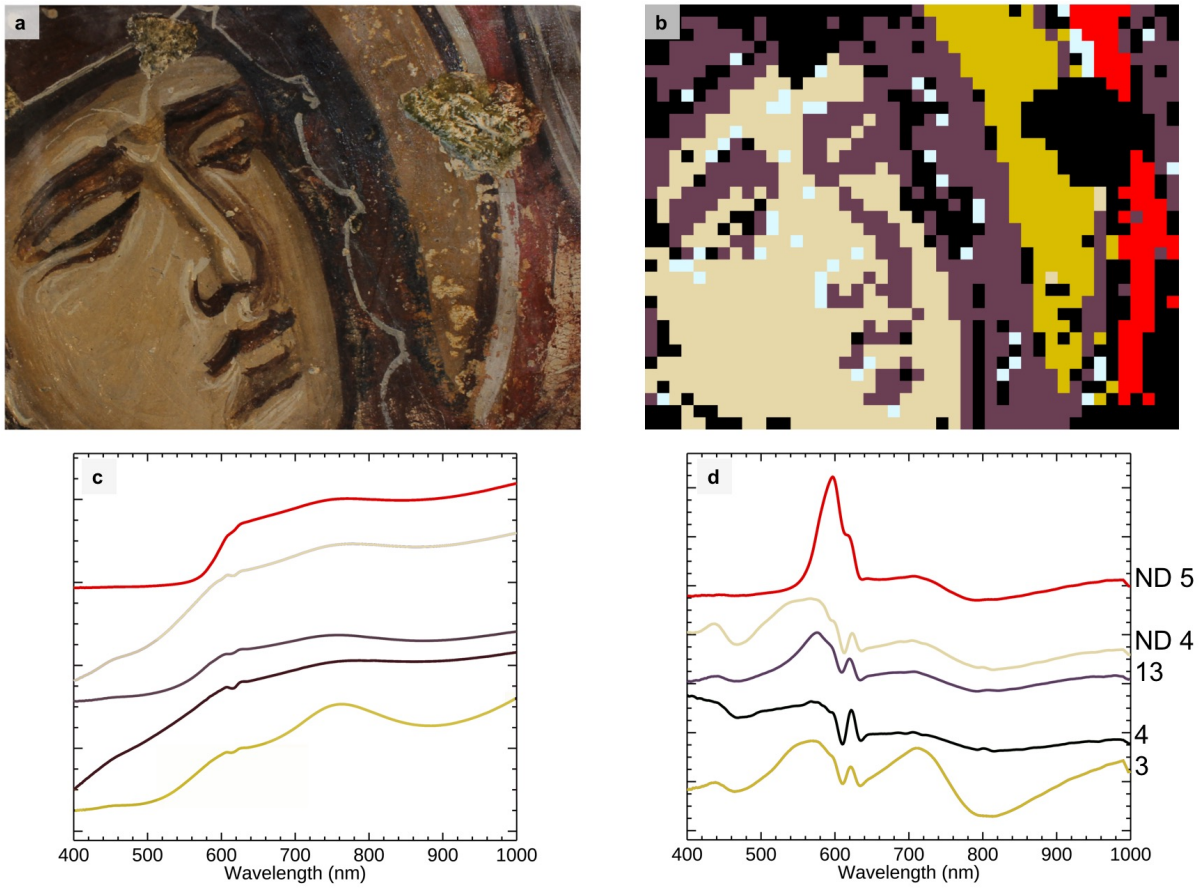

Figure 6.13: **(a)** RGB image of the Virgin Mary. **(b)** The spectral angle map using the 1st derivative endmembers **(d)**. **(c)** are the equivalent reflectance endmembers.

Five unique endmembers were extracted from the VNIR range of the 1st derivative cube that was calculated from the original reflectance dataset. The face of the Virgin was mapped by endmember ND4, which represents yellow ochre mixed with a white pigment because the profile shows increased reflectance intensity and a less saturated spectral profile compared to that of a yellow ochre sample (Appendix A.3.2). The fine white lines on her mantle and face (endmember 4) are most likely made by a calcium carbonate white ($CaCO_3$) deriving from the carbonation of calcium hydroxide ($Ca(OH)_2$), commonly used in fresco application Byzantine wall paintings [205]. The bier is painted with cinnabar (HgS) (endmember 5). The bright red hue and the inflection point with a sharp transition in the spectral profile is due to the bandgap of cinnabar at ~ 2 eV (~ 597 nm). Endmember 5 is not a pure cinnabar

Table 6.2: The 1st derivative endmembers from the scan of the Virgin Mary and their corresponding application and identification

Endmember	**Region**	**Hue**	**Materials**
ND4	Face	Light yellow	Yellow ochre
ND5	Bier	Red	Cinnabar
3	Halo	Dark yellow	Yellow ochre
4	Facial features, mantle	White	Calcium carbonate
13	Facial features, mantle	Brown	Red ochre

sample, as subtle traits of an ochre spectral profile are present, though this would need to be confirmed by XRF measurements to identify Fe. The application of cinnabar here is significant; because it was an expensive pigment and selectively used, its application for the Virgin's bier shows the significance of the scene to warrant its use. The eyes and the mantle of the Virgin are mapped by endmember 13, which is a red ochre pigment. Endmember 3 maps the dark yellow halo of the Virgin. While the endmember matches relatively closely to goethite (Appendix A.1.2), the inflection is shifted to 565–570 nm. The shift in the inflection and the darker yellow hue suggests that perhaps some umber (Fe_2O_3/MnO_2) may have been a part of this pigment. This may be confirmed by further XRF analyses.

6.3.1.2 Roman soldier (fifteenth century phase)

The second figure scanned, from the fifteenth century painting phase, is part of the large scale Crucifixion scene covering the wall. The figure is a Roman soldier (Figure 6.14a), tasked with crucifying Christ. He wears a gold-tone body armor with floral decoration, suggesting this depiction was intended to emulate gilding. His brown hair shows yellow streak tones, and his hand, as well as the arm on his proper right side, has a light yellow flesh tone, with bright white highlights on the fingertips. The collar of the soldier's shirt armor and the sleeve of the hand to his proper right have the same light blue tone. The hands, the soldier's facial features and his hair curls are outlined with sharp black lines. To his proper left is the older painting phase with the Virgin Mary. The broken painting outline of the later phase

Table 6.3: The 1st derivative endmembers extracted from the scan of the Roman soldier and their corresponding application and identification.

Endmember	**Region**	**Hue**	**Material(s) ID**
1	Background	Yellow	Yellow ochre
2	Bier (12th C)	Bright red	Cinnabar, ochre
4	Flesh highlight	White-yellow	Yellow ochre, calcium carbonate
5	Chlamys	Bright red	Cinnabar, red ochre
12	Halo (12th C)	Orange-yellow	Yellow ochre, red ochre
17	Flesh shading	Yellow-green	Green earth, yellow ochre
20	Sleeve, collar	Light blue-green	Green earth
Y2	Mantle (12th C)	Purple	Red ochre
HP1	Hair	Brown	Red ochre, yellow ochre
14	Flesh shading, hair highlights	Light yellow	Yellow ochre
25	Armor	Gold-yellow	Yellow ochre

is clearly visible. The soldier's face appears somewhat discolored, but shading effects along the cheek are clearly visible. The background scene is a yellow color.

The surface of the wall painting was uneven. The reconstructed data cube features a dark region of low signal, caused by the change in distance between the fiber optic cable and painting surface. This dark region, along with the plaster, was masked in the extraction process to remove bad pixels. Due to the fine details in the image scene and the uneven surface of the painting, influencing the spot size captured, the cubes were re-sized in ENVI by upsampling the pixels by a factor of 9 using a cubic convolution interpolation function. A 1st derivative calculation was performed on the resized cube and extracted for endmembers. The upsampling procedure seemed to improve the results of the extraction process compared to the original-sized 1st derivative cube.

Eleven endmembers were selected to characterize the painting materials in the scan scene and used for material mapping (Figure 6.14d, Table 6.3). Endmember 1 maps to the yellow background, painted with yellow ochre. Endmember 4 corresponds to the brighter flesh

tones in the fingers, forehead, and along the nose, which consisted of a mixture of yellow ochre and white, most likely a calcium carbonate-white pigment. The yellow flesh tones and hair highlights were applied with yellow ochre. The bright red tone in the later painting phase (endmember 5) used cinnabar, similar to the red in the older phase (endmember 2 in this dataset). Endmembers 12 and Y2 also represent the older layers (halo and mantle, respectively), matching the endmembers identified in the previous section.

A green earth pigment was applied in the painting for different functions. It was mixed with white and applied as the colorant of the sleeve and collar. It was also used for facial shading of the face, such as along the cheek and neck (endmember 17). The endmember shows a convolution of green earth and yellow ochre. The materials identified with the selective application indicates the use of a *proplasmos*, a dark base layer such as green earth used to outline the face, which was subsequently covered by flesh tones containing red and yellow ochre to produce the effect of darker-toned shading around facial features [147]. The build-up green earth and flesh tones produces a complex stratigraphy that was often found in the Byzantine Cypriot wall paintings, and this technique is similar to the verdaccio technique employed in Italian Medieval and Renaissance painting [37].

The brown hair (endmember HP1) is probably made from a mixture of hematite-rich red ochre and goethite. The gold tone on the armor, in a semi-transparent application, was produced with an iron oxyhydroxide pigment. The spectral features for this pigment are 445 nm (shoulder), 540 nm (inflection), 775 nm (local peak maxima), and 880-900 nm (absorption).

The SRS data cubes were able to provide quantitative in-depth characterization of pigments in the first scientific study of the wall paintings in the Church of St. Paraskevi. Though limited in scope due to the scan region, this novel imaging spectroscopy technique has provided insight into technical applications by the artists and established a preliminary list of pigments used in the twelfth century and fifteenth century-phase paintings. For example, the use of a *proplasmos* with green earth was identified in the fifteenth century phase, though on the Virgin Mary the only forms of dark shading were the same brownish-purple

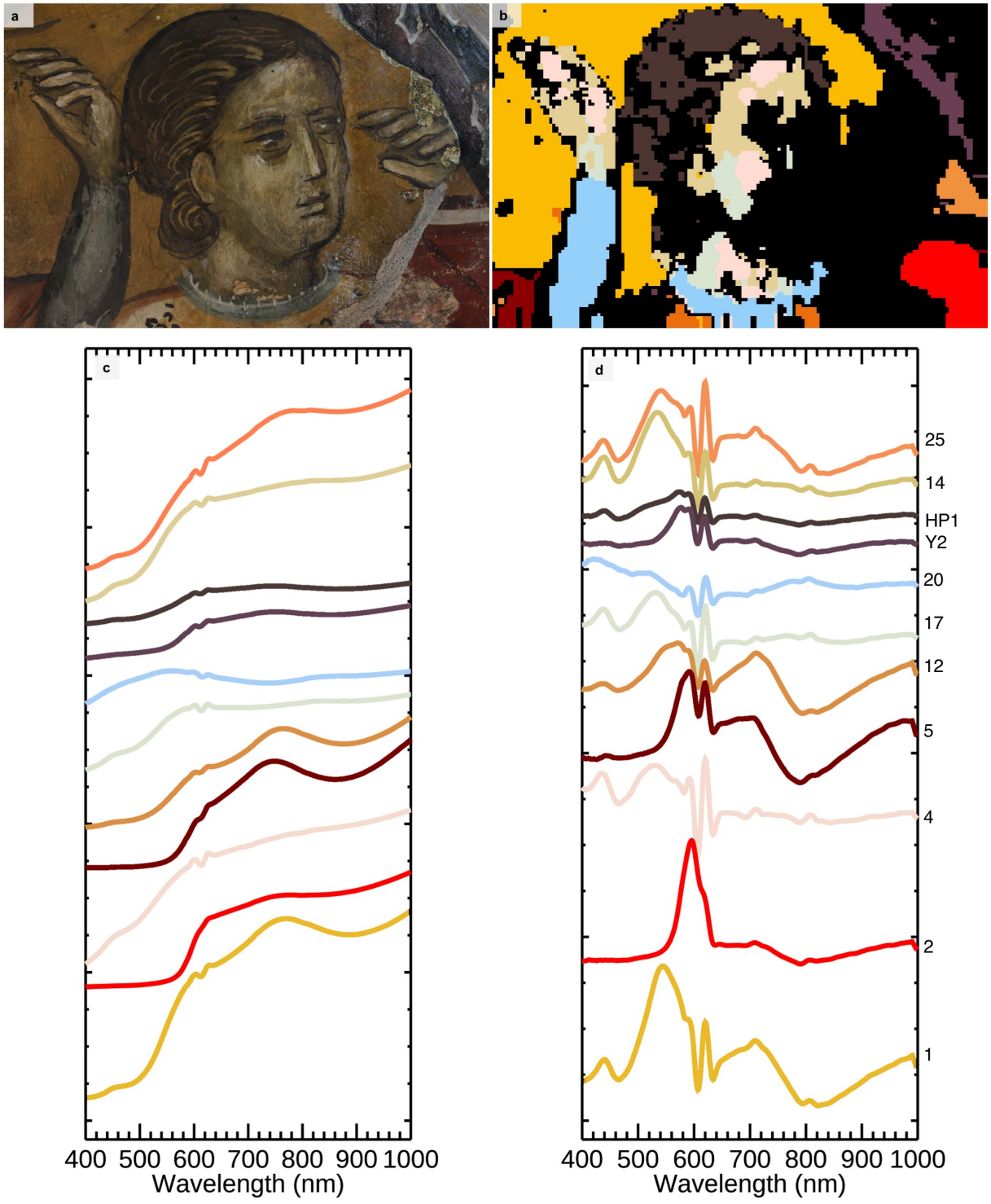

Figure 6.14: **(a)** RGB image of the Roman soldier. **(b)** The chemical map produced from mapping the 1st derivative endmembers **(d)**. **(c)** The reflectance equivalent of the 1st derivative endmembers.

pigment applied to her mantle. Additionally, cinnabar was identified as the bright red hue in the chlamys (a short cloak) in the later painting as well as in the Virgin Mary's bier. Furthermore, the seemingly blue tone was actually a mixture of green earth and white.

6.3.2 The Crucifixion of Christ, the Enkleistra of St. Neophytos

Hyperspectral imaging studies using the Specim IQ camera were performed in the Enkleistra ("place of reclusion") of St. Neophytos (Figure 6.15a), presented previously in Chapter 3. The case study here is a part of the scene of the Crucifixion of Christ, painted in the Cell of St. Neophytos, located over the mantle of the doorway to the Cell (Figure 6.15c). The Cell, along with the Bema and Naos, was one of the original carved out rooms in the Enkleistra (Figure 6.15b). St. Neophytos slept and worked in this space, as indicated by the presence of a stone couch and table. The small alcoves which stored his books served as his library, and the recess in the Cell became his tomb when St. Neophytos died.

The Enkleistra was recorded in his writings to have been painted in 1182 AD. In the Cell, however, there are two painting phases separated by a thin layer of lead white whitewash [111]. Stylistic comparison to paintings in the Bema [133] indicated that the neoclassical paintings styles between the two rooms were very similar. An artist's signature in the Bema by Theodore Apseudes was also dated to 1182/83. The Naos appears to have been painted at a different time, as the style is more monastic and has been given a date of execution for approximately ten years later. Thus, it is believed that the original painting phase in the Cell was not referenced by St. Neophytos in his writings and was performed at an earlier date, but probably not of high quality since it was eventually concealed and never discussed [133].

The region of interest imaged by the Specim IQ camera, designated by the red outline (Figure 6.15c), focused on Christ's feet, as well as a foot from the first painting phase that is most likely a previous depiction of the Crucifixion. Both painting phases have suffered extensive deterioration, as evidenced by the appearance of plaster due to paint loss. The painting also features craquelure patterns. The second painting phase, which dominates the

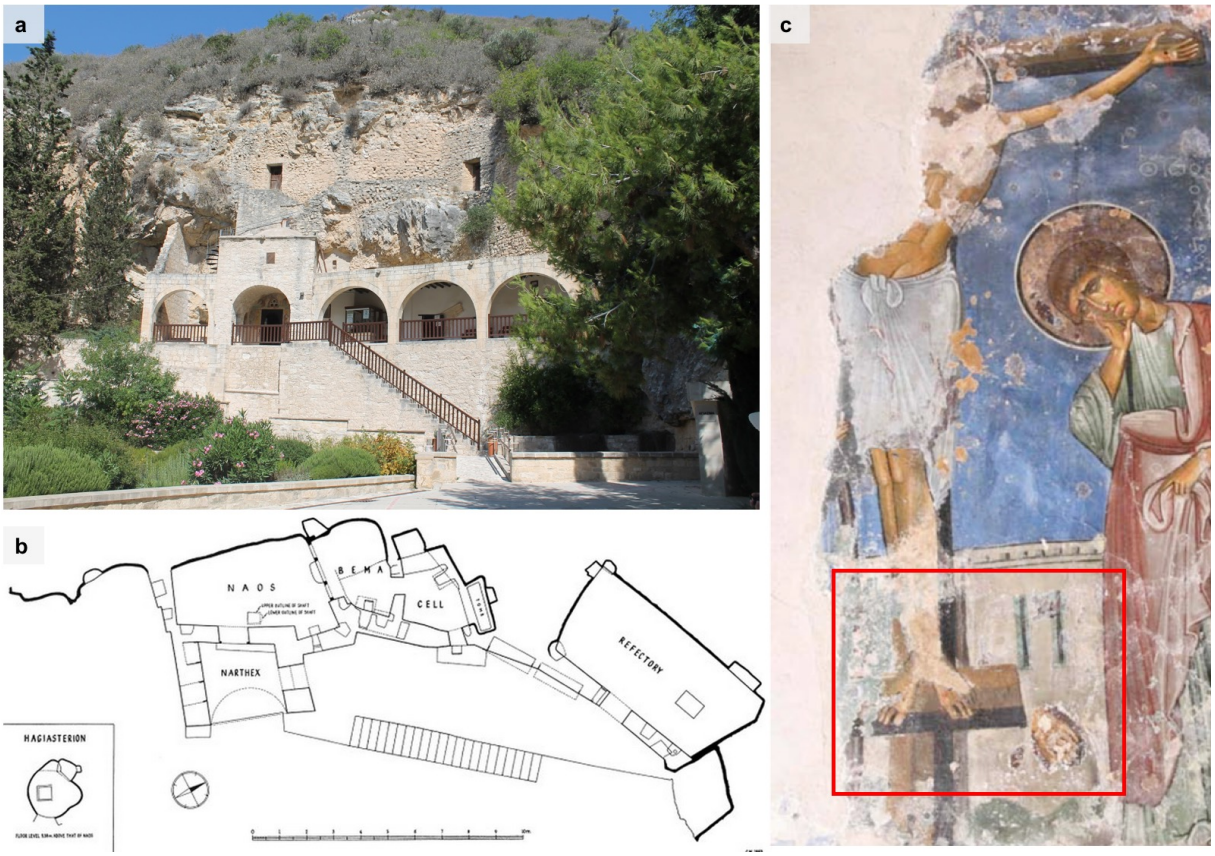

Figure 6.15: **(a)** The Enkleistra of St. Neophytos. **(b)** A top-view schematic of the Enkleistra. **(c)** The Crucifixion painting in the Cell, above the doorway. The red box indicates the scan scene.

scan scene, features a grey wall in the background with two slits featuring two different tones of green and blue-green. The cross is made up of several different hues ranging from light brown to black, representing the three different pieces of wood used to make the cross [133]. The feet of Christ have bright red blood dripping down onto the cross from the nail wounds. The flesh tones of the feet feature a gradient of hues ranging from yellow-green to a light yellow. To the proper left of the cross is St. John, in mourning. The edge of his red chlamys appears as a vertical red band in the scene. Finally, blue-green decoration from the first painting phase is also apparent on the proper right side of the cross, due to the excessive flaking of the second painting phase.

Seventeen endmembers were extracted from the 1st derivative cube and mapped (Figure

6.16b). The reflectance and 1st derivative endmembers can be found in Figures 6.16c-d, and their interpretation in Table 6.4. The flesh tones in this scene are represented by endmembers ND4 and EM22. ND4 is a mixture of red and yellow ochre, which mapped to the foot in the first painting phase, as well as the yellow tones on Christ's feet. The yellow-green flesh shading on Christ's feet was produced from the build-up of green (the *proplasmos*) and flesh-colored tones, indicated by the identification of green earth and yellow ochre spectral features. Green earth was also identified in the original green coloration of the slits in the wall, the region of green at the bottom of the wall (perhaps representing grass), as well as in the first painting phase's green hue. The green pigments identified in the two phases are mapped by two different endmembers (endmembers EM15 and HP6, respectively). Endmember EM15 has a local maximum at 566 nm, while HP6 has a maximum at 547 nm. These are both red-shifted with respect to the reference value for the Cypriot celadonite mineral in Appendix A.3.4. The remaining spectral features of endmember 15 correspond closely to green earth. The reflectance peak for endmember HP6 appears shifted to $\sim$ 845 nm. It also features a more significant absorption at 670 nm, compared to a more subtle absorption by endmember EM15 at 647 nm. The other blue-green and grey-blue tones on the building in the background are due to restoration in-fills of viridian green ($Cr_2O_3 \cdot 2H_2O$) (endmembers ND1 and ND5).

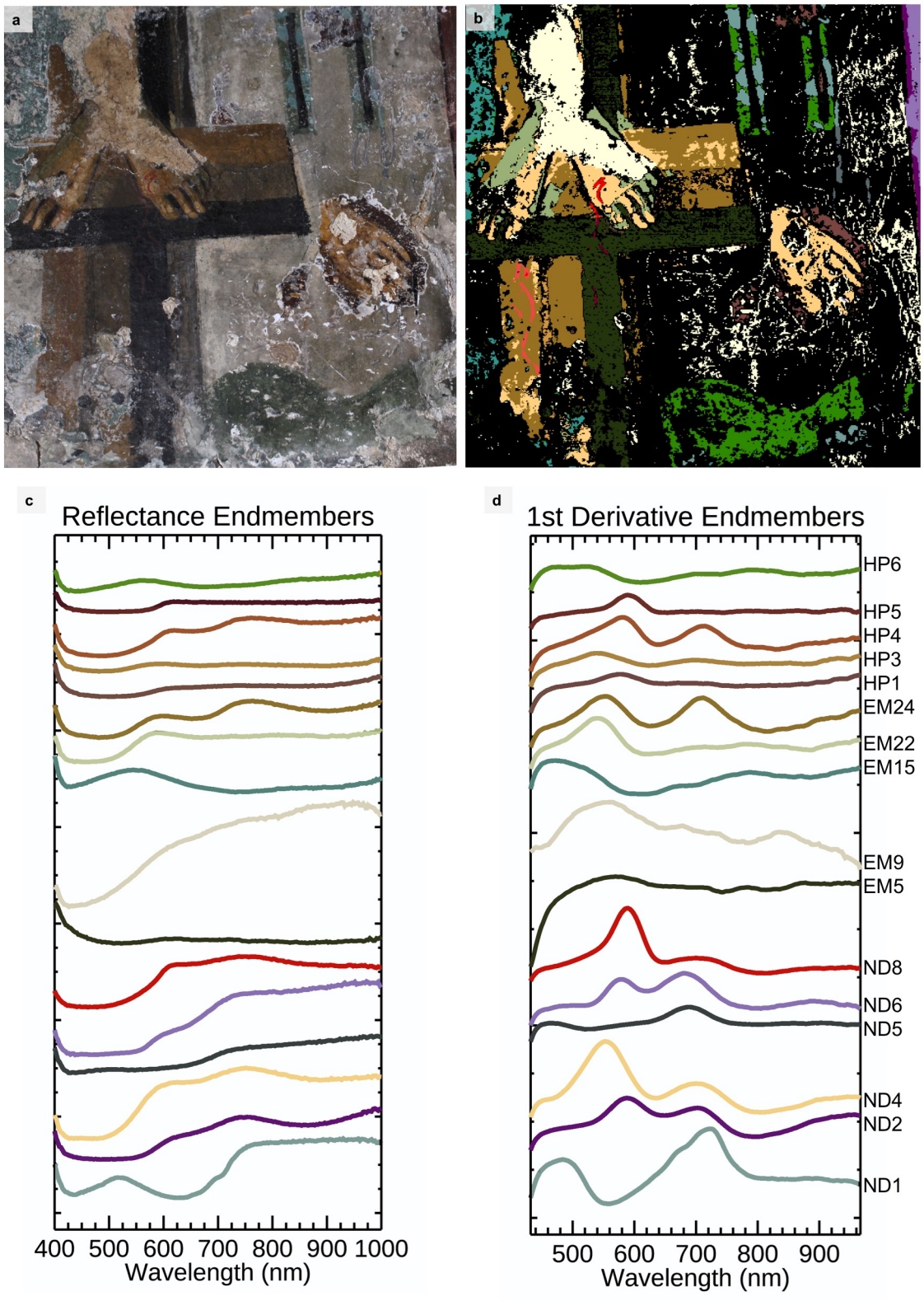

Figure 6.16: **(a)** RGB image of the scan scene in the Cell. **(b)** The SAM map of the scene, using the 1st derivative endmembers in **(d)**. **(c)** The reflectance equivalent endmembers of **(d)**.

Table 6.4: The 1st derivative endmembers extracted from the scan of Christ's feet and their corresponding application and identification

Endmember	**Region**	**Hue**	**Materials**
ND1	Building slits	Blue-green	Viridian green (restoration)
ND2	Chlamys (cloak) edge	Dark red	Red ochre
ND4	Feet	Yellow	Yellow ochre, red ochre
ND5	Building	Grey-blue	Viridian green (restoration)
ND6	Chlamys	Light red	Red ochre
ND8	Blood on feet	Bright red	Cinnabar
EM5	Cross	Black	–
EM9	–	–	Plaster/ Deterioration
EM15	Older layer	Green-blue	Green earth
EM22	Feet shading	Yellow-green	Green earth, yellow ochre
EM24	Cross	Yellow-brown	Yellow ochre
HP1	Feet outline (later and older layers)	Dark brown-red	Red ochre
HP3	Cross	Light brown	Yellow ochre
HP4	Blood on cross (brown area)	Red (faint)	Cinnabar
HP5	Blood on cross (black area)	Red (faint)	Cinnabar
HP6	Ground region	Green	Green earth

Various red tones appear throughout the scene. The red blood flowing from the wounds of Christ has different intensities due to its application over a light flesh tone (bright red), and then over the darker hues of the cross (darker red). These regions are mapped by endmembers ND8, HP4, and HP5. Each endmember clearly identifies the presence of cinnabar. The latter two have subtle ochre characteristics to their spectral profiles, due to the background paint. The selective application of cinnabar for the blood is symbolically significant – the bright red hue and the valuable nature of this pigment highlights the important religious nature of the scene. Different red ochre pigment mixtures were also applied to the chlamys (endmembers

ND2 and ND6) of St. John (the folds and edge were painted with a more intense hue - endmember ND2). Red ochre was also used in the first painting phase, surrounding the single foot (endmember HP1). Endmember HP1 also appears to map to the dark outlines of Christ's toes on the altar. Endmembers EM5, EM24, and HP3 correspond to the black, yellow-brown, and light brown hues of the cross. The black pigment (endmember EM5) was not identified by the reflectance spectrum; this would require another technique such as XRF, which would be able to identify the use of umber, if present. The brown tones of the cross were made primarily by yellow ochre, as indicated by the inflection point and NIR absorption, but the local maxima of the endmembers appear at $\sim$ 745–750 nm, thus these are not pure applications of goethite.

These results demonstrate the importance of chemical mapping in the Enkleistra to identify and interpret the pigment use. The case studies performed in the church of St. Paraskevi and in the Enkleistra are the first examples of imaging spectroscopy applied in Cyprus to analyze the valuable historical wall paintings that are part of the island's rich artistic traditions.

6.4 Challenges and limitations for IQ and SRS applications

The case studies presented here clearly demonstrated the imaging systems' powerful characterization capabilities and the ability to provide insight into ancient and Byzantine painting materials, technical artistic choices, and the pigments' spectral responses in mixtures and layers. However, these systems also have their limitations.

Due to the set fixture of the fiber-optic cable in the SRS system's fiber-optic mount, non-uniformity in the surface of the painting changed the spatial resolution of the pixels. While this would be true for all cameras in this situation, the effect is much larger for the SRS system, as the pixel sizes are $\sim$ 4 mm each, and increasing the distance would increase the amount of information a pixel is collecting, reducing the spatial resolution and introducing mixtures of reflectance signatures of separate yet adjacent pigment applications. In the

case of the Roman soldier, the fine details were already difficult to resolve at this spatial resolution. Furthermore, as the system's collection configuration relies on close proximity to the wall paintings, sloping surfaces cause regions of poor signal, either due to lack of light as the painting is too close for the right illumination projection, or the fiber-optic cable is too far to collect a proper signal from the painting. Fortunately, the tripod ball head accounted for most of the sloped wall painting surfaces, and the scene size is small enough that relatively flat (2D) scenes can be scanned with minimal issue. However, even subtle changes in the distance between the fiber-optic cable and the painting surface can cause spectral artifacts in the data ($\sim$ 600–615 nm) due to the order-sorting filter, meant to filter higher order diffracted beams from the internal diffraction grating before reaching the sensor in the ASD Fieldspec 3. Most appearances of this artifact have been relatively small, thus overall not disruptive to the characterization of the reflectance spectra.

The Specim IQ camera, while featuring a much higher spatial resolution, contains a limited analytical range and a lower SNR, preventing a more thorough characterization of the pigments, especially for subtle changes in the values of diagnostic spectral features and lacking additional characteristic absorptions in the SWIR. Additionally, the ability to manipulate data collection parameters is not practical. The focusing function by the lens of the camera is rough; the scene visualized by the RGB viewfinder does not correspond exactly to the scene scanned by the spectrometer (which is especially problematic for close-up HSI captures of small scale scenes and objects); and the integration time is the only other parameter that can be adjusted, which can only be increased up to 500 ms, impacting luminescence cube measurements. Unlike the live view of the ASD Fieldspec 3's collection software, RS3, it is difficult to get clear, instant feedback of the spectral quality on the small IQ display. The spectral response is also somewhat limiting. The reflectance data cubes often feature a sharp increase in reflectance below $\sim$ 430 nm, which is a significant deterrent for the identification of spectral features close to this wavelength, such as jarosite's diagnostic absorption at 433–435 nm (Appendix A.3.3). The camera is also sensitive to atmospheric effects and features higher noise level above 800 nm. However, as demonstrated by the case

studies presented in this thesis, it has operated as a robust field instrument with the ability to provide preliminary characterization of painting materials and their distribution on wall paintings, the results of which can guide further advanced investigations.

CHAPTER 7

3D modeling with integrated VNIR luminescence imaging

7.1 Motivation

Cameras operating at spectral ranges beyond the visible region of the electromagnetic spectrum have demonstrated the ability to document, characterize, and reveal obscured and invisible-to-the-naked-eye decoration of polychrome works of art including wall paintings, architectural surfaces and three-dimensional reliefs and sculptures [200, 113, 29]. The data output of these technologies, as reflectance and/or luminescence images or chemical maps, provide essential information on an object's history, materials and technique, and condition. However, the format of viewing these data traditionally remains two-dimensional even for three-dimensional objects; in other words, evaluation of chemical imagery in a three-dimensional (3D) space is still overwhelmingly lacking. More so in the field of digital humanities that is a relatively new inter- and multidisciplinary field, concerned with the application of computational and digital tools and methods to humanistic and social science established disciplines like art history, archaeology and conservation (of cultural heritage materials). The application of 3D modeling in these disciplines has been established as an integral method of evaluation of objects of cultural significance. By its inherent nature of storing data on object geometry, topography, color, and structure, 3D modeling serves an important role in data content management and documentation, especially in the survey of excavated archaeological sites, object conservation, and classification and recording of looted, falsified, and widely dispersed artifacts [150, 165]. 3D models of important artifacts

and monuments facilitate accurate reproductions and working models, allowing safe, hands-on interactions with the target, which is especially important for proper handling practices and guiding conservation interventions. In the form of a unique visual data repository, a 3D model is a highly important tool for sharing data, performing secondary research, and educational outreach [177, 157].

In this research, the focus is to extend visualizations beyond the traditional 3D format by incorporating luminescence data that can provide diagnostic fingerprinting of materials, using an improved method to mitigate previous challenges of integrating chemical data into 3D models. This was achieved by looking at current computational and technological methodologies utilized by digital humanities researchers and targeting weaknesses in 3D modeling pipelines that have perpetuated the gap in scientific 3D model outputs.

7.2 Significance of 3D modeling for polychrome objects

3D modeling plays a valuable role for the study of polychromy [4, 119, 180, 177, 99]. Understanding pigmented statuary and other 3D objects is accomplished by studying structure, the object's function, and relationships between the structure and the decorations/materials it features. By visualizing the pigments and decorative scheme of an object in a 3D structure, the colors are being analyzed in an improved context, reproducing the original setting in which their function was intended. The distribution of materials is more clearly seen and understood compared to 2D images. However, weathering, mishandling, and past conservation interventions may have caused loss or concealment of pigmented decoration, leaving in many cases only residual traces. This makes simple photorealistic reconstructions limiting in their capabilities to provide a better understanding of the object.

This challenge can be overcome through functional adaptations of existing methods, by incorporating non-visible radiation datasets illustrating the extent of residual pigments and/or revealing concealed decoration in the constructed 3D models. Integrating scientific data into 3D models provides a platform to visualize data conventionally analyzed in a 2D

context from techniques such as portable spectroscopy (i.e. XRF or FORS) and photoluminescence imaging. Just as identifying colors in context is extremely important for a more holistic understanding of an object, observing chemical data in 3D, also provides an additional perspective for accessibility and interpretation. As demonstrated in the previous chapters, forensic photography, reflectance imaging spectroscopy (RIS), and luminescence imaging spectroscopy (LIS) have proven to be extremely valuable for macroscale analyses in object characterization by progressing from spot collection to 2D chemical maps (on a single plane). The next step is to transition from 2D chemical maps to distribution of chemical maps in a 3D space (volume), by taking advantage of principles of multi- and hyperspectral imagery.

In the past 10 years, researchers have been actively exploring methods of developing 3D models that contain imagery acquired at different wavelengths or spectral bands to feature chemical maps. This research can be categorized by the following lines of inquiry: (1) how to generate 3D content; and (2) how to incorporate additional data into pre-existing 3D mesh structures. The former focuses on technologies and computational modeling that produce photorealistic 3D virtual models. The latter explores how to integrate additional data, i.e. 2D imagery not associated with the original 3D mesh, into the final model. Lerma et al. (2011) combined near-infrared imagery with thermography and RGB photography in different bands for false-color analysis of the monumental structures of Petra, particularly examining the condition and deterioration mechanisms found on the stones [128]. Terrestrial laser scanning was used to build the mesh of the monument and imagery acquired from the different photographic approaches were used to 'drape' over the 3D mesh.

Brusco et al. (2006), Mara et al. (2009), and Pelagotti et al. (2009) developed several of the earliest 3D multispectral imaging (MSI) systems for cultural heritage [33, 136, 151]. Brusco et al. (2006) emphasized the value of 3D modeling and MSI for building with wall paintings, as it helped to revive faded imagery, reveal decoration and trace materials, providing valuable new insight into the relationship between the architecture and the painting. Mara et al. (2009) demonstrated examples of 3D scans of wall paintings from the ultraviolet

to infrared. The 3DIS system by Kim et al. (2012), one of the first 3D HSI systems used in cultural heritage, featured a time-intensive process of approximately 96 hours, from scan to reconstruction, to complete the build of the 3D model [116].

Other researchers have applied novel methods for reconstructions of high-relief objects featuring MSI texture. Kotoula et al. (2015) used a Reflectance Transformation Imaging (RTI)-based approach to get pseudo 3D reconstructions of high-relief surfaces with integrated imagery from UV and IR wavelength ranges [118]. Van der Perre et al. (2018) developed an LED illumination dome that can reconstruct surfaces of objects with multiband data using a modified DSLR camera [154]. A custom software package and viewer was built to collect and visualize the data.

Thus far, only a few groups have documented 3D reconstructions of ancient polychromy or wall paintings clearly identifying UV-induced or Egyptian blue luminescence [126, 97, 197, 137]. A collaboration between Ny Carlsberg Glyptotek and the [HUMlab] at Copenhagen University produced the first reported 3D model in the literature featuring Egyptian blue luminescence [97]. The photorealistic 3D model was produced from a capture of 400 images. The luminescence images were aligned with the RGB images and projected onto the mesh of the model. Regions of fluorescence were filled in with a blue color in attempts to replicate the original figurine's decoration. Details of this approach are a bit unclear on how the luminescence was laid onto the mesh or how many luminescence images were utilized and from which angles, though it appears the image collection process was different for the RGB and luminescence captures. Lanteri et al. (2019) also reported constructions of UV fluorescence and Egyptian blue luminescence models [126]. The former model was produced by keeping the camera and UV excitation source in fixed positions while the object was rotated for image capture. However, it is unclear how many images were captured, nor were screenshots of the model provided to demonstrate the final visualization. Similarly, for the model featuring Egyptian blue, no details on the image dataset were provided, or how exactly the final model was produced with the luminescence, thus making their methodology non-reproducible and inaccessible.

The dearth of multispectral and luminescence-textured 3D models in cultural heritage appears to mainly be a function of the lack of a methodology that is accessible and adaptable technologically. The main challenge of performing multispectral 3D modeling, especially for imagery featuring trace luminescence as seen in the forensic photography and LIS data throughout this thesis, using the same routine as photorealistic RGB modeling is the lack of common tie points between images. A practice in luminescence imaging to get a background context for the material distribution over an object is the allowance of light leakage during capture, and comparisons are usually made between the relative intensity of the luminescent pigment and the background [197]. This is not scientifically robust and provides non-trivial interference with interpretation of the imaging data. Additionally, as shown, the few 3D models reported in the literature do not provide a reliable methodology with sufficient details to promote their approaches to other laboratories and museums. Much of current research in the area of MSI and 3D modeling are continuous adaptations to 3D computational platform or developments of imaging setups specific to the developer, laboratory, or museum. Few research efforts produce both a pipeline and results with intention of dissemination for a widely accessible approach and applicability to collections with multiple objects for comparison. Research in object digitization and 2D to 3D transformations for integration of MSI data into a 3D framework explore relatively advanced algorithms [151, 177, 176, 116], which can limit potential users. Furthermore, systems are often custom designed to a laboratory or museum setting and use non-commercial software, making the system difficult for transport, adaptation, and expensive, as well as user specific.

The objectives of this research were therefore two-fold: (1) to demonstrate multiband analytical/forensic 3D imaging producing multispectral data texture from the UV to NIR, targeting faithful reconstructions of objects with luminescent materials (pigments, binders, adhesives, restoration materials), and (2) develop a simple scientific protocol based on a photogrammetric approach that is accessible by virtually any conservation, archaeological, or scientific laboratory. The methodology proposed integrates chemical data as the source structure of the model, avoiding the requirement for a computational projection of 2D mul-

tispectral texture onto a 3D mesh. It also addresses the challenge of building 3D structures that lack tie points between adjacent images. A practical, streamlined methodology was designed to: be reproducible and adaptable amongst different laboratories using common, commercial technologies; feature relatively rapid acquisition, as the use of portable instruments and the limited access to objects necessitate this; and provide instant feedback of the quality of the imagery. The following case study was used as proof of concept for the proposed method.

7.3 Case study: Canosa funerary vase

A polychrome Canosa terracotta funerary head vase, previously referenced in the case study in Chapter 2.1, from the J. Paul Getty Museum (accession number 81.AE.157) (Figure 7.1) was selected for the 3D modeling exploratory research. In the forensic photography and spectroscopic investigation [113], the pink and blue pigmentation that covered the diadem, the robe of the figurine, and decorated the facial features as well as the surrounding leaves were identified as madder lake and Egyptian blue, respectively. Furthermore, the object has undergone conservation treatment. As such, the Canosa vase served as an excellent case study for demonstrating 3D reconstructions of a polychrome object with multispectral data texture.

7.3.1 Data collection

The workflow developed considers the size and shape of the object under study and the constituent materials used to create the object; in this case, the pink (madder lake) and blue (Egyptian blue) with characteristic VNIR luminescence emissions decorating the Canosa vase. Using the taxonomy structure developed by Pintus et al. (2016) [157], the digitization methodology applied here is classified as a global geometric analysis focused on the reconstruction of one single object to serve various cultural heritage applications (novel visualizations and interpretations of the object, conservation studies and approaches, monitoring,

Figure 7.1: RGB images of the Canosa vase (A.N. 81.AE.157).

and large collection analyses, i.e. database collections).

Image data was collected to produce three separate 3D models: (1) photorealistic (RGB), (2) visible-induced photoluminescence of ancient pigments Egyptian blue and madder lake and (3) UV-induced visible fluorescence. This was achieved applying the photogrammetric approach 'structure-from-motion' (SFM) using RGB photography and forensic photography principles described in Chapter 2. SFM photogrammetry requires multiple images to be acquired at numerous angles with significant overlap between them and coverage over the object to provide multiple common tie points between adjacent images (Figure 7.2). This minimizes the gaps within the 3D mesh and facilitates reliable feature extraction in a 3D reconstruction algorithm [204].

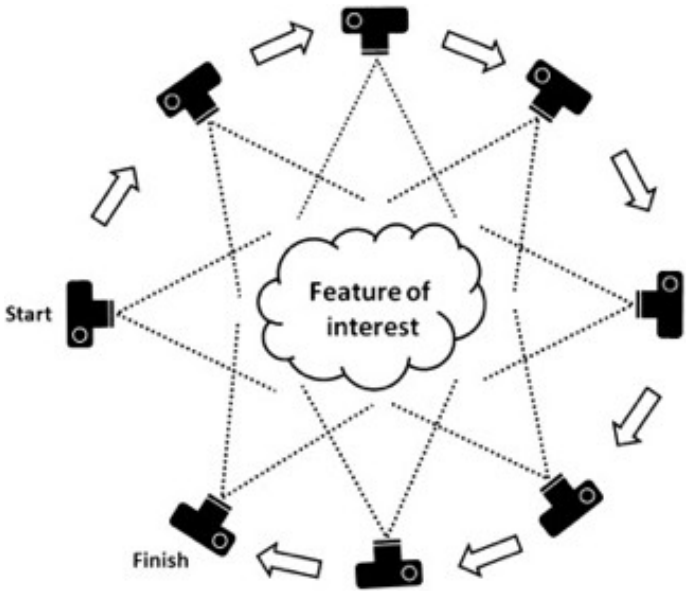

Figure 7.2: Schematic demonstrating the implementation of the 'structure-from-motion' imaging approach to achieve sufficient coverage over the object to build a complete 3D mesh [204].

Image acquisition utilized both systematic imaging at set degree intervals and free-hand acquisition for high relief surfaces on the top and bottom of the figurine to ensure full photographic coverage in the SFM approach. Both image acquisition methods utilized a Nikon D90 12.3-megapixel digital single-lens reflex (DSLR) modified camera (internal hot filter removed) with a 60 mm lens. For the systematic imaging, the figurine was placed upon a PAMCO VR1040 360 photography turntable and photographed at 15-degree intervals. Four sets of twenty four raw data (.NEF) images (visible, Egyptian blue capture, madder lake capture, UV-induced visible fluorescence) from the systematic imaging and ten RGB images from free-hand acquisition were taken to create the three 3D models. The camera, vase, and turntable were kept in the exact same location for each set of images.

First, the RGB image set was collected using the Nikon D90 modified camera and a visible filter (λ = 400–700 nm; PECA 916) (f-stop 16, exposure time $\frac{1}{4}$ s), This dataset served two purposes: to create the RGB model and to provide a background context to increase the number of common tie points in the visible (Vis)-induced luminescence model construction.

Second, analytical forensic photography was applied to acquire the scientific imagery integrated into the UV and visible-induced luminescence 3D models. A Mini-Crimescope MCS-400® from SPEX Forensics was used for photoexcitation of luminescent materials on the surface of the object. Coupled with the modified Nikon D90 camera and the appropriate bandpass filters on the camera lens, the photoluminescence of Egyptian blue and madder lake were acquired separately in consecutive image sets. The photoluminescence of Egyptian blue was acquired with photoexcitation $\lambda_{ex,max}$ = 600 nm and emission capture between $\sim$ 900–1000 nm (f-stop 8, exposure time 2 s) using a Peca 910 filter. For madder lake, photoexcitation was achieved with $\lambda_{ex,max}$ = 535 nm and emission capture between $\sim$ 580–700 nm using a red filter plate (f-stop 10, exposure time 1 s). Finally, for the UV-induced visible luminescence model, to capture the luminescence of potential binder materials and past conservation treatments, photoexcitation occurred in the UV (λ_{ex} = 300–400 nm) and emission was captured in the visible with a PECA 916 filter (f-stop 8, exposure time 4 s). A Spectralon® SRM-99 diffuse reflectance standard and X-Rite Color Checker Passport was photographed with the object as a calibration target for image pre-processing. Further technical specifications of the Mini-Crimescope MCS-400® and the filters used for luminescence excitation and capture are detailed in [113].

7.3.2 Model construction

The model construction process required two steps: image pre-processing for color correction and necessary image overlay, and model assembly, using Agisoft Photoscan Professional, a commercial SFM Dense Multi-View 3D reconstruction (SFM-DMVR) software.

7.3.2.1 Image pre-processing

The raw (.NEF) images were converted to .DNG files using the Adobe DNG converter program and imported into Adobe Photoshop. In Camera Raw, the visible images were color corrected, the only requirement for the RGB model. For the visible-induced luminescence model, at each capture angle, corresponding images of madder lake luminescence (Figure

7.3a) and Egyptian blue luminescence (Figure 7.3b) were inserted into R and B channels, respectively, of a single image (a black image was inserted into the G channel). This composite image was overlaid onto gray-scaled images from the visible dataset of the Canosa vase (Figure 7.3c) to create a set of 2D false-color photoluminescence images mapping the distribution of the pigments at each angle (Figure 7.3d). The UV-induced luminescence images were not processed beyond slight brightness/contrast adjustments. This was a test for the UV-induced luminescence model to see if the fluorescence images had sufficient context from the object's overall fluorescence to produce a complete 3D model. Thus, they were not overlaid onto the gray-scaled images. These final three image sets were used as the source data for the RGB, the visible-induced luminescence, and the UV-induced luminescence models.

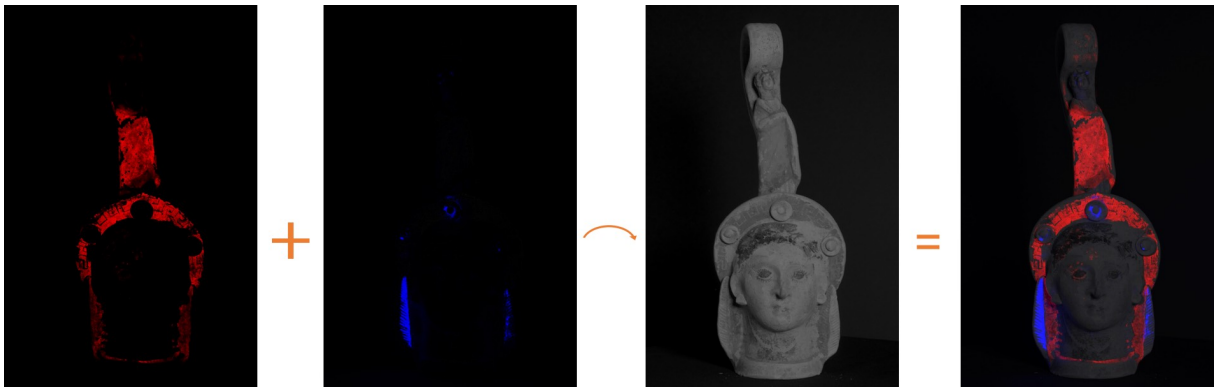

Figure 7.3: **(a)** Madder lake photoluminescence resulting from excitation at 535 nm and capture between $\sim$ 580 – 700 nm. **(b)** Egyptian blue photoluminescence, excited at 600 nm and captured between $\sim$ 900 – 1000 nm. **(a)** and **(b)** were combined in Adobe Photoshop and overlaid onto gray-scaled images of the vase **(c)**, resulting in the final visible-induced luminescence composite image **(d)**.

7.3.2.2 Model assembly

Each model was constructed separately within Agisoft Photoscan Professional at the UCLA Technology Sandbox. Images from the data collection were imported into Agisoft Photoscan Professional, a commercial SFM Dense Multi-View 3D reconstruction (SFM-DMVR) program. This powerful software allows extraction of features acquired at different images depths to form a 3D mesh of non-uniform density [120]. This is extremely advantageous when

working in non-laboratory settings as free-hand photography becomes a viable approach for data collection and input into the reconstruction algorithm; additionally, regardless of environment, it facilitates rapid data acquisition, significantly speeding up the imaging process and therefore the overall 3D modeling time frame.

The RGB model was the first construction, followed by the visible-induced and UV-induced luminescence models. Each image in the RGB set was masked within Photoscan to remove the background in the model construction. To expedite the removal background process in subsequent constructions, the masks were saved and applied to the image data for luminescence-texture 3D models, which was possible due to maintaining the same capture angles between the image sets. After masking, the images underwent automatic alignment, using the highest accuracy settings. Some minor, yet straightforward manual alignments were also necessary in the RGB and visible-induced luminescence models – these corresponded to the regions of freehand photography at the top of the Canosa vase.

Next, the highest quality dense point cloud was formed (an example of the visible-induced luminescence model progression can be seen in Figure 7.4a), which facilitated the mesh construction (the largest polygon/face count was selected) (Figure 7.4b). Lastly, the texture was applied (Figure 7.4c), culminating in the final form of the 3D models. It is important to note that in the visible-induced and UV-induced luminescence models the luminescence texture was inherent in the source imagery, and therefore no additional images or manipulation of the texture were necessary in this stage of the construction.

Table 7.1 summarizes the camera parameters for image capture, the number of images used in the model construction, and the number of points in the dense point cloud used to form the 3D models' meshes.

Table 7.1: Summary of image acquisition details and the number of points in the dense point cloud per model.

Model	Images	Capture details	Points in dense cloud
RGB	34	f/16; 1/4 sec	4,189,776
Vis-induced luminescence	33	–	4,026,872
Madder lake capture	33	f/10; 1 sec	
Egyptian blue capture	33	f/8; 2 sec	
UV-induced visible luminescence	24	f/8; 4 sec	11,614,184

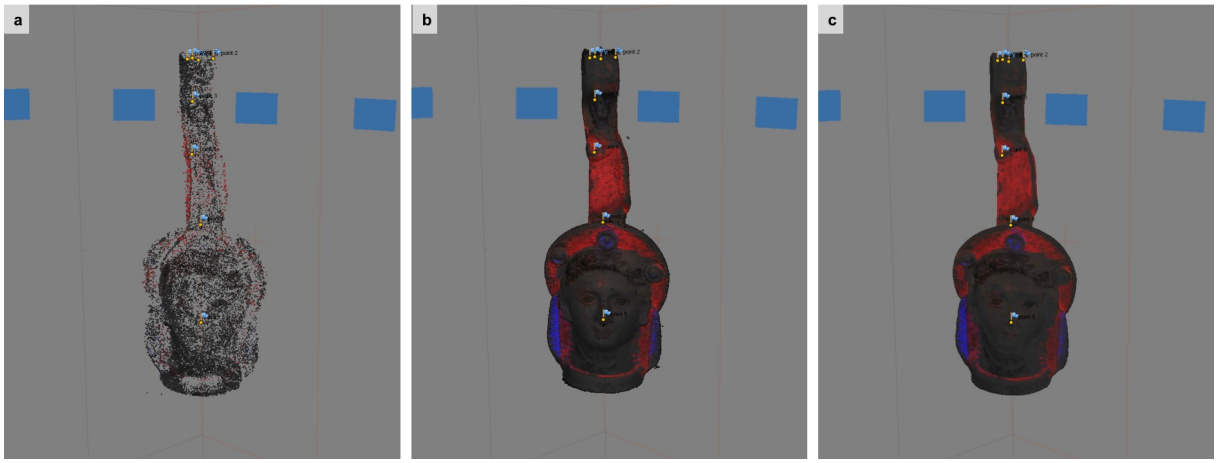

Figure 7.4: **(a)** The dense cloud formed in Agisoft Photoscan Professional of the visible-induced luminescence model. **(b)** The model after mesh construction. **(c)** After application of texture; the final form of the 3D model. The small flags on the model correspond to the points of manual alignment.

7.3.3 Results and discussion

Three models were produced from the image collection and model assembly process: the RGB, visible-induced and UV-induced luminescence models. 2D captures of each 3D model from the front, side, and back are shown in Figures 7.5-7.7. The RGB model (Figure 7.5) provides a realistic reconstruction of the Canosa vase in its present state. It provides a tool for recording and monitoring the condition of the vase. Future documentation of the vase, whether it be 2D images or a new 3D model, can be compared to the current model.

Figure 7.5: The final photorealistic (RGB) model, shown from the front, side, and back.

The visible-induced luminescence model (Figure 7.6) shows the distribution of two pigments, madder lake and Egyptian blue, whose luminescence were collected separately but integrated into a single model. The areas appearing in blue correspond to Egyptian blue, as assigned in the false-color composite images. Egyptian blue was used to decorate the disks on the diadem of the vase, as well as the leaves on either side of the head. A faint luminescence also appears on the wreath of the small figurine located on the handle of the vase. The application of madder lake, appearing in red, extends much further over the vase. It was applied liberally on the other half of the feathers by the face, the diadem, and the robe of the small figurine on the handle. The forensic imagery also detected trace applications on the disk decoration on the top of the handle, as well as her proper right eye, forehead, in her hair, and on the back of the handle.

Figure 7.6: The final integrated visible-induced madder lake and Egyptian blue luminescence model, shown from the front, side, and back.

In the UV-induced visible luminescence model (Figure 7.7), a faint red luminescence appears over the pink regions of the diadem, feathers, and the robe of the small figure on the handle. A white-blue luminescence is present in the eyes of the face, more so in her proper right eye, as well as in her hair above her eye. This luminescence also appears along her neck, along her forehead between the diadem, and in the feathers. A bright region is present on the back of the handle.

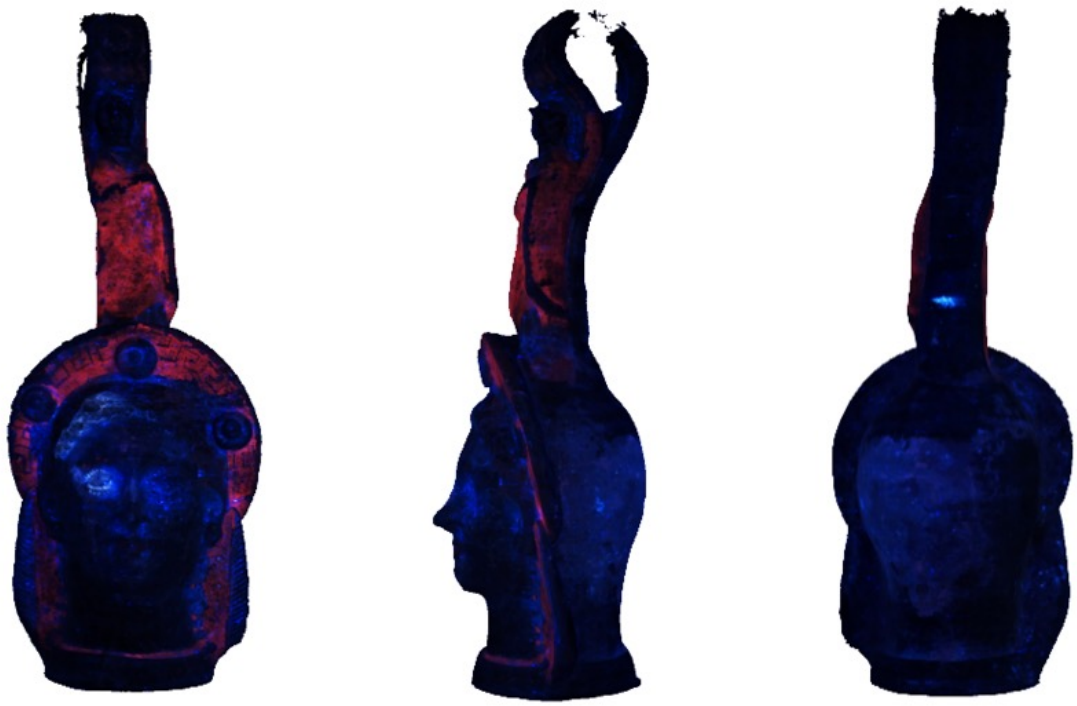

Figure 7.7: The final UV-induced visible luminescence model, shown from the front, side, and back.

Using the models as complementary 3D documentation is also extremely informative. For example, the UV-induced visible luminescence model is an important resource for conservators to identify past interventions and to document new treatments, because glues, adhesives, and other consolidants tend to absorb in the UV and emit in the visible. However, due to the lack of spectral data in this type of imaging (i.e. using a DSLR camera), the UV-induced visible luminescence model alone cannot confidently identify madder lake, which also absorbs in the UV and emits in the visible, similar to those other organic luminescent materials in the object. The visible-induced luminescence model on the other hand, targets madder lake based on its characteristic structured double absorption in the green region of the visible spectrum. Therefore, based on its visible-induced visible luminescence, madder lake can be mapped. However, other red lake pigments used in antiquity such as cochineal and lac with similar absorption and emission behaviors may also be responsible for this luminescence [66, 122, 182, 135]. Additional non-invasive characterization

by FORS, or minimally-invasive analyses by surface-enhanced Raman spectroscopy (SERS) or high performance liquid chromatography (HPLC) can confidently identify the organic red colorant.

In the proper right eye of the vase, the bright white-blue luminescence in the UV-induced visible luminescence model (Figure 7.8a) matches the false-color red luminescence that appears in the visible-induced luminescence model (Figure 7.8b). This appears the same for the luminescence in the black hair. The faint red in the UV-induced luminescence model and the red in the visible-induced luminescence model that appear along the eyebrow and forehead also correspond to similar regions. This suggests that all of these regions contain madder lake. In the eye, using the RGB model as a reference, it appears that madder lake was mixed with a white material to dilute the pigment and reduce the intensity of the hue, hence the difference in luminescence compared to the pink dots that appear red. The black lines of the eyelash painted over the white background also support that this is not a restoration. However, the soft white luminescence that appears throughout the head (nose, inner proper right eye, left eye, along the forehead) and the feathers suggest the application of a conservation or retouching material.

The comparison of the UV-induced visible luminescence and visible-induced luminescence model also provides important insights into the artistic production and restorations. By comparing the regions of the red false-color luminescence to the decoration in the RGB model, it is possible to distinguish between madder lake and other red pigments (such as hematite-rich red ochre) used to paint the figurine. For example, the red-pink tear drops in the eyes, the lips, the pink ear decoration on the head, as well as the brick red hair of the small figurine do not fluoresce in the visible-induced luminescence model. This suggests that a pigment such as red ochre, which absorbs in both the UV and up to $\sim$ 550 nm and quenches the luminescence, was used.

The visible-induced luminescence model also gives insight into how Egyptian blue and madder lake were used together. In this figurine, it seems that the two pigments were used completely distinctly. The purple-like tones that appear on the small figurine were therefore

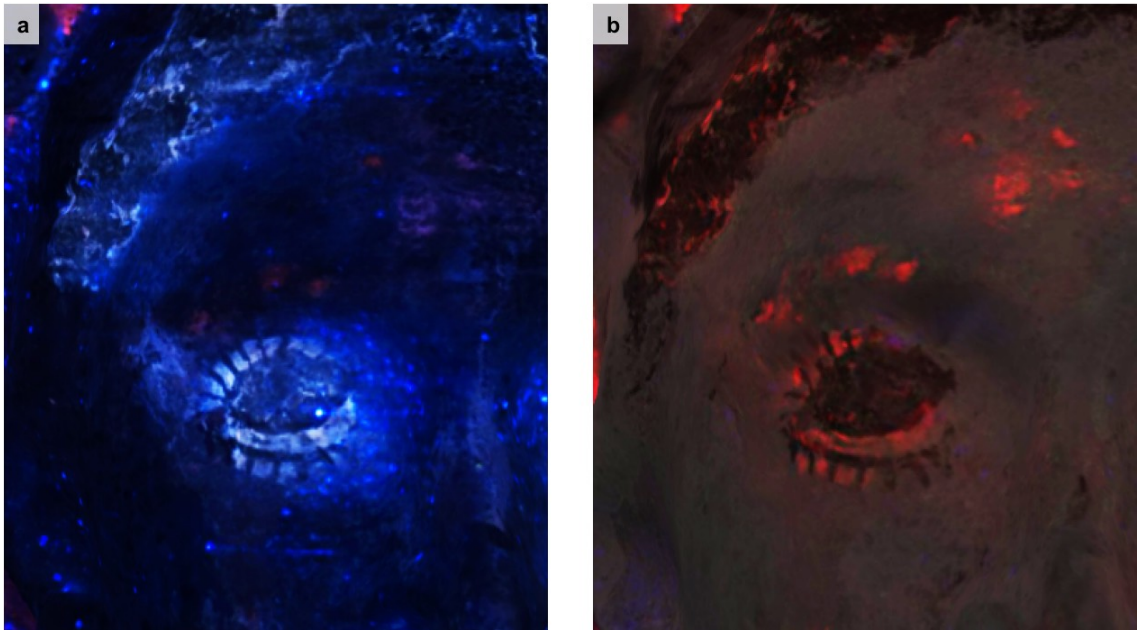

Figure 7.8: Close-up of the proper right eye of the Canosa vase in the **(a)** UV-induced visible luminescence model and the **(b)** visible-induced luminescence model.

not produced using a mixture of Egyptian blue and madder lake.

The test to construct the UV-induced visible luminescence model without overlaying the images over a background produced positive results. Examination of the model revealed gaps at the top of the handle and the inner curve, as well as the very bottom of the vase. The gaps in the inner handle were due to the extremely dark capture conditions where there was no luminescence, while the tops and the bottoms of the model corresponded to the regions that required free-hand photography (only performed for the RGB photographs). However, the remainder of the model featured no gaps, suggesting that UV-induced visible luminescence models can be created with even faster processing than the visible-induced luminescence models featuring ancient pigments, which do require a background context.

7.4 Evaluation of the 3D luminescence imaging methodology

The applied methodology and resulting models will be evaluated by parameters in the criteria framework developed by Pavlidis et al. (2007) [150]. The adaptability of this methodology

is also considered.

Accessibility of technology

The methodology aimed to utilize instruments and software common within scientific and conservation laboratories, such as Adobe Photoshop, regular and modified DSLR cameras, UV and visible light sources, as well as filters for visible and infrared capture. If necessary, low-cost motorized 360-degree photography turntables are available. In this research, Agisoft PhotoScan was available through UCLA Technology Sandbox. However, an accessibly-priced node-locked license may be purchased for the SFM-DMVR software. Additionally, free, open-source 3D modeling packages with the ability to build models from imported photographs can potentially be utilized, as the luminescence texture is inherent to the images and no advanced post-processing is necessary. Image datasets can be pre-masked in Adobe Photoshop, in this case. Computer system requirements to build the models can vary on the complexity of the target object. For small scale models ($<$ 100 photos) built under the highest quality settings in PhotoScan, 8 GB should be the minimum system memory, which is relatively standard amongst laboratory computers. Note that these models used less than 35 photos in their construction. In consideration of working hours, the time required to acquire the data, pre-process the images, and produce a single 3D model was under two days.

Material of the target object

The Canosa vase was constructed with pigments common for ancient polychrome statuary. Forensic photography was an ideal approach to identify and map the diagnostic photoluminescence [201], as well as conservation treatments. Visible-induced near-infrared (NIR) luminescence imaging is often applied on wall paintings and polychrome sculptures from antiquity to identify the presence of Egyptian blue, as the use of this special pigment was quite widespread in the Old World [109]. Museum and archaeological collections would benefit greatly from 3D chemical mapping to identify Egyptian blue, madder lake, and other photoluminescent materials. However, other materials and signatures can be probed by varying

the illumination and capture configurations (this is an advantage of using an alternate light source (ALS)).

Size of the target object

The size and weight of the Canosa vase allowed it to be placed on the photography turntable. It must be noted here that care should be taken to select a turntable with a sufficient load capacity. However, if an object is immovable, too large or too heavy to be placed on a rotational stage, this methodology can be adapted to mobile image collection. In moving around the object, RGB, UV-induced luminescence, and visible-induced luminescence imagery should be collected at the same vantage point before moving on to the next angle. The image pre-processing and 3D construction methods remain the same.

Portability of the equipment

All of the instrumentation utilized in the image acquisition are highly portable. For data collection in the field, lighting can be adapted to battery powered sources, or a field-deployable generator can be used.

Accuracy of system

As a result of the 3D analytical imaging, four high-resolution image datasets were produced. With this straightforward technique using commercial software packages, it is inevitable that a small amount of resolution will be lost in the models' construction. However, the level of resolution in the reconstructed luminescence models provide a sufficient detail to visualize the application and distribution of the conservation materials and the pigments.

Minute manual alignment of a few madder lake and Egyptian blue photoluminescence images were performed in Photoshop in the creation of the false color composites, as the object and/or turntable seemed to have shifted slightly within the rotation of the turntable between the different imaging schemes.

Texture Acquisition

One of the most important advantages of this methodology addresses the challenge of constructing 3D models with multispectral texture. Attempts to build a model in Photoscan from images such as Figure 2a and 2b would be unsuccessful as there is insufficient overlap and 'background' information to build a proper mesh of the figurine; additionally, proper context is missing for where the luminescence is located. This is demonstrated in Figure 7.9 - a visible-induced luminescence reconstruction of the masked composite luminescence images without a gray-scale RGB image as background (i.e. Figures 7.3a + 7.3b only). The results are quite poor and demonstrate the long-standing difficulty of producing multispectral-textured models.

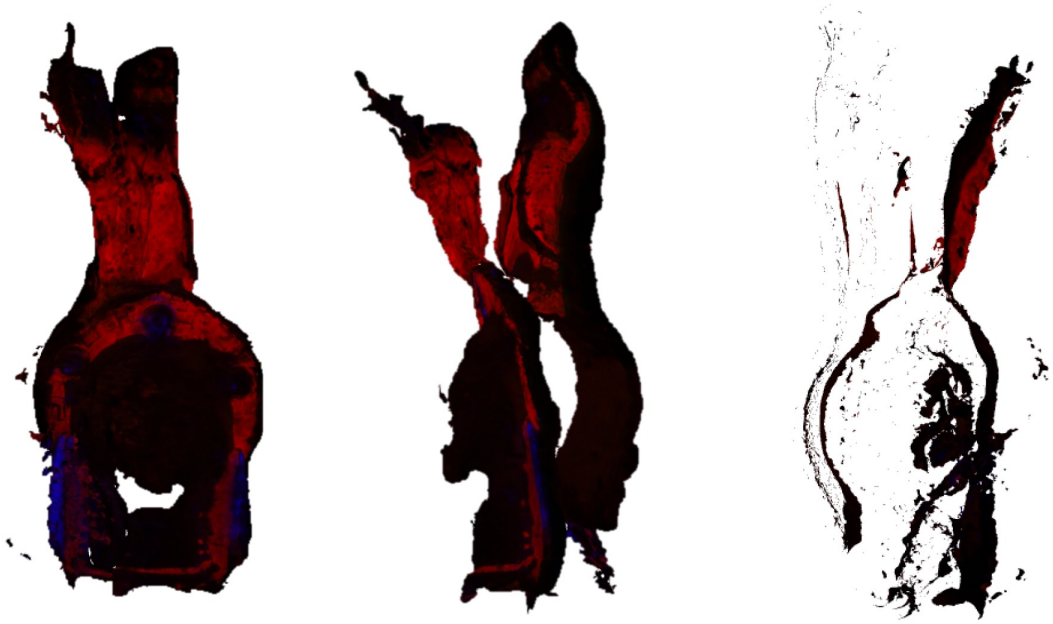

Figure 7.9: An alternate visible-induced luminescence 3D model, shown from the front, side, and back, constructed from masked composite luminescence images but with no overlay onto the gray-scaled RGB dataset for a background context. The poor reconstruction demonstrates the challenge of multispectral texture mapping due to the lack of common tie points between images.

By using the photoluminescence imagery as the source data of the point cloud, it re-

moved the requirement to map any additional texture to the mesh, simplifying the model construction. It was also demonstrated that the masked UV-induced luminescence images had a relatively sufficient luminescence from various materials to produce an accurate mesh, not including the gaps at the top and bottom of the model which were extremely dark or not directly imaged with UV excitation. It would be interesting to perform more tests of UV-induced luminescence model constructions of different objects to further evaluate the approach with minimal image processing.

Productivity of technique

The productivity of a technique is a measure of automation and efficiency in the approach. The simplified construction of the multispectral texture 3D models in Agisoft Photoscan relies on careful image acquisition and pre-processing. The image pre-processing, including the manual overlay of the photoluminescence imagery in Adobe Photoshop, is slightly time-intensive (several hours). However, the reconstruction in Photoscan is relatively fast and the multispectral 3D constructions take less than two days to produce, from collection to reconstruction, using the straightforward, repeatable methodology detailed here.

Skill requirements

Another important advantage of this methodology is the removal of the requirement for in-depth computational knowledge for the digital mapping of luminescence texture on an object. The aim for this approach was to be accessible by archaeologists, conservators, and investigators from various specialties by employing standardized laboratory instrumentation and commercial software with ease of use, using available documentation, without additional computation. This was successfully achieved and suggests this technique to be viable for use across many archaeological, cultural heritage, and forensic laboratories.

Adaptability

This approach can be easily adapted through variation of cameras, filters, and excitation sources to produce reflectance and emission signatures and subsequent mapping of other features of interest in 3D. Extending this approach to UV or IR reflectography, or further to MSI applications with multiple spectral bands will produce valuable models to help with an object's interpretation. 2.5–3D artifacts of various sizes can be imaged and modeled, as well. Furthermore, the imagery produced can be input into other image reconstruction softwares besides Agisoft Photoscan.

7.5 Summary

Macroscale 3D chemical imaging and the integration of multispectral texture in 3D models for cultural heritage applications are relatively under-developed at this point in time. In this exploratory study, two novel luminescence-textured 3D models were successfully produced utilizing a user-friendly, technologically-accessible approach, developed for 3D luminescence imaging with diagnostic emission signatures of important ancient pigments and conservation interventions.

CHAPTER 8

Conclusion

In this research, different advanced imaging spectroscopy systems and chemical sensing technologies were tested to characterize archaeological and historical paintings (materials, production sequences, condition, etc.) and to demonstrate the effectiveness of these methodologies in filling the technological gap in scientific fieldwork.

An extensive in situ non-invasive analytical study of ancient and Byzantine Cypriot wall paintings ranging from macroscale hyperspectral imaging spectroscopy (HSI) to field-deployable chemical sensing techniques such fiber-optic reflectance spectroscopy (FORS), X-ray fluorescence spectroscopy (XRF) and forensic photography provided high specificity analysis leading to unbiased identification of painting materials used in wall painting decoration of domestic and funerary spaces from the ancient city of Nea Paphos and other Byzantine monuments, and the operational sequences for their production. Pigments identified for the first time in ancient Cypriot paintings and sites such as red lead, madder lake and realgar (the latter two identified only as raw pigment pellets), expanded the ancient artists' palette and raised new questions about the function of specific pigment use in Cyprus during this time. Reflectance and luminescence imaging spectroscopy, not previously applied for characterization of wall paintings on the island, helped to deconstruct and interpret the stylistic practices of the ancient artists through in-depth materials characterization of complex pigments mixtures and multi-layered stratigraphy to achieve specific aesthetic qualities. Derivative spectroscopy proved to be a powerful approach in the extraction of unique endmembers by distinguishing subtle changes between pigment mixtures and identifying diagnostic spectral features. The materials characterization and mapped distribution of the various mixtures used to shade and decorate facial features on the figurative paintings

helped to provide scientific support to the technical styles described in ancient texts.

Using both forensic photography and luminescence imaging spectroscopy (LIS) to identify Egyptian blue in the ancient paintings provided several important results: it facilitated the recovery of weathered and concealed decoration in ancient tombs; it identified the presence of Egyptian blue in mixtures where its signature was masked and unable to be confidently assigned by reflectance spectroscopy alone; and it revealed artistic applications of Egyptian blue mixed with white to produce cold tones in the tunics and outline facial features of figurative paintings, as well as for creating three-dimensionality through shading in the face and neck. The distinctive application of outlining facial features with washes containing Egyptian blue in a Cypriot figurative painting, not previously observed in ancient paintings, establishes a new identifying trait for an artist manner of painting.

The development of a new high spectral resolution scanning reflectance spectroscopy (SRS) system, using a low-cost robotic arm, transformed a field-deployable spectroradiometer into a powerful scanning system with extended analytical capabilities, through the construction of hyperspectral 3D data cubes in the wavelength range between 350 and 2500 nm. The extended applications of the SRS system for on-site analysis of painted surfaces decorating subterranean tombs and Byzantine churches and painting fragments in museum galleries and storerooms attest to its robustness and versatility. The SWIR wavelength range identified and mapped diagnostic signatures beyond the visible-NIR (VNIR) of mineral and clay materials used in painting, salts such as gypsum formed through environmentally-linked effects and organic coatings applied in previous conservation/restoration treatments. Chemical maps of gypsum provided an important topographic map of the condition of the paintings and demonstrated the value of the SRS system as a tool for environmental monitoring. Furthermore, the high spectral resolution of the system coupled with derivative analyses allowed for confident identification of subtle absorptions and individual constituents in material mixtures.

The application of this protocol for the study of Cypriot Byzantine wall paintings also revealed very interesting results on the materials used and their application. Two different

painting phases were analyzed in the Church of St. Paraskevi. As this was the first scientific analyses conducted in this church, a preliminary list of pigments was identified and compared between the two phases. One distinct difference between the two was the lack of *proplasmos* in the earlier twelfth century painting phase, a greenish underpainting for the flesh tone commonly encountered in the Byzantine painting tradition. HSI analyses were also conducted in the historically-significant Enkleistra of St. Neophytos, where two overlapping painting phases were analyzed in the Cell of St. Neophytos. The diversity of the pigment palette was exemplified in the endmember list produced by derivative analyses, and the significance of material use was identified by mapping, such as the assignment of cinnabar to the blood flow from Christ's feet. A *proplasmos* was identified in the later twelfth century phase, but not in the earlier painting phase.

An important outcome of this research are the insightful complementary results obtained from the application of both the Specim IQ camera and the SRS system. The extended analytical range of the high spectral resolution SRS system coupled with the high spatial resolution of the IQ camera facilitate a thorough materials characterization of the painting's decoration with high spatial chemical mapping, providing a deeper understanding of the painting's execution. Though adaptations cannot be made to the hardware of the Specim IQ to improve system performance, the SRS system can be further modified to improve its spatial resolution. Driving the fiber-optic cable closer to the painting surface (where possible) and smaller step sizes in the Axidraw scanner can produce a higher spatial resolution in the data cubes. This would require a light source with a longer lifetime, which can be feasible with a small bulb driven by an external battery pack. Additionally, the system can theoretically be converted into luminescence mode by adapting the mount to hold a filter in front of the fiber-optic cable and used a colorful bulb to excite the surface of the painting.

Another important collection of paintings was analyzed using forensic photography, FORS, XRF, and HSI analyses: the Greco-Roman funerary portraits produced in Egypt from the first to fourth centuries AD. While the portraits exhibited a diverse set of individuals and artistic skill, the material use in the portraits followed interesting trends, such as the

use of copper carboxylate as a green pigment, jarosite mixed with white to produce warm tones in the flesh and white tunics, and madder lake for clothing decoration and enhancing flesh tones. Egyptian blue was also used in flesh tones and in mixtures of white to produce a colder hue, which was a technical practice for producing similar hues in the ancient Cypriot paintings, indicating a possible knowledge transfer amongst artists.

Madder lake and Egyptian blue were mapped over the surface of the portraits using forensic photography and luminescence imaging spectroscopy (LIS). Through quantitative spectral mapping, LIS could produce a simultaneous collection and visualization of these ancient pigments' emission, especially in regions of low pigment concentration inaccessible by reflectance spectroscopy. Applications of LIS for the characterization of ancient Cypriot and Greco-Roman paintings have demonstrated the immense potential of the system to detect and map the presence of ancient luminescence pigments across the surface of archaeological paintings. Preliminary studies in Appendix D have begun to characterize the response of an IS system's ability to record the emission of Egyptian blue in the presence of dilute and concealed pigment mixtures.

The last imaging modality employed in this research was direct-detection terahertz (THz) imaging. Using a novel system architecture adopted from biomedical imaging research, different multi-layered targets representing panel and wall paintings, integrated with various types of concealed imagery and hidden defects, were imaged. Structural and topographical details of the targets were enhanced by this contrast sensing-focused modality; hidden pigments and air gaps between layers were identified; and layers of the same material painted and dried at different times could be discriminated in the THz image, which would be less feasible in time-domain imaging. One of the most promising advantages of this system was its ability to penetrate strong signal scatters such as lead white and chalk. This suggests that the system would be able to penetrate thin concealing layers of plaster on wall paintings, or, in the specific case of the Enkleistra of St. Neophytos, the layer of lead white whitewash in the Cell to identify features and/or decoration in the older painting. Next stages in this research should involve adaptation of the imaging optics on the system to scan over a surface

to achieve this and the system structure for field robustness, as well as a mechanism to tune with high precision the position of the optics to improve control of the THz signal's focus location.

The chemical maps of painting materials produced from forensic photography, reflectance imaging spectroscopy and luminescence imaging spectroscopy motivated the exploratory study of producing 3D models of polychrome objects with multispectral texture employing a streamlined, technologically-accessible approach. Two successful 3D reconstructions of a polychrome Canosa terracotta vase were produced featuring chemical maps of: 1) the two luminescent pigments Egyptian blue and madder lake through visible-induced NIR and visible-induced visible luminescence imaging, respectively and 2) conservation materials visualized through UV-induced visible fluorescence imaging. This methodology integrated individual luminescence from separate image captures into a false-color composite image with high resolution detail; by overlaying the composite onto a gray-scaled image, two things were accomplished: (1) the luminescence imagery quality was not sacrificed by letting in residual light to produce a background context, which would otherwise interfere with an accurate interpretation of the luminescence; and (2) using the 'layered' luminescence composite image as the camera source data in the reconstruction software mitigated the challenges of having a low number of tie points to construct an accurate mesh or using an advanced post-processing technique to 'drape' the luminescence over the RGB model. It should be noted that the UV-induced fluorescence model did not require a layered image, as the luminescence from the object throughout provided a sufficient context to build the model, simplifying the image post-processing even further. While the image acquisition methodology in this study used instruments commonly found in conservation and research laboratories with minimal computational processing, more advanced imaging tools can be used following a similar protocol reproduce multispectral-textured models. 3D luminescence imaging is a necessary progression from 2D chemical maps to visualize materials, whether ancient or modern, in the context for which they were originally applied in and understand their true function. This will play an especially important role in archaeological forensics as the interpretation of the

model and the model itself will provide key trace evidence in investigations of undocumented artifacts, addressing questions of authenticity and provenance.

The research presented in this thesis has demonstrated how imaging and spectroscopic techniques have advanced archaeological understanding of ancient paintings through sophisticated chemical characterization and mapping methods to visualize materials distribution. The novel imaging spectroscopy and chemical sensing modalities as well as data processing/visualization approaches, developed and applied in this research for the study of ancient polychromy in archaeological and Byzantine artifacts, represent a step forward in archaeometric studies establishing a new paradigm in scientific protocols in archaeological materials science and archaeological forensics. It should be noted that while the complexity of technical study presented by ancient painting motivated the experimental and data analysis approaches and therefore the select case studies, this work has only thus far applied this methodology to a specific subset of cultural heritage, i.e. a certain group of painting materials, artists, technical styles, and monuments. However, this research has demonstrated how the versatility and analytical capabilities of these commercial and custom spectroscopy systems can be broadened to address other demanding questions, objects, and sites in cultural heritage. These methodologies are, in fact, necessary to broach historical and conservation questions arising from subsequent periods of history where rapid developments in artists' materials, technical artistic styles, and monumental works, along with the societal contexts in which they were manifested and exist within today, present new analytical and preservation challenges that must be addressed by advanced, non-invasive scientific technologies.

APPENDIX A

Spectral characteristics of natural minerals and pigments

Reference reflectance spectra in the visible to near-infrared (VNIR) wavelength range and their respective 1st derivative profiles for common minerals and synthetic colorants found in the paintings are provided here. The spectra were acquired from the USGS spectral database, as well as from commercial pigments and Cypriot rock samples. Data collection from the last two groups were taken with the UCLA Molecular and Nano Archaeology Laboratory's spectroradiometer, the ASD Fieldspec 3. Diagnostic spectral features for material characterization were extracted from the plots. Additional details on spectral features can be found in [cite sources].

A.1 USGS

A.1.1 Hematite ($\mathbf{Fe_2O_3}$)

Table A.1: Spectral features (in nm) of hematite due to spin-forbidden ligand field (i.e. crystal field) transitions. (i) – inflection; (m) – peak maximum; (a) – absorption.

$^{\mathbf{6}}\mathbf{A_{1g}}(^{\mathbf{6}}\mathbf{S}) \rightarrow {}^{\mathbf{4}}T_{\mathbf{2g}}(^{\mathbf{4}}G)$	$^{\mathbf{6}}\mathbf{A_{1g}}(^{\mathbf{6}}\mathbf{S}) \rightarrow {}^{\mathbf{4}}T_{\mathbf{1g}}(^{\mathbf{4}}G)$
586 (i), 660 (a)	749 (m), 871 (a)

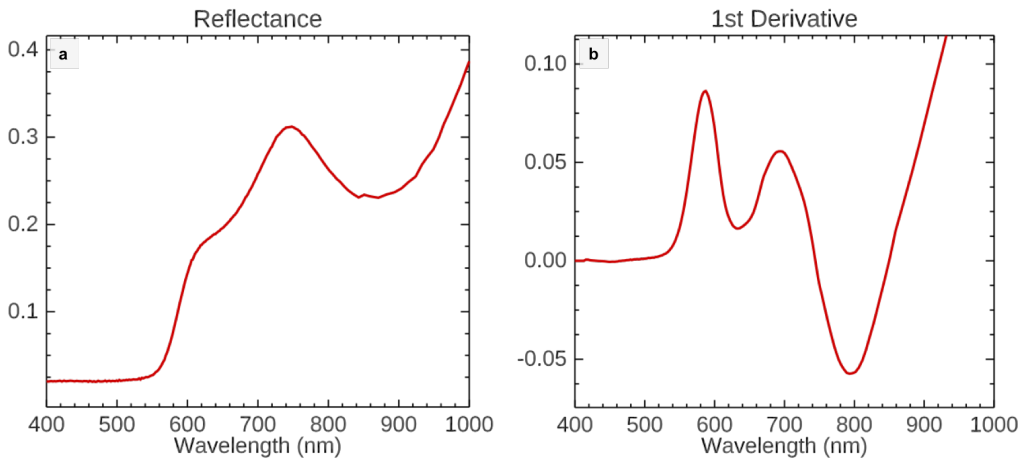

Figure A.1: **(a)** Reflectance spectrum of hematite (source: USGS database). **(b)** 1st derivative of the reflectance spectrum.

A.1.2 Goethite (FeO(OH))

Table A.2: Spectral features (in nm) of goethite due to spin-forbidden ligand field (i.e. crystal field) transitions. (i) – inflection; (m) – peak maximum; (a) – absorption; (s) – shoulder.

$^{6}\mathbf{A_{1g}}(^{6}\mathbf{S}) \rightarrow {}^{4}A_{1g}, {}^{4}\mathbf{E_g}(^{4}\mathbf{G})$	$^{6}\mathbf{A_{1g}}(^{6}\mathbf{S}) \rightarrow {}^{4}T_{2g}(^{4}G)$	$^{6}\mathbf{A_{1g}}(^{6}\mathbf{S}) \rightarrow {}^{4}T_{1g}(^{4}G)$
445 (s)	553 (i), 670 (a)	765 (m), 924 (a)

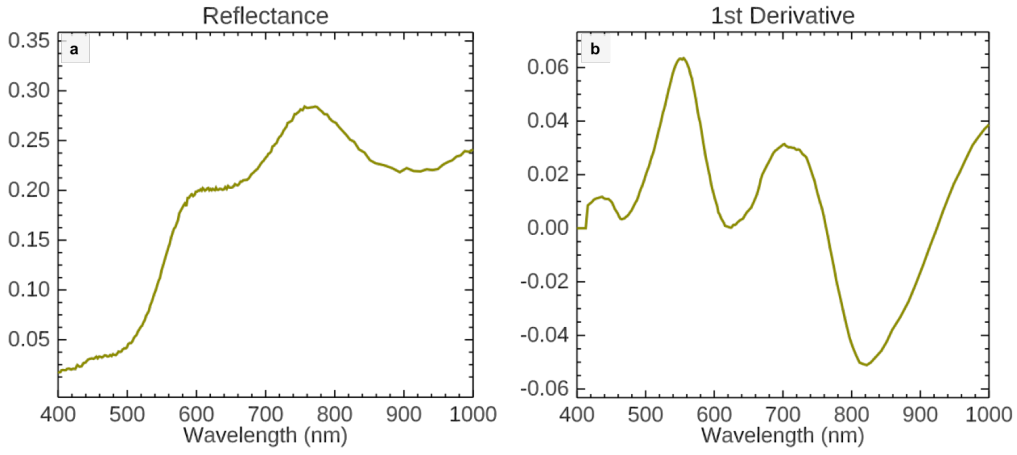

Figure A.2: **(a)** Reflectance spectrum of goethite (source: USGS database). **(b)** 1st derivative of the reflectance spectrum.

A.1.3 Jarosite ($(K,Na)Fe_3^{3+}(OH)_6(SO_4)_2$)

Table A.3: Spectral features (in nm) of jarosite due to spin-forbidden ligand field (i.e. crystal field) transitions. The substitution of Na for K (natrojarosite) results in a subtle hypsochromic shift of the $^6A_{1g}(^6S)$ transition absorption by a few nm. (i) – inflection; (m) – peak maximum; (a) – absorption; (s) – shoulder.

$^6\mathbf{A_{1g}}(^6\mathbf{S}) \rightarrow {}^4A_{1g}, {}^4\mathbf{E_g}(^4\mathbf{G})$	$^6\mathbf{A_{1g}}(^6\mathbf{S}) \rightarrow {}^4T_{2g}(^4G)$	$^6\mathbf{A_{1g}}(^6\mathbf{S}) \rightarrow {}^4T_{1g}(^4G)$
436 (a)	577 (s), 648 (a)	712 (m), 941 (a)

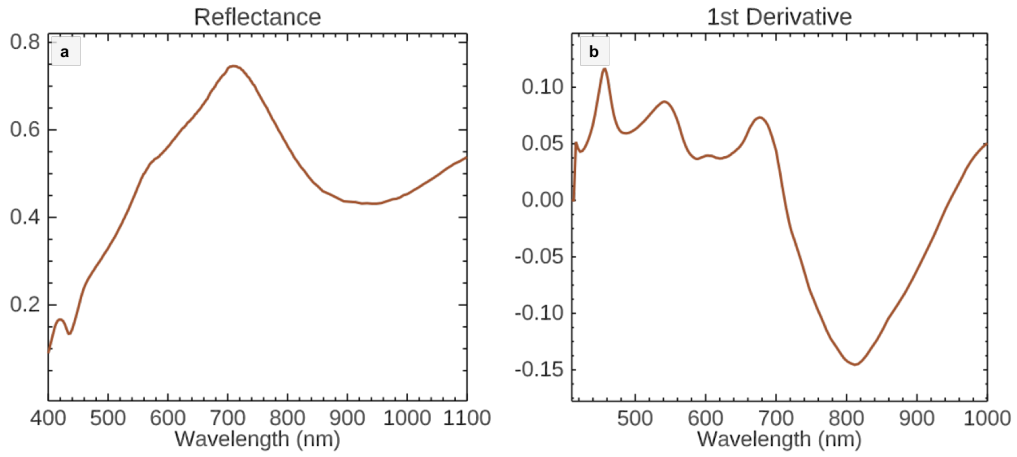

Figure A.3: **(a)** Reflectance spectrum of jarosite (source: USGS database). **(b)** 1st derivative of the reflectance spectrum.

A.1.4 Cinnabar (HgS)

The sharp transition of cinnabar is due to the band gap of S. The band gap energy is traditionally reported as 2.1 eV [89], with a conduction band inflection in the reflectance spectrum at $\sim$ 590 nm [7]. In this reference spectra (Figure A.4, the inflection point is at 612 nm, corresponding to a band gap energy of 2.03 eV ($E = \frac{hc}{\lambda}$).

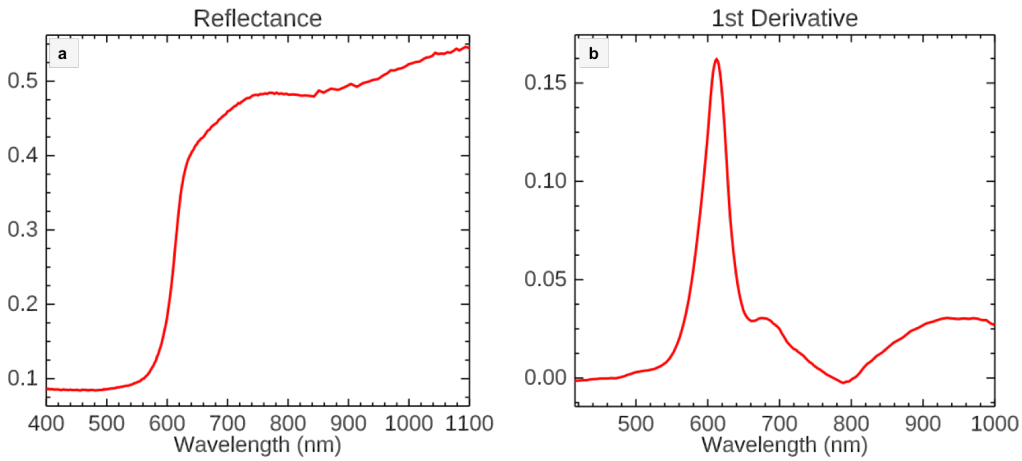

Figure A.4: **(a)** Reflectance spectrum of cinnabar (source: USGS database). **(b)** 1st derivative of the reflectance spectrum.

A.2 Commercial

A.2.1 Egyptian blue ($CaCuSi_4O_{10}$)

Table A.4: Spectral features (in nm) of Egyptian blue due to $d \rightarrow d$ electronic transitions. (a) – absorption.

$^2\mathbf{A_{1g}} \rightarrow {}^2B_{\mathbf{1g}}$	$^2\mathbf{E_g} \rightarrow {}^2B_{\mathbf{1g}}$	$^2\mathbf{B_{2g}} \rightarrow {}^2B_{\mathbf{1g}}$
560 (a)	630 (a)	790 (a)

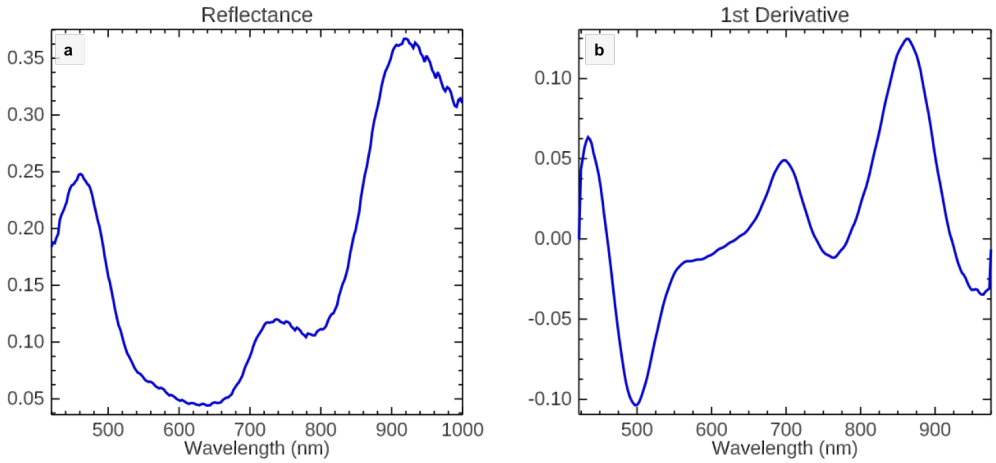

Figure A.5: **(a)** Reflectance spectrum of Egyptian blue (source: Kremer Pigments). **(b)** 1st derivative of the reflectance spectrum.

A.2.2 Madder lake

The reflectance spectrum (Figure A.6) of madder lake features the structured double absorption band at 510 and 545 nm due to the presence of Al(III)- 1,2,4 HAQ (purpurin).

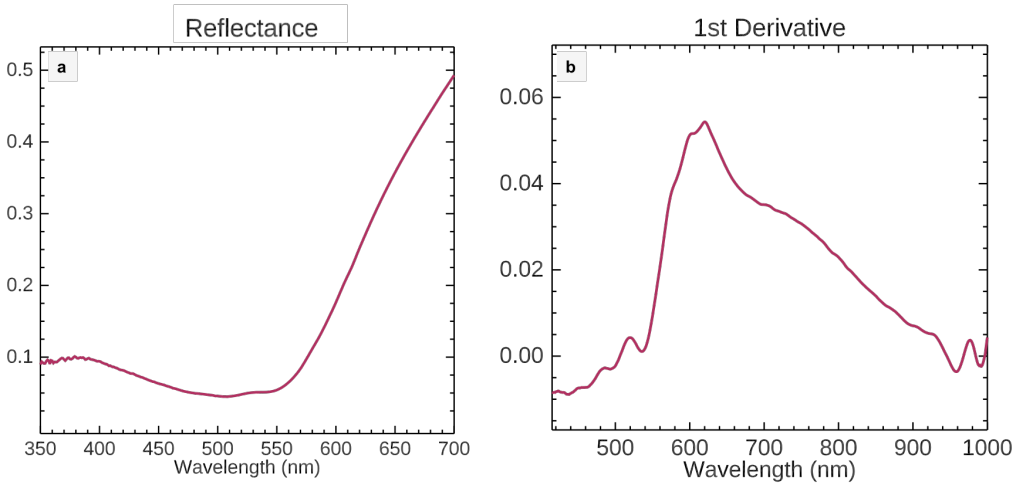

Figure A.6: **(a)** Reflectance spectrum of madder lake (source: Kremer Pigments). **(b)** 1st derivative of the reflectance spectrum.

A.2.3 Red lead (Pb_3O_4)

Red lead is a semiconductor pigment with an inflection point in the transition curve at 572 nm, corresponding to a band gap energy of 2.17 eV (Pb(II)(6s) → Pb(IV)(6s)). Impurities in the red lead such as lead oxide (PbO) modify the band gap energy, hence the variability of the inflection point in the reflectance spectrum.

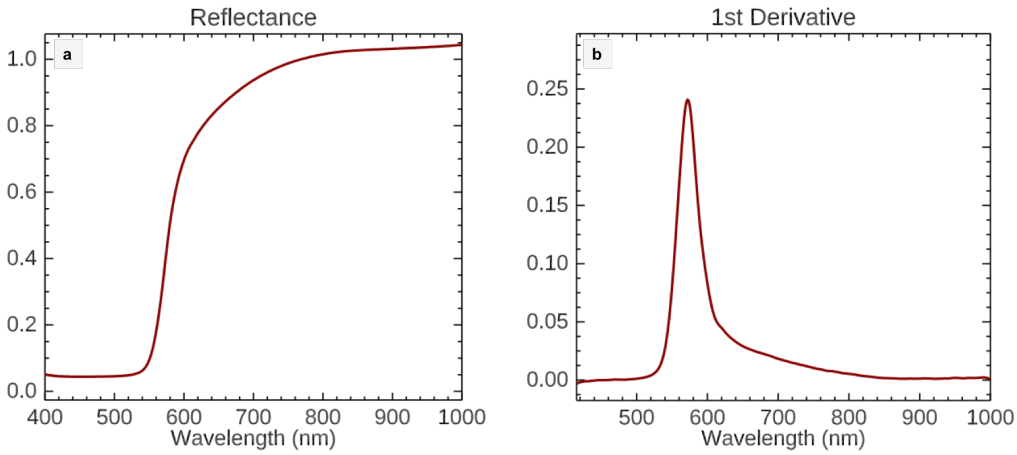

Figure A.7: **(a)** Reflectance spectrum of red lead (source: Kremer). **(b)** 1st derivative of the reflectance spectrum.

A.3 Cyprus

A.3.1 Red ochre

The spectral features of this rock sample from Cyprus (Table A.5, Figure A.8) contains a small shoulder at 450 nm, similar to what is seen in goethite. This shows the impurity of the sample, though it primarily consists of hematite.

Table A.5: Spectral features (in nm) of a red ochre sample due to spin-forbidden ligand field (i.e. crystal field) transitions. (i) – inflection; (m) – peak maximum; (a) – absorption.

$^6\mathbf{A_{1g}}(^6\mathbf{S}) \rightarrow {}^4T_{\mathbf{2g}}(^4G)$	$^6\mathbf{A_{1g}}(^6\mathbf{S}) \rightarrow {}^4T_{\mathbf{1g}}(^4G)$
577 (i), 670 (a)	749 (m), 885 (a)

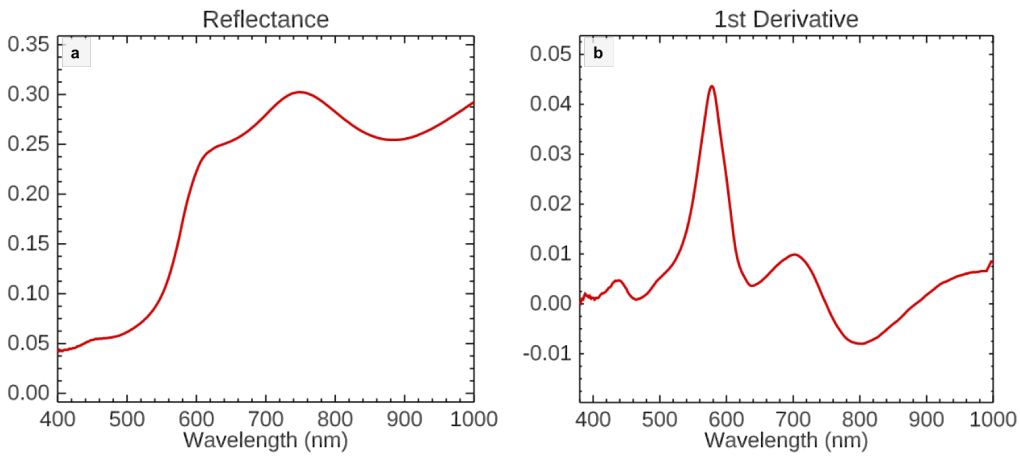

Figure A.8: **(a)** Reflectance spectrum of a red ochre rock sample (source: Cyprus). **(b)** 1st derivative of the reflectance spectrum.

A.3.2 Yellow ochre

Table A.6: Spectral features (in nm) of a yellow ochre sample due to spin-forbidden ligand field (i.e. crystal field) transitions. (i) – inflection; (m) – peak maximum; (a) – absorption; (s) – shoulder.

$^{6}\mathbf{A_{1g}}(^{6}\mathbf{S}) \rightarrow {}^{4}A_{1g}, {}^{4}\mathbf{E_g}(^{4}\mathbf{G})$	$^{6}\mathbf{A_{1g}}(^{6}\mathbf{S}) \rightarrow {}^{4}T_{2g}(^{4}G)$	$^{6}\mathbf{A_{1g}}(^{6}\mathbf{S}) \rightarrow {}^{4}T_{1g}(^{4}G)$
450 (s)	553 (i), 665 (a)	762 (m), 922 (a)

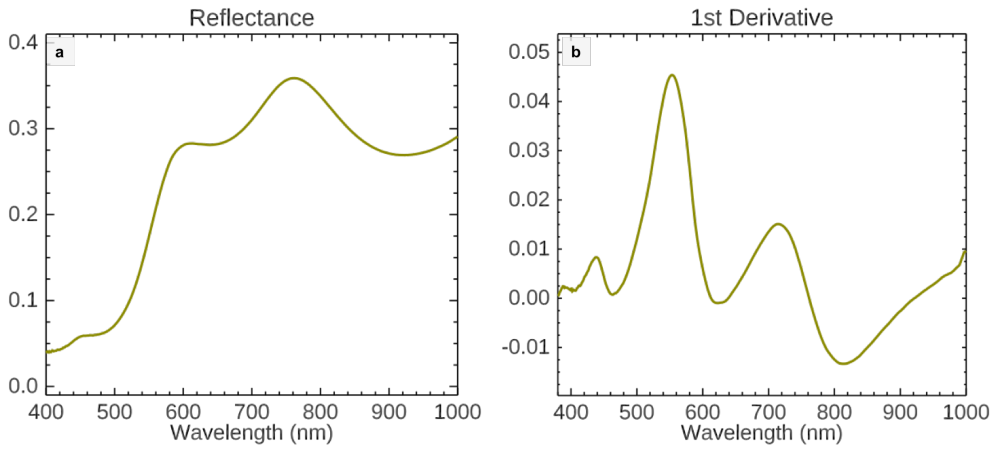

Figure A.9: **(a)** Reflectance spectrum of a yellow ochre rock sample (source: Cyprus). The reflectance spectra matches closely to the USGS goethite reference. **(b)** 1st derivative of the reflectance spectrum.

A.3.3 Jarosite ($\mathbf{(K,Na)Fe_3^{3+}(OH)_6(SO_4)_2}$)

Table A.7: Spectral features (in nm) of jarosite due to spin-forbidden ligand field (i.e. crystal field) transitions. (i) – inflection; (m) – peak maximum; (a) – absorption; (s) – shoulder.

$^6\mathbf{A_{1g}}(^6\mathbf{S}) \rightarrow {}^4A_{1g}, {}^4\mathbf{E_g}(^4\mathbf{G})$	$^6\mathbf{A_{1g}}(^6\mathbf{S}) \rightarrow {}^4T_{2g}(^4G)$	$^6\mathbf{A_{1g}}(^6\mathbf{S}) \rightarrow {}^4T_{1g}(^4G)$
435 (a)	576 (s), 644 (a)	711 (m), 917 (a)

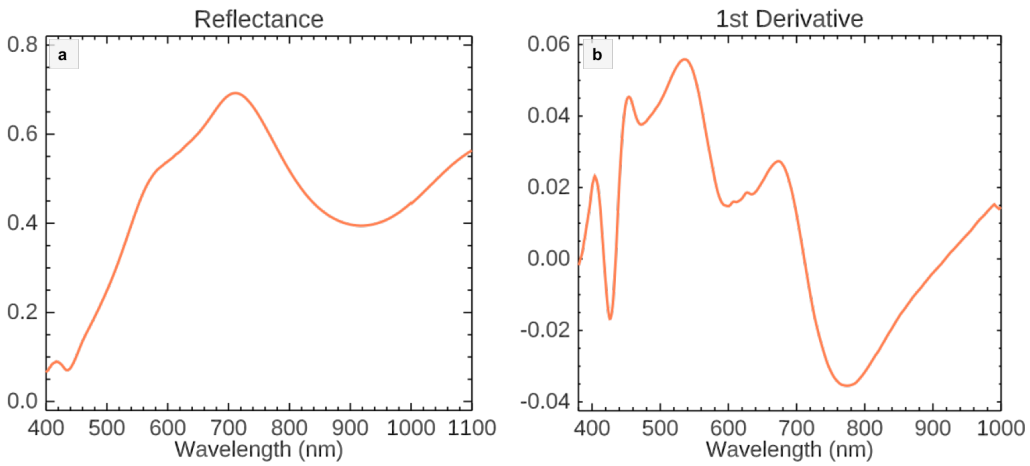

Figure A.10: **(a)** Reflectance spectrum of a jarosite rock sample (source: Cyprus). **(b)** 1st derivative of the reflectance spectrum.

A.3.4 Celadonite-rich green earth ($(K(Mg,Fe^{2+})(Fe^{3+},Al)[Si_4O_{10}](OH)_2)$)

Table A.8: Spectral features (in nm) of a celadonite-rich green earth due to spin-forbidden ligand field (i.e. crystal field) transitions (top table) and OH combination bands due to different cations in the short-wave infrared (SWIR) in the celadonite mineral. (i) – inflection; (m) – peak maximum; (a) – absorption; (s) – shoulder.

$^6\mathbf{A_{1g}}(^6\mathbf{S}) \rightarrow {}^4A_{1g}, {}^4\mathbf{E_g}(^4\mathbf{G})$	$^6\mathbf{A_{1g}}(^6\mathbf{S}) \rightarrow {}^4T_{2g}(^4G)$	$^6\mathbf{A_{1g}}(^6\mathbf{S}) \rightarrow {}^4T_{1g}(^4G)$
485 (s)	537 (m)	749 (a), 835 (m), 1043 (a)

Table A.9: Spectral features (in nm) of a celadonite-rich green earth caused by OH combination bands due to different cations in the short-wave infrared (SWIR) of the celadonite mineral. (a) – absorption.

$\mathbf{AlFe^{3+}}$	$\mathbf{Fe^{3+}Fe^{3+}}$	$\mathbf{MgMgMg}$
2257 (a)	2302 (a)	2348 (a)

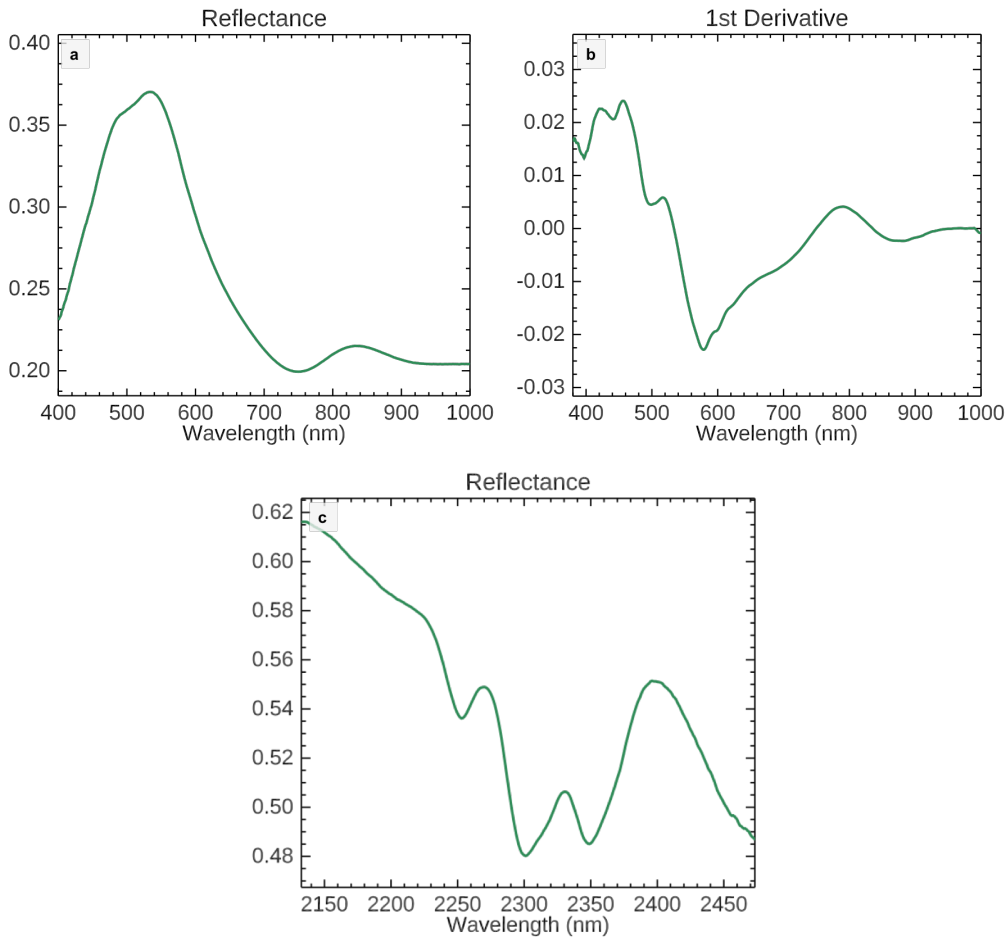

Figure A.11: **(a)** Reflectance spectrum of a celadonite-rich green earth rock sample (source: Cyprus). **(b)** 1st derivative of the reflectance spectrum. **(c)** Short-wave infrared from $\sim$ 2100 - 2500 nm showing the triplet feature of celadonite due to OH-combination bands.

APPENDIX B

Ancient Cypriot paintings' pigment tables

The following tables detail the hues, colorants, and application found in the ancient Cypriot paintings as a result of XRF, FORS, and forensic photography.

B.1 Egyptian blue

Table B.1: Detailed list of the identification and application methodology of Egyptian blue in the Cypriot wall paintings.

Painting	Hue	Main colorant(s)	Other phases	Application	Location/function
A1	Blue	Egyptian blue	Green earth	Applied over plaster	Decorative feature
A2	Blue	Egyptian blue	Green earth	Applied over yellow ochre	N/A
B3	Blue	Egyptian blue	N/A	Applied over plaster	N/A
E2	Sky blue	Egyptian blue	N/A	N/A	Background
E2	Pinkish blue	Egyptian blue	N/A	N/A	Background shading; applied over light blue wash
E5	Light blue-purple	Egyptian blue	Red ochre	N/A	Background
E5	Light white-blue	Egyptian blue	N/A	Applied over plaster	Background; tunic
E6	Light white-blue	Egyptian blue	N/A	Applied over plaster	Background
E6	Light blue	Egyptian blue	N/A	Applied over light blue background wash and red head decoration	Head decoration
E6	Grey-blue	Mn-compounds	Egyptian blue	Applied over yellow	Tunic shading
E8	Light blue	Egyptian blue	N/A	Applied over plaster	Background
E9	Light blue	Egyptian blue	N/A	Applied over tunic	Tunic decoration
E9	Faded blue	Egyptian blue	N/A	Applied over tunic	Tunic decoration
E10	Light blue	Egyptian blue	N/A	Applied over plaster	Background
F1	Light blue	Egyptian blue	N/A	N/A	Dado level
F1	Hazy white	Egyptian blue	N/A	Applied over red pigment	Inner arch; flower decoration
G	Blue	Egyptian blue	N/A	Applied over plaster	Floral decoration
H3	Blue	Egyptian blue	N/A	Applied over green	Leaf
H3	Dark blue	Egyptian blue	N/A	Applied over plaster	Dot decoration
H3	Light blue	Egyptian blue	N/A	Applied over plaster	Line
I	Blue	Egyptian blue	N/A	Applied over plaster	Aedicule; chiton
J	Light blue	Egyptian blue	N/A	Applied over red dot	Dot decoration on bird's tail
J	Dark grey-blue	Egyptian blue	N/A	Applied over plaster	Small bird
K	Blue	Egyptian blue	N/A	Applied over plaster; concealed by encrustation	Dot decoration
L1	Blue	Egyptian blue	N/A	Layered over red/yellow	Oval decoration
L2	Blue	Egyptian blue	N/A	Applied over plaster	Floral decoration
N1	Blue	Egyptian blue	N/A	Applied over plaster	Triangle
N2	Blue	Egyptian blue	N/A	Applied over plaster	Leaf
N3	Blue	Egyptian blue	N/A	Applied over plaster	Geometric pattern

B.2 Green earth

Table B.2: Detailed list of the identification and application methodology of green earth in the Cypriot wall paintings.

Painting	Hue	Main colorant(s)	Other phases	Application	Location/function
A1	Green-blue	Green Earth	Egyptian blue	Applied over yellow ochre on plaster	Band
B1	Light blue-green	Green Earth	Few particles of Egyptian blue	Undercoat for Egyptian blue; applied over black, then over yellow ochre on plaster	N/A
B1	Dark blue-green	Green Earth	N/A	Applied over black on plaster	N/A
B1	Olive green	Green Earth	Yellow ochre	Applied over plaster	N/A
C4	Green	Green Earth	N/A	N/A	Older paint layer (mostly concealed)
E5	Light green	Green earth	Yellow ochre; Cu-compounds	Applied over hair and background	Wreath leaf
E5	Dark olive green	Green earth	Yellow ochre; Cu and Mn-compounds	Applied over white tunic (containing Egyptian blue)	Tunic shading
E6	Light blue-green	Green earth	Mn-compounds	Applied over dark purple	N/A
E9	Light green	Green earth	Cu-compounds	Applied over red hair	Wreath leaf
G	Green	Green Earth	N/A	Applied over plaster	Floral decoration
H3	Green	Green Earth	N/A	Applied over plaster	Floral decoration
H3	Green (weathered)	Green Earth	N/A	Applied over plaster	Floral decoration
I	Faint green	Egyptian blue	Green earth	Applied over plaster	Garland, 2nd slab.
J	Green	Green earth	N/A	N/A	Arch and floral decoration
K	Green (weathered)	Green earth	N/A	N/A	N/A
L1/L2	Green	Green earth	Egyptian blue	Applied over plaster	Floral decoration
L2	Green	Green earth	N/A	Applied over plaster	Floral decoration
N1	Olive green	Green earth	Yellow ochre	Applied over plaster	Floral decoration
N2	Olive green	Green earth	Yellow ochre	Applied over plaster	Stem
N2	Dark blue-green	Green earth	Egyptian blue	Applied over yellow ochre	Triangle band
N3	Green	Green earth	N/A	Applied over plaster	Plant decoration

B.3 Red pigments

Table B.3: Detailed list of the identification and application methodology of red pigments in the Cypriot wall paintings

Painting	Hue	Main colorants	Other phases	Application	Location/function
A1	Orange	Red Lead	N/A	Applied over white layer with blue particles	Band
A1	Red	Red Ochre	N/A	Applied over plaster	N/A
B1	Red	Red Ochre	N/A	Applied over yellow ochre	Band
B2	Bright pink-red	Cinnabar	Red ochre; Pb- compounds	Applied over pink plaster	N/A
B3	Orange-red	Cinnabar	Red ochre; Pb- compounds	Applied over plaster	N/A
B3	Red	Cinnabar	Red ochre; Pb- compounds	N/A	N/A
C1	Red	Red Ochre	N/A	Applied over plaster	N/A
C2	Red	Red Ochre	N/A	Applied over plaster	N/A
C3	Red	Red Ochre	N/A	Applied over plaster	Older paint layer; N/A
C4	Red	Red Ochre	N/A	Applied over plaster	Older paint layers; N/A
D	Red	Red Ochre	N/A	N/A	Bands; Uniform wall decoration
E1	Orange-red	Red ochre	N/A	Applied over flesh	Eye crease shading
E1	Purple	Red ochre	N/A	Applied over flesh	Tunic
E1	Light purple	Red ochre	N/A	Applied over purple	Tunic lightening
E1	Reddish purple	Red ochre	N/A	N/A	Band
E3	Brown-red	Red ochre	N/A	N/A	N/A
E3	Flesh	Red ochre	N/A	N/A	Cheek
E3	Dark brown	Red ochre	N/A	Touches of yellow paint above; applied over brown-red	Hair layering
E5	Red	Red ochre	N/A	N/A	Band
E6	Cream	Red ochre	N/A	Facial toning	Cheek
E5	Orange-red	Red ochre	N/A	N/A	Cape
E5	Purple	Red ochre	Egyptian blue	Layered shading with Mn-based black pigment	Tunic
E5	Dark purple	Red ochre	N/A	Micrograph shows mixture with black and blue pigments	Shoulder
E5	Light purple	Red ochre	Egyptian blue	N/A	Background bands
E6	Dark purple	Red ochre	N/A	N/A	Tunic
E6	Red	Red ochre	N/A	N/A	Hair layering
E6	Reddish pink	Red ochre	N/A	Facial toning	Cheek
E6	Light pink	Red ochre	N/A	N/A	Neck
E8	Purple	Red ochre	N/A	N/A	N/A
E9	Dark purple	Red ochre	N/A	layering	Garment
E9	Light orange-red	Red ochre	N/A	N/A	Background
E9	Light purple	Red ochre	N/A	N/A	Background
E9	Red	Red ochre	N/A	N/A	Garment
E9	Flesh	Red ochre	N/A	N/A	Cheek

Table B.3: *Cont.*

Painting	Hue	Main colorants	Other phases	Application	Location/function
E10	Light purple	Red ochre	Egyptian blue	N/A	N/A
E10	Red	Red ochre	N/A	N/A	Band
E10	Light pink	Red ochre	Egyptian blue	N/A	N/A
G	Red	Red Ochre	N/A	Applied over plaster	Band
H3	Reddish Orange	Red Ochre	Yellow ochre	Applied over plaster	Band
H3	Red	Red Ochre	N/A	Applied over plaster	Bands/lines
H3	Pink	Red Ochre	N/A	Applied over plaster	Floral decoration
I	Dark Red	Red Ochre	N/A	N/A	Shoe
I	Dark Pink-red	Red Ochre	N/A	N/A	Himation
I	Light Pink	Red Ochre	N/A	N/A	Neck
I	Pink	Red Ochre	N/A	N/A	Garlands
I	Flesh	Red ochre	N/A	Shading - light wash over plaster	Arm
J	Red	Red Ochre	N/A	Applied over plaster	Dog
J	Red	Red Ochre	Pb-compounds	Applied over plaster	Arch decoration
J	Pink	Red Ochre	N/A	Applied over plaster	Chair
J	Purple	Red Ochre	N/A	Applied over plaster / pink chair	Outline of chair
K	Red	Red Ochre	N/A	Applied over plaster	Band
K	Pink	Red Ochre	N/A	Applied over plaster	Marble imitation
L1	Red	Red Ochre	N/A	Applied over plaster	lines
L2	Pink	Red Ochre	N/A	Applied over plaster	Floral decoration
L2	Red	Red Ochre	N/A	Applied over plaster	N/A
N1	Red	Red Ochre	Pb-compounds	Applied over plaster	Line
N1	Pink	Red Ochre	N/A	Applied over plaster	N/A
N2	Dark red	Red Ochre	N/A	Applied over plaster	Wave pattern
N2	Pink	Red Ochre	N/A	Applied over plaster	Marble imitation
N2	Red	Red Ochre	Pb-compounds	Applied over plaster	Marble imitation
N3	Red	Red Ochre	N/A	Applied over plaster	Square border
N3	Pink	Red Ochre	N/A	Applied over plaster	Triangles
O	Red	Red Ochre	N/A	Applied over plaster	Band

B.4 Yellow ochre

Table B.4: Detailed list of the identification and application methodology of yellow ochre in the Cypriot wall paintings.

Painting	Hue	Main Colorant(s)	Other Phases	Application	Location/Function
B1	Yellow	Yellow ochre	N/A	Uniform	N/A
C3	Yellow	Yellow ochre	N/A	Applied over plaster	N/A
C4	Yellow	Yellow ochre	N/A	Applied over plaster	Top layer
D	Yellow	Yellow ochre	N/A	Applied over plaster	N/A
E1	Dark yellow	Yellow Ochre	N/A	N/A	N/A
E1	Light yellow	Yellow ochre	N/A	N/A	N/A
E2	Yellow	Yellow ochre	N/A	Over blue background of Egyptian blue	N/A
E3	Yellow	Yellow ochre	N/A	N/A	N/A
E5	Yellow	Yellow ochre	N/A	N/A	Cape
E5	Cream	Yellow ochre	N/A	Facial toning	Forehead
E6	Dark yellow	Red ochre	Yellow ochre	N/A	Belt
E6	Light Yellow	Yellow ochre	N/A	N/A	Tunic, background
E9	Light Yellow	Yellow ochre	N/A	N/A	Belt
E9	Yellow	Yellow ochre	N/A	Applied over red	Mantle
E10	Light yellow-white	Yellow ochre	Red ochre	N/A	Cheek
E10	Dark yellow	Yellow ochre	N/A	N/A	Hair
G	Reddish Yellow	Yellow ochre	Red ochre	N/A	Floral decoration
G	Yellow	Yellow ochre	N/A	Applied over plaster	Floral decoration
H3	Orange-Yellow	Yellow ochre	Red ochre	N/A	Decorative fragment
H3	Yellow	Yellow ochre	N/A	Applied over plaster	Decorative fragment
I	Reddish Yellow	Yellow ochre	Red ochre	Shading	Skirt
J	Reddish Yellow	Yellow ochre	N/A	Preparation layer for red pigment	Floral decoration
K	Yellow	Yellow ochre	Red ochre	Applied over plaster	N/A
L	Yellow	Yellow ochre	N/A	Applied over plaster	Line
N1	Yellow (discolored)	Yellow Ochre	N/A	N/A	N/A
N2	Yellow	Yellow Ochre	N/A	Applied over plaster	Band
N3	Yellow	Yellow Ochre	N/A	N/A	Floral decoration
N3	Yellow	Yellow Ochre	N/A	Applied over plaster	Band
O	Yellow	Yellow Ochre	N/A	Applied over plaster	Window

APPENDIX C

Near-infrared luminescence images of ancient Cypriot wall paintings

This appendix is a compilation of additional images produced by forensic photography and luminescence imaging spectroscopy (LIS) applications on the ancient paintings in Paphos, Cyprus to identify the presence and map the distribution of Egyptian blue. The site map and list for the domestic and funerary sites can be referenced in Figure 2.8 and Table 2.1. The regions of white in the near-infrared (NIR) luminescence images correspond to emission of Egyptian blue.

The RGB image and NIR luminescnece images are shown side by side, followed by an overlay of the NIR luminescence image over the RGB to map the distribution of Egyptian blue.

C.1 House of Aion

Ten figurative paintings were excavated from room 7 in the House of Aion [54]. Imaging results from forensic photography and LIS studies of painting E9 were presented in Chapter 2 (Figure 2.28) and Chapter 7 (Figure 6.8).

Figurative painting 1

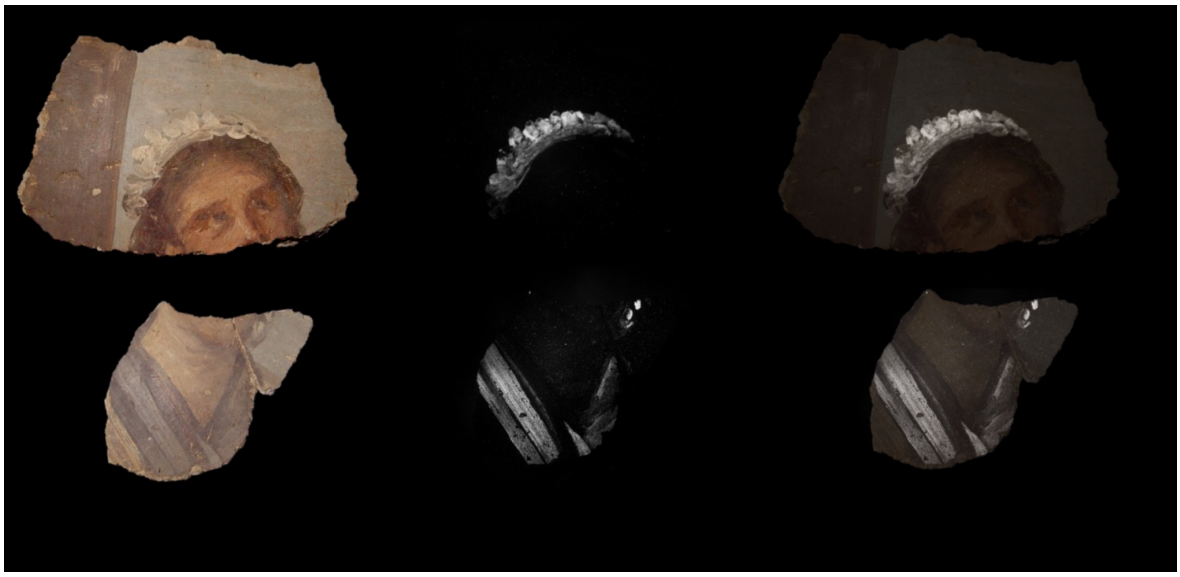

Figurative painting 2

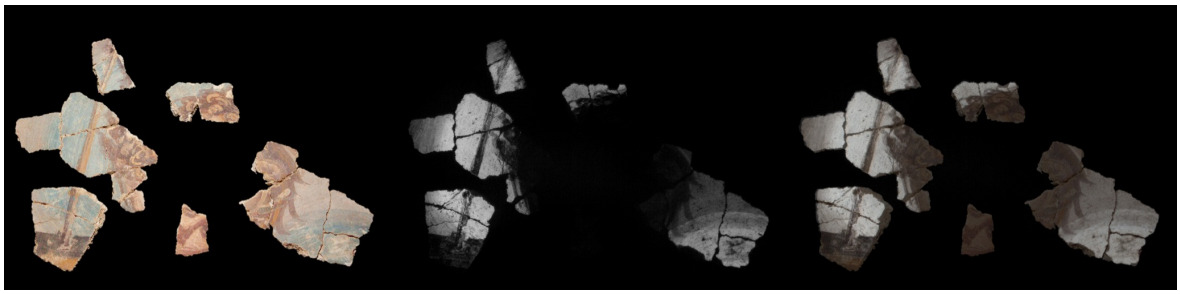

Figurative painting 3

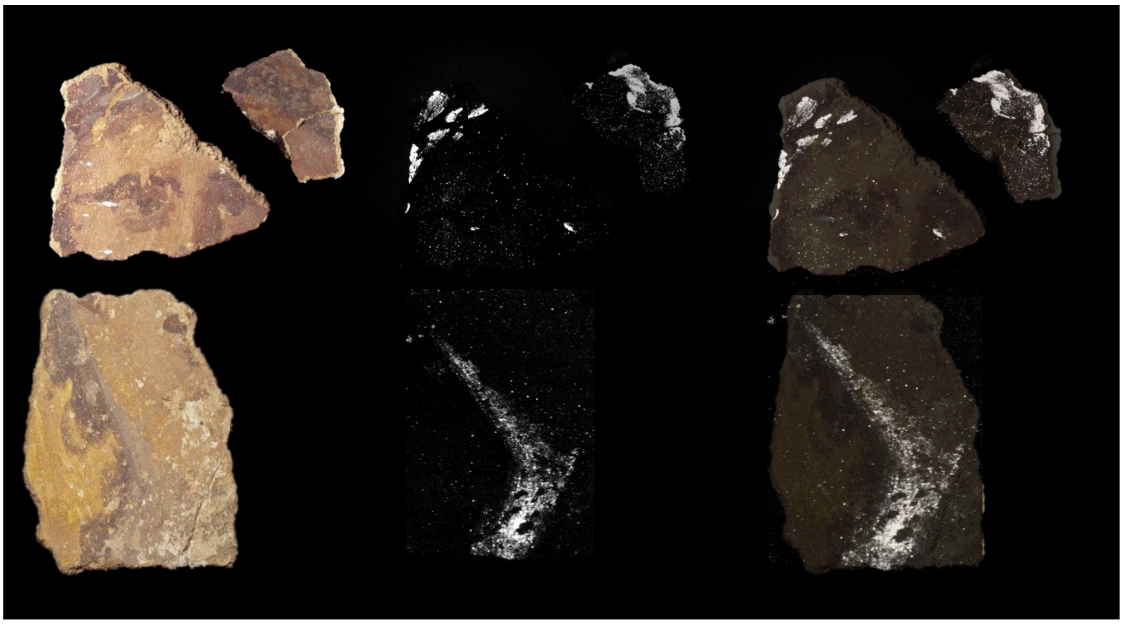

Figurative painting 4

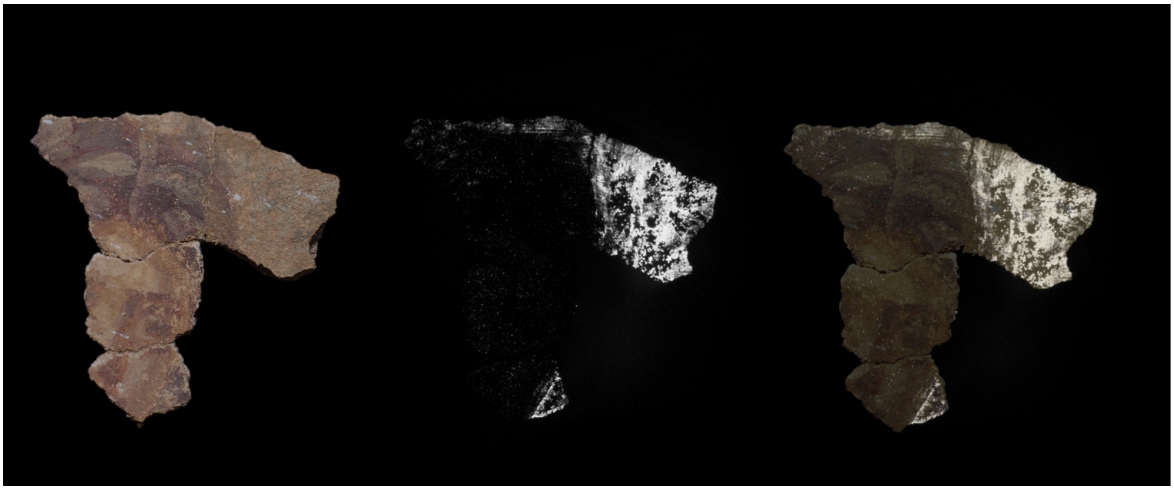

Figurative painting 5

Figurative painting 6

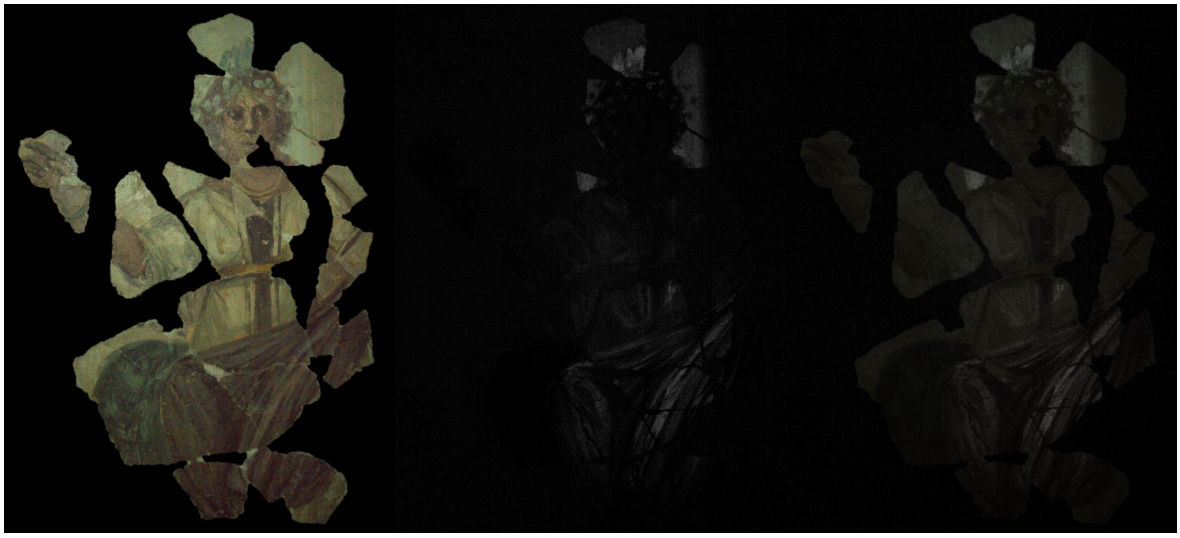

Figurative painting 7

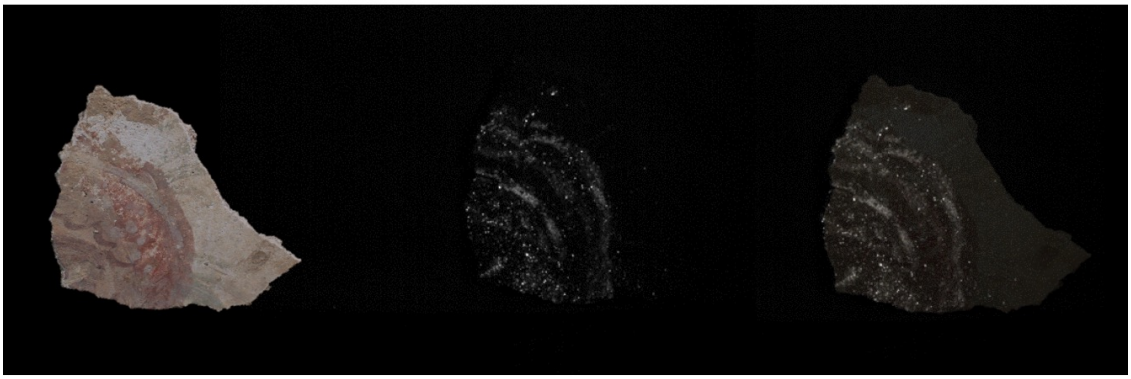

Figurative painting 8

Figurative painting 9

The following image is a close-up view of the tunic to see the faint blue patterns.

Figurative painting 10

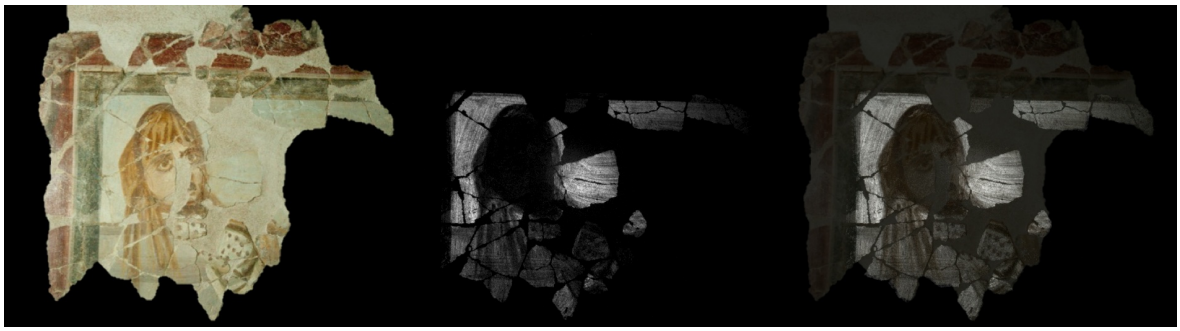

C.2 Tomb at Glyky Nero

The use of Egyptian blue was sparsely seen on the paintings in the tomb at Glyky Nero (which were highly degraded). It was identified as accent tones on the flowers on the inner arches of the arcosolia, and one residual pattern on the dado level was recovered.

C.3 Tomb Annabelle 47

A large-sized painting fragment recovered from Tomb Annabelle 47.

C.4 Tomb at Costis Palamas square

Two painted faces were recovered from the tomb at Costis Palamas square. The first image was presented in Chapter 2 (Figure 2.27).

C.5 Tomb 3510

A rare full-scale funerary figurative painting was excavated from Tomb 3510 near the Tomb of the Kings. The top and bottom halves were imaged separately.

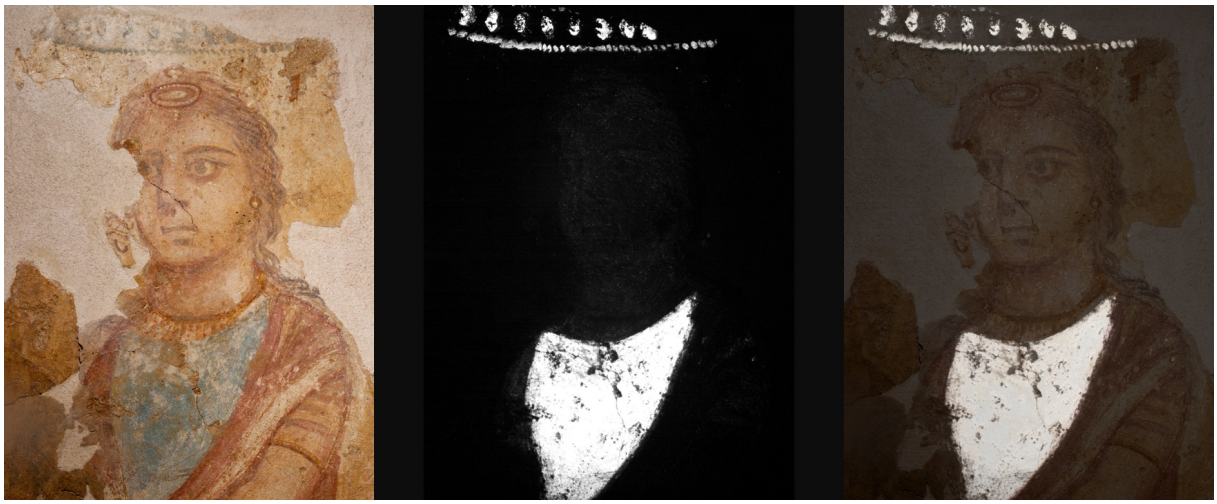

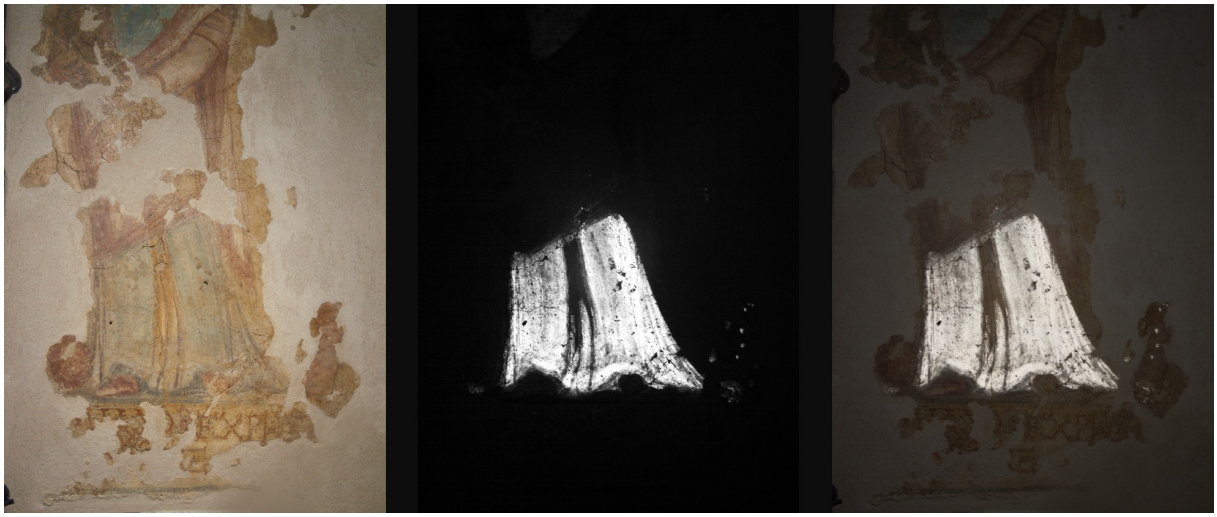

C.6 Tombs Roma 1

Several depictions in Egyptian blue were identified on the dado level of the central arcosolium in Tomb Roma 1. These were presented in Chapter 2 (Figures 2.29, 2.30).

C.7 Tomb Roma 2

Decoration with Egyptian blue were identified under the salt crusts of the large stone slab in Tomb Roma 2. These were presented in Chapters 2 and 6 (Figures 2.31, 6.11).

C.8 Tomb 3882

Egyptian blue was identified in the northwest and southeast arcosolia in Tomb 3882. Results from LIS imaging and forensic imaging from an imitation marble pattern in one of the lozenge shapes from the southeast arcosolium were presented in Chapter 4 (Figure 4.18) (next page).

The dado level of the southeast arcosolium:

The painting on the tympanum of the southeast arcosolium:

The painting on the tympanum of the northwest arcosolium:

APPENDIX D

Preliminary luminescence imaging spectroscopy study of Egyptian blue in pigment mixtures

A preliminary study on the application of luminescence imaging spectroscopy (LIS) for the capture of Egyptian blue luminescence was performed on a test panel featuring unique pigment mixtures with Egyptian blue, motivated by those identified from the materials characterization of the ancient Cypriot paintings (Figure D.1). Five pigment mixtures using commercial pigments were painted with an acrylic binder in squares on a gesso-prepared panel - A: Egyptian blue (EB) with calcium carbonate ($CaCO_3$); B: Egyptian blue with red ochre; C: Egyptian blue with green earth; D: Egyptian blue with carbon black; E: Egyptian blue with red ochre, yellow ochre, and calcium carbonate. A pure application of Egyptian blue was also painted for reference (F). These pure and mixed pigments were also concealed by calcium carbonate to test the penetration of Egyptian blue's luminescence through concealing layers and the IS system's ability to record the signal. One row of the pigment grid was concealed by one semi-transparent layer of calcium carbonate (bottom row, Figure D.1). Another row was painted with two layers of calcium carbonate to appear visibly opaque (middle row, Figure D.1).

The National Gallery of Art (Washington D.C.) Surface Optics hyperspectral camera was used for this imaging study. The panel was illuminated with a 430–540 nm excitation light, and the luminescence was captured from 540–1072 nm at a 300 ms integration time.

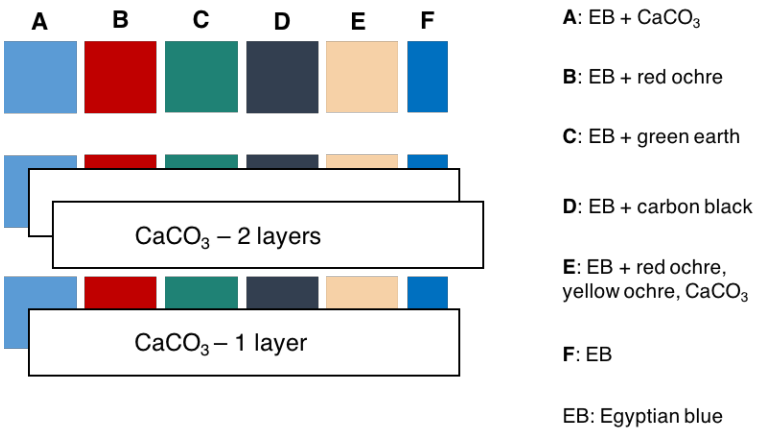

Figure D.1: Schematic of the test panel painted with different pigment mixtures containing Egyptian blue.

The imaging results can be found in Figure D.2. In Figure D.2a is an RGB reference image of the panel. The luminescence image of the test panel, extracted at 896 nm (the peak location for emission bands in the luminescence data cube). The pure application of Egyptian blue (F) and its mixture with calcium carbonate (A) luminescence the greatest amount. The pigment squares with carbon black (D) show no luminescence. When the mixtures are concealed with one semi-transparent layer of calcium carbonate, the emission can still be detected. However, concealment by two layers of calcium carbonate prevented a visible identification of the luminescence (the bright outline around the squares are due to the exposure of the original layer at the edges). Figure D.2c is another representation of the luminescence from the test panel by summing the emission bands in the data cube from 800–1000 nm, meant to imitate the use of a modified camera filtered by a NIR filter. There was not much difference in the visible intensity – only a very slight increase noticeable by eye.

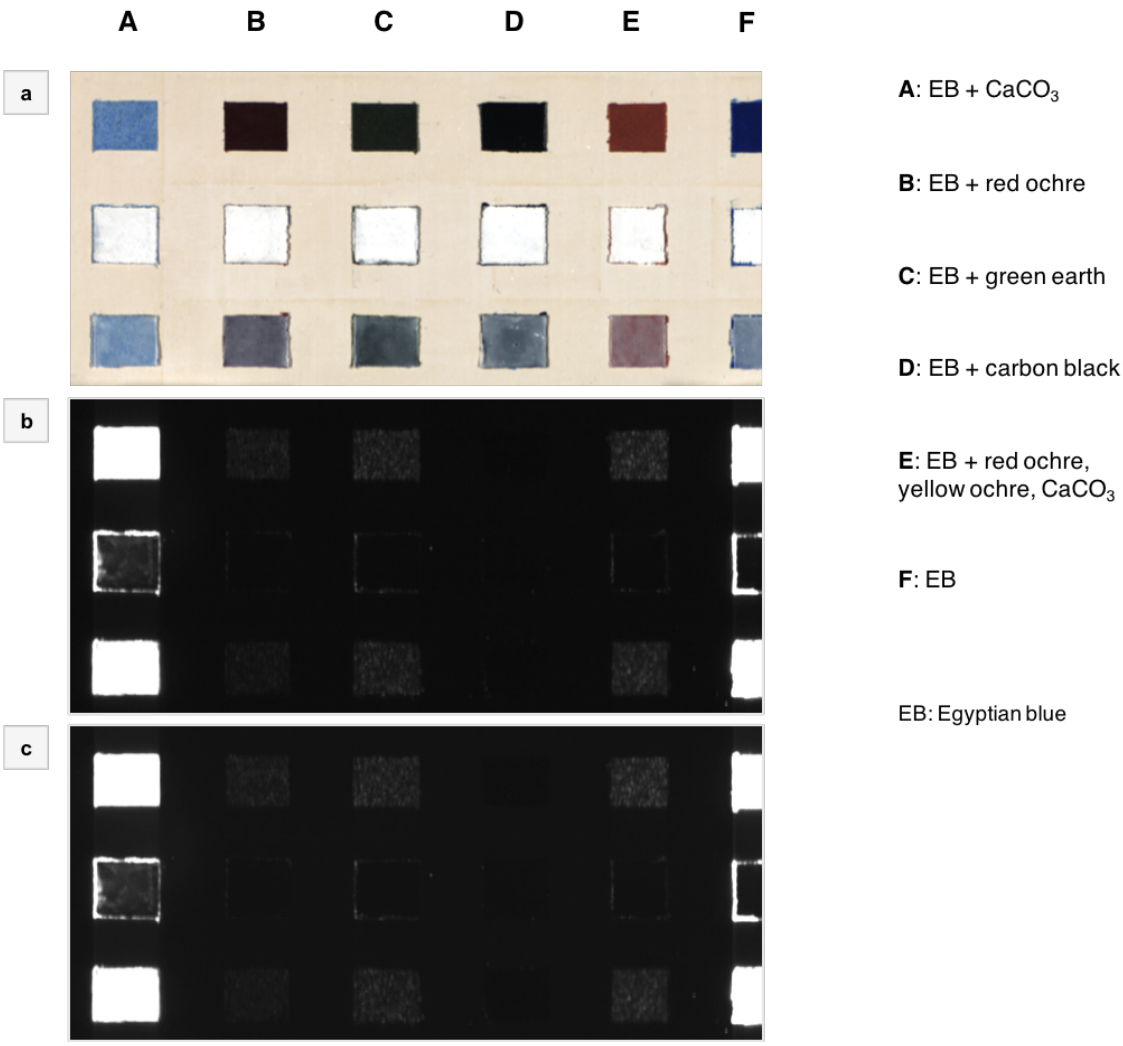

Figure D.2: **(a)** RGB image of test panel. **(b)** Luminescence image at 896 nm spectral band. **(c)** Luminescence image of bands summed from 800 – 1000 nm. The brightness for each luminescence image was increased by the same amount to show the luminescence more clearly.

The emission profiles were then examined. Figure D.1 shows for each pigment application (A to F) their respective emissions from the uncovered and covered squares. The most intense emissions came from the pure Egyptian blue application (F) and from the mixture containing calcium carbonate (A).

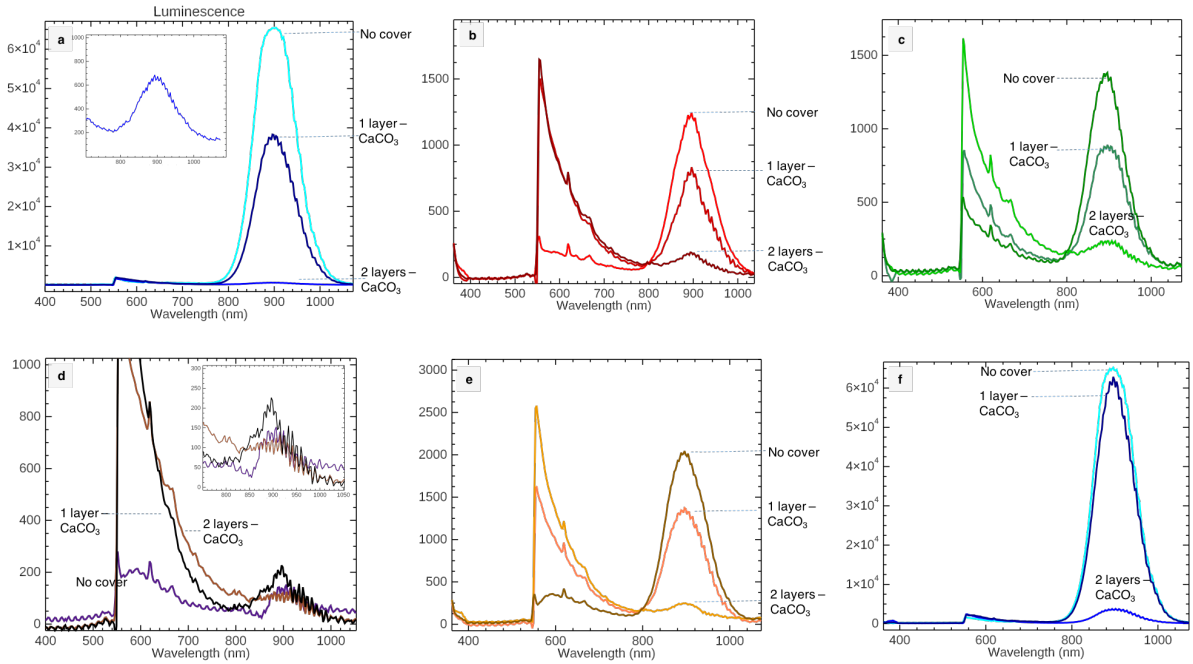

Figure D.3: Luminescence spectra from each pigment application. **(a)** to **(f)** corresponds linearly with samples A to F.

From the unconcealed and one-layer concealment, the emission peaks showed a consistent peak value from 896–899 nm. This is lower than the reported literature values for Egyptian blue luminescence [6, 159]. The emission signature from the two-layer concealment were inconsistent and asymmetric, but peaks attributable to Egyptian blue were visible. More analyses need to be done to see best method for extraction, but signal is visible in some areas of the covered squares. The carbon black pigment squares (Figure D.1d) did not show a reliable, consistent signature; however, in the unconcealed pigment square, peaks did appear at $\sim$ 896–899 nm.

The Egyptian blue emission does not appear to shift whether concealed or in the presence of different pigment pictures. This is expected, as the emission peak should theoretically only be affected by changes in the chemical environment, such as the presence of impurities or other changes in the chemical environment that would affect the electrostatic field around the Cu^{2+} ion, or another material in the mixtures that luminesce at $\sim$ 910–930 nm (cite

Pozza and the other papers). Furthermore, the spectral data was able to reveal the presence of Egyptian blue where the visible images could not, which is a powerful indicator for the use of luminescence imaging spectroscopy for the identification of trace or partially-masked luminescent signatures on wall paintings and polychrome decoration.

It should be noted that there is a significant response in the luminescence data set at $\sim$ 590–600 nm which increases as the layering is increased. In the case where this signal appears as a sharp rise, this suggests a potential light leak as the increase in $CaCO_3$ produces more reflection. However, in some regions, including the panel background (a gesso preparation), the emission peak shifts more towards 600 nm and broadens. This is most likely due to the fluorescence of an organic material like a binder, as the unconcealed carbon black sample shows a small fluorescence peak. On the black and white Spectralon standards recorded in the image scene, an emission signal is present at these wavelengths, but the spectral response is not uniform in shape or intensity. Further tests need to be conducted to test the cause of this signal in the spectral data and to adapt the testing method to remove the signal if possible. However, this spectral feature does not seem to impact the NIR luminescence.

Comparative analyses will also need to be done with other IS cameras (such as with the Specim IQ, which has less spectral resolution than the Surface Optics system) as well as with modified digital single-lens reflex (DSLR) cameras to compare visible responses. Also, the excitation can be swept to different wavelengths to observe the emission responses. Understanding system performances and their spectral responses, along with adapting excitation and capture conditions based on the test panel performances, will improve interpretation of complex, archaeological paintings.

Bibliography

[1] The Annual Report for the Department of Antiquities of Cyprus, 1974.

[2] High-resolution multi-spectral image archives: A hybrid approach. *Color and Imaging Conference*, 1998(1), 1998.

[3] Physical techniques in the study of art, archaeology and cultural heritage. volume 1. Elsevier, 2006.

[4] Tracking Colour: The polychromy of Greek and Roman sculpture in the Ny Carlsberg Glyptotek, 2012.

[5] Emmanuel Abraham, Ayesha Younus, Jean-Christophe Delagnes, and Patrick Mounaix. Non-invasive investigation of art paintings by terahertz imaging. *Applied Physics A*, 100(3):585–590, 2010.

[6] Gianluca Accorsi, Giovanni Verri, Margherita Bolognesi, Nicola Armaroli, Catia Clementi, Costanza Miliani, and Aldo Romani. The exceptional near-infrared luminescence properties of cuprorivaite (Egyptian blue). *Chemical Communications*, (23):3392–3394, 2009.

[7] Maurizio Aceto, Angelo Agostino, Gaia Fenoglio, Ambra Idone, Monica Gulmini, Marcello Picollo, Paola Ricciardi, and John K Delaney. Characterisation of colourants on illuminated manuscripts by portable fibre optic UV-visible-NIR reflectance spectrophotometry. *Analytical Methods*, 6(5):1488–1500, 2014.

[8] Auréle J.L. Adam, Paul Planken, Sabrina Meloni, and Joris Dik. Terahertz imaging of hidden paint layers on canvas. *Optics Express*, 17(5):3407–3416, 2009.

[9] Alfred Aldrovandi, D. Bertani, M. Cetica, M. Matteini, A. Moles, P. Poggi, and P. Tiano. Multispectral image processing of paintings. *Studies in Conservation*, 33(3):154–159, 1988.

[10] Matthias Alfeld, Maud Mulliez, Jonathan Devogelaere, Laurence De Viguerie, Philippe Jockey, and Philippe Walter. Ma-xrf and hyperspectral reflectance imaging for visualizing traces of antique polychromy on the frieze of the siphnian treasury. *Microchemical Journal*, 141:395–403, 2018.

[11] Matthias Alfeld, Silvia Pedetti, Philippe Martinez, and Philippe Walter. Joint data treatment for Vis–NIR reflectance imaging spectroscopy and XRF imaging acquired in the Theban Necropolis in Egypt by data fusion and t-SNE. *Comptes Rendus Physique*, 19(7):625–635, 2018.

[12] Chryssa Apostolaki, Vassilis Perdikatsis, E Repuskou, Harikleia Brecoulaki, and Sarah Lepinski. Analysis of Roman wall paintings from ancient Corinth/Greece. *Advances in mineral resources management and environmental geotechnology. Hania*, pages 729–734, 2006.

[13] Lorenzo Appolonia, Davide Vaudan, Valentina Chatel, Maurizio Aceto, and Piero Mirti. Combined use of FORS, XRF and Raman spectroscopy in the study of mural paintings in the Aosta Valley (Italy). *Analytical and Bioanalytical Chemistry*, 395(7):2005–2013, Dec 2009.

[14] Sebastien Aze, Jean-Marc Vallet, V Detalle, Olivier Grauby, and Alain Baronnet. Chromatic alterations of red lead pigments in artworks: A review. *Phase Transitions - PHASE TRANSIT*, 81:145–154, 02 2008.

[15] Mauro Bacci, Marcello Picollo, Giorgio Trumpy, Masahiko Tsukada, and Diane Kunzelman. Non-invasive identification of white pigments on 20th-century oil paintings by using fiber optic reflectance spectroscopy. *Journal of the American Institute for Conservation*, 46(1):27–37, 2007.

[16] Claire Balandier, Celine Joliot, Matthieu Menager, Frederique Vouve, and Catherine Vieillescazes. Chemical analyses of Roman wall paintings recently found in Paphos, Cyprus: The complementarity of archaeological and chemical studies. *Journal of Archaeological Science: Reports*, 14:332–339, 2017.

[17] Stefano Baronti, Andrea Casini, Franco Lotti, and Simone Porcinai. Multispectral imaging system for the mapping of pigments in works of art by use of principal-component analysis. *Applied optics*, 37(8):1299–1309, 1998.

[18] David B. Bennett, Zachary D. Taylor, Shijun Sung, Neha Bajwa, Ashkan Maccabi, Rahul S. Singh, Priyamvada Tewari, Martin O. Culjat, Warren S. Grundfest, and Elliot R. Brown. Terahertz time-lapse video of hydration in physiological tissues. *SPIE BiOS, San Fransisco, CA*, 2011.

[19] David B. Bennett, Zachary D. Taylor, Priyamvada Tewari, Rahul S. Singh, Martin O. Culjat, Warren S. Grundfest, Daniel J. Sassoon, R. Duncan Johnson, Jean-Pierre Hubschman, and Elliott R. Brown. Terahertz sensing in corneal tissues. *Journal of biomedical optics*, 16(5):057003–057003, 2011.

[20] Heinz Berke. The invention of blue and purple pigments in ancient times. *Chemical Society Reviews*, 36(1):15–30, 2007.

[21] Michael S. Bessell. Standard photometric systems. *Annual Review of Astronomy and Astrophysics*, 43(1):293–336, 2005.

[22] Janice L. Bishop, Melissa D. Lane, Melinda D. Dyar, and Adrian J. Brown. Reflectance and emission spectroscopy study of four groups of phyllosilicates: smectites, kaolinite-serpentines, chlorites and micas. *Clay minerals*, 43(1):35–54, 2008.

[23] Bernhard Blümich, Federico Casanova, Juan Perlo, Federica Presciutti, Chiara Anselmi, and Brenda Doherty. Noninvasive testing of art and cultural heritage by mobile nmr. *Accounts of Chemical Research*, 43(6):761–770, 2010. PMID: 20345119.

[24] Joseph W Boardman. Analysis, understanding, and visualization of hyperspectral data as convex sets in n space. In *Imaging spectrometry*, volume 2480, pages 14–22. International Society for Optics and Photonics, 1995.

[25] Joseph W. Boardman. Leveraging the high dimensionality of AVIRIS data for improved sub-pixel target in unmixing and rejection of false positives : Mixture Tuned Matched Filtering. 1998.

[26] Barbara E. Borg. Painted funerary portraits. 2010.

[27] Harikleia Brecoulaki. Precious colours in ancient Greek polychromy and painting: Material aspects and symbolic values. *Revue Archéologique*, (1):3–35, 2014.

[28] Harikleia Brecoulaki, Sophia Sotiropoulou, Christos Katsifas, and Andreas G Karydas. A microcosm of colour and shine. the polychromy of chryselephantine couches from ancient Macedonia. *Technè: la science au service de l'histoire de l'art et des civilisations*, (40):p–9, 2014.

[29] Cecilie Brøns and Maria Papadopoulou. True colours: Polychromy in ancient Greek art and its dissemination in museum collections.

[30] Christopher J. Brooke. Ground-based remote sensing for archaeological information recovery in historic buildings. *International Journal of Remote Sensing*, 8(7):1039–1048, 1987.

[31] Elliott R. Brown, Zachary D. Taylor, Priyamvada Tewari, Rahul S. Singh, Martin O. Culjat, David B. Bennett, and Warren S. Grundfest. THz imaging of skin tissue? exploiting the strong reflectivity of liquid water. In *Infrared Millimeter and Terahertz Waves (IRMMW-THz), 2010 35th International Conference on*, pages 1–2. IEEE, 2010.

[32] Bruno G. Brunetti, Mauro Matteini, Costanza Miliani, Luca Pezzati, and Daniela Pinna. MOLAB, a mobile laboratory for in situ non-invasive studies in arts and archaeology. In *Lasers in the Conservation of Artworks*, pages 453–460. Springer, 2007.

[33] Nicola Brusco, S. Capeleto, M. Fedel, Anna Paviotti, Luca Poletto, Guido M. Cortelazzo, and Giuseppe Tondello. A system for 3d modeling frescoed historical buildings with multispectral texture information. *Machine Vision and Applications*, 17(6):373–393, Dec 2006.

[34] Earle Radcliffe Caley. The Leyden Papyrus X. An English translation with brief notes. *Journal of Chemical Education*, 3(10):1149, 1926.

[35] Earle Radcliffe Caley. The Stockholm Papyrus. an English translation with brief notes. *Journal of Chemical Education*, 4(8):979, 1927.

[36] Giuseppe Capobianco, Silvia Serranti, Giuseppe Bonifazi, and Fernanda Prestileo. Hyperspectral imaging-based approach for the in-situ characterization of ancient Roman wall paintings. *PERIODICO di MINERALOGIA*, 84(3A), 2015.

[37] Cennino Cennini and Daniel Varney Thompson. *The Craftsman's Handbook; Translated by Daniel V. Thompson, Jr.* 1954.

[38] Wai Lam Chan, Jason Deibel, and Daniel M Mittleman. Imaging with terahertz radiation. *Reports on Progress in Physics*, 70(8):1325, 2007.

[39] Eleni Cheilakou, Michail Troullinos, and Maria Koui. Identification of pigments on Byzantine wall paintings from Crete (14th century ad) using non-invasive fiber optics diffuse reflectance spectroscopy (fors). *Journal of Archaeological Science*, 41:541 – 555, 2014.

[40] Robert Chenciner. *Madder red: a history of luxury and trade*. Routledge, 2003.

[41] Roger N. Clark, Trude V.V. King, Matthew Klejwa, Gregg A. Swayze, and Norma Vergo. High spectral resolution reflectance spectroscopy of minerals. *Journal of Geophysical Research: Solid Earth*, 95(B8):12653–12680, 1990.

[42] Catia Clementi, Brenda Doherty, Pier Luigi Gentili, Costanza Miliani, Aldo Romani, Brunetto Giovanni Brunetti, and Antonio Sgamellotti. Vibrational and electronic properties of painting lakes. *Applied Physics A*, 92(1):25–33, 2008.

[43] Edward A. Cloutis, Frank C. Hawthorne, Stanley A. Mertzman, Katherine Krenn, Michael A. Craig, Dionne Marcino, Michelle Methot, Johnathon Strong, John F. Mustard, Diana L. Blaney, James F. Bell, and Faith Vilas. Detection and discrimination of sulfate minerals using reflectance spectroscopy. *Icarus*, 184(1):121 – 157, 2006.

[44] Dave Cohen, Andreas Zissimos, and Eleni Georgiou-Morisseau. *Geochemical Atlas of Cyprus*. Geological Survey Department of Cyprus, 2011.

[45] Daniela Comelli, Valentina Capogrosso, Christian Orsenigo, and Austin Nevin. Dual wavelength excitation for the time-resolved photoluminescence imaging of painted ancient Egyptian objects. *Heritage Science*, 4(1):21, 2016.

[46] Daniela Comelli, Austin Nevin, Alex Brambilla, Iacopo Osticioli, Gianluca Valentini, Lucia Toniolo, Maria Fratelli, and Rinaldo Cubeddu. On the discovery of an unusual luminescent pigment in Van Gogh's painting "Les bretonnes et le pardon de pont Aven". *Applied Physics A*, 106(1):25–34, Jan 2012.

[47] Damon M. Conover, John K. Delaney, and Murray H. Loew. Automatic registration and mosaicking of technical images of Old Master paintings. *Applied Physics A*, 119(4):1567–1575, 2015.

[48] Antonino Cosentino, Milene Gil, Manuel Ribeiro, and Raffaello Di Mauro. Technical photography for mural paintings: the newly discovered frescoes in Aci Sant'Antonio (Sicily, Italy). *Conservar Património*, (20):23–33, 2014.

[49] Costanza Cucci, Andrea Casini, Lorenzo Stefani, Marcello Picollo, and Jouni Jussila. Bridging research with innovative products: a compact hyperspectral camera for investigating artworks: a feasibility study. In *Optics for Arts, Architecture, and Archaeology VI*, volume 10331, page 1033106. International Society for Optics and Photonics, 2017.

[50] Costanza Cucci, John K. Delaney, and Marcello Picollo. Reflectance hyperspectral imaging for investigation of works of art: Old Master paintings and illuminated manuscripts. *Accounts of chemical research*, 49(10):2070–2079, 2016.

[51] Costanza Cucci, Marcello Picollo, Leandro Chiarantini, and Barbara Sereni. Hyperspectral remote sensing techniques applied to the noninvasive investigation of mural paintings: a feasibility study carried out on a wall painting by Beato Angelico in Florence. In *SPIE Optical Metrology*, pages 95270P–95270P. International Society for Optics and Photonics, 2015.

[52] Corinna Ludovica Koch Dandolo and Peter Uhd Jepsen. Wall painting investigation by means of non-invasive terahertz time-domain imaging (THz-TDI): inspection of subsurface structures buried in historical plasters. *Journal of Infrared, Millimeter, and Terahertz Waves*, 37(2):198–208, 2016.

[53] Floréal Daniel, Aurélie Mounier, Josefina Pérez-Arantegui, Carlos Pardos, Nagore Prieto-Taboada, S Fdez-Ortiz de Vallejuelo, and Kepa Castro. Hyperspectral imaging applied to the analysis of Goya paintings in the Museum of Zaragoza (Spain). *Microchemical Journal*, 126:113–120, 2016.

[54] Wiktor A. Daszewski. Nea Paphos 1990: Report. *Polish Archaeology in the Mediterranean II, Reports 1990*, pages 78–84, 1991.

[55] JRJ van Asperen De Boer. Infrared reflectography: a method for the examination of paintings. *Applied Optics*, 7(9):1711–1714, 1968.

[56] John K. Delaney, Damon M. Conover, Kathryn A. Dooley, Lisha Glinsman, Koen Janssens, and Murray Loew. Integrated X-ray fluorescence and diffuse visible-to-near-infrared reflectance scanner for standoff elemental and molecular spectroscopic imaging of paints and works on paper. *Heritage Science*, 6(1):31, May 2018.

[57] John K. Delaney, Kathryn A. Dooley, Roxanne Radpour, and Ioanna Kakoulli. Macroscale multimodal imaging reveals ancient painting production technology and the vogue in Greco-Roman Egypt. *Scientific Reports*, 7(1):15509, 2017.

[58] John K. Delaney, Mathieu Thoury, Jason G. Zeibel, Paola Ricciardi, Kathryn M. Morales, and Kathryn A. Dooley. Visible and infrared imaging spectroscopy of paintings and improved reflectography. *Heritage Science*, 4(1):6, 2016.

[59] John K Delaney, Giorgio Trumpy, Marie Didier, Paola Ricciardi, and Kathryn A Dooley. A high sensitivity, low noise and high spatial resolution multi-band infrared reflectography camera for the study of paintings and works on paper. *Heritage Science*, 5(1):32, 2017.

[60] John K. Delaney, Elizabeth Walmsley, Barbara H. Berrie, and Colin F. Fletcher. Multispectral imaging of paintings in the infrared to detect and map blue pigments. *Scientific Examination of Art: Modern Techniques in Conservation and Analysis*, pages 120–136, 2005.

[61] John K. Delaney, Jason G. Zeibel, Mathieu Thoury, Roy Littleton, Michael Palmer, Kathryn M. Morales, E. René de La Rie, and Ann Hoenigswald. Visible and infrared imaging spectroscopy of Picasso's Harlequin musician: mapping and identification of artist materials in situ. *Applied spectroscopy*, 64(6):584–594, 2010.

[62] Kathryn A. Dooley, Damon M. Conover, Lisha Deming Glinsman, and John K. Delaney. Complementary standoff chemical imaging to map and identify artist materials in an early Italian Renaissance panel painting. *Angewandte Chemie International Edition*, 53(50):13775–13779, 2014.

[63] Kathryn A. Dooley, Suzanne Lomax, Jason G. Zeibel, Costanza Miliani, Paola Ricciardi, Ann Hoenigswald, Murray Loew, and John K. Delaney. Mapping of egg yolk and animal skin glue paint binders in Early Renaissance paintings using near infrared reflectance imaging spectroscopy. *Analyst*, 138(17):4838–4848, 2013.

[64] Kathryn A. Dooley et al. Angewandte Chemie International Edition (submitted), 2019.

[65] Euphrosyne Doxiadis. *The mysterious Fayum portraits: faces from ancient Egypt*. Harry N. Abrams, 1995.

[66] Joanne Dyer, Diego Tamburini, and Sophia Sotiropoulou. The identification of lac as a pigment in ancient Greek polychromy - the case of a Hellenistic oinochoe from Canosa di Puglia. *Dyes and Pigments*, 149:122 – 132, 2018.

[67] Henry Elderfield, IG Gass, A Hammond, and LM Bear. The origin of ferromanganese sediments associated with the Troodos Massif of Cyprus. *Sedimentology*, 19(1-2):1–19, 1972.

[68] Anna Fostiridou, Ioannis Karapanagiotis, Svetlana Vivdenko, Dimitrios Lampakis, Dimitrios Mantzouris, L. Achilara, and Panagiotis Manoudis. Identification of pigments in Hellenistic and Roman funeral figurines. *Archaeometry*, 58(3):453–464, 2016.

[69] Kaori Fukunaga. Terahertz imaging in conservation. *The Encyclopedia of Archaeological Sciences*, pages 1–3, 2018.

[70] Kaori Fukunaga and Iwao Hosako. Innovative non-invasive analysis techniques for cultural heritage using terahertz technology. *Comptes Rendus Physique*, 11(7):519–526, 2010.

[71] Kaori Fukunaga, Tyler Meldrum, Wasif Zia, Misao Ohno, Takeshi Fuchida, and Bernhard Blümich. Non-destructive investigation of the internal structure of fresco paintings. In *2013 Digital Heritage International Congress (Digital Heritage)*, volume 1, pages 81–88. IEEE, 2013.

[72] Kaori Fukunaga, Yuichi Ogawa, Shin'ichiro Hayashi, and Iwao Hosako. Terahertz spectroscopy for art conservation. *IEICE Electronics Express*, 4(8):258–263, 2007.

[73] Kaori Fukunaga, Yuichi Ogawa, Shini'chiro Hayashi, and Iwao Hosako. Terahertz imaging for analysis of historic paintings and manuscripts. In *Infrared, Millimeter and Terahertz Waves, 2008. IRMMW-THz 2008. 33rd International Conference on*, pages 1–3. IEEE, 2008.

[74] Francesca Gabrieli, Kathryn A. Dooley, Michelle Facini, and John K. Delaney. Near-UV to mid-IR reflectance imaging spectroscopy of paintings on the macroscale. *Science Advances*, 5(8), 2019.

[75] William E. Gallahan and Robert A. Duncan. Spatial and temporal variability in crystallization of celadonites within the Troodos ophiolite, Cyprus: Implications for low-temperature alteration of the oceanic crust. *Journal of Geophysical Research: Solid Earth*, 99(B2):3147–3161, 1994.

[76] Gian Piero Gallerano, A Doria, Emilio Giovenale, G Messina, Alberto Petralia, Ivan Spassovsky, Kaori Fukunaga, and Iwao Hosako. THz-ARTE: non-invasive terahertz diagnostics for art conservation. In *Infrared, Millimeter and Terahertz Waves, 2008. IRMMW-THz 2008. 33rd International Conference on*, pages 1–2. IEEE, 2008.

[77] Monica Ganio, Johanna Salvant, Jane Williams, Lynn Lee, Oliver Cossairt, and Marc Walton. Investigating the use of Egyptian blue in Roman Egyptian portraits and panels from Tebtunis, Egypt. *Applied Physics A*, 121(3):813–821, 2015.

[78] Pablo García-Fernandez, Miguel Moreno, and Jose Antonio Aramburu. Origin of the exotic blue color of copper-containing historical pigments. *Inorganic chemistry*, 54(1):192–199, 2014.

[79] Isabel Garofano, Jose Luis Perez-Rodriguez, Maria Dolores Robador, and Adrian Duran. An innovative combination of non-invasive UV–Visible-FORS, XRD and XRF techniques to study Roman wall paintings from Seville, Spain. *Journal of Cultural Heritage*, 22:1028 – 1039, 2016.

[80] Svetlana Gasanova, Sandrine Pagès-Camagna, Maria Andrioti, and Sorin Hermon. Non-destructive in situ analysis of polychromy on ancient Cypriot sculptures. *Archaeological and Anthropological Sciences*, 10(1):83–95, 2018.

[81] L3 Harris Geospatial. What is Raster Data? [Online].

[82] Chiara Germinario, Izzo Francesco, Mariano Mercurio, Alessio Langella, Diego Sali, Ioanna Kakoulli, Alberto De Bonis, and Celestino Grifa. Multi-analytical and non-invasive characterization of the polychromy of wall paintings at the Domus of Octavius Quartio in Pompeii. *The European Physical Journal Plus*, 133(9):359, 2018.

[83] Rutherford J. Gettens, Robert L. Feller, and W. T. Chase. Vermilion and Cinnabar. *Studies in Conservation*, 17(2):45–69, 1972.

[84] Rutherford J. Gettens, Hermann Kühn, and W. T. Chase. Lead white. *Studies in Conservation*, 12(4):125–139, 1967.

[85] Daniel E. Gibbons and Richard R. Richard. Determination of noise equivalent reflectance for a multispectral scanner: A scanner sensitivity study. 1979.

[86] Alexander F.H. Goetz. Three decades of hyperspectral remote sensing of the Earth: A personal view. *Remote Sensing of Environment*, 113:S5–S16, 2009.

[87] Alma Montserrat Gomez-Sepulveda, Arturo I Hernandez-Serrano, Roxanne Radpour, Corinna L Koch-Dandolo, S. Carolina Rojas-Landeros, LF Ascencio-Rojas, Alvaro Zarate, Gerardo Hernandez, RC Gonzalez-Tirado, M Insaurralde-Caballero, et al. History of Mexican easel paintings from an altarpiece revealed by non-invasive terahertz time-domain imaging. *Journal of Infrared, Millimeter, and Terahertz Waves*, 38(4):403–412, 2017.

[88] Victor Gonzalez, Didier Gourier, Thomas Calligaro, Kathleen Toussaint, Gilles Wallez, and Michel Menu. Revealing the origin and history of lead-white pigments by their photoluminescence properties. *Analytical chemistry*, 89(5):2909–2918, 2017.

[89] Sergo V. Gotoshia and Lamara V. Gotoshia. Laser Raman and resonance Raman spectroscopies of natural semiconductor mineral cinnabar, α-HgS, from various mines. *Journal of Physics D: Applied Physics*, 41(11):115406, 2008.

[90] Chiara Grazia, Catia Clementi, Costanza Miliani, and Aldo Romani. Photophysical properties of alizarin and purpurin Al (iii) complexes in solution and in solid state. *Photochemical & Photobiological Sciences*, 10(7):1249–1254, 2011.

[91] Celestino Grifa, Laetitia Cavassa, Alberto De Bonis, Chiara Germinario, Vincenza Guarino, Francesco Izzo, Ioanna Kakoulli, Alessio Langella, Mariano Mercurio, and Vincenzo Morra. Beyond Vitruvius: new insight in the technology of Egyptian blue and green frits. *Journal of the American Ceramic Society*, 99(10):3467–3475, 2016.

[92] John H. Gruninger, Anthony J. Ratkowski, and Michael L. Hoke. The Sequential Maximum Angle Convex Cone (SMACC) endmember model. In *Algorithms and technologies for multispectral, hyperspectral, and ultraspectral imagery X*, volume 5425, pages 1–14. International Society for Optics and Photonics, 2004.

[93] Anne-Marie Guimier-Sorbets and Demetrios Michaelides. Alexandrian influences on the architecture and decoration of the Hellenistic tombs of Cyprus. In *Proceedings of the International ConferenceEgyptand Cyprus in Antiquity Nicosia*, pages 3–6, 2003.

[94] Agnes Haber, Bernhard Blümich, Daria Souvorova, and Eleonora Del Federico. Ancient Roman wall paintings mapped non-destructively by portable NMR. *Analytical and Bioanalytical Chemistry*, 401(4):1441, Jun 2011.

[95] Maria Hadjicosti, Ioannis Hadjisavvas, Demetris Michaelides, Andreas Foulias, Giorgos Philotheou, Aikaterini Chr. Aristeidou, Christos Aristeidou, Chr. Andreou, Petros Papapolyviou, Euphrosyne Rizopoulou-Egoumenidou, Evi Fiouri, Maria Philokyprou, Christodoulos Hadjichristodoulou, and Andreas Constantinides. *Geroskipou: From Antiquity to the Present*. Chr. Andreou Publishers, 2008.

[96] Gareth D. Hatton, Andrew J. Shortland, and Michael S. Tite. The production technology of Egyptian blue and green frits from second millennium bc Egypt and Mesopotamia. *Journal of Archaeological Science*, 35(6):1591–1604, 2008.

[97] Signe Buccarella Hedeaard, Cecilie Brøns, Iulian Drug, Pavel Saulins, Christian Bercu, Alexandr Jakovlev, and Lars Kjær. Multispectral Photogrammetry: 3D models highlighting traces of paint on ancient sculptures. In *DHN*, pages 181–189, 2019.

[98] Fabrice Heitz, Henri Maître, and Charles de Couessin. Event detection in multisource imaging: application to fine arts painting analysis. *IEEE transactions on acoustics, speech, and signal processing*, 38(4):695–704, 1990.

[99] Mona Hess and Stuart Robson. 3D colour imaging for cultural heritage artefacts. 2010.

[100] David Hradil, Tomáš Grygar, Janka Hradilová, and Petr Bezdička. Clay and iron oxide pigments in the history of painting. *Applied Clay Science*, 22(5):223–236, 2003.

[101] Binbin B. Hu and Martin C. Nuss. Imaging with terahertz waves. *Optics letters*, 20(16):1716–1718, 1995.

[102] J. Bianca Jackson, John Bowen, Gillian Walker, Julien Labaune, Gerard Mourou, Michel Menu, and Kaori Fukunaga. A survey of terahertz applications in cultural heritage conservation science. *Terahertz Science and Technology, IEEE Transactions on*, 1(1):220–231, 2011.

[103] J. Bianca Jackson, Marie Mourou, John F. Whitaker, Irl N. Durling III, Steven L. Williamson, Michel Menu, and Gérard A. Mourou. Terahertz imaging for non-destructive evaluation of mural paintings. *Optics Communications*, 281(4):527–532, 2008.

[104] Heiner Jaksch, Werner Seipel, Kenneth L. Weiner, and Ahmed El Goresy. Egyptian blue—cuprorivaite a window to ancient Egyptian technology. *Naturwissenschaften*, 70(11):525–535, 1983.

[105] Elżbieta Jastrzebowska. Wall paintings from the House of Aion at Nea Paphos. *Polish Archaeology in the Mediterranean 27/1*, pages 527–597.

[106] Ioanna Kakoulli. Hellenistic and Roman wall paintings in Cyprus: a scientific examination of their technology. Master's thesis, Courtauld Institute of Art, University of London, 1995.

[107] Ioanna Kakoulli. Late Classical and Hellenistic painting techniques and materials: a review of the technical literature. *Studies in Conservation*, 47(sup1):56–67, 2002.

[108] Ioanna Kakoulli. Egyptian blue in Greek painting between 2500 and 50 BC. *From Mine to Microscope: Advances in the Study of Ancient Technology*, pages 101–112, 2009.

[109] Ioanna Kakoulli. *Greek painting techniques and materials from the fourth to the first century BC*. 2009.

[110] Ioanna Kakoulli and Christian Fischer. An innovative noninvasive and nondestructive multidisciplinary approach for the technical study of the Byzantine wall paintings in the Enkleistra of St. Neophytos in Paphos, Cyprus (Phase I). Dumbarton Oaks Report, 2008-2009.

[111] Ioanna Kakoulli and Christian Fischer. The techniques and materials of the wall paintings at the Enkleistra of St. Neophytos (Phase II). Dumbarton Oaks Report, 2011-2012.

[112] Ioanna Kakoulli, Christian Fischer, and Demetrios Michaelides. Painted rock-cut tombs in Cyprus from the Hellenistic and Roman periods to Byzantium: material properties, degradation processes and sustainable preservation strategies. *Studies in Conservation*, 55(sup2):96–102, 2010.

[113] Ioanna Kakoulli, Roxanne Radpour, Yuan Lin, Marie Svoboda, and Christian Fischer. Application of forensic photography for the detection and mapping of Egyptian blue and madder lake in Hellenistic polychrome terracottas based on their photophysical properties. *Dyes and Pigments*, 136:104–115, 2017.

[114] Vasiliki Kassianidou. Mining landscapes of prehistoric Cyprus. *Metalla*, 20(2):5–57, 2013.

[115] Eva Keuls. Skiagraphia once again. *American Journal of Archaeology*, 79(1):1–16, 1975.

[116] Min H. Kim, Todd Alan Harvey, David S. Kittle, Holly Rushmeier, Julie Dorsey, Richard O. Prum, and David J. Brady. 3D imaging spectroscopy for measuring hyperspectral patterns on solid objects. *ACM Trans. Graph.*, 31(4):38:1–38:11, July 2012.

[117] Corinna L. Koch-Dandolo, Troels Filtenborg, Kaori Fukunaga, Jacob Skou-Hansen, and Peter Uhd Jepsen. Reflection terahertz time-domain imaging for analysis of an 18th century Neoclassical easel painting. *Applied optics*, 54(16):5123–5129, 2015.

[118] Eleni Kotoula et al. Reflectance transformation imaging beyond the visible: ultraviolet reflected and ultraviolet induced visible fluorescence. In *Proceedings of the 43rd Annual Conference on Computer Applications and Quantitative Methods in Archaeology, Oxford*, pages 909–919, 2015.

[119] Anestis Koutsoudis, George Pavlidis, Fotis Arnaoutoglou, Despina Tsiafakis, and Christodoulos Chamzas. Qp: A tool for generating 3D models of ancient Greek pottery. *Journal of Cultural Heritage*, 10(2):281 – 295, 2009.

[120] Anestis Koutsoudis, Blaž Vidmar, George Ioannakis, Fotis Arnaoutoglou, George Pavlidis, and Christodoulos Chamzas. Multi-image 3D reconstruction data evaluation. *Journal of Cultural Heritage*, 15(1):73 – 79, 2014.

[121] Fred A. Kruse. Use of Airborne Imaging Spectrometer data to map minerals associated with hydrothermally altered rocks in the northern Grapevine mountains, Nevada, and California. *Remote Sensing of Environment*, 24(1):31–51, 1988.

[122] Horst Kunkely and Arnd Vogler. Absorption and luminescence spectra of cochineal. *Inorganic Chemistry Communications*, 14(7):1153–1155, 2011.

[123] The Jet Propulsion Laboratory. Airborne Visible InfraRed Imaging Spectrometer (AVIRIS). [Online].

[124] M. Gabriela Lagorio, Lelia E. Dicelio, Marta I. Litter, and Enrique San Román. Modeling of fluorescence quantum yields of supported dyes aluminium carboxyphthalocyanine on cellulose. *J. Chem. Soc., Faraday Trans.*, 94:419–425, 1998.

[125] Sophia Lahlil, Matthieu Lebon, Lucile Beck, Hélène Rousselière, Colette Vignaud, Ina Reiche, Michel Menu, Patrick Paillet, and Frédéric Plassard. The first in situ micro-Raman spectroscopic analysis of prehistoric cave art of Rouffignac St-Cernin, France. *Journal of Raman Spectroscopy*, 43(11):1637–1643, 2012.

[126] Luca Lanteri, Giorgia Agresti, and Claudia Pelosi. A new practical approach for 3D documentation in ultraviolet fluorescence and infrared reflectography of polychromatic sculptures as fundamental step in restoration. *Heritage*, 2(1):207–215, 2019.

[127] Marco Leona. Microanalysis of organic pigments and glazes in polychrome works of art by surface-enhanced resonance Raman scattering. *Proceedings of the National Academy of Sciences*, 106(35):14757–14762, 2009.

[128] José Luis Lerma, Talal Akasheh, Naif Haddad, and Miriam Cabrelles. Multispectral sensors in combination with recording tools for cultural heritage documentation. *Change over time*, 1(2):236–250, 2011.

[129] Haida Liang. Advances in multispectral and hyperspectral imaging for archaeology and art conservation. *Applied Physics A*, 106(2):309–323, Feb 2012.

[130] Haida Liang, Andrei Lucian, Rebecca Lange, Chi Shing Cheung, and Bomin Su. Remote spectral imaging with simultaneous extraction of 3D topography for historical wall paintings. *ISPRS Journal of Photogrammetry and Remote Sensing*, 95:13 – 22, 2014.

[131] Ravit Linn. Layered pigments and painting technology of the Roman wall paintings of Caesarea Maritima. *Journal of Archaeological Science: Reports*, 11:774–781, 2017.

[132] Maite Maguregui, Ulla Knuutinen, Irantzu Martínez-Arkarazo, Anastasia Giakoumaki, Kepa Castro, and Juan M. Madariaga. Field Raman analysis to diagnose the conservation state of excavated walls and wall paintings in the archaeological site of Pompeii (Italy). *Journal of Raman Spectroscopy*, 43(11):1747–1753, 2012.

[133] Cyril A Mango and Ernest JW Hawkins. *The hermitage of St. Neophytos and its wall paintings*. Trustees for Harvard University, the Dumbarton Oaks Research Library, 1942.

[134] Dimitris Manolakis, David Marden, Gary A Shaw, et al. Hyperspectral image processing for automatic target detection applications. *Lincoln laboratory journal*, 14(1):79–116, 2003.

[135] Dimitrios Mantzouris and Ioannis Karapanagiotis. Armenian cochineal (*Porphyrophora hamelii*) and purpurin-rich madder in ancient polychromy. *Coloration Technology*, 131(5):370–373, 2015.

[136] Hubert Mara, Bernd Breuckmann, and Claudia Lang-Auinger. Multi-spectral high-resolution 3D-acquisition for rapid archaeological documentation and analysis. In *2009 17th European Signal Processing Conference*, pages 1205–1209, Aug 2009.

[137] Aurore Mathys, R Jadinon, and Pierre Hallot. Exploiting 3d multispectral texture for a better feature identification for cultural heritage. *ISPRS Annals of the Photogrammetry, Remote Sensing and Spatial Information Sciences*, 4(W6):91–97, 2019.

[138] Demetrios Michaelides. Cypriot painted tombs and their ceilings. In *Plafonds et voûtes à l'époque antique. Actes du VIIIe Colloque International de l'Association Internationale pour la Peinture Murale Antique*. Pytheas Publishing, 2004.

[139] Stella Miller. Hellenistic painting in the eastern Mediterranean, mid-fourth to mid-first century B.C. In Jerome Jordan Pollitt, editor, *The Cambridge history of painting in the classical world*. Cambridge University Press, 2014.

[140] Piero Mirti, Lorenzo Appolonia, Antonella Casoli, Rosa P. Ferrari, Enzo Laurenti, A Amisano Canesi, and Giacomo Chiari. Spectrochemical and structural studies on a Roman sample of Egyptian blue. *Spectrochimica Acta Part A: Molecular and Biomolecular Spectroscopy*, 51(3):437–446, 1995.

[141] Daniel M Mittleman, Rune H Jacobsen, and Martin C Nuss. T-ray imaging. *Selected Topics in Quantum Electronics, IEEE Journal of*, 2(3):679–692, 1996.

[142] Morris Hicky Morgan. Vitruvius. *De Architectura translated by MH Morgan (Vitruvius: The Ten Books on Architecture. 1960 edition (first published 1914). New York*, 1960.

[143] The J. Paul Getty Museum. The APPEAR (Ancient Panel Paintings: Examination, Analysis, and Research) Project. [Online].

[144] NASA. Moderate resolution Imaging Spectroradiometer (MODIS). [Online].

[145] Marco Nicola, Maurizio Aceto, Vincenzo Gheroldi, Roberto Gobetto, and Giacomo Chiari. Egyptian blue in the Castelseprio mural painting cycle. imaging and evidence of a non-traditional manufacture. *Journal of Archaeological Science: Reports*, 19:465–475, 2018.

[146] Kyriakos Nicolaou. Archaeological News from Cyprus, 1977-1978. *American Journal of Archaeology*, 84(1):63–73, 1980.

[147] Dionysios (of Fourna) and P. Hetherington. *The 'Painter's Manual' of Dionysius of Fourna: An English Translation [from the Greek] with Commentary of Cod. Gr. 708 in the Saltykov-Shchedrin State Public Library, Leningrad*. Oakwood Press & Video Library, 1981.

[148] Maitane Olivares, Kepa Castro, M. Soledad Corchón, Diego Gárate, Xabier Murelaga, Alfredo Sarmiento, and Nestor Etxebarria. Non-invasive portable instrumentation to study Palaeolithic rock paintings: the case of La Peña Cave in San Roman de Candamo (Asturias, Spain). *Journal of Archaeological Science*, 40(2):1354 – 1360, 2013.

[149] Umberto Pappalardo. *The Splendor of Roman Wall Painting*. Getty Publications, 2009.

[150] George Pavlidis, Anestis Koutsoudis, Fotis Arnaoutoglou, Vassilios Tsioukas, and Christodoulos Chamzas. Methods for 3D digitization of cultural heritage. *Journal of Cultural Heritage*, 8(1):93 – 98, 2007.

[151] Anna Pelagotti, Andrea Del Mastio, Francesca Uccheddu, and Fabio Remondino. Automated multispectral texture mapping of 3D models. *2009 17th European Signal Processing Conference*, pages 1215–1219, 2009.

[152] Maite Pérez-Alonso, Kepa Castro, Irantzu Martinez-Arkarazo, Mishell Angulo, Maria A. Olazabal, and Juan M. Madariaga. Analysis of bulk and inorganic degradation products of stones, mortars and wall paintings by portable Raman microprobe spectroscopy. *Analytical and Bioanalytical Chemistry*, 379(1):42–50, May 2004.

[153] Jose Luis Perez-Rodriguez, Maria del Carmen Jimenez de Haro, Belinda Siguenza, and José María Martinez-Blanes. Green pigments of Roman mural paintings from Seville Alcazar. *Applied Clay Science*, 116-117:211 – 219, 2015.

[154] Athena Van Der Perre, Hendrik Hameeuw, Vanessa Boschloos, Luc Delvaux, France Ossieur, Bruno Vandermeulen, Marc Proesmans, and Dennis Braekmans. Final report Brain.be Pioneer Project BR/121/PI/EES: CONSERVATION, IR, UV AND 3D-IMAGING: THE EGYPTIAN EXECRATION STATUETTES PROJECT (EES), 2018.

[155] Marcello Picollo, Mauro Bacci, Andrea Casini, Franco Lotti, Simone Porcinai, Bruno Radicati, and Lorenzo Stefani. *Fiber Optics Reflectance Spectroscopy: A Non-destructive Technique for the Analysis of Works of Art*, pages 259–265. Springer US, Boston, MA, 2000.

[156] Marcello Picollo, Yohsei Kohdzuma, Kaori Fukunaga, and Iwao Hosako. Application of terahertz imaging methodologies for the investigation of paintings. In *Int. Conf. on nondestructive investigations and microanalysis for the diagnostics and conservation of cultural and environmental heritage (ART 2011)*, pages 13–15, 2011.

[157] Ruggero Pintus, Kazim Pal, Ying Yang, Tim Weyrich, Enrico Gobbetti, and Holly Rushmeier. A survey of geometric analysis in cultural heritage. *Computer Graphics Forum*, 35(1):4–31, 2016.

[158] Pliny. Natural History, Vol. IX: Books XXXIII–XXXV. *With an English translation by H. Rackham.(Loeb Classical Library.), 1954. The Classical Review*, 4(2):136–138.

[159] Giorgio Pozza, David Ajò, Giacomo Chiari, Franco De Zuane, and Marialuisa Favaro. Photoluminescence of the inorganic pigments Egyptian blue, Han blue and Han purple. *Journal of Cultural Heritage*, 1(4):393–398, 2000.

[160] Roxanne Radpour, Neha Bajwa, James Garritano, Shijun Sung, Magdalena Balonis-Sant, Priyamvada Tewari, Warren Grundfest, Ioanna Kakoulli, and Zachary Taylor. THz imaging studies of painted samples to guide cultural heritage investigations at the Enkleistra of St. Neophytos in Paphos, Cyprus. In *SPIE Optical Engineering+ Applications*, pages 91990Q–91990Q. International Society for Optics and Photonics, 2014.

[161] Roxanne Radpour, Christian Fischer, and Ioanna Kakoulli. New insight into Hellenistic and Roman Cypriot wall paintings: An exploration of artists' materials, production technology, and technical style. *Arts*, 8(2), 2019.

[162] Roxanne Radpour, Yuan Lin, Marie Svoboda, Giacomo Chiari, Christian Fischer, and Ioanna Kakoulli. Materials characterization of Greco-Roman mummy portraits using forensic photography and noninvasive spectroscopy. Presented at Technart 2017, May 3, 2017, Bilbao, Spain, 2017.

[163] Eustathios Raptou. A painted Roman tomb at Paphos (pm 3510). *Mediterranean Archaeology*, pages 311–321, 2004.

[164] Eustathios Raptou. Painted tombs of Roman Paphos. *Κυπριακή Αρχαιολογία Τόμος V (Archaeologia Cypria, Volume V)*, 2007.

[165] Fabio Remondino, Stefano Girardi, Alessandro Rizzi, and Lorenzo Gonzo. 3D modeling of complex and detailed cultural heritage using multi-resolution data. *J. Comput. Cult. Herit.*, 2(1):2:1–2:20, July 2009.

[166] Limin Ren, David R. Cohen, Neil F. Rutherford, Andreas M. Zissimos, and Eleni G. Morisseau. Reflections of the geological characteristics of Cyprus in soil rare earth element patterns. *Applied Geochemistry*, 56:80 – 93, 2015.

[167] Francois P Retief and Louise Cilliers. Lead poisoning in ancient Rome. *Acta Theologica*, 26(2):147–164, 2006.

[168] Neda Rohani, Emeline Pouyet, Marc Walton, Oliver Cossairt, and Aggelos K. Katsaggelos. Nonlinear unmixing of hyperspectral datasets for the study of painted works of art. *Angewandte Chemie*, 130(34):11076–11080, 2018.

[169] Johanna. Salvant, J. Williams, M. Ganio, F. Casadio, C. Daher, K. Sutherland, L. Monico, F. Vanmeert, S. De Meyer, K. Janssens, C. Cartwright, and M. Walton. A Roman Egyptian painting workshop: Technical investigation of the portraits from Tebtunis, Egypt. *Archaeometry*, 60(4):815–833, 2018.

[170] David Saunders and Johan Cupitt. Image processing at the National Gallery: The VASARI project. *National Gallery technical bulletin*, 14(1):72–85, 1993.

[171] Kyriakos Savvopoulos. *Alexandria in Aegypto: The role of Egyptian Tradition in the Hellenistic and Roman periods.* dissertation, Universiteit Leiden, 2011.

[172] Sebastiano Sciuti, Gabriele Fronterotta, Margherita Vendittelli, Antonio Longoni, and Carlo Fiorini. A non-destructive analytical study of a recently discovered Roman wall painting. *Studies in Conservation*, 46(2):132–140, 2001.

[173] David A. Scott. A review of ancient Egyptian pigments and cosmetics. *Studies in Conservation*, 61(4):185–202, 2016.

[174] Gary A Shaw and Hsiao-Hua K Burke. Spectral imaging for remote sensing. *Lincoln Laboratory Journal*, 14(1):3–28, 2003.

[175] Ruth Siddall. Not a day without a line drawn. *InFocus Magazine: Proc. R. Microsc. Soc*, 2:18–23, 2006.

[176] Camille Simon, Uwe Huxhagen, Alamin Mansouri, Adrian Heritage, Frank Boochs, and Franck S. Marzani. Integration of high-resolution spatial and spectral data acquisition systems to provide complementary datasets for cultural heritage applications. In David G. Stork, Jim Coddington, and Anna Bentkowska-Kafel, editors, *Computer Vision and Image Analysis of Art*, volume 7531, pages 166 – 174. International Society for Optics and Photonics, SPIE, 2010.

[177] Camille Simon, Alamin Mansouri, Franck Marzani, and Frank Boochs. Integration of 3D and multispectral data for cultural heritage applications: Survey and perspectives. *Image Vision Comput.*, 31:91–102, 2013.

[178] Rahul S. Singh, Zachary D. Taylor, Priyamvada Tewari, David Bennett, Martin O. Culjat, Hua Lee, Elliott R. Brown, and Warren S. Grundfest. THz imaging of skin hydration: motivation for the frequency band. In *BiOS*, pages 755513–755513. International Society for Optics and Photonics, 2010.

[179] Rahul S. Singh, Priyamvada Tewari, Jean Louis Bourges, Jean Pierre Hubschman, David B. Bennett, Zachary D. Taylor, Hua Lee, Elliott R. Brown, Warren S. Grundfest, and Martin O. Culjat. Terahertz sensing of corneal hydration. In *Engineering in Medicine and Biology Society (EMBC), 2010 Annual International Conference of the IEEE*, pages 3021–3024. IEEE, 2010.

[180] Eliana Siotto, Marco Callieri, Matteo Dellepiane, and Roberto Scopigno. Ancient polychromy: Study and virtual reconstruction using open source tools. *JOCCH*, 8:16:1–16:20, 2015.

[181] Sophia Sotiropoulou, Sister Daniilia, Costanza Miliani, Francesca Rosi, Laura Cartechini, and Demetra Papanikola-Bakirtzis. Microanalytical investigation of degradation issues in Byzantine wall paintings. *Applied Physics A*, 92(1):143–150, Jul 2008.

[182] Sophia Sotiropoulou, Ioannis Karapanagiotis, L Meijer, N Guyard, L Skaltsounis, and G Eisenbrand. Conchylian purple investigation in prehistoric wall paintings of the Aegean area. *Indirubin, the red shade of indigo*, pages 71–78, 2006.

[183] Charles A. Stewart. *Domes of Heaven: The Domed Basilicas of Cyprus*. ProQuest LLC, 2016.

[184] Jonathan Y. Suen, Wenzao Li, Zachary D. Taylor, and Elliott R. Brown. Characterization and modeling of a terahertz photoconductive switch. *Applied Physics Letters*, 96(14):141103, 2010.

[185] Meijun Sun, Dong Zhang, Zheng Wang, Jinchang Ren, Bolong Chai, and Jizhou Sun. What's wrong with the murals at the Mogao Grottoes: a near-infrared hyperspectral imaging method. *Scientific reports*, 5, 2015.

[186] Shijun Sung. *Terahertz Imaging and Remote Sensing Design for Applications in Medical Imaging*. PhD thesis, UCLA, 2013.

[187] Abu Md Niamul Taufique and David W Messinger. Hyperspectral pigment analysis of cultural heritage artifacts using the opaque form of Kubelka-Munk theory. In *Algorithms, Technologies, and Applications for Multispectral and Hyperspectral Imagery XXV*, volume 10986, page 1098611. International Society for Optics and Photonics, 2019.

[188] Zachary D. Taylor, Elliott R. Brown, Jon E. Bjarnason, Maxwell P. Hanson, and Arthur C. Gossard. Resonant-optical-cavity photoconductive switch with 0.5% conversion efficiency and 1.0 W peak power. *Optics letters*, 31(11):1729–1731, 2006.

[189] Zachary D. Taylor, Rahul S. Singh, David B. Bennett, Priyamvada Tewari, Colin P. Kealey, Neha Bajwa, Martin O. Culjat, Alexander Stojadinovic, Hua Lee, J-P Hubschman, et al. THz medical imaging: in vivo hydration sensing. *Terahertz Science and Technology, IEEE Transactions on*, 1(1):201–219, 2011.

[190] Zachary D. Taylor, Rahul S. Singh, Martin O. Culjat, Jonathan Y. Suen, Warren S. Grundfest, and Elliot R. Brown. THz imaging based on water-concentration contrast. In *SPIE Defense and Security Symposium*, pages 69490D–69490D. International Society for Optics and Photonics, 2008.

[191] Zachary D. Taylor, Rahul S. Singh, MO Culjat, Jonathan Y Suen, Warren S. Grundfest, Hua Lee, and Elliot R. Brown. Reflective terahertz imaging of porcine skin burns. *Optics letters*, 33(11):1258–1260, 2008.

[192] Priyamvada Tewari, Martin O. Culjat, Zachary D. Taylor, Jonathan Y. Suen, Benjamin O. Burt, Hua Lee, Elliott R. Brown, Warren S. Grundfest, and Rahul S. Singh. Role of collagen in terahertz absorption in skin. In *SPIE BiOS: Biomedical Optics*, pages 71691A–71691A. International Society for Optics and Photonics, 2009.

[193] Priyamvada Tewari, Colin Kealey, Shijun Sung, Ashkan Maccabi, Neha Bajwa, Rahul Singh, Martin Culjat, Alexander Stojadinovic, Warren Grundfest, and Zachary D. Taylor. Advances in biomedical imaging using THz technology with applications to burn-wound assessment. In *Terahertz Technology and Applications V*, volume 8261, page 82610T. International Society for Optics and Photonics, 2012.

[194] Theophrastus. On Stones. *Introduction, Greek text, English translation, and commentary by Caley and Richards (1956)*.

[195] Mathieu Thoury, John K Delaney, E René de la Rie, Michael Palmer, Kathryn Morales, and Jay Krueger. Near-infrared luminescence of cadmium pigments: in situ identification and mapping in paintings. *Applied Spectroscopy*, 65(8):939–951, 2011.

[196] José Torrent and Vidal Barrón. Diffuse reflectance spectroscopy of iron oxides. *Encyclopedia of surface and Colloid Science*, 1:1438–1446, 2002.

[197] Paolo AM Triolo, Martina Spingardi, Giorgio A Costa, and Federico Locardi. Practical application of visible-induced luminescence and use of parasitic IR reflectance as relative spatial reference in Egyptian artifacts. *Archaeological and Anthropological Sciences*, pages 1–8, 2019.

[198] Fuan Tsai and William Philpot. Derivative analysis of hyperspectral data. *Remote Sensing of Environment*, 66(1):41–51, 1998.

[199] Masayuki Uda. In situ characterization of ancient plaster and pigments on tomb walls in Egypt using energy dispersive X-ray diffraction and fluorescence. *Nuclear Instruments and Methods in Physics Research Section B: Beam Interactions with Materials and Atoms*, 226(1-2):75–82, 2004.

[200] Giovanni Verri. The application of visible-induced luminescence imaging to the examination of museum objects. In *O3A: Optics for Arts, Architecture, and Archaeology II*, volume 7391, page 739105. International Society for Optics and Photonics, 2009.

[201] Giovanni Verri, David Saunders, Janet Ambers, and Tracey Sweek. Digital mapping of Egyptian blue : Conservation implications. *Studies in Conservation*, 55(sup2):220–224, 2010.

[202] Gillian C Walker, John W Bowen, Wendy Matthews, Soumali Roychowdhury, Julien Labaune, Gerard Mourou, Michel Menu, Ian Hodder, and J Bianca Jackson. Subsurface terahertz imaging through uneven surfaces: visualizing Neolithic wall paintings in Çatalhöyük. *Optics express*, 21(7):8126–8134, 2013.

[203] Ruth C. Westgate. Space and decoration in Hellenistic houses. *The Annual of the British School at Athens*, 95:391–426, 2000.

[204] Matthew J. Westoby, James Brasington, Neil F. Glasser, Michael J. Hambrey, and Jennifer M. Reynolds. 'Structure-from-Motion' photogrammetry: A low-cost, effective tool for geoscience applications. *Geomorphology*, 179:300 – 314, 2012.

[205] David C. Winfield. Middle and Later Byzantine wall painting methods. A comparative study. *Dumbarton Oaks Papers*, 22:61–139, 1968.

[206] Diana Wood Conroy. Roman wall paintings in the Pafos theatre. 2004.

[207] Roberta H Yuhas, Alexander FH Goetz, and Joe W Boardman. Discrimination among semi-arid landscape endmembers using the Spectral Angle Mapper (SAM) algorithm. 1992.